

**Simulation of IceACT With TARGET, Validation of the  
H.E.S.S. Simulation Chain, and a New H.E.S.S. 3D Analysis  
of the Crab Using the ABRIR Method for Improved  
Background Rejection**

Simulation von IceACT mit TARGET, Validierung der H.E.S.S. Simulationskette und eine  
neue H.E.S.S. 3D-Analyse des Krebsnebel unter Verwendung der ABRIR-Methode zur  
verbesserten Hintergrundunterdrückung

Der Naturwissenschaftlichen Fakultät  
der Friedrich-Alexander-Universität Erlangen-Nürnberg  
zur Erlangung des Doktorgrades Dr. rer. nat.

Vorgelegt von  
**Johannes Schäfer**  
aus Forchheim



Als Dissertation genehmigt von der Naturwissenschaftlichen Fakultät  
der Friedrich-Alexander-Universität Erlangen-Nürnberg

Tag der mündlichen Prüfung:

25.07.2023

Gutachter:

Prof. Dr. Stefan Funk

Prof. Dr. Manami Sasaki

Prof. Dr. Hanno Sahlmann



## Abstract

Monte Carlo simulations of extensive air showers, their Cherenkov emission, and the telescope response to this emission are essential to many modern Imaging Air Cherenkov Telescope (IACT) experiments and their event reconstruction techniques. Therefore, the validity of these simulations is of critical importance for all scientific analyses performed with the reconstructed data. One such Imaging Air Cherenkov Telescope (IACT) array is the High Energy Stereoscopic System (H.E.S.S.), featuring four small (CT1-4) and one central large-mirror telescope (CT5). A recent analysis of CT5 Crab data revealed a mismatch of  $\approx 46\%$  in the reconstructed spectral norm compared to results using CT1-4, found to be caused by an incorrect telescope response simulation. CORSIKA is used for the air shower and Cherenkov emission simulation and *sim\_telarray* to simulate the telescope response. This work presents the author's significant contributions to this Monte Carlo validation effort. Multiple discrepancies between observations and simulations are identified and include the size of the optical Point Spread Function (PSF), the atmospheric transmission profile, the telescope trigger thresholds, the mirror reflectivities, and the Night Sky Background (NSB) settings. The observed deviations are reduced to satisfactory levels, resulting in a better match between the simulated and observed telescope trigger rates. Post-validation, the deviation of the reconstructed spectral norm is reduced to  $11\%$  and now matches previous results within systematic errors.

A 3D analysis of Crab data using the ABRIR method for improved background rejection is presented and compared to the results obtained with the existing BDT approach. No statistically significant difference is found for the derived spectral and spatial parameters. Whilst the significance of calculated flux points below 10 TeV is reduced, it rises again for higher energies when the ABRIR method is used.

Background events can also be rejected by an array of telescopes that issue an event-wise veto. A candidate for such a telescope is the IceACT telescope. It is a low-cost ( $<10\text{ k}\text{€}$ ) and compact IACT conceived initially as part of the surface detector of IceCube. This work presents a simulation of a modified version of this telescope with TARGET, based on CORSIKA and *sim\_telarray*. The simulation implementation is discussed extensively and validated on data acquired during a joint measurements campaign with the H.E.S.S. array in early 2019. The determined proton energy threshold  $E_{\text{th}}^{\text{p}} = (11.3 \pm 0.5)\text{ TeV}$  is in agreement with previous estimates.



## Zusammenfassung

Monte-Carlo-Simulationen ausgedehnter Luftschauer, ihrer Cherenkov-Emission und der Reaktion des Teleskops auf diese Emission sind für viele moderne Imaging Air Cherenkov Telescope (IACT) Experimente und deren Energierekonstruktionstechniken unerlässlich. Daher ist die Gültigkeit dieser Simulationen von entscheidender Bedeutung für alle wissenschaftlichen Analysen, die mit den rekonstruierten Daten durchgeführt werden. Ein solches Imaging Air Cherenkov Telescope (IACT)-Array ist das High Energy Stereoscopic System (H.E.S.S.), das aus vier kleinen (CT1-4) und einem zentralen Großspiegelteleskop (CT5) besteht. Eine kürzlich durchgeführte Analyse der Krebsnebel-Daten von CT5 ergab eine Abweichung von  $\approx 46\%$  in der rekonstruierten Spektralnorm im Vergleich zu den Ergebnissen von CT1-4. Diese Abweichung wurde auf eine fehlerhafte Simulation der Teleskopreaktion zurückgeführt. In dieser Arbeit werden die wesentlichen Beiträge des Autors zu dieser Monte-Carlo-Validierung vorgestellt. CORSIKA wird für die Luftschauer- und Cherenkov-Emissionssimulation und *sim\_telarray* für die Simulation der Teleskopreaktion verwendet. Es wurden mehrere Diskrepanzen zwischen Beobachtungen und Simulationen identifiziert, darunter die Größe der optischen Point Spread Function (PSF), dem atmosphärischen Transmissionsprofil, den Triggerschwellen, den Spiegelreflexionsgraden und den Night Sky Background (NSB)-Einstellungen. Diese Abweichungen werden auf ein zufriedenstellendes Niveau reduziert, was zu einer besseren Übereinstimmung zwischen den simulierten und beobachteten Triggerraten der Teleskope führt. Nach der Validierung ist die Abweichung der rekonstruierten Spektralnorm auf  $11\%$  reduziert und stimmt nun mit den früheren Ergebnissen innerhalb der systematischen Fehler überein.

Eine 3D-Analyse von Krebsnebel-Daten unter Verwendung der ABRIR-Methode zur verbesserten Hintergrundunterdrückung wird vorgestellt und mit den Ergebnissen verglichen, die mit dem bestehenden Boosted Decision Tree (BDT) Ansatz erzielt werden. Für die abgeleiteten spektralen und räumlichen Parameter wird kein statistisch signifikanter Unterschied festgestellt. Während die Signifikanz der berechneten Flusspunkte unterhalb von  $10\text{ TeV}$  abnimmt, steigt sie für höhere Energien wieder an, wenn die ABRIR-Methode verwendet wird.

Hintergrundereignisse können auch durch eine Reihe von Teleskopen zurückgewiesen werden, die ein ereignisbezogenes Veto einlegen. Ein Kandidat für ein solches Teleskop ist IceACT. Es ist ein kostengünstiges ( $<10\text{ k€}$ ) und kompaktes IACT, das ursprünglich als Teil des Oberflächendetektors von IceCube konzipiert wurde. Diese Arbeit präsentiert eine Simulation einer modifizierten Version dieses Teleskops mit TARGET, basierend auf CORSIKA und *sim\_telarray*. Die Simulationsimplementierung wird ausführlich diskutiert und anhand von Daten validiert, die während einer gemeinsamen Messkampagne mit dem H.E.S.S.-Array Anfang 2019 gewonnen wurden. Die ermittelte Protonenenergieschwelle  $E_{\text{th}}^{\text{p}} = (11.3 \pm 0.5)\text{ TeV}$  stimmt mit früheren Schätzungen überein.





# Contents

<b>1</b>	<b>Cosmic Rays</b>	<b>1</b>
1.1	Diffusive Shock Acceleration . . . . .	2
1.2	Cosmic Rays Beyond the Spectral Knee . . . . .	4
1.3	Gamma Ray Emission . . . . .	5
1.3.1	Hadronic Scenario . . . . .	6
1.3.2	Leptonic Scenario . . . . .	6
<b>2</b>	<b>Detection on Earth</b>	<b>8</b>
2.1	Electromagnetic Air Showers . . . . .	8
2.2	Hadronic Air Showers . . . . .	10
2.3	Cherenkov Light . . . . .	12
2.4	Imaging Air Cherenkov Telescopes . . . . .	15
2.5	The High Energy Stereoscopic System . . . . .	17
2.5.1	Phase-I . . . . .	18
2.5.2	Phase-II . . . . .	19
2.5.3	Camera Upgrades . . . . .	19
2.5.4	Camera Calibration . . . . .	20
2.5.5	Optical Efficiency Calibration Using Muon Rings . . . . .	21
2.5.6	Atmospheric Transparency Coefficient . . . . .	24
2.5.7	Image Cleaning and Event Reconstruction . . . . .	24
2.6	Cherenkov Telescope Array . . . . .	27
2.6.1	The Camera Design for SSTs . . . . .	29
2.6.2	The TARGET ASICs . . . . .	29
2.7	Monte Carlo Simulations of Air Showers . . . . .	31
2.7.1	Air Shower Simulation With CORSIKA . . . . .	32
2.7.2	Telescope Response Simulation With <i>Sim.telarray</i> . . . . .	33
<b>3</b>	<b>Desert Air Cherenkov Telescope</b>	<b>35</b>
3.1	IceACT . . . . .	35
3.2	The Mechanical and Optical Design Of IceACT . . . . .	35
3.3	DesertACT's Modifications . . . . .	36
3.4	The Namibia Measurement Campaign . . . . .	38
3.5	A Simulation for DesertACT . . . . .	39
3.5.1	Implementation and Validation of the DesertACT Optics . . . . .	39
3.5.2	Winston Cones . . . . .	41
3.5.3	Camera Geometry . . . . .	45
3.5.4	Orafol SC 943 Fresnel lens . . . . .	48
3.5.5	Modification of the Electronic Signal Chain Based on TARGET . . . . .	62
3.5.6	First Cherenkov Shower Simulations . . . . .	65
3.5.7	Recreation of the Namibia Measurement Campaign . . . . .	73
3.5.8	Validation of the Simulation . . . . .	83
3.5.9	Determining Simulated Telescope Properties . . . . .	92
3.6	Summary and Outlook . . . . .	96

<b>4</b>	<b>Validation of the H.E.S.S. Monte Carlo Simulation Chain</b>	<b>100</b>
4.1	Basic Monte Carlo Consistency . . . . .	102
4.1.1	Telescope Optics . . . . .	102
4.1.2	Waveform-Level validation . . . . .	107
4.1.3	Atmospheric Transmission . . . . .	108
4.1.4	Telescope Trigger Threshold . . . . .	111
4.1.5	Mirror Reflectivity . . . . .	114
4.1.6	Simulated Viewcone . . . . .	115
4.2	Single Telescope Consistency . . . . .	118
4.2.1	Photo Electron Definition . . . . .	118
4.2.2	Night Sky Background Setting . . . . .	119
4.2.3	Mono Trigger Rates . . . . .	120
4.3	High-Level Array Validation . . . . .	128
4.3.1	Stereo Trigger Rates . . . . .	128
4.3.2	Image Cleaning . . . . .	131
4.4	Summary and Outlook . . . . .	132
<b>5</b>	<b>3D Analysis of the Crab Using the ABRIR Method</b>	<b>135</b>
5.1	The Crab Nebula . . . . .	135
5.2	The ABRIR Method . . . . .	136
5.3	3D Crab Analysis With <i>gammapy</i> . . . . .	139
5.3.1	Run Selection . . . . .	140
5.3.2	3D Analysis . . . . .	141
5.4	Summary and Outlook . . . . .	146
<b>A</b>	<b>Appendix A</b>	<b>153</b>
<b>B</b>	<b>Appendix B</b>	<b>163</b>
	<b>Bibliography</b>	<b>165</b>

# 1 Cosmic Rays

The observed cosmic ray spectrum consists of contributions from a large population of charged particles ranging from protons to iron nuclei. The largest population is formed by protons ( $\approx 87\%$ ), followed by Helium nuclei with  $\approx 12\%$ , and only  $\approx 1\%$  contribution by heavier nuclei (Longair, 2011). The joint energy spectrum of all these contributing particles is referred to as the all-particle cosmic ray spectrum, as shown in Figure 1.

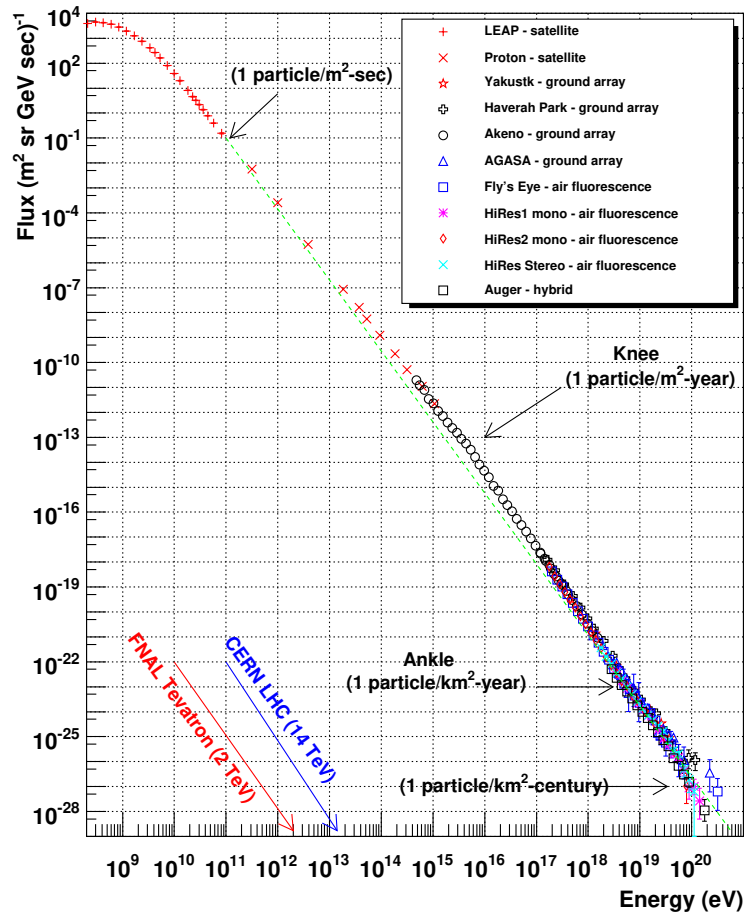


Figure 1: The all-particle cosmic ray spectrum as measured by different experiments. The regions of changing spectral indices are highlighted, and expected particle rates are shown. A power law spectrum with a spectral index of 2.7 is shown as a green dashed line. The plot is adapted from W. Hanlon (2021).

The observed cosmic ray spectrum is near isotropic but exhibits significant, albeit small, fluctuations (Abbasi et al., 2021). It spans over ten orders of magnitude in energy, over 30 orders of magnitude in flux and is well studied by multiple experiments in different energy ranges. The cosmic rays reach energies far beyond those currently achieved in accelerator experiments such as the Large Hadron Collider (LHC) at CERN (Evans and Bryant, 2008). Despite the extensive energy range over which cosmic rays are detected,

the flux approximately follows a simple power law of the form

$$\frac{dN}{dE} \propto E^{-\gamma}, \quad (1)$$

with a spectral index  $\gamma \sim 2.7$  (Figure 1). However, the observed cosmic ray spectrum shows slight but notable deviations from this spectral index. The review of these features follows the one given in Tjus and Merten (2020). At the lowest energies  $\sim 1$  GeV, a significant portion of the cosmic ray particles are shielded from the earth by the solar wind, and the flux is subject to solar modulation. Even with the modulation accounted for, the spectrum shows a distinctive deviation from the expected power-law flux distribution, likely caused by ionisation losses of the particles while traversing the Interstellar Medium (ISM). A spectral softening to an index of  $\gamma \approx 3.0$  is observed above an energy of  $\sim 3 \cdot 10^{15}$  eV (3 PeV), commonly referred to as the spectral knee. Up to these energies, cosmic ray acceleration is believed to be dominated by galactic sources. The spectrum hardens again at even higher energies  $\sim 10^{18.7}$  eV (5 EeV) with a spectral index of  $\gamma \approx 2.3$ . This feature is called the spectral ankle. A transition from galactic to extragalactic sources takes place in the region between the spectral knee and the ankle. The position of the spectral ankle marks the energy after which extragalactic sources dominate.

For energies above  $\sim 5 \cdot 10^{19}$  eV (50 EeV) (Longair, 2011), the spectrum is expected to show a substantial reduction in flux possibly due to the Greisen–Zatsepin–Kuzmin (GZK) effect. At these energies, the cosmic rays can interact with Cosmic Microwave Background (CMB) photons to form pions, limiting the maximum energy of cosmic ray particles. Another likely candidate for reduction in flux is the Peters cycle (Peters, 1961), postulating that at the highest energies the contributions of heavier nuclei to the observed cosmic ray flux increases. The overall smoothness and consistency of the observed cosmic ray power law spectrum enable the formulation of two hypotheses:

- Only a few types of astrophysical sources can accelerate particles to the observed energies.
- There exists a similar underlying mechanism for cosmic ray acceleration.

The expected spectral deviations remain small in both cases, similar to the observed cosmic ray spectrum.

The discussion of the different acceleration and emission processes in the next sections follows the one in Longair (2011) and Tjus and Merten (2020).

## 1.1 Diffusive Shock Acceleration

A proposed dominant acceleration mechanism for cosmic rays is the Diffusive Shock Acceleration (DSA), describing the acceleration of particles in the vicinity of strong shocks in the context of a first-order Fermi acceleration mechanism (Fermi, 1954). This mechanism can replicate the cosmic ray spectral index of  $\gamma \approx 2$ , which results in a harder spectrum than the required  $\gamma \approx 2.7$ . Therefore, this process can form the basis of the observed cosmic ray spectrum. The outline of the DSA mechanism follows the one in Longair (2011). DSA considers a supersonic but non-relativistic overdensity (shockwave) moving through interstellar gas with speed  $U \ll c_0$  much slower than the

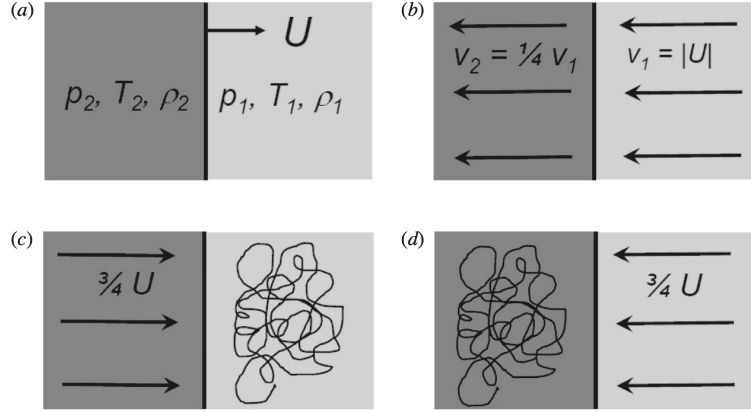


Figure 2: Illustration of a shockfront propagating into an upstream medium with speed  $U$  for an unmoving observer (a), in the rest frame of the shockfront (b), in the upstream rest frame (c) and the downstream rest frame (d). The relative velocities, initial pressure  $p$ , temperature  $T$ , and density  $\rho$  of the upstream and downstream gas are highlighted. The plots are taken from Longair (2011).

vacuum speed of light  $c_0$ . The region in which the shockwave contacts the unshocked medium is the shockfront. The region in front of the shock is called the upstream, and the region behind the shockfront is called the downstream. The DSA mechanism is commonly described in terms of reference frame shifts, illustrated in Figure 2.

Initially, the system is studied in the rest frame of the shockfront (Figure 2b). In this reference frame, the upstream gas flows into the shock with speed  $v_1 = U$  and leaves the shock with speed  $v_2$  into the downstream region. Requiring the conservation of the transported mass through the shock, it can be shown that  $v_2 = (a - 1)/(a + 1) \cdot v_1$ , with  $a$  the specific heat capacity ratio of the traversed gas. In the case of a monoatomic and fully ionised gas,  $a = 5/3$  and therefore  $v_2 = U/4$ .

When moving into the rest frame of the upstream gas (Figure 2c), the downstream gas approaches incoming particles with a speed of  $V = 3/4U$ . It can be shown that particles crossing the shock by diffusion into the downstream region experience a mean energy gain of  $\Delta E/E_0 \propto \frac{2V}{3c_0}$ . In the rest frame of the downstream gas (Figure 2d), the directions of the now-accelerated particles are randomised by scattering processes. Thus, they can cross the shock again into the upstream region, which approaches the particles with the same speed of  $V = 3/4U$ , facilitating a similar energy gain. When considering a round trip of the particle, the mean energy gain

$$\left\langle \frac{\Delta E}{E_0} \right\rangle \propto \frac{4V}{3c_0} = \frac{U}{c_0} \quad (2)$$

is directly proportional to the speed  $U$  of the shock. The expected energy spectrum can be derived by formulating the fractional energy after one round trip as  $\beta = E/E_0 = 1 + \frac{U}{c_0}$  with the probability  $P = 1 - \frac{U}{c_0}$  that the particle rejoins the acceleration process. For an initial population of  $N_0$  particles,  $N = N_0 \cdot P^k$  particles with a mean energy of  $E = E_0 \cdot \beta^k$  remain after  $k$  round trips. By eliminating the parameter  $k$ , it can be shown

that the resulting spectrum yields the required spectral index of  $\gamma \approx 2$ :

$$\frac{dN}{dE} \propto E^{\frac{\ln P}{\ln \beta} - 1} = E^{-2} \quad (3)$$

For typical magnetic field strengths in the ISM of  $\sim 3 \mu\text{G}$  (Longair, 2011), this process can accelerate particles up to the spectral knee. Higher energies can only be reached in sources with larger magnetic fields.

## 1.2 Cosmic Rays Beyond the Spectral Knee

To identify sources of the highest energy cosmic rays up to  $10^{20}$  eV, one must consider the magnetic field strength of the accelerator. For magnetic field strengths beyond those found in the ISM, particles can be accelerated to energies beyond the spectral knee by keeping them confined in the acceleration region. This confinement of charged particles with a charge  $Ze$  and a momentum  $p$  in a magnetic field of magnitude  $B$  is often expressed in terms of the gyro radius  $r_g = p/ZeB$ . In common units for astrophysical applications and an energy  $E \gg m_0c_0$  far greater than the rest mass  $m_0$ , this can be expressed as

$$r_g \approx 1.081 \text{ pc} \cdot Z^{-1} \cdot \left( \frac{E}{1 \text{ PeV}} \right) \cdot \left( \frac{B}{1 \mu\text{G}} \right)^{-1}. \quad (4)$$

Charged particles can escape the acceleration region when  $r_g$  is larger than the size of the acceleration region. By rearranging Equation 4, an expression can be derived that provides suitable combinations of the magnetic field strength and the size of the acceleration region to support the acceleration of particles up to chosen energies. Astrophysical objects that fulfil this so-called Hillas criterion (Hillas, 1984) can be identified in the Hillas plot, shown in Figure 3. It shows the typical magnetic field and accelerator size parameter regions for different astrophysical objects and the Hillas criteria for different maximum achievable energies.

The three lines in Figure 3 highlight the exact threshold for the magnetic field and accelerator size required to accelerate protons to a given energy from the spectral knee to the highest observed energies. If an astrophysical object is located at or above such a threshold in parameter space, it might be an accelerator candidate for cosmic rays of this energy. It should be noted that the highest attainable particle energy in an astrophysical source depends on the individual acceleration mechanism and the energy losses experienced by the particles (section 1.3). Neither does the Hillas criterion consider the abundance of the different object types. For SNRs, the magnetic field strength in shock fronts can exceed that of the ISM by orders of magnitude and particle energies up to the spectral ankle can theoretically be reached by DSA. As seen in Figure 3, different types of sources can contribute to different regions of the spectrum. Galactic sources like Supernova Remnants (SNRs), pulsars, and Pulsar Wind Nebulae (PWNe) can accelerate particles up to the spectral knee. For even higher energies beyond the spectral knee, the gyro radius increases beyond the thickness of the galactic disk ( $\sim 300$  pc (Longair, 2011)) and protons with energies of the order  $10^{18}$  eV can escape<sup>1</sup>. Therefore, extragalactic sources such as Starburst Galaxies (SBGs) (Condoirelli

---

<sup>1</sup>This calculation assumes a typical magnetic field strength of  $3 \mu\text{G}$  for the galactic disk (Longair, 2011).

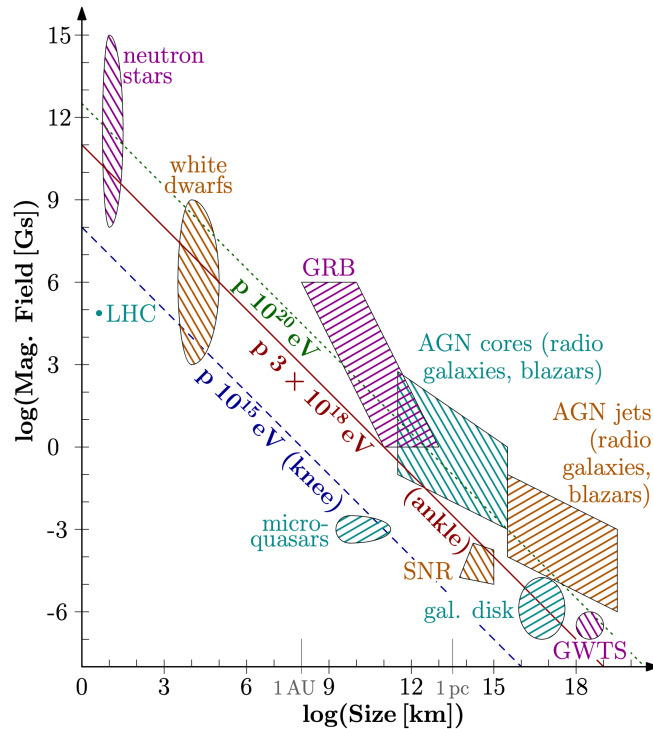


Figure 3: Hillas plot with possible sources of cosmic ray protons up to energies of the spectral knee (blue), the spectral ankle (brown), and energies beyond  $10^{20}$  eV (green). The plot is taken from Tjus and Merten (2020).

et al., 2023), Gamma Ray Bursts (GRBs), and Active Galactic Nuclei (AGN) are thought to be the accelerators of cosmic rays with energies beyond the spectral ankle. Heavier nuclei have a bigger charge and can be accelerated to even larger energies before escaping the galactic disk.

### 1.3 Gamma Ray Emission

While propagating away from the acceleration site, cosmic rays are deflected by ambient magnetic fields in the galactic disk, losing their original travel direction. Consequently, they cannot be used directly to locate the origins of possible cosmic ray accelerators. However, secondary interactions of cosmic rays with ambient photon fields or particle populations can result in the emission of gamma rays, which traverse the ISM undeflected. The probability of these interactions is partially dependent on the ambient photon or matter density, resulting in enhanced emission in the local region of cosmic ray accelerators. Gamma-ray emissions created far away from the acceleration site form a diffuse gamma-ray background. Depending on the type of accelerated particle, multiple interactions are possible. Commonly, the gamma-ray emissions are divided into a hadronic and leptonic scenario (Longair, 2011).

### 1.3.1 Hadronic Scenario

In the hadronic scenario, proton-proton or proton-photon interactions produce multiple types of mesons and hadrons. The mesons produced in proton-proton interactions eventually decay into a population of charged or neutral pions. The neutral pions promptly decay into photons with a threshold energy of  $E_\gamma = m_{\pi^0}/2 \approx 67.5$  MeV in the rest frame of the neutral pion:

$$\pi^0 \longrightarrow \gamma + \gamma$$

The produced photons are emitted isotropically in every direction. Changing into the laboratory reference frame, the observed photon energies are uniformly distributed in logarithmic energy space and centred around the rest frame threshold energy of  $m_{\pi^0}/2$ . This feature is independent of the initial energy of the neutral pion and creates the so-called pion bump at a kinetic energy of  $\approx 289$  MeV in the observed photon spectrum (De Angelis and Mallamaci, 2018).

The decay of the charged pions results in end states with electrons, positrons, and different types of neutrino-antineutrino combinations following:

$$\begin{aligned} \pi^+ &\longrightarrow \mu^+ + \nu_\mu \longrightarrow e^+ + \nu_e + \nu_\mu + \bar{\nu}_\mu \\ \pi^- &\longrightarrow \mu^- + \bar{\nu}_\mu \longrightarrow e^- + \bar{\nu}_e + \nu_\mu + \bar{\nu}_\mu. \end{aligned}$$

Consequently, the presence of a pion bump in the source spectrum or the observation of neutrino emission is directly linked to the hadronic scenario. Heavier nuclei can be treated as superpositions of single nucleons and follow a similar process.

### 1.3.2 Leptonic Scenario

In the leptonic scenario, photon emission is created by bremsstrahlung, synchrotron radiation, and inverse Compton scattering.

#### Bremsstrahlung

Charged particles can be deflected or decelerated by the electric fields of nuclei in a medium, resulting in the emission of gamma rays. This bremsstrahlung is discussed extensively in Bethe et al. (1934) and Blumenthal and Gould (1970). The energy loss rate of a particle of mass  $m$ , Energy  $E$  and charge  $q$  follows

$$-\left(\frac{dE}{dt}\right)_{\text{br}} \propto \frac{q^4}{m^2} E. \quad (5)$$

The energy loss is directly proportional  $E$  and shows suppression for particles with higher mass. To compare this process to the other possible leptonic processes, the expression of the loss timescale

$$\tau = \frac{E}{dE/dt} \quad (6)$$

is introduced. For bremsstrahlung, the loss timescale  $\tau_{\text{br}}$  is constant with energy. Other processes show significantly shorter loss timescales for highly relativistic energies and dominate the emission.



### Synchrotron Radiation

A charged particle that travels through a region with a magnetic field component perpendicular to the particle's momentum begins a gyration along the magnetic field vector. This constant acceleration results in the emission of synchrotron radiation. As shown in (Tjus and Merten, 2020), the energy loss rate for a charged particle of mass  $m$ , charge  $q$ , and energy  $E$  in a magnetic field  $B$  follows

$$-\left(\frac{dE}{dt}\right)_{\text{sync}} \propto \left(\frac{q}{m}\right)^4 E^2 B^2. \quad (7)$$

The corresponding loss timescale is

$$\tau_{\text{sync}} \propto \left(\frac{m}{q}\right)^4 E^{-1} B^{-2}. \quad (8)$$

The energy loss by synchrotron emission is strongly suppressed for heavier particles. Comparing the energy loss of a proton and an electron of equal kinetic energy, the synchrotron emission of the proton is suppressed by a factor of  $\approx 8 \cdot 10^{-14}$ .

### Inverse Compton

A charged particle can interact with ambient low-energy photon fields like the CMB or starlight and transfer parts of its energy into a photon. These Inverse Compton (IC) photons can reach energies in the TeV range. Extensive derivations and discussions of this process are given in Aharonian et al. (2013) and Longair (2011).

Commonly, the IC process is divided into the non-relativistic Thomson and relativistic Klein-Nishina (KN) regime. In both cases, the energy loss rate is directly proportional to the energy density of the photon field  $\eta_{\text{ph}}$  ( $\approx 1 \text{ eVcm}^{-3}$  (Longair, 2011))<sup>2</sup> and shows similar suppression for higher mass particles when compared to the synchrotron process.

$$-\left(\frac{dE}{dt}\right)_{\text{IC}}^{\text{Th}} \propto \left(\frac{q}{m}\right)^4 E^2 \eta_{\text{ph}} \quad (9)$$

$$-\left(\frac{dE}{dt}\right)_{\text{IC}}^{\text{KN}} \propto \left(\frac{q}{m}\right)^4 \ln(E) \eta_{\text{ph}}. \quad (10)$$

The energy loss rate in the Thomson regime (Equation 9) shows a stronger dependence on the charged particle's energy compared to the KN regime energy loss rate (Equation 10) The latter is almost constant in energy for relativistic charged particles. The corresponding loss timescales are

$$\tau_{\text{IC}}^{\text{Th}} \propto \left(\frac{m}{q}\right)^4 E^{-1} \eta_{\text{ph}}^{-1} \quad (11)$$

$$\tau_{\text{IC}}^{\text{KN}} \propto \left(\frac{m}{q}\right)^4 \frac{E}{\ln(E)} \eta_{\text{ph}}^{-1}. \quad (12)$$

While the IC process can create higher energy photons compared to synchrotron emission, the energy loss rate of synchrotron emission already dominates the one of IC at typical values for the ISM ( $B \approx 3 \mu\text{G}$ ) (Longair, 2011).

<sup>2</sup>The energy density of  $\approx 1 \text{ eVcm}^{-3}$  considers the influence of ambient starlight and the CMB.

## 2 Detection on Earth

Cosmic rays and their secondary gamma ray emission can be detected directly by space-based experiments such as the Fermi Large Area Telescope (Fermi-LAT) (Atwood et al., 2009) (gamma rays) or the Alpha Magnetic Spectrometer (AMS-02) (Kounine, 2012) (cosmic rays) onboard the International Space Station (ISS). These instruments are highly successful for energies of hundreds of GeV. However, for higher energies, the cosmic ray flux reduces such that instruments with larger detection areas are required to maintain a reasonable detection rate. As the launch costs of satellites increase with weight and size, ground-based detectors become more practical for energies above 1 TeV. Whilst transparent in the radio and optical range, the earth's atmosphere becomes opaque to gamma rays above a few keV (Bose et al., 2022). As neither cosmic nor gamma rays can reach the ground at these energies, direct measurement methods are inaccessible for ground-based experiments, and only the interactions of the primary particles with the earth's atmosphere can be observed. Depending on the primary particle type, these interactions create different types of so-called air showers, which are introduced in this section.

### 2.1 Electromagnetic Air Showers

Electromagnetic air showers can be induced by cosmic electrons, positrons, and gamma rays. The latter is used to describe air shower development, as the resulting air shower structures and observables are nearly identical for all these particles. When a high-energy cosmic gamma-ray enters the atmosphere, it interacts with the Coulomb field of nearby atomic nuclei through electron-positron pair production. To simplify the discussion of the air shower process, the term electron describes both the positrons and the electrons. Due to the high primary particle's energy (GeV to TeV range), the produced electrons are highly relativistic. The produced photons, in turn, can create electron-positron pairs if their energy is sufficient ( $> 2m_e$ ) (Longair, 2011).

This process continues until the particle energy drops below a critical energy at which ionisation losses dominate, and the development of the air shower rapidly slows. These air showers develop on timescales of only a few microseconds. Observables and their proportionalities for electromagnetic air showers can be derived from the simplified cascade model introduced in Heitler (1944), further referred to as the Heitler model. This Heitler model for electromagnetic air showers is illustrated in Figure 4.

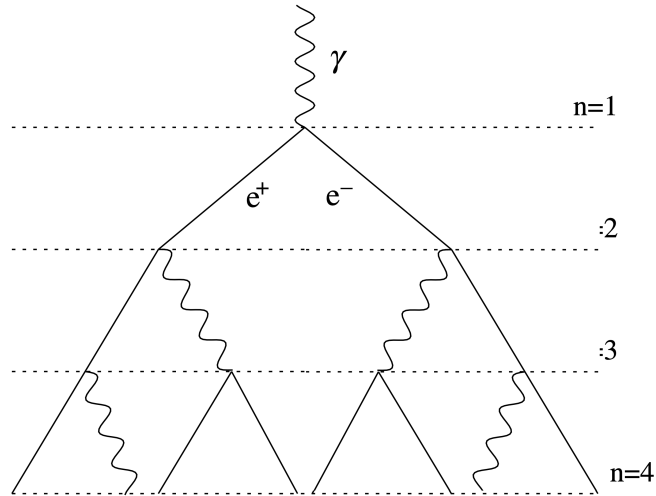


Figure 4: Heitler model for an air shower induced by a high energy cosmic gamma-ray for  $n$  radiation lengths. The illustration is adapted from Matthews (2005).

This model assumes that the energies of the interaction products are highly relativistic. In this regime, the interaction lengths for bremsstrahlung and electron-positron pair production become identical (Longair, 2011). The model then characterises the longitudinal air shower development in  $n$ -steps of this shared radiation length  $X_{\text{rad}} \sim 37 \text{ g cm}^{-2}$  (Ulrich et al., 2011). This length is given in units of the slant depth ( $\text{g cm}^{-2}$ ) to make it independent of the traversed medium. For a particle arriving from space at zenith  $\theta = 0$ , the slant depth at an altitude  $H$  above sea level is calculated as

$$X(H) = \int_H^{\infty} \rho_{\text{atm}}(h) dh, \quad (13)$$

with  $\rho_{\text{atm}}(h)$  the height-dependent atmospheric density.

At each step in the Heitler model, photons undergo pair-production, and leptons produce an additional photon due to bremsstrahlung. For each such step, the energy of the particles is reduced to 50%. After  $n$ -steps, the mean particle energy is  $E_n = E_p/N(n)$  with  $N(n) = 2^n$  the number of particles and  $E_p$  the energy of the primary particle. The cascade maximum is reached at

$$X_{\text{max}} = X_{\text{rad}} \cdot \ln \left( \frac{E_p}{E_c} \right) \propto \ln(E_p), \quad (14)$$

when the mean particle energy falls below  $E_c \approx 85 \text{ MeV}$  in air (Ulrich et al., 2011). The number of particles in the cascade maximum reaches

$$N_{\text{max}} = \frac{E_p}{E_c} \propto E_p, \quad (15)$$

with 1/3 of the produced particles being photons and 2/3 electrons. As these processes are statistical in nature, the results of Equation 14 and Equation 15 are interpreted as expected values. While the atmospheric depth of the air shower maxima (see Equation 14) depends logarithmically on the primary particle's energy, the number of

particles at the air shower maxima goes linear with the energy. For a 1 TeV gamma-ray, typical cascade maxima are reached at slant depths  $X_{\max} \sim 350 \text{ g cm}^{-2}$ . Adopting a simple exponential density description for the atmospheric density  $\rho_{\text{atm}}(h)$  (Zombeck, 2006), the maxima is located  $\sim 15 \text{ km}$  above sea level. In contrast, the expected location of the first interaction is significantly higher in the atmosphere at  $\sim 35 \text{ km}$ . The lateral extension of the air shower is dominated by multiple scattering of the produced particles in the local medium.

## 2.2 Hadronic Air Showers

Hadronic air showers are induced by hadronic cosmic rays and generally show a more complex structure than electromagnetic air showers, as strong and weak interactions are possible. Cosmic ray protons are used to describe the hadronic air shower development due to their abundance in cosmic rays (section 1). The incident cosmic ray proton interacts with the nucleons of ambient nuclei in the earth's atmosphere. Generally, these interactions can create neutral and charged pions, strange mesons and additional spallation products. The strange mesons, however, rapidly decay into additional pions. An illustration of such a hadronic air shower is shown in Figure 5

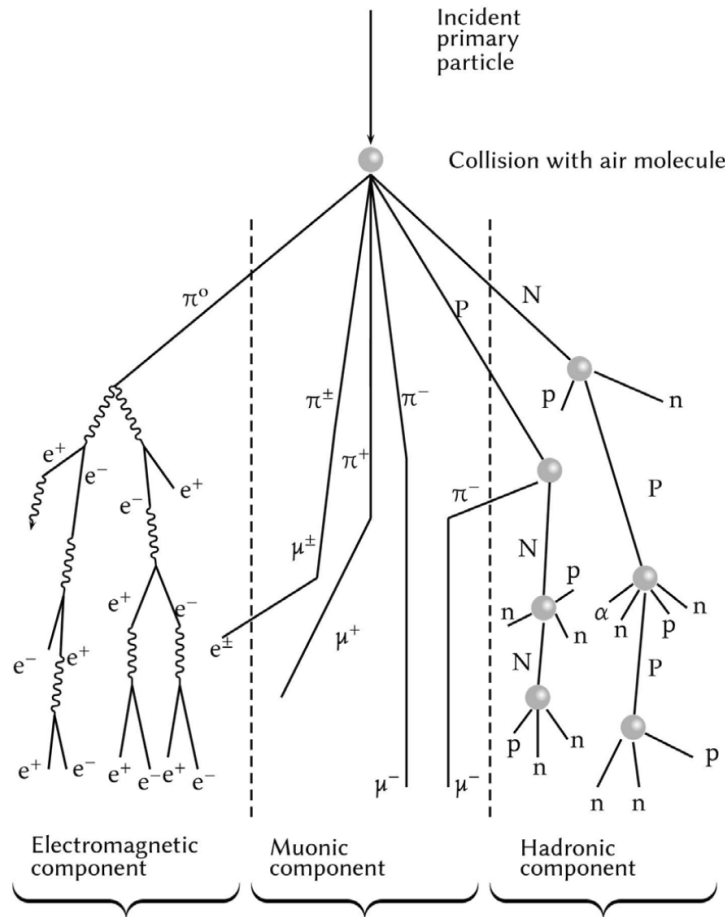


Figure 5: Illustration of typical hadronic air shower constituents. The illustration is adapted from Barrantes et al. (2018).

The air shower can be split into electromagnetic, muonic and hadronic components. The muonic component is formed by the decay of charged pions into muons and neutrinos:

$$\pi^+ \longrightarrow \mu^+ + \nu_\mu \quad (16)$$

$$\pi^- \longrightarrow \mu^- + \bar{\nu}_\mu \quad (17)$$

High-energy muons are highly penetrating and can reach the ground despite their short lifetime due to time dilation. Lower energy muons may decay into electrons and the corresponding neutrinos. These, in turn, add to the electromagnetic component of the hadronic air shower. This component is dominated by the rapid decay of neutral pions into photons, which causes an electromagnetic sub-shower. The hadronic component consists of spallation products that yield further nuclear interactions. These nuclear interactions can contribute to the muonic component of the hadronic air shower until the energy drops below the pion production energy ( $\sim 1$  GeV) (Longair, 2011).

A Heitler formalism for hadronic air showers has been introduced by Matthews (2005). This formalism treats an incident primary cosmic ray nucleus of mass  $A$  and energy  $E_p$  as single nucleons with an energy of  $E_p/A$  each. The atmospheric depth of the air shower maxima shows a logarithmic dependence  $\ln(E_p/A)$  and the number of particles a dependence on  $E \cdot A^{0.15}$ . For the number of particles, the dependence on the atomic mass can be approximated by  $\ln(A)$  with a  $< 6\%$  residual error for atomic masses between  $A = 4$  to  $A = 56$ . Further, the electromagnetic air shower component carries a significant fraction of the primary particle's energy. This fraction already exceeds 50% above 2 TeV primary particle energy. Due to the different components in hadronic showers, and the subsequently created sub-showers, the lateral extension is larger than the one of electromagnetic showers at the same energy. A side projection view of an electromagnetic and a hadronic air shower is shown in Figure 6.

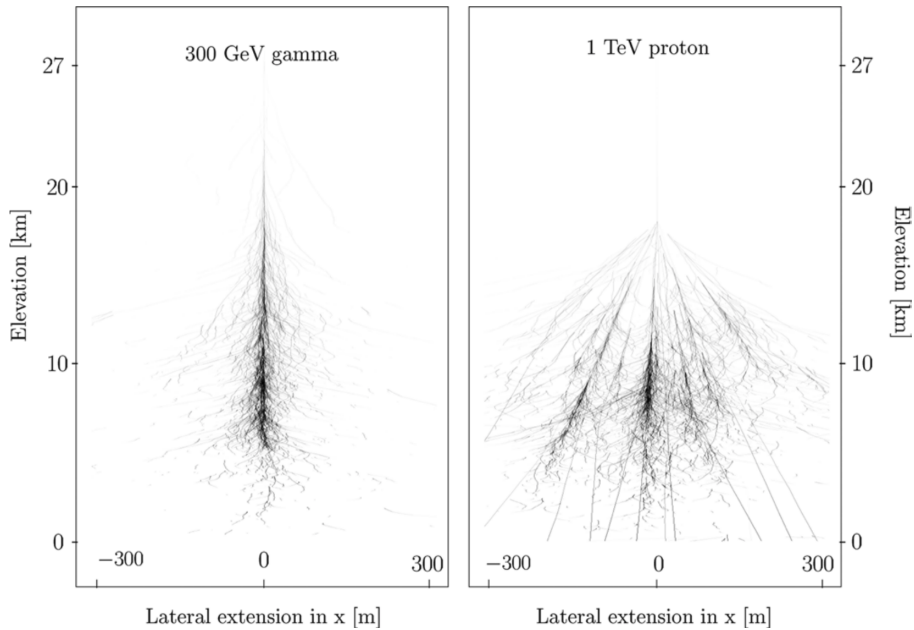


Figure 6: Side projection of simulated air showers initiated by a 300 GeV photon (left) and a 1 TeV proton (right). The plots are taken from Aharonian et al. (2008).

### 2.3 Cherenkov Light

Charged particles that travel faster than the local speed of light in a medium  $c = c_0/n$  of refractive index  $n$  result in the emission of Cherenkov radiation. The traversed medium is polarised by the charged particle in the vicinity of the particle's position, forming local dipole radiators. This polarisation relaxes when the particle leaves the local region, and each local dipole emits an electromagnetic wave. For particles that travel faster than the local speed of light in the medium, the resulting polarisation is asymmetrical, and the resulting dipole emission is coherent (Cherenkov, 1937; Burden and Hieftje, 1998). The emission is beamed in the particle's travel direction and is radiated under the Cherenkov angle

$$\cos(\theta_C) = \frac{1}{n \cdot \beta}, \quad (18)$$

with  $\beta = v/c_0$ , the fraction of the particle's speed to the speed of light in a vacuum. The number of photons emitted for a certain unit distance and wavelength has been calculated by Frank and Tamm (1991) as

$$\frac{d^2N}{d\lambda dx} = \frac{2\pi\alpha}{\lambda} \cdot Z^2 \left( 1 - \frac{1}{\beta^2 n(\lambda)^2} \right). \quad (19)$$

Here,  $\alpha$  is the fine structure constant, and  $Z$  is the charge of the particle. The number of particles per unit length is inversely proportional to the emitted wavelength. Hence, the majority of the emission is expected at smaller wavelengths. Generally, the refractive index in the atmosphere is dependent on the wavelength, considering the medium's dispersion. For an optically transparent medium, the emission is only allowed in specific wavelength intervals (Kolanoski and Wermes, 2016). Taking dispersion and atmospheric

absorption in the UV range into account, the Cherenkov emission peaks in the optical blue range ( $\lambda \sim 300$  nm) (Lipatov et al., 2020).

The described Cherenkov emission must also be considered when describing the phenomenon of air showers. As the created charged particles are highly relativistic, Cherenkov emission is created. To study this emission, complex software frameworks (later introduced in section 2.7) are used to simulate both the particle interactions in the atmosphere and the resulting Cherenkov emission. For such simulations, it is essential to incorporate an accurate model of the atmosphere, which proves to be a challenge. Not only is the index of refraction  $n$  dependent on the wavelength, but also on the local pressure in the atmosphere. The modelling of the atmosphere's vertical structure is of particular importance, encoding not only the pressure profile but also molecular densities, essential to accurately simulate the absorption and scattering of Cherenkov light. A change in this vertical profile can alter the Cherenkov light yield for air showers by up to 60 % (Bernlöhr, 2000).

A simple toy model for the atmospheric pressure can be used to illustrate the effect of a height-dependent index of refraction  $n$ . The resulting index of refraction decreases exponentially with the height  $h$  above sea level following

$$n(h) = 1 + (n_0 - 1)e^{-\frac{h}{H}}, \quad (20)$$

with  $n_0 = 1.00029$  the index of refraction at sea level and the scale-height  $H = 7.4$  km (Purvinskis et al., 2003). This approximation also reproduces the typical Cherenkov angles in the atmosphere, ranging from  $\approx 1.4$  deg at sea level to  $\approx 0.4$  deg for positions higher up in the atmosphere (Lipatov et al., 2020).

The Cherenkov emission is studied for a charged muon with an energy of 300 GeV travelling downward from the zenith at a starting height of 25 km above sea level. Using the toy model for the refractive index (Equation 20), the Cherenkov angle of the emission is calculated in height intervals of 1.5 km. The emission is traced to the sea level, assuming no further interactions or atmospheric scattering processes. To illustrate the effect of a height-dependent index of refraction, the process is repeated for a fixed Cherenkov angle of  $\theta_C = 1.37$  deg (expected at sea level). The result for both scenarios can be seen in Figure 7.

With a constant Cherenkov angle (Figure 7b), the lateral extension of the emission on the ground increases linearly with the emission height. Considering the change of refractive index with height above sea level, the lateral extension of the emission on the ground is significantly reduced. This reduction is quantified in Figure 8, showing the diameter of the Cherenkov emission on the ground level as a function of the emission height.

In the case of the altitude-dependent refractive index, the diameter of the Cherenkov emission on the ground reaches a maximum of  $\approx 250$  m, commonly referred to as the Cherenkov light pool size, for an emission height of  $\approx 15$  km. The latter is close to the expected locations of shower maxima in electromagnetic air showers (section 2.1). The determined size of the Cherenkov light pool agrees with more sophisticated simulations of electromagnetic air showers (Aharonian et al., 2008).

It should be noted that this is only valid for a charged particle arriving from the zenith. For zenith angles  $\theta > 0$ , the dimension of the Cherenkov pool is subject to

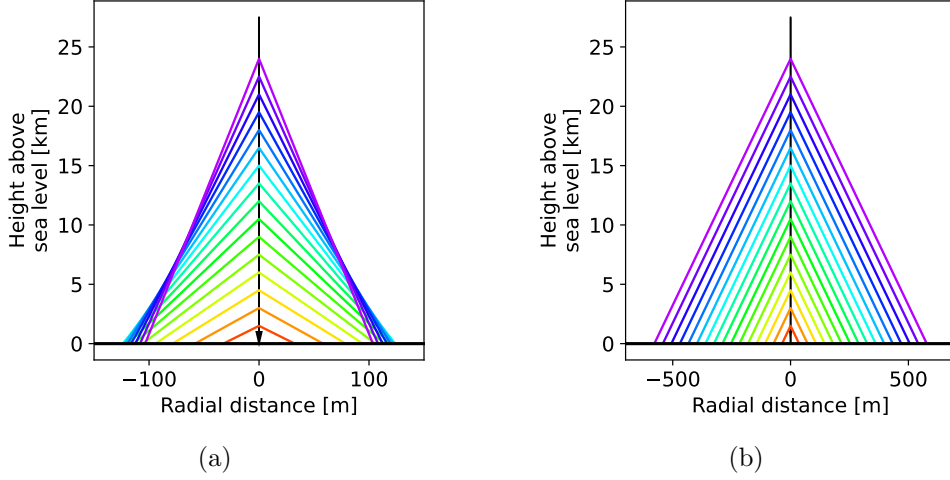


Figure 7: Toy model of Cherenkov photon paths assuming an exponential model for the refractive index of the atmosphere (a) and a constant Cherenkov angle of 1.37 deg (b) for Cherenkov photons emitted by a 300 GeV muon travelling downwards from the zenith at a starting height of 25 km above sea level.

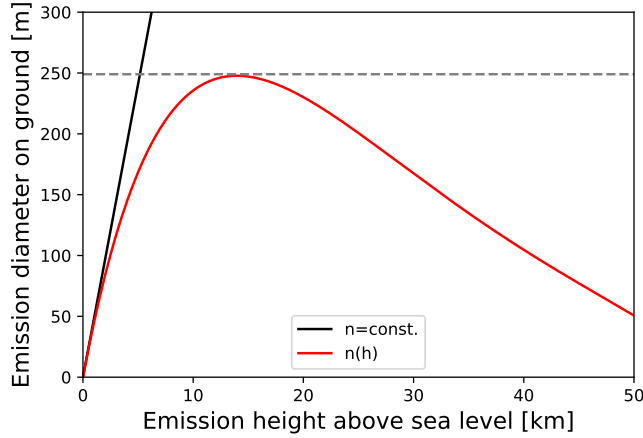


Figure 8: Emission diameter of Cherenkov light on the ground, assuming a constant (black) and altitude-dependent (red) refractive index  $n$  for different emission altitudes above sea level. The height-dependent refractive index is based on an exponential model following Equation 20.

projection effects, resulting in an elliptical shape. The apparent size increase along the major axis can be characterised by  $1/\cos(\theta)$ . The presented toy model only considers a single particle, while the actual Cherenkov photon distribution on the ground is a superposition of the Cherenkov emissions from all charged particles in an air shower. Furthermore, the lateral distribution of the air shower and scattering in a more complex atmospheric model must be considered, resulting in a smearing of the resulting photon distribution. More sophisticated simulations (section 2.7) consider these effects, and resulting Cherenkov photon distributions on the ground are shown in Figure 9.



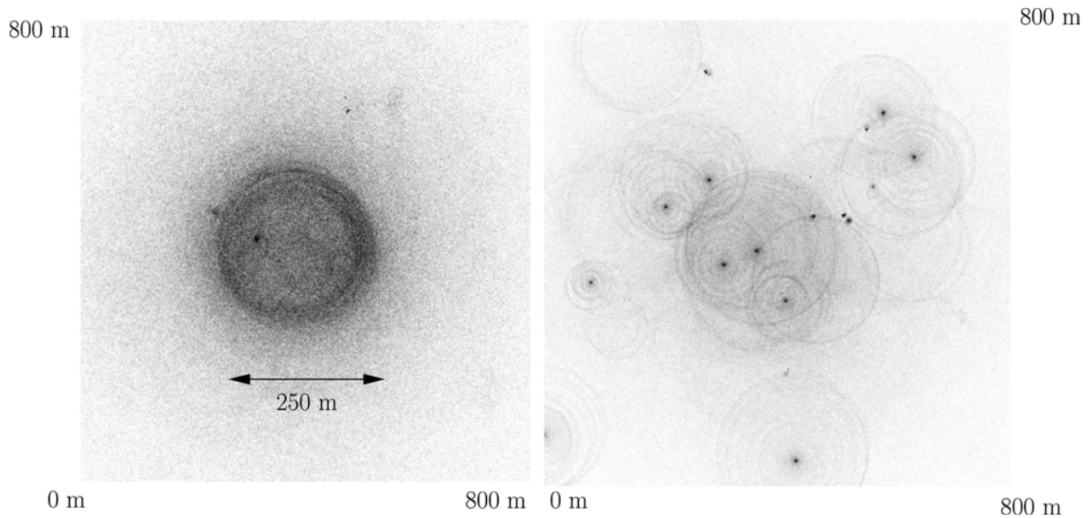


Figure 9: Cherenkov light pool of simulated air showers initiated by a 300 GeV photon (left) and a 1 TeV proton (right). The more extensive lateral profile of the proton-induced air shower with side showers shown in Figure 6 directly reflects on the light distribution on the ground. The Images are taken from Aharonian et al. (2008).

The sub-shower structure of hadronic air showers results in a more asymmetrical and extended Cherenkov photon distribution on the ground (see Figure 9), with the majority of the Cherenkov light yield concentrated in the centre of each sub-shower. The term Cherenkov shower is commonly used to refer to the collective Cherenkov emissions of particles in air showers. As the velocity of the Cherenkov-light emitting particles inside these air showers is faster than the local speed of light, multiple effects can be observed:

- If shower particles can reach the ground, they arrive before the Cherenkov light emission.
- Cherenkov light emitted near the end of the air shower arrives before Cherenkov emission from further up the shower.
- Nearly all Cherenkov photons arrive within a few nanoseconds as a wavefront.

## 2.4 Imaging Air Cherenkov Telescopes

The Cherenkov light emitted by air showers can be detected by telescopes on the ground using the air Cherenkov technique. Telescopes that use this technique take images of the Cherenkov shower, from which the properties of the primary particle (direction, impact point on the ground, and energy) can be reconstructed. Such telescopes are commonly referred to as Imaging Air Cherenkov Telescopes (IACTs). These telescopes usually featured a large primary mirror to gather Cherenkov light produced by air showers. This light is focused on a camera with nanosecond time resolution to capture the wavefront of Cherenkov light.

The Whipple telescope on Mount Hopkins, Arizona, was one of the first widely successful telescopes of this type and remained in operation until 2006. It was constructed in 1968 and features a 10 m diameter primary mirror and a 37 pixel camera (Weekes et al., 1989). The optical construction of the telescope follows the Davies-Cotton design (Lewis, 1990), with a segmented primary mirror. Another such telescope is the High Energy Gamma Ray Astronomy (HEGRA) system built in 1995, located on the Canary Island of La Palma. It featured five identical telescopes with 8.5 m<sup>2</sup> mirror area each. These telescopes were arranged in a square of  $\sim 100$  m edge length, with the fifth telescope at the centre. HEGRA pioneered a stereoscopic approach to image the same air shower with multiple telescopes while implementing a coincidence trigger between the telescopes. This resulted in a reduced background and better reconstruction of the primary particle's properties. (Daum et al., 1997).

This stereoscopic approach has since been used in the current generation of IACTs. The technique is highlighted in Figure 10.

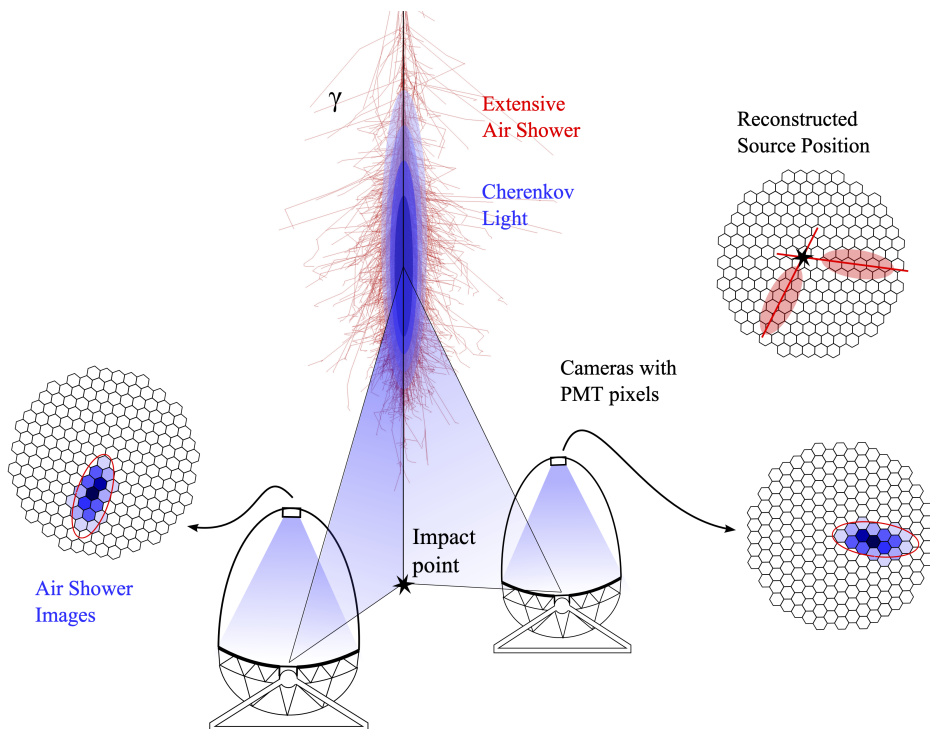


Figure 10: Illustration of the stereoscopic Cherenkov technique for two telescopes. The camera images of both telescopes are transformed into a common coordinate system to reconstruct the source position and impact distance. The illustration is taken from Fruck (2015).

The telescopes are positioned at distances of  $\sim 100$  m, similar to the expected radial size of the Cherenkov light pool, to increase the stereoscopic separation (section 2.3). The Cherenkov light of the air shower is focused on the telescope's camera, with example images shown in Figure 10. IACTs image in angular space and the resulting images of Cherenkov air showers are of elliptical shape. These images are transformed into a

common coordinate system, and the major axes of the reconstructed shower images are intersected. The shower direction and impact point on the ground can be reconstructed from this joined information. Introducing more telescopes further constrains these parameters and increases the resolution (Puehlhofer et al., 2003).

Current generations of IACTs such as MAGIC (Aleksić et al., 2016), VERITAS (Holder et al., 2009), and H.E.S.S. (Aharonian et al., 2006) use this stereoscopic approach with even mirror diameters per telescope (10 m to 25 m) and higher resolution cameras. This current generation of telescope systems enables energy thresholds of below 100 GeV, allowing for connections to results from space-born experiments.

## 2.5 The High Energy Stereoscopic System

The High Energy Stereoscopic System (H.E.S.S.) array is located in the Khomas highlands in Namibia at an altitude of 1835 m above sea level. The initial array consists of four identical telescopes (CT1-4) with a mirror diameter of 12 m and finished construction at the end of 2003. Following the principles of the stereoscopic technique, the telescopes are arranged on the corners of a square with 120 m side length. This positioning provides good stereoscopic shower image separation while offering a good light yield for all telescopes. A multi-telescope trigger criterion is implemented to reduce the impact of random telescope triggers, enabling energy thresholds in the 100 GeV range. Details on this multi-telescope trigger are provided later in this section. This four-telescope array layout is referred to as phase-I. Phase-II saw the addition of a central 28 m mirror diameter telescope in 2012, which extended the energy threshold to  $\sim 30$  GeV (Giavitto et al., 2018). A photograph of the H.E.S.S. array is shown in Figure 11. The different telescope types, their hardware, and their calibration are introduced in this section.

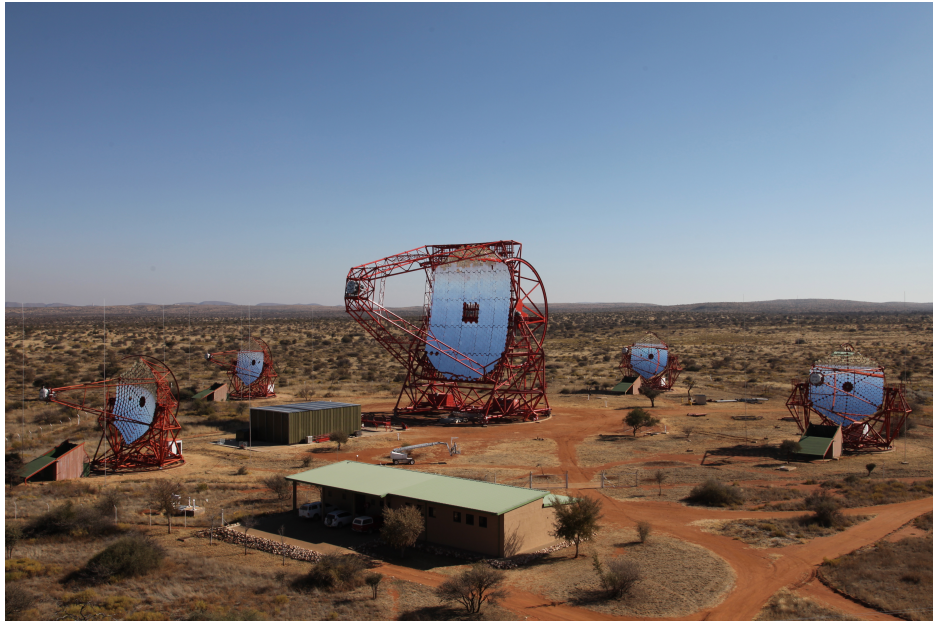


Figure 11: Photograph of the H.E.S.S. array in Namibia, taken from *H.E.S.S. website* (2022). Image credit: Clementina Medina.

### 2.5.1 Phase-I

The four telescopes constructed during phase-I of the H.E.S.S. array are of an identical type, which is illustrated in Figure 12

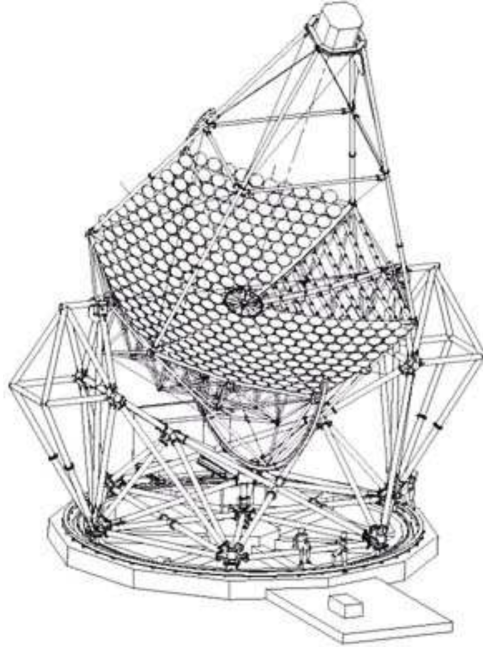


Figure 12: Illustration of a 13 m H.E.S.S. telescope with part of the mirror segments removed to reveal the support structure. The illustration is taken from Bernlöhner et al. (2003).

With a total mirror collection area of  $107 \text{ m}^2$  (Mohrmann et al., 2019), a monolithic mirror is impractical regarding manufacturing costs and logistics. Instead, the telescopes follow the Davies-Cotton (DC) design (Davies and Cotton, 1957). The telescope's primary mirror is segmented into 380 spherical mirror facets with a diameter of 60 cm and a focal length of 15 m each. These facets, in turn, are positioned on a spherically shaped support structure with a radius of curvature equivalent to the focal length of the individual facets. Each facet is mounted to an actuator that allows for the precise alignment of an individual facet. This mirror design results in an up to 20% better focus spot size compared to a parabolic layout of the mirror facets at the designed focal length of 15 m (Bernlöhner et al., 2003).

The camera of this telescope type is referred to as the HESS1-camera and features 960 pixels. Due to the comparably low light yield of Cherenkov showers, Photo Multiplier Tubes (PMTs) are used as photodetectors. In addition to the usual high-gain (HG) channel, the used PMTs also provide a low-gain (LG) channel, extending the available dynamic range for signals with increasingly large amplitudes. To reduce the wasted space between the tiled round PMT entrance windows in the camera, hexagonal Winston cones (also referred to as light funnels) are added. These light guides forward incoming light to the round PMT entrance window. Each pixel has a Field of View (FoV) of 0.16 deg, resulting in a total camera FoV of 5 deg. The camera is assembled out of 60 so-called drawers with 16 pixels each. These drawers also contain the high voltage

supply and the read-out electronics. The latter uses Analogue Ring Samplers (ARS) with a sampling frequency of 1 GHz and a buffer depth of 128 samples (Funk et al., 2004). The sampled signals are converted using an Analogue to Digital Converter (ADC) and output in ADC-counts. The camera’s focal plane is protected by a lid that can be opened and closed.

The telescope camera is divided into 38 overlapping sectors with 64 pixels each for triggering. A telescope-level trigger is issued when the signal of at least  $N$  pixels (sector threshold) in a sector is above a specified pixel threshold. The telescope trigger signals are processed in a central station to form an array trigger. A minimum participation of two telescopes is required within a coincidence window of 80 ns for the array trigger to be issued (Giavitto et al., 2018). As implemented, the expected trigger rates are  $\sim 300$  Hz, dominated by the Cherenkov emissions of hadronic air showers.

The complete telescope assembly is supported by an altitude-azimuth mount, making most of the night sky accessible for observations<sup>3</sup>. Together with a parameterised pointing error correction, the pointing error RMS is reduced to 2.5 arcsec (Benbow, 2005b).

### 2.5.2 Phase-II

The construction of the central 28 m telescope (CT5) marked the beginning of phase-II of the H.E.S.S. array. Due to a significant mirror size increase, a parabolic support structure was chosen for the 850 hexagonal mirror facets to reduce the time dispersion between photons arriving from the edge and those closer to the mirror’s centre. CT5 features a significantly larger light collection area of  $614 \text{ m}^2$  compared to CT1-4. This increased light collection area enables fainter, less energetic Cherenkov air showers to be detected. This, in turn, increases the expected telescope trigger rate by an order of magnitude to  $\sim 3$  kHz compared to the phase-I telescopes (Vincent, 2005).

The overall camera design and trigger logic of CT5 remains similar to that of the HESS1-camera, with an increased number of 2048 PMT-based pixels with Winston cones and 96 sectors of 64-pixel each. Compared to CT1-4, CT5 features a smaller  $3.5$  deg FoV ( $\approx 0.07$  deg per pixel) but a reduced energy threshold of  $\sim 30$  GeV. CT5 was integrated into the array trigger system, allowing for the formation of a stereo pair with the phase-I telescopes and being able to trigger on its own (mono). This mode is referred to as hybrid mode instead of the initial stereo mode of phase-I.

### 2.5.3 Camera Upgrades

Since the trigger rates of CT5 are larger by almost an order of magnitude, the H.E.S.S. system trigger rate is dominated by the CT5 trigger rate. This also results in a significantly higher stereo trigger rate, where the phase-I telescopes form a stereo pair with CT5. However, this rate is limited by the relatively large  $\sim 450 \mu\text{s}$  dead-time of the HESS1-camera after initiating a trigger (Ashton et al., 2020). Reducing this dead time was the main focus of the HESS1-camera upgrade (HESS1U) while also replacing the

---

<sup>3</sup>The telescope structure does not allow for zenith angles  $< 0.01$  deg (Aharonian et al., 2006)

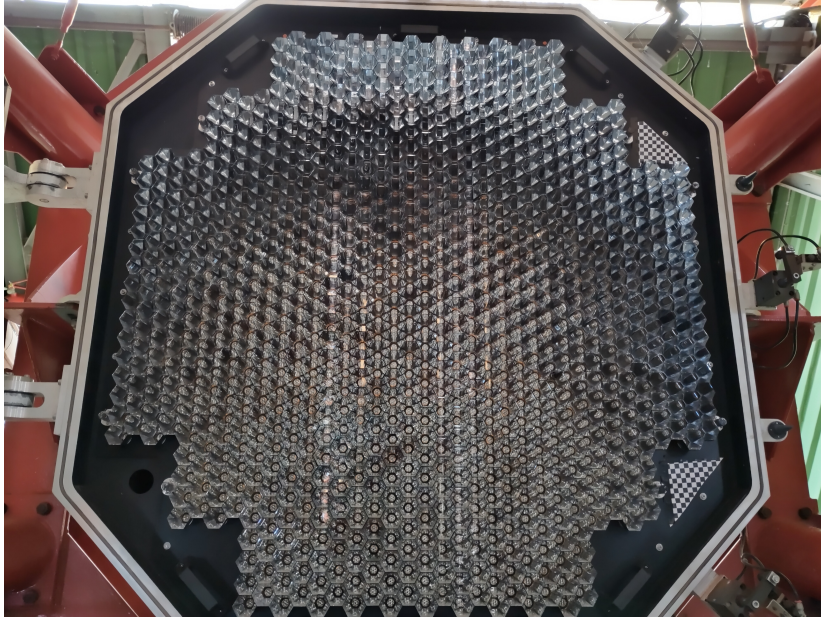


Figure 13: Photograph of the upgraded CT1 focal plane taken by Leuschner (2023). The camera layout is identical to the one of the HESS1-camera.

ageing electronics. The latter have been replaced with new electronics based on the NECTAR-chip (Naumann et al., 2013) originally developed for CTA. The dead time of the system was reduced to  $\sim 7 \mu\text{s}$ , eliminating the trigger rate limit for expected trigger rates of  $\sim 3 \text{ kHz}$ . Components of the optical system, such as the PMTs, have not been replaced, and the trigger mechanism stayed the same. The upgrade of all phase-I telescopes was completed in late 2016, and regular observations were resumed in February 2017 (Ashton et al., 2020). A photograph of the focal plane of CT1 after the upgrade is shown Figure 13.

The camera of the 28 m telescope was upgraded in October 2019 with an advanced prototype of the FlashCam developed for CTA (see section 2.6). FlashCam features 1758 active PMT-type pixels with Winston cones and can trigger on rates exceeding 30 kHz without any dead time. FlashCam’s trigger system divides the camera into 588 non-overlapping patches, with three pixels per patch. The trigger threshold is set on the sum of three neighbouring patches. The latter is constantly evaluated for all available patch combinations. Regular operation resumed in November 2019 (Bi et al., 2021).

#### 2.5.4 Camera Calibration

The stereoscopic technique (section 2.4) and the accuracy of the reconstructed shower parameters rely on the accuracy of the produced camera images and, therefore, the pixel amplitudes. Hence, the calibration of the camera pixel amplitudes is of particular importance. The calibration is extensively discussed in Aharonian et al. (2004) and is summarized below.

### Pedestal

The pedestal  $P$  is the pixel-wise camera response without illumination of the camera pixels. The camera lid is closed for this measurement, and the ADC-Count distribution for each pixel is recorded. For each pixel  $i$ , the mean value of this distribution is calculated for both the LG and HG channel identified as the pedestal  $P_i^{\text{LG}}$  and  $P_i^{\text{HG}}$ , respectively.

### Flat Field Coefficient

As the Winston cone light transmission and the PMT detection efficiency varies from pixel to pixel, a pixel-wise flat field coefficient  $F_i$  is introduced. The camera is illuminated with LED flashers in the wavelength range of 390 nm to 420 nm, which are positioned in the centre of the main dish, pointing towards the telescope camera. The mean value of the pixel amplitude distribution is set to one, and the deviation to the mean of each pixel  $i$  is identified as  $F_i$ .

### Gain

The camera is uniformly illuminated with diffused LED pulsers that provide approximately one photo electron (p.e.) per pixel, and the amplitude distribution is recorded. The expected distribution follows a convolution between the Poissonian emission of the light source and the Gaussian distributed telescope's response. The expected distribution is fit to the measurements, and the HG value  $\gamma_e^{\text{HG}}$  [ADC-counts/p.e] is determined. Using the determined properties, the raw pixel amplitudes in ADC-counts are converted into the detected charge for the HG and LG channels, respectively.

$$A^{\text{HG}}[\text{p.e.}] = \frac{ADC_i^{\text{HG}} - P_i^{\text{HG}}}{\gamma_e^{\text{HG}}} \cdot F_i \quad (21)$$

$$A^{\text{LG}}[\text{p.e.}] = \frac{ADC_i^{\text{LG}} - P_i^{\text{LG}}}{\gamma_e^{\text{HG}}} \cdot \frac{\text{HG}}{\text{LG}} \cdot F_i. \quad (22)$$

The LG value  $\gamma_e^{\text{LG}} = \gamma_e^{\text{HG}} \cdot \text{HG}/\text{LG}$  is calculated from the HG value using the fraction of the HG and LG amplification ( $\text{HG}/\text{LG} \sim 13$ ).

#### 2.5.5 Optical Efficiency Calibration Using Muon Rings

In addition to the camera calibration, the optical efficiency of each telescope must be monitored. The optical efficiency of the telescopes includes the reflectivity of the primary mirror, its shadowing by the telescope structure, the transmission of the Winston cones, and the detection efficiency of the used PMTs. While the shadowing of the primary mirror due to the telescope structure remains nearly unchanged over time, the other contributions to the optical efficiency are subject to variations. Such variations may include the ageing of the hardware, dust build-up on the mirror facets, or cleaning by rain. As the optical efficiency directly scales the number of detected photons, such a variation strongly influences the telescope trigger rates. Consequently, changes in the optical efficiency must be monitored regularly and accounted for.

The potential use of the muonic component found in hadronic air showers (Figure 5) for this purpose has long been recognised (Vacanti et al., 1994) and finds application in all modern IACT experiments including the H.E.S.S. array. In the relevant energy

ranges for IACT experiments, most muons are created at  $\sim 10$  km above sea level with energies reaching up to  $\sim 100$  GeV (Olivera-Nieto et al., 2021). On their way to the ground, they emit Cherenkov radiation if their energy exceeds the Cherenkov emission threshold  $E_{\text{thresh}}^{\mu}$ . This threshold is calculated from the requirement that the muon must travel faster than the local speed of light  $c = c_0/n(h)$  with  $n(h)$  the height-dependent refractive index of the atmosphere. The threshold is then calculated as

$$E_{\text{thresh}}^{\mu} = \frac{m_0^{\mu}}{\sqrt{1 - n(h)^{-2}}}. \quad (23)$$

Using the exponential model for the refractive index introduced in Equation 20, the threshold energy of a muon at an altitude of 2 km above sea level is  $\approx 5$  GeV.

The expected image seen by a Cherenkov telescope camera can be illustrated by a toy model that assumes a constant Cherenkov emission angle (section 2.3) and no scattering or absorption of photons in the atmosphere.

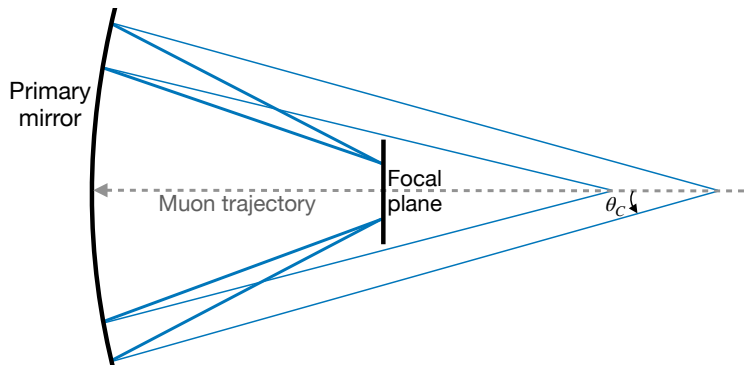


Figure 14: Illustration of the light path in the optical system of a typical IACT for Cherenkov light emitted by a muon arriving on the telescope's optical axis.

Cherenkov telescopes image in angular space, such that all light incident under a common angle to the optical axis is focused on the same point in the camera's focal plane. This imaging behaviour for Cherenkov light emitted by a muon with a trajectory on the telescope's optical axis is shown in Figure 14 as 2D projection. In this 2D scenario, the Cherenkov light of the muon is reflected onto two distinct points on the focal plane. In the complete three-dimensional scenario, the light is emitted in a cone, forming a ring image. As the image is created in angular space, the radius of the ring is equal to the Cherenkov emission angle. However, the muons' trajectory rarely follows the telescope's optical axis, changing the resulting image. The three major scenarios are illustrated in Figure 15 together with the corresponding phase-II Cherenkov camera image of CT5.

A complete muon ring can only form when the muon's trajectory intersects the primary mirror. Muons that hit the primary mirror but don't hit the centre of the primary mirror still produce a ring image, albeit with a non-uniform intensity distribution (left side in Figure 15) For impact distances outside the primary mirror, only a fraction of the emission is still imaged by the telescope optics, resulting in a partial muon ring (centre in Figure 15). The fraction of the ring visible in the camera decreases with increasing impact distance, such that at some point, they resemble the expected



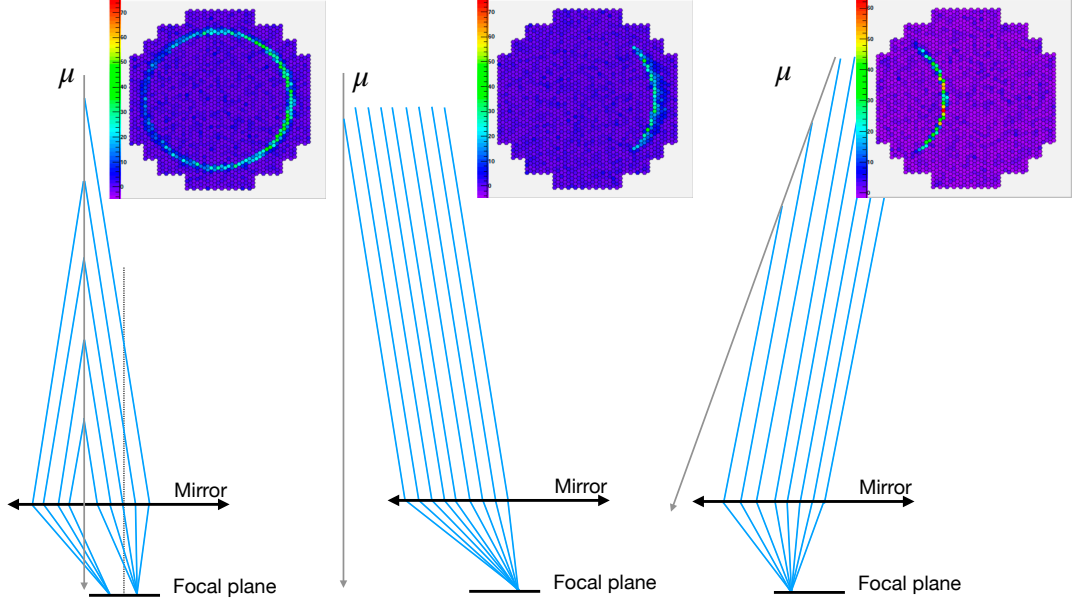


Figure 15: Illustration of different muon impact distances and incidence angles to the optical axis with corresponding camera images in the initial phase-II camera of CT5. The shown scenarios are a muon parallel to the optical axis with an impact distance smaller than the mirror radius (left), an impact distance larger than the mirror radius (centre), and an additional inclination towards the telescope’s optical axis (right). A single optical element miming a parabolic mirror’s imaging behaviour is used for illustration. The illustration is adapted from Chalme-Calvet et al. (2014).

image of electromagnetic air showers. For non-zero incidence angles of the muon to the telescope’s optical axis, the position of the muon ring relative to the camera centre is changed (right side in Figure 15).

Further, the angular distribution of Cherenkov light and, therefore, the width of the muon ring is broadened by multiple effects. These effects include the variability of the Cherenkov angle with height above sea level, the pixelation of the camera, multiple scattering of the Cherenkov light in the atmosphere, and the optical resolution of the telescope optics (Vacanti et al., 1994; Gaug et al., 2019). Generally, larger mirror diameters are beneficial to detect the faint muon ring signal by collecting more light and increasing the likelihood that a muon’s trajectory intersects the primary mirror.

The impact distance, energy, and muon efficiency are determined by a spatial fit of the muon ring intensity distribution introduced for H.E.S.S. in Bolz (2004) and Chalme-Calvet et al. (2014). The muon efficiency is given as the ratio between the observed  $\eta_{\text{obs}}$  and expected light yield  $\eta_{\text{exp}}$  following

$$\epsilon^{\mu} = \frac{\eta_{\text{obs}}}{\eta_{\text{exp}}}. \quad (24)$$

The derivation of the expected light yield and distribution for an ideal camera can be found in Vacanti et al. (1994). Using this definition of the muon efficiency, the difference

in the muon efficiency between telescope runs can be accounted for. H.E.S.S. telescope simulations are grouped into so-called muon phases, introduced once a significant deviation between the measured and simulated muon efficiencies is observed. The new muon phase takes into account the change in the optical efficiency.

### 2.5.6 Atmospheric Transparency Coefficient

The aforementioned H.E.S.S. telescope simulations are produced for average atmospheric conditions. These conditions, however, can be subject to change on a minute scale due to the aerosol content or the presence of clouds. To enable a valid comparison between the telescope observations and simulations, observation runs during which the atmospheric conditions deviate significantly from the average conditions must be removed. This is done by introducing a cut on the so-called transparency coefficient  $T$  extensively discussed in Hahn et al. (2014). It is calculated based on multiple telescope-level observables, such as the used PMT gain  $g_i$  and the muon efficiency  $\epsilon_i^\mu$ . The transparency coefficient also takes into account the zenith angle corrected telescope participation rate  $R_i$  in the stereo trigger and is calculated as

$$T = \frac{1}{N \cdot k(N)} \sum_i^N \frac{R_i^{\frac{1}{1.7}}}{\epsilon_i^\mu \cdot g_i}. \quad (25)$$

Here,  $k(N)$  is a scaling factor to correct for the influence of the telescope multiplicity  $N$  with usual values of  $k(3) = 3.11$  and  $k(4) = 3.41$  such that the mean of the distribution is at unity. The time series of  $T$  from 2004 until 2012 is shown in Figure 16 together

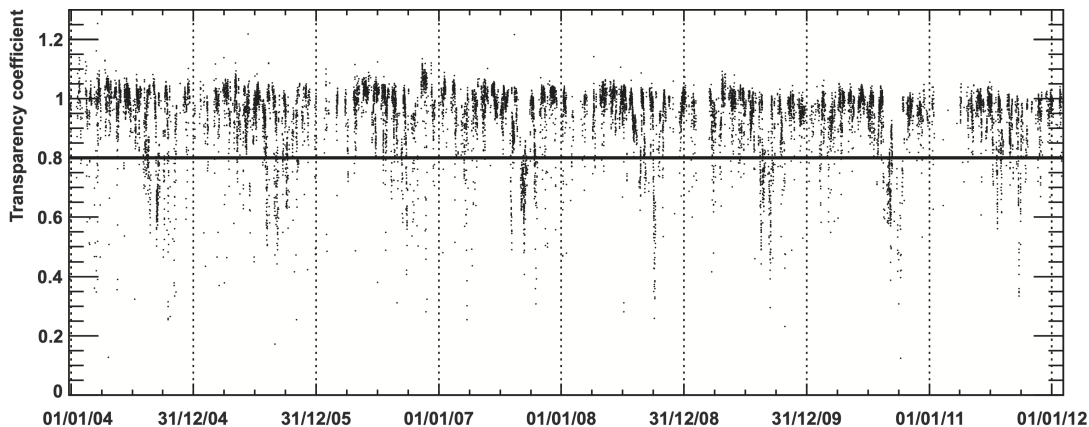


Figure 16: Time series of the calculated transparency coefficient for H.E.S.S. with the highlighted 0.8 criteria. The plot is taken from Hahn et al. (2014).

with the usual cut criterion of  $T > 0.8$ .

### 2.5.7 Image Cleaning and Event Reconstruction

The camera images of Cherenkov showers also contain signal from Night Sky Background (NSB), which originates from atmospheric effects such as airglow, diffuse starlight in the telescopes FoV and artificial light pollution. The so-called tail cut method rejects pixels that do not contain shower information. In the case of CT1-4, camera pixels are

required to have an amplitude of at least 5 p.e. and a next neighbour of 10 p.e., and vice versa (Aharonian et al., 2006).

The residual camera image of an electromagnetic air shower is elliptical and parametrised with a method introduced by Hillas (1985). This parametrisation includes the width, length, contained signal, and distance from the camera centre to the Centre of Gravity (CoG) of the ellipsoid. Following the stereoscopic technique, the camera images of multiple telescopes are transformed into a common coordinate system in the sky. This is illustrated in Figure 17 for two telescopes.

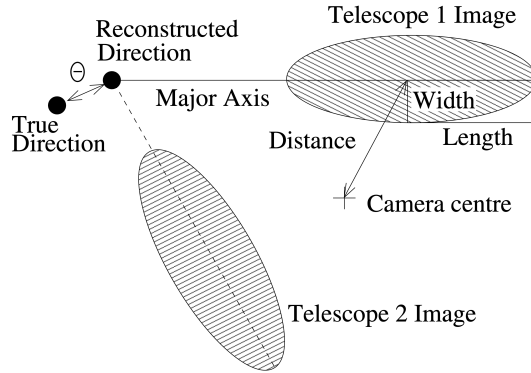


Figure 17: Illustration of the stereo reconstruction of the shower origin using the Hillas parameters of two telescopes with required parameters. The illustration is taken from Aharonian et al. (2006).

The intersection between the major axes defines the reconstructed direction  $D_{\text{reco}}$  of the shower. Here,  $\theta$  defines the difference between the reconstructed and true shower direction  $D_{\text{true}}$ .

The distribution of  $\theta^2$  is referred to as the Point Spread Function (PSF) and is usually determined using simulations. The 68% containment radius of the PSF is used to express the spatial resolution of H.E.S.S. ( $\sim 0.1$  deg). The impact point defines where the primary particle's trajectory would have intersected the ground. It can be found similarly by transforming the camera images into the ground coordinate system and intersecting the major axes.

The total pixel signal inside the ellipsoid is commonly called the image size. The size and impact distance can be used to reconstruct the primary particle's energy using a lookup table. These lookup tables are created on a per-telescope basis using air shower and telescope response simulations of the H.E.S.S. telescopes. Lookup tables are created for thirteen zenith angles from 0 deg to 70 deg and are interpolated in between. An example lookup table is shown in Figure 18. As the lookup tables are created from a simulation with a specific muon phase with  $\epsilon_{\text{sim}}^{\mu}$ , they are corrected for the muon efficiency at the time of observation  $\epsilon_{\text{obs}}^{\mu}$  such that

$$E^{\text{pred}} = E \cdot \frac{\epsilon_{\text{obs}}^{\mu}}{\epsilon_{\text{sim}}^{\mu}}. \quad (26)$$

The reconstructed energy  $E_{\text{reco}} = (N)^{-1} \sum_i^N E_i^{\text{pred}}$  is calculated as the mean predicted energy of all  $N$  participating telescopes. In simulations, this reconstructed energy is

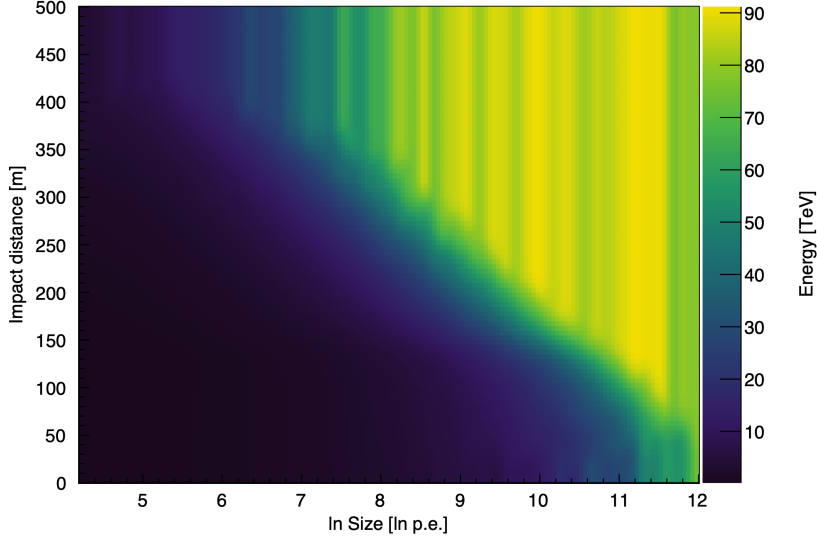


Figure 18: Energy lookup table for a single telescope with applied interpolation. The plot is taken from Jankowsky (2020).

compared to the true energy by calculating the energy dispersion  $(E_{\text{reco}} - E_{\text{true}})/E_{\text{true}}$  as a function of the true energy  $E_{\text{true}}$ . An example dispersion matrix is shown Figure 19. The mean and standard deviation of the distribution for each  $E_{\text{true}}$  defines the energy bias and resolution, respectively, and is determined with a Gaussian fit. The energy bias provides information about a systematic shift in the reconstructed energies and should be zero. As seen in Figure 19, the energy bias shows a positive trend below 1 TeV and a negative trend above 30 TeV.

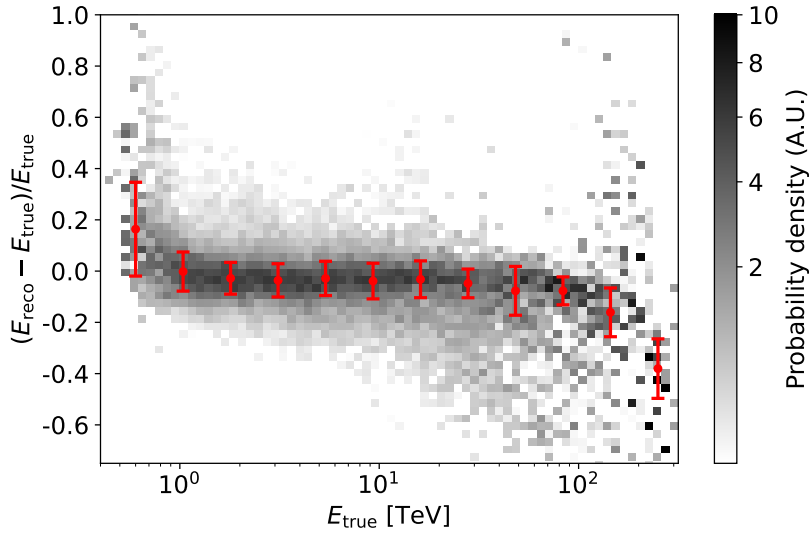


Figure 19: Example energy dispersion matrix with highlighted energy bias and resolution at specific energies (red). A Gaussian is fit to the probability density distribution in each true-energy slice, and the mean and standard deviation are identified as the energy bias and resolution, respectively.

At low energies, the signal of camera images is close to the trigger threshold. Random fluctuations in the light yield due to NSB allow some showers with initial signals below the telescope trigger threshold to trigger the telescope. Due to the increased signal, the energy is reconstructed too high, resulting in a positive bias. The negative bias towards larger energies is caused by showers that saturate pixels or are not entirely contained in the camera. This results in underestimating the energy because only a part of the signal is recorded. The energy resolution of H.E.S.S. is  $\approx 15\%$  for the full energy range (Benbow, 2005a).

## 2.6 Cherenkov Telescope Array

The Cherenkov Telescope Array (CTA) (Acharya et al., 2013) represents the next generation of IACTs. In the proposed form, CTA will be five to ten times more sensitive than current experiments like H.E.S.S., with an extended energy range from 20 GeV to beyond 300 TeV. To reach these goals, CTA will feature two telescope sites and multiple telescope types. The first site is located in the northern hemisphere (CTA-North) in La Palma (Spain). The second site, referred to as CTA-South, is located in the southern hemisphere in Paranal (Chile). This dual-hemisphere approach offers full sky coverage, presenting greater possibilities to study galactic and extragalactic sources of VHE gamma-rays and transients. The initial layout of both sites is referred to as the alpha layout and is shown in Figure 20.

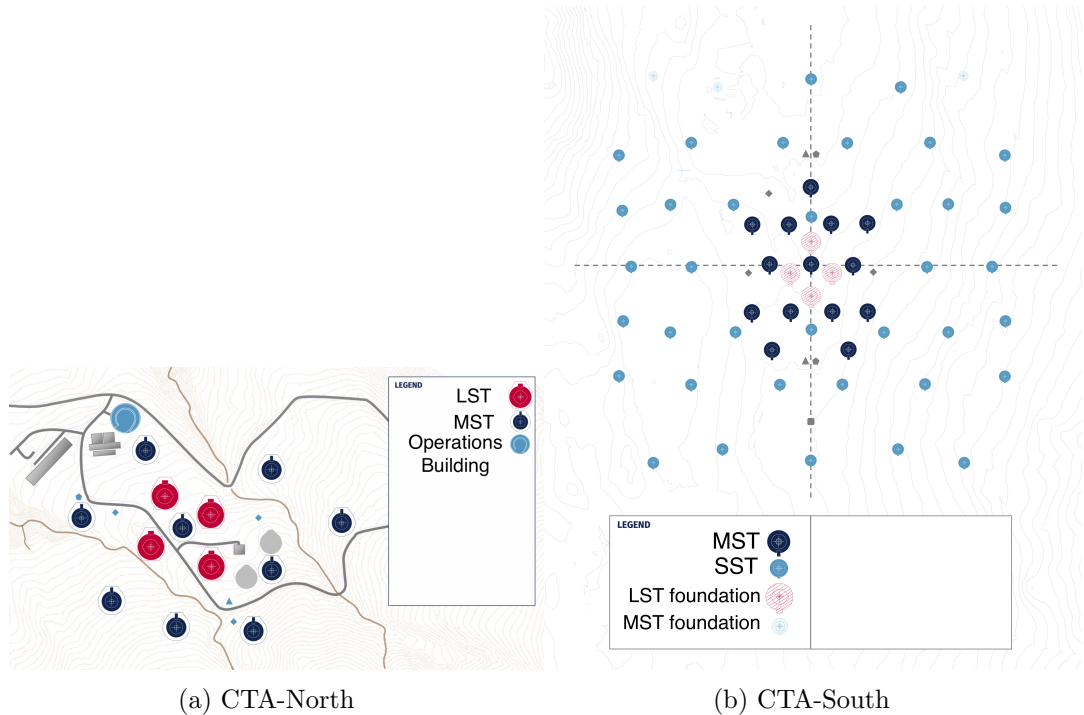


Figure 20: Telescope layout of the CTA sites in the northern hemisphere (a) and southern hemisphere (b). The plots are adapted from the *CTA observatory website* (2023).

The different telescope types are shown in Figure 21. The alpha layout features four Large-Sized Telescopes (LSTs) and nine Medium-Sized Telescopes (MSTs), covering

an area of  $\approx 0.5 \text{ km}^2$  for the northern side. Due to its location, CTA-North will be well positioned to study extragalactic sources. CTA-South features 14 MSTs and 37 Small-Sized Telescopes (SSTs), covering an even larger  $3 \text{ km}^2$  area (Abdalla et al., 2022).

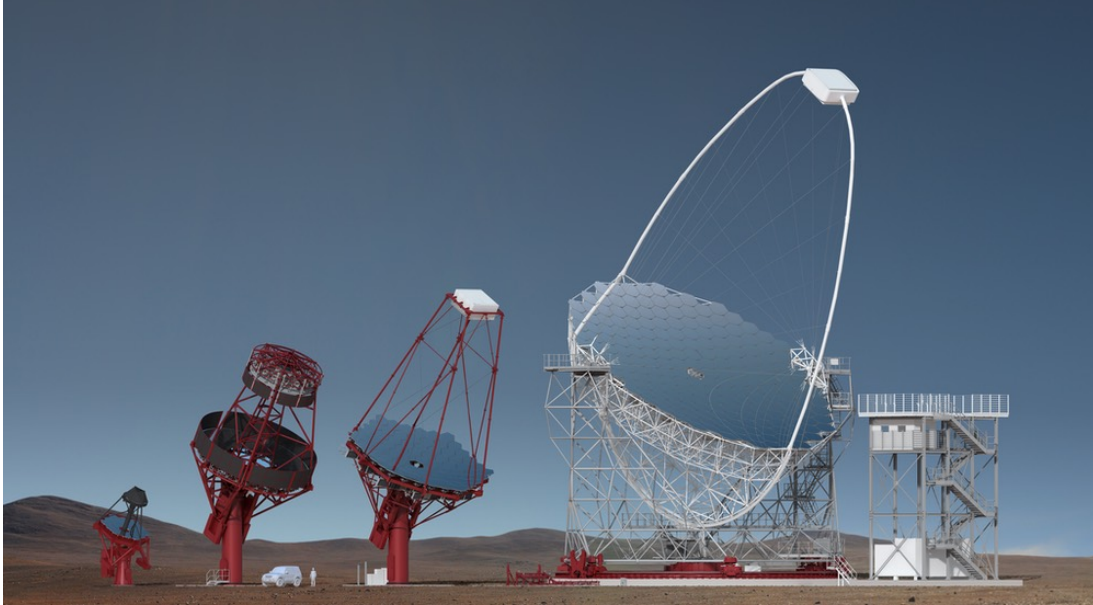


Figure 21: Render of the four CTA telescopes. From left to right, the telescopes are the SST, SC-design MST, DC-design MST, and LST. The image is taken from *CTA observatory website* (2023). Image credit: Gabriel Pérez Diaz, IAC

The LSTs feature a parabolic 23 m diameter mirror with an effective collection area of  $370 \text{ m}^2$ . A 1855 pixel camera with a pixel FoV of 0.1 deg is used, resulting in a total telescope FoV of 4.3 deg. Due to the large collection area, the Cherenkov emission of low-energy air showers can be detected, with an effective energy range from 20 GeV to 3 TeV. The MSTs adopt a modified DC design, with a primary mirror diameter of 11.5 m. Currently, FlashCam (CTA-South)(section 2.5.3) and NectarCAM (CTA-South) (Tavernier et al., 2019) are proposed for the MSTs, with a resulting FoV of  $\approx 8 \text{ deg}$ . Due to the reduced mirror area but increased FoV, the effective energy range of the MSTs is shifted towards higher energies (80 GeV to 50 TeV) (Abdalla et al., 2022; *CTA observatory website* 2023).

The SSTs follow the dual-mirror Schwarzschild-Couder (SC) (Vassiliev et al., 2007) telescope design with a primary mirror of 4.3 m and a secondary mirror of 1.8 m diameter. The SSTs with their comparably small primary mirror and large FoV of  $\sim 10 \text{ deg}$  extend the energy range of CTA to beyond 300 TeV (White, 2021). This is also supported by the large area covered by the SSTs (see Figure 20b), increasing the detection rate for highly energetic air showers.

### 2.6.1 The Camera Design for SSTs

The cameras of the SSTs will be based on the Compact High Energy Camera with Silicon PMTs (CHEC-S) (Watson and Zorn, 2020) that was a proposed camera candidate. The camera features 2048 Silicon Photomultiplier (SiPM) pixels divided into 32 tiles of 64 pixels with a size of  $6\text{ mm} \times 6\text{ mm}$ . The focal plane, defined by the orientation of the SiPM tiles, is curved to consider the image of the telescope’s SC optical design. It is protected by a UV-transparent window and a motorised camera lid. The electronics are constructed in a modular fashion, featuring a backplane that provides power, connectivity, a system clock, and the camera trigger decision for 32 front-end electronics modules that are matched up to each SiPM tile. These front-end electronics modules consist of a SiPM tile assembly and a TARGET-Module (TM). The latter is responsible for amplification and shaping of the SiPM signal and provides a trigger and digitisation logic using TARGET Application Specific Integrated Circuits (ASICs) (section 2.6.2). An image of CHEC-S together with an assembled front-end electronics module and highlighted camera components is shown in Figure 22.

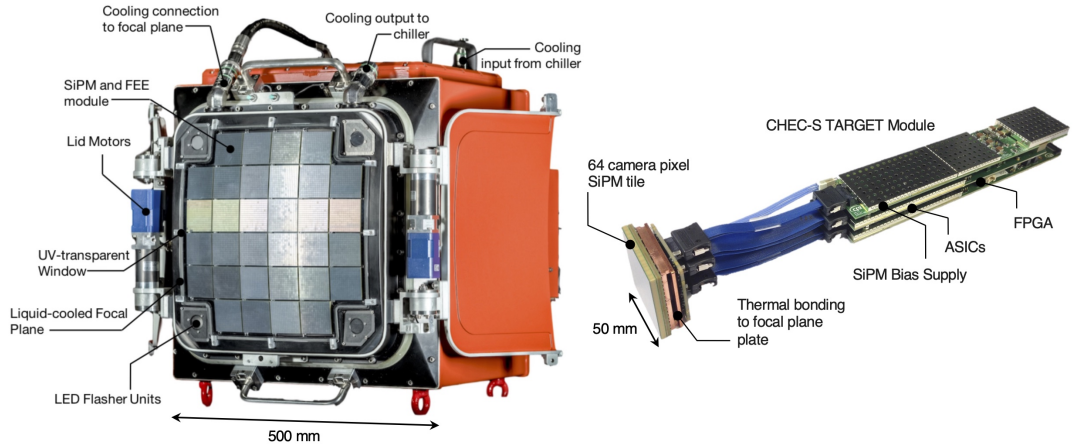


Figure 22: The CHEC-S prototype camera and an assembled front-end electronics module featuring the TARGET-Module with highlighted components. The images are taken from White (2021).

### 2.6.2 The TARGET ASICs

Each TARGET-Module is equipped with four TeV Array Readout electronics with GSa/s sampling and Event Trigger (TARGET) ASIC (Funk et al., 2017) pairs. Each pair consists of a CTA-TARGET-5TEA version (CT5TEA) ASIC for triggering, and a CTA-TARGET-C version (CTC) ASIC for signal sampling, storage and readout (White, 2021). Because these pairs are always used together in the camera, they are commonly referred to as the TARGET ASIC.

The overview of the TARGET ASIC follows the one in White (2021) and Funk et al. (2017). Each TARGET ASIC can process the signal of 16 pixels, for a total of 64 pixels per TARGET-Module. CT5TEA creates a low-level trigger signal based on the 16-pixel signals it is provided with. The signal of four neighbouring pixels is summed

together to form a so-called superpixel. The signal of the superpixel is compared to an adjustable threshold, and the superpixel trigger information is forwarded to the backplane. CT5TEA is capable of triggering on single photons with a noise level of less than 10% of the single-photon-corresponding amplitude of  $\approx 6$  mV (Zink, 2021). The backplane issues a camera-level trigger signal when receiving a trigger signal of at least two neighbouring superpixels. In this case, the signal readout with CTC is initiated.

A simplified schematic of CTC's sampling and storage array is shown in Figure 23. The pixel signal is continuously sampled at 1 GSa/s by a sampling array of two blocks

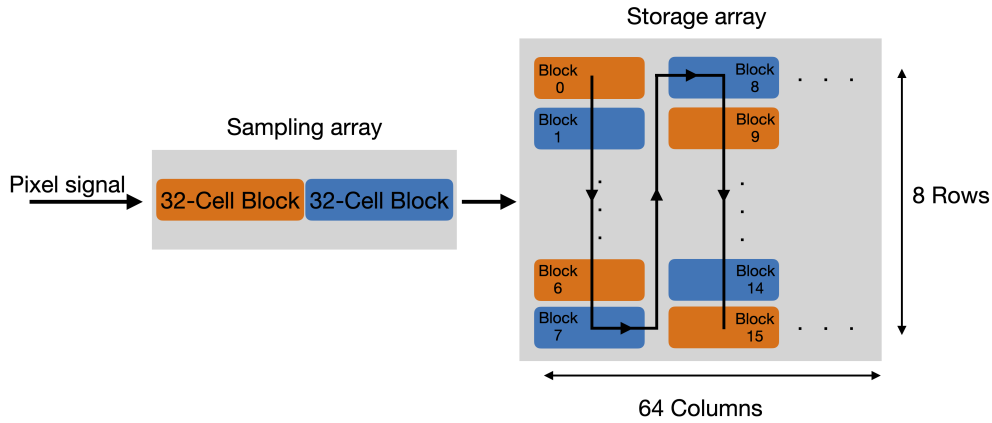


Figure 23: Schematic of the CTC sampling mechanism, highlighting the sampling and storage array. Each storage block consists of 32 cells equivalent to 32 ns of waveform storage capacity at a sampling speed of 1 GSa/s. The description is found in the text.

of 32 switched capacitors (cells). This array is operated in an alternating fashion, such that the signal is sampled into one block while the stored signal in the second block is written to the storage array. Data is written sequentially from the non-sampling block into the storage array in the fashion indicated by the arrows in the storage array in Figure 23. The storage array consists of 512 blocks, storing up to  $\sim 16$   $\mu$ s of signal data at a sampling speed of 1 GSa/s. However, only the first 128 blocks (4096 cells) are used during normal camera operation, as the resulting  $\approx 4$   $\mu$ s storage time offers sufficient look-back time in case of a camera trigger.

If a camera-level trigger signal is issued by the backplane, the location of interest in the storage array is digitised by Wilkinson ADC and output in ADC-counts. The ADC allows for 12-bit output, resulting in a maximum value of 4095 ADC-counts. Each storage cell is a single capacitor with varying capacitance within the allowed specification. Therefore, the so-called Transfer Function (TF), relating the pixel input voltage to the digitised ADC value, is different for each storage cell. An example of the TF of the first 4096 cells in the sampling array for a single pixel is shown in Figure 24.

TFs are created by injecting an artificial pixel signal of known input amplitude and determining the resulting digitised value. The single-cell TFs show a non-linear behaviour, especially towards the saturation regime of the ADC. Since the pixel signal is modified with a constant voltage offset subtracted from the ADC output, the saturation



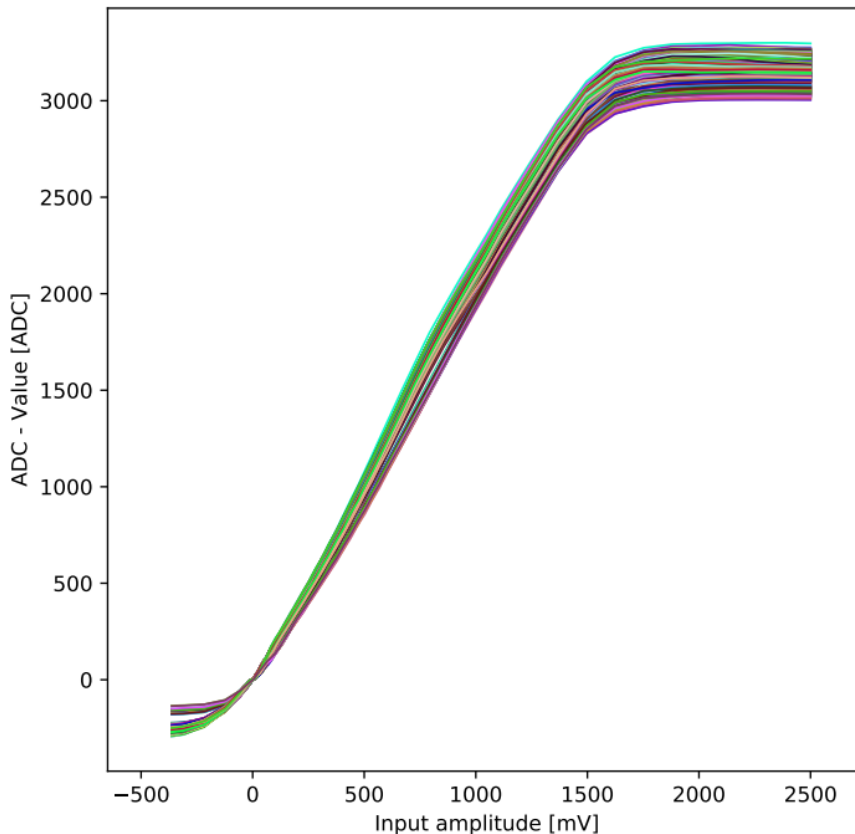


Figure 24: The single-pixel TFs of the TARGET-Module with the serial number SN0007 for the first 4096 storage cells of the first pixel channel at 20 °C ambient temperature. The plot is taken from Schaefer (2019).

is reached before the maximum ADC value of 4095. The average deviation between the TFs of different cells increases with the input amplitude.

## 2.7 Monte Carlo Simulations of Air Showers

The simulation of air showers, their Cherenkov emissions, and the corresponding telescope response is an integral part of modern IACTs operations. The stereoscopic technique (section 2.4), employed by nearly all modern IACTs, can provide information regarding the impact location on the ground and the air shower direction but fails to provide an estimate for the primary particle energy directly. The reconstructed energy  $E_{\text{reco}}$  is extracted from lookup tables, usually containing the image size and the impact distance of the shower (section 2.5.7). Further, the reconstructed energy must be converted into the true energy  $E_{\text{true}}$  of the primary particle using the energy dispersion matrix. In both cases, an accurate simulation of the air shower, its Cherenkov emission, and the telescope response are needed. CTA and H.E.S.S. adopt the CORSIKA and *sim\_telarray* Monte Carlo (MC) software framework for Cherenkov air shower and telescope response simulation, respectively.

### 2.7.1 Air Shower Simulation With CORSIKA

The Cosmic Ray Simulations for Kascade (CORSIKA) software package, initially developed for the KASCADE experiment (Klages et al., 1997; Heck and Pierog, 2021), is a software framework for the simulation of extensive air showers (Heck et al., 1998). It allows for the simulation of air showers initiated by a wide range of particles, including gamma-rays and atomic nuclei up to a mass number of 56 (iron). CORSIKA *v7.7402* is used for the simulations presented in later sections. The user can specify a large selection of parameters, ranging from those influencing the air shower simulation to location-specific parameters. Parameters for the air shower simulation include the type of primary particle, a spectral power law index together with an energy range from which the population of the primary particle is sampled, and the arrival direction of the primary particle. In the case of IACT simulations, location-specific parameters include the observation height (observation level) above sea level (1835 m for H.E.S.S.), the telescope array layout, local magnetic field ( $|\vec{B}_{\text{H.E.S.S.}}| \sim 25 \mu\text{T}$ ), and atmospheric pressure profile. The simulated atmosphere is modelled in 5 distinct altitude layers with 78.2 % N<sub>2</sub>, 21 % O<sub>2</sub>, 0.9 % Ar (Heck et al., 1998). The air shower development outlined in section 2 presents a simplified approach, and the processes that influence the air shower development are significantly more complex. For a primary particle approaching the atmosphere from space, the height of the first interaction is determined by the particle’s mean free path length in the atmosphere, after which the development of the air shower depends on the type of particle and its energy.

The simulation of electromagnetic showers or electromagnetic components in hadronic showers uses a modified version of the Electron Gamma Shower system 4 (EGS4) (Nelson and Namito, 1990) software package. In its unmodified form EGS4 considers annihilation, Bhabha scattering, bremsstrahlung, Møller scattering, and multiple scattering (Moliere’s theory) for electrons and positrons. Compton scattering, electron-positron pair production, and photoelectric reactions are considered for gamma rays. The modifications include the consideration of muon-antimuon pair production, photo-nuclear interactions, and the consideration of the barometric density dependence of the atmosphere (Heck et al., 1998).

The interactions in hadronic air showers are more complex and can happen at energies above those currently achievable in modern accelerator experiments. Multiple interaction models are available in the high and low-energy regimes that model these interactions based on extrapolated experimental data assuming the current understanding of particle interactions. Differences between these interaction models arise predominantly from the number of modelled processes and assumptions made for the extrapolation towards higher energies. The high-energy regime is reached for particles with energies above 80 GeV, with multiple available interaction models (Heck et al., 1998). The presented work uses the QGSJET II-4 (Ostapchenko, 2014) interaction model, but also compares it to the EPOS LHC (Pierog and Werner, 2009) and SIBYLL (Ahn et al., 2009) interaction model. At energies below 80 GeV, the Ultra relativistic Quantum Molecular Dynamics (UrQMD) interaction model is used. The decay of unstable particles such as pions, muons, strange baryons or particle resonances is included independently. The emission of Cherenkov light is handled according to the methods described in section 2.1. Emitted Cherenkov photons are not treated individually but grouped into bunches of a specific size to reduce the required computing time. However, the

absorption of Cherenkov photons in the atmosphere is not considered and is included in the telescope response simulation. The trajectory of these Cherenkov photon bunches is tracked and traced to the observation level and forwarded to the telescope response simulation if the trajectory intersects with a specified telescope position. Simulated air showers can be reused and repositioned relative to the specified telescope array to increase the simulation performance, resulting in new Cherenkov camera images.

### 2.7.2 Telescope Response Simulation With *Sim\_telarray*

*Sim\_telarray* (Bernlöhr, 2008) is a software package for telescope response simulations. Initially developed by Konrad Bernloehr for HEGRA, it has since been modified, updated, and adopted by H.E.S.S. and CTA. It enables the modular simulation of telescope optics and the electronics response to incident Cherenkov light, producing output files that mimic actual telescope output. As an accurate telescope response simulation is critical to the energy reconstruction of cosmic rays and subsequent analysis of its properties, each part of the simulation must replicate the telescope response as closely as possible. *Sim\_telarray* offers many configuration options to define the telescope’s optical components and electronics, which are well documented in the official documentation (Bernlöhr, 2022b).

This vast parameter space allows for single or dual-mirror telescope designs with an experimental Fresnel lens option. Both primary and secondary mirrors can be segmented into hexagonal or round facets with user-defined positions and sizes. The set focal length defines the alignment of the facets. This alignment, however, can be subject to user-defined random fluctuations. To simulate the optical throughput, a wavelength-dependent mirror reflectivity is defined. In the case of H.E.S.S., five one-mirror telescopes are defined this way with a systematic mirror degradation factor accounting for a change in the muon phase (section 2.5.5).

The optical camera system is configured similarly, offering the free positioning and shaping of camera pixels on a plane or curved surface, with control over the wavelength-dependent quantum efficiency. Further, *sim\_telarray* allows for the simulation of Winston cones like they are used for H.E.S.S., incorporating both their angular-acceptance and wavelength-dependent transmittance.

The photon bunches produced by CORSIKA are used as input for the telescope response simulation. Initially, the trajectory information of the photon bunches is used to apply atmospheric extinction, which is defined in a lookup table in altitude segments and wavelength intervals. The surviving photons are then ray traced through the telescope’s optical components, taking into account all angular efficiencies and wavelength dependencies.

The simulation of the telescope electronics includes waveform level simulation of the telescope and array level trigger, reproducing the stereo and hybrid trigger configuration of the H.E.S.S. array. This trigger simulation is performed on the level of small components, such as signal discriminators and comparators, reproducing an accurate representation of the trigger system. In the case of a successful array trigger, the signal digitization and readout are simulated on the waveform level, and the output

is reduced to the integrated charge in a specified waveform readout window. A full per-pixel waveform output is also possible. In addition to the existing simulation, a fixed per-pixel NSB rate ( $\sim 100$  MHz for CT1-4 and  $\sim 300$  MHz for CT5) is included when simulating the Cherenkov camera image. To accurately reproduce the telescope response simulations, most simulation parameters are based on measurements that are performed regularly, such as the muon efficiency. However, small fluctuations in these parameters significantly impact the resulting simulated telescope response, which is detrimental to the energy reconstruction of observed air showers. This work uses the *sim\_telarray* release *version 2021-02-04*. The simulation for the H.E.S.S. telescopes is subject to validation in section 2.7.

### 3 Desert Air Cherenkov Telescope

The Desert Air Cherenkov Telescope (DesertACT) is a modification of the IceACT initially developed for IceCube (IceCube Collaboration, 2013; Aartsen et al., 2020a). The introduced modifications enabled a joint measurement campaign with the H.E.S.S. array in Namibia, extensively described in Dietz (2018). A telescope response simulation in *sim\_telarray* is created based on hardware properties derived from measurements or manufacturer-provided values. The Namibia measurement campaign is recreated in simulation, and the telescope response is compared to the campaign data. Using this new telescope response simulation, telescope properties and parameters are determined, including the energy threshold for the detection of hadronic air showers induced by a cosmic ray proton.

#### 3.1 IceACT

IceACT is a compact IACT with a comparably low anticipated cost (about 10 k€) designed to be deployed as part of a large array. Featuring a pixel size of approximately  $1.6^\circ$ , detecting Cherenkov showers is the main focus of IceACT. As of the time of writing, an array of IceACTs is proposed as an element for the Gen2 upgrade of IceCube, a high-energy neutrino instrument located at the South Pole. Here it would extend the capability of an existing cosmic ray detector called IceTop (Aartsen et al., 2017; Aartsen et al., 2020a). Other applications might include the use as an outrigger array for the High-Altitude Water Cherenkov Observatory (HAWC), deploying many small telescopes far from the array centre to collect information on showers with large impact distances. Due to the comparably small cost, this type of telescope would also be affordable for educational purposes such as student experiments and outreach projects.

#### 3.2 The Mechanical and Optical Design Of IceACT

The mechanical and optical design of IceACT is kept relatively simple to accomplish its primary design goal of easy deployment and low cost. The hardware description follows the one given in Aartsen et al. (2020b). The primary optical element of the telescope is a Orafol SC 943 Fresnel lens with a clear aperture of 549.7 mm and a focal length of 502.1 mm, shown in Figure 25.

The Fresnel lens is protected by a UV-transparent fused silica glass plate, offering enhanced weather and scratch protection (Zink, 2021). Both are held in place by a flange attached to the top of the main telescope body. The latter is constructed from a thin carbon-fibre barrel to reduce weight whilst maintaining structural stability. The telescope features a 61-pixel camera, using rectangular  $6\text{ mm} \times 6\text{ mm}$  SensL MicroFJ-60035-TSV Silicon photomultipliers (SiPMs). To increase the light-gathering area of these pixels, solid acrylic glass Winston-shaped cones (further referred to as Winston cones) are optically bonded to the front glass of the SiPMs. These Winston cones (seen in Figure 25) feature a hexagonal entrance window with a flat-edge width of 1.5 cm. In this design, the telescope is mounted on top of a box containing the required power supply and the data acquisition electronics. As described, the prototype has a total weight of  $\approx 50\text{ kg}$  (Aartsen et al., 2020a).

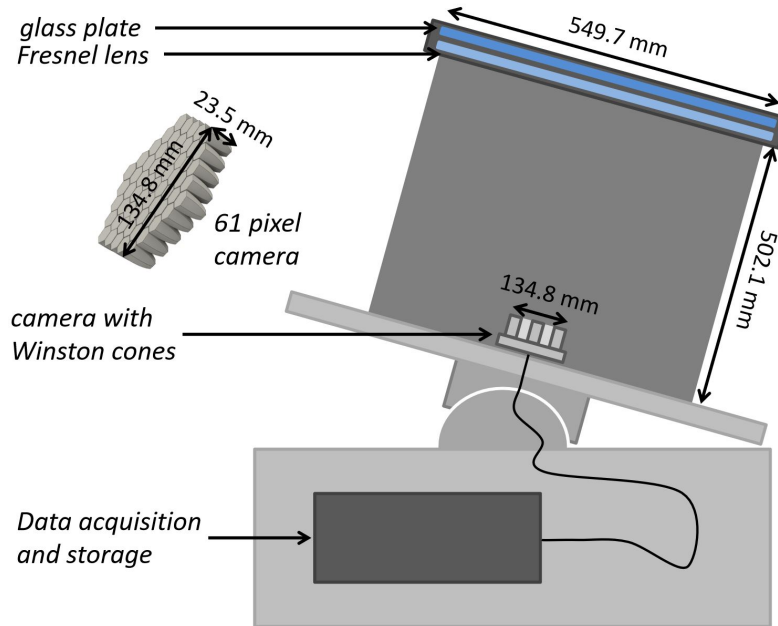


Figure 25: Schematic cross-section of the IceACT demonstrator, with highlighted dimensions and components. The 61-pixel camera with hexagonal light funnels is shown separately to the left. The illustration is taken from Aartsen et al. (2020a).

### 3.3 DesertACT's Modifications

DesertACT is a variation of IceACT, adapted to perform measurements together with the H.E.S.S. array in Namibia. As a result, some constraints present in the IceACT design, such as the elemental resistance in extreme environments, could be loosened. The outline of the modifications included in the DesertACT design is based on the one given in Dietz (2018).

DesertACT adopts the TARGET-Module (section 2.6.2) for its trigger, sampling, and readout electronics. Following the time of the Namibia measurements, this change was also adopted for the IceACT telescope design in early 2020 (Paul et al., 2021). In addition, the system's overall weight has been reduced by replacing the former carbon-fibre body with a cylindrical 1 mm thick PVC cover. This decrease in weight enables the use of a commercial telescope mount to add a star-tracking capability to the system, allowing DesertACT to follow the observation schedule of the H.E.S.S. array. A photograph of the DesertACT setup with highlighted essential components is shown in Figure 26. The previously used fused silica glass plate, protecting the Fresnel lens, is replaced with a 3 mm thick plate of PLEXIGLAS SUNACTIVE GS 2458. The bottom flange of the telescope, housing the camera and DAQ electronics box, is connected with stainless-steel rods. The complete telescope weighs 17.6 kg and is mounted on a commercial Skywatcher EQ8 GoTo mount for tracking. This mount is capable of a tracking precision of 5 arcmin  $\approx 0.083^\circ$  (Corp., 2022) (5% of a camera pixel). However, slight deviations in the tracking speed can accumulate over the length of an observation night, resulting in a drift from the specified pointing direction. To mitigate this issue, an additional guiding camera (Lodestar X2) is mounted to the top of the telescope. It



Figure 26: Image of DesertACT’s telescope body, showing 1: Fresnel lens (behind protective glass), 2: optional guiding camera, 3: 3” prism bar for telescope mount connection, 4: light shielding, 5: bottom flange (camera box not shown), 6: telescope mount, 7: power supply and auxiliary electronics.

tracks the shift in the star positions over time and sends corrections to the mount.

Each SiPM pixel output is directly connected to a trans-impedance amplifier to drive the signal over a coax cable to the data acquisition system. A single TARGET-Module featuring a 64-channel trigger and full-waveform sampling is used for digitisation. Some modifications to the pulse shaping electronics had to be made, as the signal shape of the DesertACT SiPMs is different compared to the Hamamatsu SiPMs used in CHEC-S due to capacity differences. Additional adapter boards connect individual coax lines, power, and networking equipment.

The analogue part of the board consists of a shaping circuit, shortening the length of the photon pulses to an FWHM of  $\approx 10$  ns. This modification also reduces the pile-up of signals in the trigger path due to NSB. Four 16-channel T5TEAs perform a trigger on the sum of four neighbouring channels, commonly referred to as a superpixel or trigger group. The trigger group assignment in the DesertACT camera is shown in Figure 34 in a later section. In addition, four 16-channel CTCs are responsible for digitising the signal. The communication with the downstream computer is based on UDP and a software package called TargetDriver, developed by the CHEC collaboration (Zorn et al., 2018).

### 3.4 The Namibia Measurement Campaign

Stefan Dietz organised and conducted a joint measurement campaign between DesertACT and H.E.S.S. as part of his master’s thesis between the 1st and 7th of April 2019. The campaign overview follows the one given in Dietz (2018). The campaign aimed to determine DesertACT’s energy threshold using the established event energy reconstruction of the H.E.S.S. array (section 2.5). During the campaign, DesertACT was set up on the roof of an instrument container close to the centre of the H.E.S.S. array, as shown in Figure 27. This position was chosen as a compromise between



Figure 27: Photograph of the DesertACT setup on the instrument container close to the H.E.S.S. array centre during the Namibia campaign. A zoomed-in view of the DesertACT setup is also shown. The images are provided by Funk (2021).

the rate of coincident events with H.E.S.S. and the viewable portion of the night sky, limited by the large structure of CT5. The star tracking capability added to DesertACT (section 3.3) enabled the telescope to follow the scheduled H.E.S.S. observation program for six consecutive nights. During these observations, DesertACT was self-triggering and simultaneously acquiring data independently of the H.E.S.S. array. The cosmic ray events detected by both telescopes simultaneously have been determined after the campaign by matching the event timestamps.

Cosmic ray events were simultaneously detected by both instruments, and DesertACT events were matched using the timestamps of reconstructed H.E.S.S. events. In addition, the H.E.S.S. Field of View (FoV)  $\approx 5$  deg (Hofmann, 2012) was consistently contained within the  $> 12$  deg DesertACT FoV (see section 3.5.1).

The trigger threshold of DesertACT was varied during measurements to account for changing observation conditions (e.g. zenith angle and NSB) and to keep a stable trigger rate of  $\approx 3$  kHz per trigger group. Since data was only collected during dark moonless nights, the trigger rate of DesertACT is dominated by NSB events, inducing random telescope triggers. The subsequently performed timestamp-based matching of joint events with H.E.S.S. eliminates these NSB-only events due to the H.E.S.S.



stereo trigger. In total, 33 h of data were collected during the campaign, with targets spanning zenith angles from  $6.5^\circ$  to  $61.2^\circ$ . The campaign data was processed to extract camera images consisting of pixel amplitude and pixel timing information. The original unprocessed pixel-level waveform data of the matched events is no longer available due to a data loss incident that occurred after the Namibia campaign. As a consequence, only the processed data is available. In this work, this dataset and its properties are used to validate a novel simulation of DesertACT, which is introduced and validated step-by-step in the upcoming sections.

### 3.5 A Simulation for DesertACT

As mentioned in section 2.7, this work uses CORSIKA and *sim\_telarray* for both the Cherenkov shower and telescope response simulation. The electronics simulation for DesertACT is based on that of the CHEC-S camera<sup>4</sup>, as it uses the TARGET-Module (TM) for telescope trigger and readout. The remaining simulation parameters, such as the telescope location, observation level, simulated energy range, and atmospheric transmission profile, are adapted from the most recent H.E.S.S. implementation. The validation of which is presented in section 4.

However, adjustments to the *sim\_telarray* configuration are required to accommodate DesertACT’s physical and electronic properties. The upcoming sections focus on the optical and electronic systems, their implementation, and performance validation. *Sim\_telarray* offers a vast list of available parameters to allow for the customization of each telescope. The available parameter space and descriptions are extensive and provided in the official documentation of *sim\_telarray* (Bernlöhr, 2022b). These parameters and their values are stored in configuration files, commonly separated by component or telescope system. Due to the extensive nature of the official parameter descriptions, only short descriptions relevant to the implementation are provided. An overview of the used configuration files for the DesertACT simulation is shown Table 1.

#### 3.5.1 Implementation and Validation of the DesertACT Optics

This section focuses on implementing and validating the DesertACT’s optical system in *sim\_telarray*. The optical system consists of the primary Fresnel lens, the Winston cones and the SiPM pixels to which the Winston cones are optically bonded. To determine the properties of this optical system, the internal ray tracing of *sim\_telarray* is utilised. When compiled with the `-DDEBUG_TRACE 99` option, the internal ray tracing simulation creates an extensive list of photon positions inside the telescope. Generally, this list includes the photon position and incidence angle on the primary mirror, secondary mirror, camera lid and pixel plane, and the pixels hit by a given photon. Due to the simplified design of DesertACT, only some of these output positions apply. For DesertACT, the list only contains the photon positions and incidence angles on the Fresnel lens and the pixel plane. To use the internal ray tracing, the configuration parameters of all major components must be specified. In the case of DesertACT, the minimum requirement is the primary optical element (Fresnel lens) and the camera geometry definition, including pixel positions.

The ray tracing in this section is performed with parallel light under different incident

---

<sup>4</sup>At the time of writing, PROD4 is the identifier for the most recent available configuration in *sim\_telarray*.

Filename	Description
DACT.cfg	Main config file that links to all other config files in this table.
common.cfg	Common settings for the experimental site of the telescope, such as altitude and the number of telescopes.
optics.cfg	Configuration parameters related to the optical system of the telescope.
camera.cfg	Camera configuration for most electronic system parameters and trigger settings.
sipm.cfg	Additional configuration parameters for the SiPM modules.
pixels.dat	Contains pixel types, positions, and trigger group assignments.
lens.dat	Contains fresnel lens position, diameter, and shape.
filter.dat	Describes the wavelength dependant transmittance of the telescope's optical system.
cone_acceptance.dat	Contains the angular acceptance of the Winston cone funnels for different incidence angles.
dact_pulse.dat	Contains an amplitude normalized and shaped SiPM signal as seen by the signal electronics.
dact_PDE.dat	Contains the PDE/quantum efficiency curve of the SiPM modules used.

Table 1: Filenames of the used *sim\_telarray* configuration files, and short descriptions of the information they contain.

angles to the telescope's optical axis. In *sim\_telarray*, this is done by positioning an artificial star at an infinite distance<sup>5</sup> and pointing the telescope at its coordinates. The star's position is defined in a star file (*star.dat*). Shifts in the telescope pointing relative to the star's position are then used to generate off-axis<sup>6</sup> parallel light. The star is positioned at a zenith angle of  $\theta_{\text{star}} = 45^\circ$  to allow for offsets in both the azimuth and zenith direction. Incident photons are propagated through the telescope's optical components, and their positions at the previously mentioned locations stored. The photon positions in these locations are only stored when the photon trajectory starts on the primary optical element (i.e. the Fresnel lens) and ends on the pixel plane. Thus, an explicit definition of the PVC cover that cuts off stray light (section 3.3) is not required.

<sup>5</sup>The star itself is not placed at an infinite distance, but the light emission properties are changed such that parallel light is emitted.

<sup>6</sup>Relative to the telescope's optical axis.

### 3.5.2 Winston Cones

As a first step, the focal plane (characterised by the Winston cone arrangement) is defined in *sim\_telarray*. As mentioned in section 3.3, the camera features 64 SiPM pixels, to which full acrylic Winston cones (often referred to as funnels) are optically bonded. These forward incoming light from a hexagonal surface down to the SiPM's square surface. The hexagonal entrance has a flat-edge width of 1.5 cm and the entire cone a z-height (measured length from square SiPM surface to hexagonal entrance face) of 2.5 cm. An example Winston cone used in the final camera is shown in Figure 28. The Winston cones are made from PLEXIGLAS XT 0A770, the properties of which are

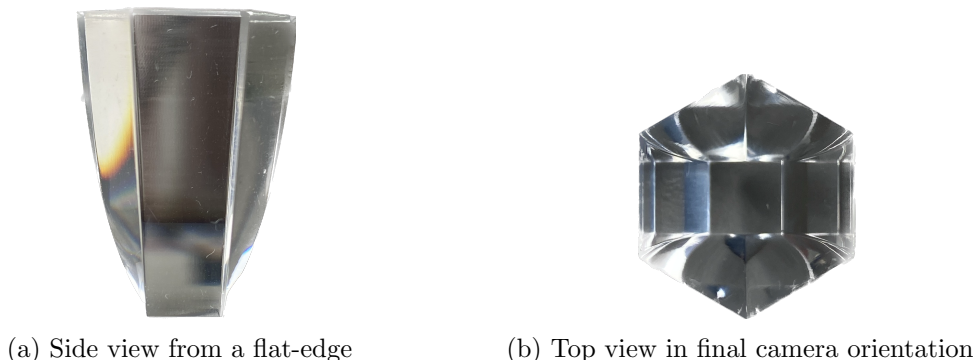


Figure 28: Top and side view of an acrylic Winston cone used in the IceACT/DesertACT camera design.

provided in the manufacturer's datasheet (Roehm, 2002b). The transmittance curve, detailing the wavelength-dependent transmissivity of light passing through the material, is especially important for the optical simulation. As stated by the manufacturer, the material's transmittance curve is initially subject to change with continued UV-A<sup>7</sup> exposure on the order of a few hours. This change in the transmittance curve remains constant even after a tested 4000 h of additional exposure. The two transmittance curves are shown in Figure 29.

Due to the handling of the Winston cone material during manufacturing and storage, it is almost certain that it was irradiated by a few hours of sunlight before the finished Winston cones were bonded to the SiPMs. At the time of writing, the initial prolonged UV-A exposure is now part of the manufacturing process. Hence, the transmittance curve after 4000 h of UV-A exposure will be used in the simulation and is further referred to as the Winston cone transmittance curve. For wavelengths  $\gtrsim 320$  nm, this transmittance curve shows a plateau with transmittance  $T \approx 0.88$ , which is likely caused by Fresnel losses experienced by light passing through the air-PLEXIGLAS-air interface during the measurement process. Considering a transition from a medium with an index of refraction  $n_1$  to a medium with an index of refraction  $n_2$ , the transmittance after accounting for the Fresnel loss is

$$T_F(n_1, n_2) = \frac{4n_1n_2}{(n_1 + n_2)^2}, \quad (27)$$

for non-absorbing media and incoming light with an incidence angle of zero (Bass and Optica, 1995). Considering the nominal refractive indices of air  $n_{\text{air}} \approx 1$  and

<sup>7</sup>UV-A denotes a wavelength interval from 315 nm to 400 nm (World Health Organization, 2022).

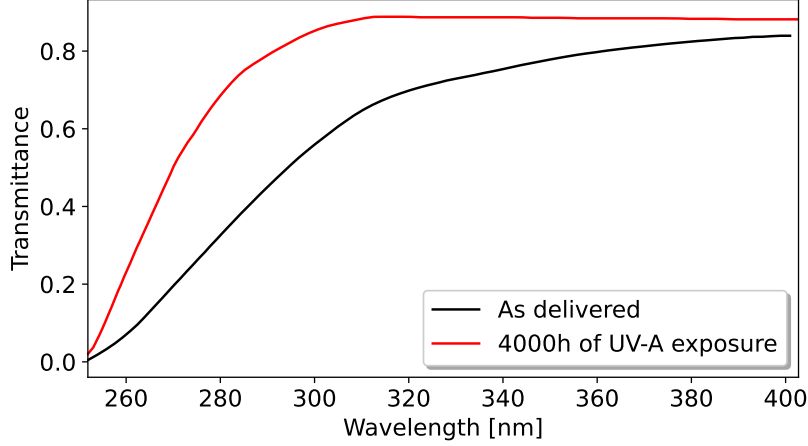


Figure 29: Transmittance of PLEXIGLAS XT 0A770 in the as-delivered condition (black) and after 4000 h of UV-A exposure (red). Data is extracted from the manufacturer’s datasheet (Roehm, 2002b) using webplotdigitizer (Rohatgi, 2022).

$n_{\text{plex}} \approx 1.5$  (Schwartz, 2002) for the PLEXIGLAS, the expected transmittance of the air-PLEXIGLAS-air interface is  $(T_{\text{F}}(n_{\text{air}}, n_{\text{plex}}))^2 \approx 0.92$ . The remainder is likely caused by additional absorption of light in the PLEXIGLAS. In the DesertACT camera, however, the Winston cones are optically bonded to the glass window of the SiPM with a glue of refractive index  $n_{\text{gl}} = 1.55$  (Zink, 2021). Therefore, the expected Fresnel losses differ between the manufacturer-provided air-PLEXIGLAS-air scenario and the air-PLEXIGLAS-glue-glass scenario in the DesertACT camera. The Fresnel losses caused by the PLEXIGLAS-glue-glass interface are smaller than 0.1 %, for a nominal index of refraction  $n_{\text{glass}} \approx 1.5$  and can be neglected. Therefore, the transmittance of the complete air-PLEXIGLAS-glue-glass interface is  $T_{\text{F}}(n_{\text{air}}, n_{\text{plex}}) \approx 0.96$ , equating to a 4 % increase in the transmittance compared to the manufacturer provided values. The latter is considered by adding the 4 % additional transmittance to the manufacturer-provided values.

*sim.telarray* allows for a so-called camera filter that defines the wavelength-dependent transmittance of the entire telescope system. An additional part that must be included in the total transmittance curve is the acrylic plate protecting the Fresnel lens. Again, the manufacturer provides a transmittance curve for the front acrylic plate made from PLEXIGLAS SUNACTIVE GS 2458 (Roehm, 2002a). Like the Winston cone material, the front acrylic plate’s transmittance changes after prolonged UV-A exposure. The manufacturer, again, provides a transmittance curve for the required thickness of 3 mm after 1000 h of UV-A exposure. As no optical bonding is used for the front acrylic plate, the provided transmittance curves can be used without modifications. With the same reasoning as for the Winston cone material, the transmittance curve after prolonged UV-A exposure is adapted and referred to as front glass transmittance, shown in Figure 30. Since a dense sampling of the manufacturer’s provided transmittance curves was possible, the provided values can be linearly interpolated. This, in turn, enables the resampling of both the front glass and Winston cone transmittance curves, with a step size of 1 nm in the wavelength range from 260 nm to 400 nm. The latter is chosen such that data from both the front glass and Winston cone material is avail-

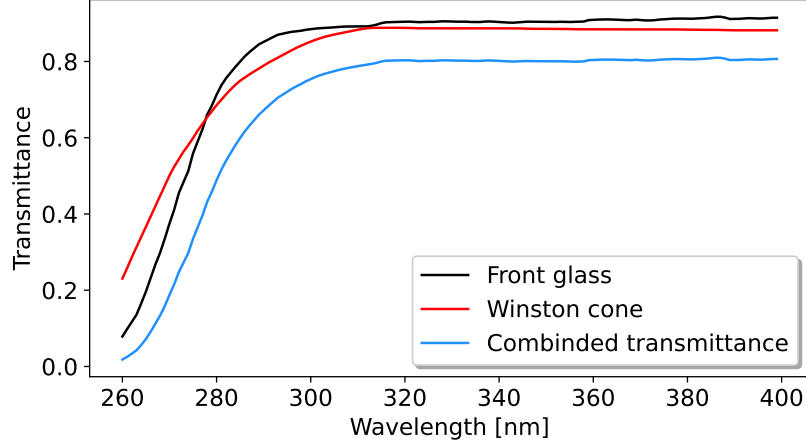


Figure 30: Transmittance curves of the Winston cone (red) and front glass material (black) after prolonged UV-A exposure. The combined transmittance curve (blue) is the product of both materials. Data is extracted from the manufacturer’s datasheet (Roehm, 2002b; Roehm, 2002a) with the webplotdigitizer (Rohatgi, 2022).

able. The combined transmittance curve is the product of the Winston cone and front glass material transmittance curves. The total transmittance curve is exported into the *filter.dat* file as a two-column table containing a wavelength and a corresponding transmittance in each row.

In addition to a transmittance curve, *sim.telarray* allows specifying an angular acceptance curve for the Winston cones. The angular acceptance of the full-material Winston is investigated in Koschinsky (2017). In his work, an optics simulation of the Winston cone and SiPM coupled system is created. This simulation considers the transmittance  $T$  of the Winston cone material and the Photo Detection Efficiency (PDE) of the SiPM. From this simulation, the efficiency  $\epsilon$  is defined as

$$\epsilon(\theta, \lambda) = \text{PDE}(\lambda) \cdot T(\lambda) \cdot \psi(\theta), \quad (28)$$

with the angular acceptance  $\psi(\theta)$ . The system’s efficiency is evaluated at different incidence angles  $\theta$  for light of 380 nm wavelength. Due to the hexagonal shape of the Winston Cone entrance and square pixel shape, multiple axes were considered when simulating the efficiency curves. A side view of this simulation is shown in Figure 31. The four investigated axes represent symmetry lines for the combined Winston Cone and SiPM system. The axes themselves are identified using a location identifier (Edges or Sides) highlighting if an axis crosses through an edge or a side of the hexagonal entrance (Hex) or square exit (Square) plane. Due to the Winston cone’s symmetry, the ”Hex Sides” and ”Hex Edges” axes have twice the multiplicity of the remaining axes. The corresponding detection efficiency curves are densely sampled and linearly interpolated. The results are shown in Figure 32. The angular acceptance  $\psi(\theta)$  can be calculated from the efficiency curves shown in Figure 32 by rearranging Equation 28:

$$\psi(\theta) = \frac{\epsilon(\theta, \lambda = 380 \text{ nm})}{\text{PDE}(\lambda = 380 \text{ nm}) \cdot T(\lambda = 380 \text{ nm})}. \quad (29)$$

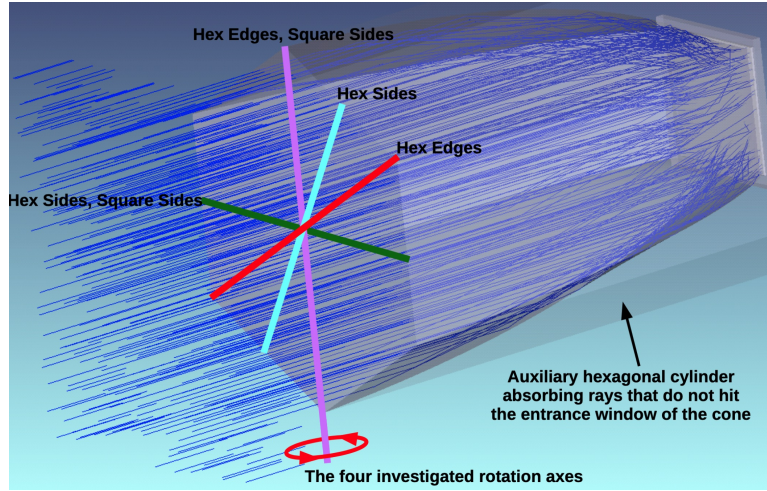


Figure 31: Side view of the angular efficiency simulation for a hexagonal Winston cone used in the newest IceACT design. Photon paths are shown in blue. The axes along which the angular efficiency was simulated are highlighted with coloured lines. The plot is taken from Koschinsky (2017).

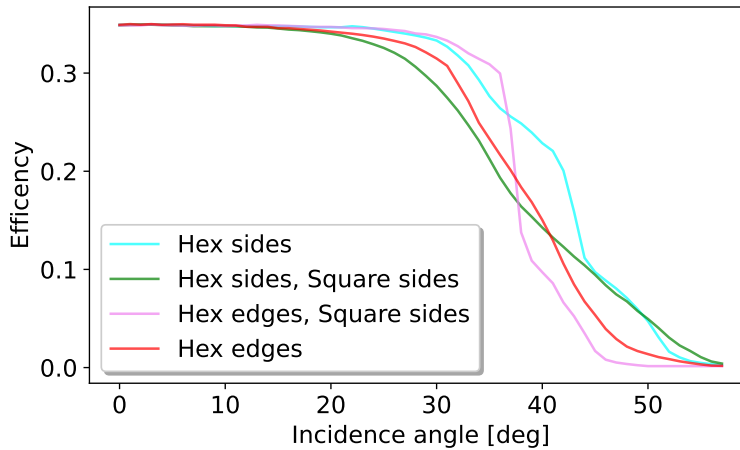


Figure 32: Detection efficiency for the Winston cone and SiPM system along different rotational axes (compare Figure 31). The data is taken from Koschinsky (2017) and extracted using the webplotdigitizer (Rohatgi, 2022).

The Winston cone transmittance for the simulated wavelength  $T(\lambda = 380 \text{ nm}) \approx 0.88$  is taken from Figure 30 and the PDE of the used SiPMs at this wavelength  $\text{PDE}(\lambda = 380 \text{ nm}) \approx 0.4$  is provided in Koschinsky (2017). The resulting angular acceptance is shown in Figure 33. As expected,  $\psi(\theta)$  is close to unity at small incidence angles. Since *sim.telarray* only allows for a single angular acceptance curve, the average curve between all Winston cone axis weighted with their multiplicity is calculated (Figure 33). The result is resampled in  $1^\circ$  steps and exported as a two-column table (*cone\_acceptance.dat*) containing the incidence angle and a corresponding acceptance in each row.

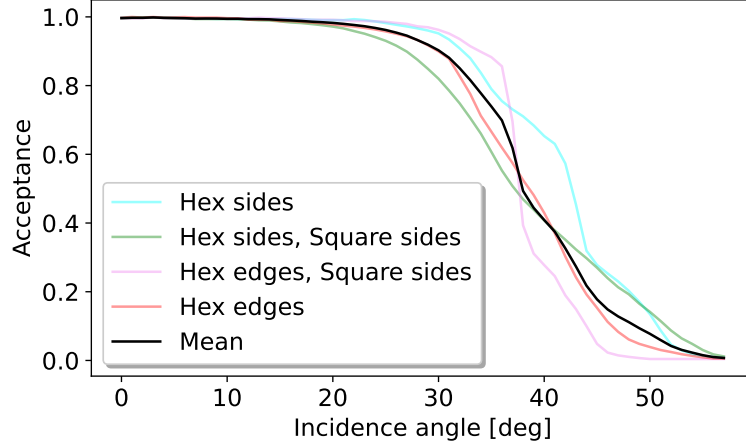


Figure 33: Calculated angular acceptance for the Winston cone and SiPM system along different rotational axes (compare Figure 31). The average acceptance curve over all rotational axes, weighted with their multiplicity, is shown in black.

### 3.5.3 Camera Geometry

The telescope’s focal plane is implemented using each camera pixel’s exact position, shape, orientation, and trigger group assignment. In the case of DesertACT, the focal plane is the entrance plane of the Winston cones. The hexagonal Winston cones are tiled so that the 64-pixel camera of DesertACT is formed. This tiling is shown in Figure 34. The pixel numbers (shown on the Winston cones) and the trigger group assignment (colour map) are predetermined by the electronic construction of DesertACT. The arrangement of the Winston cones is modelled after the first-generation IceACT prototype, with three additional outlying pixels with the numbers 44, 45, and 46. However, *sim.telarray* does not support solid-material light funnels as of the time of

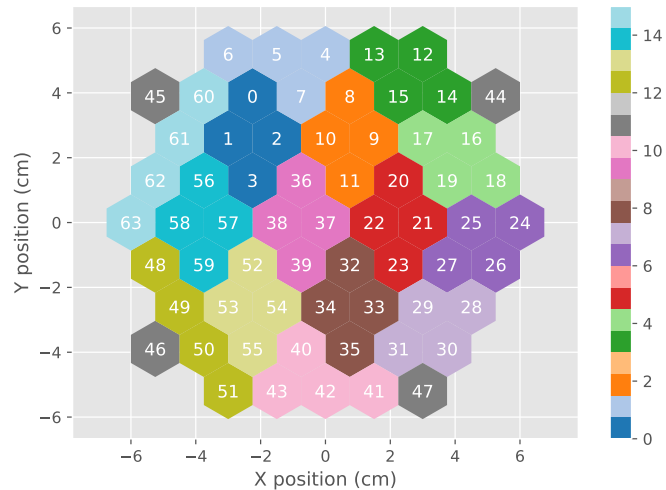


Figure 34: Pixel entrance positions with channel number assignment on the hexagonal Winston cone entrances and trigger groups differentiated by a colour map. The plot adapted from Dietz (2018).

writing. As a substitute, the hexagonal entrance plane of the Winston cones is chosen as pixel geometry directly. This can be done as long as the proper wavelength-dependant transmittance of the Winston cones (see Figure 29) is respected in the simulation.

This camera geometry is implemented in the *pixels.dat* file. However, a scaling factor of three is applied to both the Winston cone flat-edge width and the pixel positions. This choice is explained and justified further in this section as part of the Fresnel lens implementation (section 3.5.4).

In *sim\_telarray*, each pixel of the camera must carry a pixel type (PixType) defining the shape, size, and orientation of the camera pixel and the light funnel. In the case of DesertACT only a single pixel type is required. The implementation of the pixel type with the required parameters is shown in Configuration 1. Due to the choice that the pixels are defined by the shape and position of the Winston cone entrance planes, the PMT cathode and light funnel share the same shape and diameter, whereas the light funnel depth is zero. The diameter represents the scaled flat-edge width of the Winston cones.

```

1 # PixType format:
2 #   1: ID of this pixel type
3 #   2: PMT type (must be 0)
4 #   3: PMT cathode shape (hexagonal=1)
5 #   4: PMT cathode diameter [cm]
6 #   5: Light funnel shape (hexagonal=1)
7 #   6: Light funnel diameter (flat-to-flat) [cm]
8 #   7: Light funnel depth [cm]
9 #   8: Light funnel angular acceptance file
10 PixType 1 0 1 4.5 1 4.5 0.000 "cone_acceptance.dat"
11

```

Configuration 1: Definition of the DesertACT pixel type as part of the *pixels.dat* configuration file. The pixel size is scaled by a factor of three. The parameter descriptions are adapted from Bernlöhr (2022b).

The properties of the individual camera pixels are defined in the same configuration file. An example configuration for the 0th trigger group of DesertACT is shown in Configuration 2. Each pixel is uniquely identified with a pixel ID equal to the pixel number (Figure 34) and its X-Y-coordinate. Whilst *Sim\_telarray* supports assigning individual pixels to a TARGET-Module, only a single TARGET-Module is used in DesertACT's design. Consequently, the TARGET-Module number and ID are zero.



```

1 # Pixel format:
2 #   1: Pixel ID (starting at 0)
3 #   2: Pixel Type ID
4 #   3: Pixel X-coordinate [cm]
5 #   4: Pixel Y-coordinate [cm]
6 #   5: TARGET-Module Number
7 #   6: Pixel number (here equal to Pixel ID)
8 #   7: Dummy parameter (not currently used)
9 #   8: TARGET-Module ID hex number ('0x...')
10 #   9: Pixel is turned on (1) or off (0)
11
12 Pixel    0 1  -6.750 11.691  0 0  0 0x00 1
13 Pixel    1 1  -9.000 7.794   1 0  0 0x00 1
14 Pixel    2 1  -4.500 7.794   2 0  0 0x00 1
15 Pixel    3 1  -6.750 3.897   3 0  0 0x00 1
16

```

Configuration 2: Definition of the individual pixels in the *pixels.dat* configuration file using the example of the 0th trigger group of DesertACT (compare Figure 34). Pixel positions are scaled by a factor of three. The parameter descriptions are adapted from Bernlöhr (2022b).

The last component of the *pixels.dat* configuration file defines the so-called majority trigger. This setting defines the pixels in each trigger group and the superpixel trigger behaviour. In the case of DesertACT, each trigger group is defined by an entry of the form  $A[B,C,D]$ . Here,  $A$ ,  $B$ ,  $C$ , and  $D$  are the pixels IDs that constitute a given trigger group.  $A$  is the leading pixel of the trigger group, also used for internal identification purposes, and can be chosen freely from the pixel IDs in the trigger group but should remain consistent while defining the majority trigger. This choice has no ramifications for the later simulation.

Furthermore, a + symbol can be prepended to the leading trigger group pixel, indicating that this trigger group must have issued a trigger signal. As a TARGET-Module (TM) is used for triggering, two neighbouring trigger groups (Figure 34) must issue a trigger signal for the telescope to issue a global trigger. The number of required trigger groups is the so-called multiplicity, which is usually not defined in the majority trigger definition directly (denoted by a \*) but later set in the *camera.dat* configuration file (Table 1). An example of such an implementation is provided in Configuration 3 for the 0th trigger group and its available trigger partners (compare Figure 34).

```

1 # Majority trigger format:
2 #   1: Trigger multiplicity
3 #   Here, a '*' denotes that this is set
4 #   later in the camera definition
5 #   2: Primary trigger group that issued the trigger signal
6 #   3: Possible partner group that could lead to a global trigger
7 MajorityTrigger * of +0[1,2,3] 60[61,62,63]
8 MajorityTrigger * of +0[1,2,3] 56[58,57,59]
9 MajorityTrigger * of +0[1,2,3] 36[37,38,39]
10 MajorityTrigger * of +0[1,2,3] 8[9,10,11]
11 MajorityTrigger * of +0[1,2,3] 4[5,6,7]
12

```

Configuration 3: The trigger group and behaviour definition in *pixels.dat* using the example of the 0th trigger group of DesertACT (compare Figure 34). The parameter descriptions are adapted from Bernlöhr (2022b).

### 3.5.4 Orafol SC 943 Fresnel lens

The Fresnel lens is the primary optical component of the telescope. As mentioned in section 3.2, the telescope uses an Orafol SC 943 (positive) Fresnel lens with a clear aperture of  $D = 2R = 549.7$  mm and a measured focal length of  $f = 513.2$  mm. An optical property of this Fresnel lens is the PSF which refers to the photon distribution on the focal plane. Instead of referring to the PSF directly, its size is commonly expressed as the 90% containment radius  $R_{90\%}$ . It defines the radius of a circle around the CoG, that contains 90% of the total signal. A measurement of which has been conducted for DesertACT’s Orafol SC 943 Fresnel lens in Niggemann (2016). In his work, the Fresnel lens is illuminated with parallel light from a 550 nm laser diode under different offsets to the optical axis of the lens. The resulting PSF is recorded with multiple CMOS camera images combined into a single image of the PSF. This process is repeated for different distances between the CMOS camera and the Fresnel lens. The results are shown in Figure 35. A polynomial is fit to the data of each measured offset, and the  $R_{90\%}$  for the DesertACT focal distance of  $z = f = 513.2$  mm is determined. The extracted containment radii are shown in Table 2. These measurements are used as a reference to

Offset to the optical axis [deg]	0	2	4	6	8
$R_{90\%}$ [mm]	3.24	2.41	4.25	6.19	8.41

Table 2: Measured  $R_{90\%}$  of the Orafol SC 943 Fresnel lens at a focal distance of  $f = 513.2$  mm for different offsets to the optical axis. The data is taken from Niggemann (2016).

compare the simulation results to. *Sim\_telarray* allows for the simulation of a Fresnel lens, albeit with imposed restrictions. These restrictions include the inability to specify the surface structure of the Fresnel lens, which would enable a more detailed optic simulation. Instead, a spherical lens of a given focal length  $f$  and index of refraction  $n$  is simulated to approximate the imaging behaviour of the Fresnel lens (Bernlöhr, 2022b). Furthermore, the user-specified index of refraction is assumed to be wavelength-independent. A schematic view of such a spherical lens can be found in Figure 36. Here,

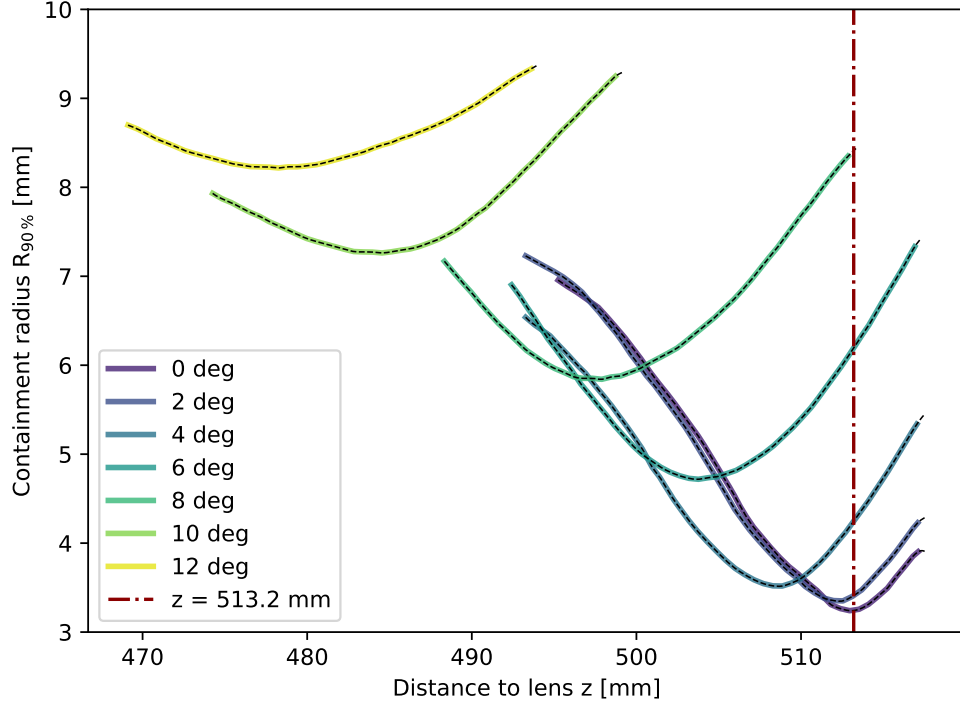


Figure 35: Measured  $R_{90\%}$  of the Orafol SC 943 Fresnel lens for incoming parallel light of different offsets to the optical axis and distances  $z$  to the lens. The dashed lines are polynomial fits to the curves for different offsets to the optical axis. The focal distance of the lens is highlighted as  $z = f = 513.2$  mm. Data is taken from Niggemann (2016) and extracted using the webplotdigitizer (Rohatgi, 2022).

$h$  is the distance of incoming parallel light to the optical axis,  $\alpha$  the angle of incidence and  $\beta$  the refraction angle relative to the spherical lens's surface normal. The radius of curvature  $r_{\text{curve}}$  of the spherical lens is not a free parameter in *sim\_telarray*, but instead is calculated as a function of  $n$  and  $f$ :

$$r_{\text{curve}} = f \cdot (n - 1) \quad (30)$$

Unlike the lens shown in Figure 36, however, the simulated spherical lens is a quasi-planar surface that behaves like a spherical lens with the provided parameters (Bernlöhr, 2022b). With sufficiently tuned parameters, the image of this simulated lens can approximate the one of the DesertACT's Fresnel lens, especially considering the large pixel size of the camera. This parameter tuning is discussed in the following.

The initial lens parameters for DesertACT are defined in the *optics.cfg* configuration file and are shown in Table 3 with short descriptions. The used Orafol SC 943 Fresnel lens is manufactured out of acrylic material, with a nominal index of refraction of  $n \approx 1.5$  (Schwartz, 2002). Random optical fluctuations in the lens's horizontal and vertical imaging behaviour are removed by setting the `MIRROR_ALIGN_RANDOM_VERTICAL` and `MIRROR_ALIGN_RANDOM_HORIZONTAL` parameters to zero. The position of the Fresnel lens relative to the telescope camera is controlled with `MIRROR_OFFSET` parameter and set to the negative focal length of the system, with negative values indicating a camera

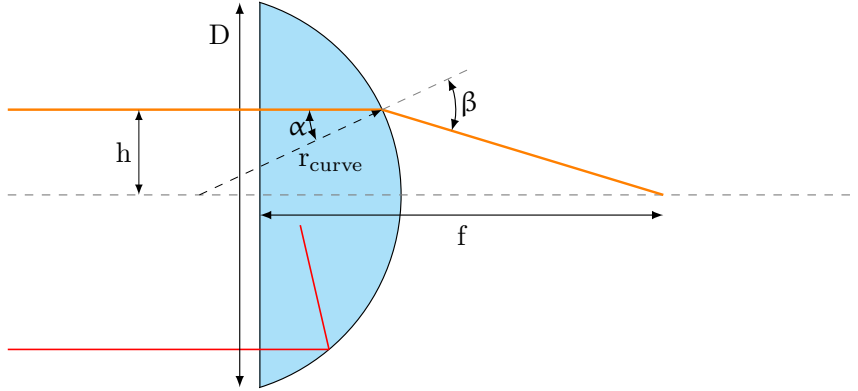


Figure 36: Illustration of a spherical lens of diameter  $D$  and focal distance  $f$ , with an incoming parallel light ray of a distance  $h$  to the optical axis. The radius of curvature  $r_{\text{curve}}$ , the angles of incidence  $\alpha$  and refraction  $\beta$  relative to the local surface normal are highlighted. The orange light ray results in a normal image, while the red light ray undergoes total internal reflection.

position behind the Fresnel lens. The `CAMERA_TRANSMISSION` defines the wavelength-dependent transmittance of the optical system, specified in `filter.dat` (section 3.5.2). The size and shape of the Fresnel lens are specified in the `DACT_lens.dat` configuration file shown in Configuration 4.

```

1 # Lens parameters
2 #   1: X-position
3 #   2: Y-position
4 #   3: Fresnel lens diameter [cm]
5 #   4: Fresnel lens focal length [cm]
6 #   5: Fresnel lens shape [0: round]
7 0.0   0.0   54.97   0   51.32   0
8

```

Configuration 4: The Fresnel lens parameter configuration is specified in the `DACT_lens.dat` configuration file. The parameter descriptions are adapted from Bernlöhr (2022b).

A first ray tracing simulation for this initial configuration of DesertACT’s optical system is performed for 50k simulated photons. The resulting photon positions on the Fresnel lens are shown in Figure 37a.

It is apparent from Figure 37a that only a central region of the lens with a diameter of 34.21 cm shows tracked photons. Photons outside this region do not reach the pixel plane. This is due to the spherical nature of the simulated lens, as the radius of curvature is small enough to result in total internal reflection for distances  $h < R$  to the optical (central) axis (compare Figure 36). The critical distance  $h_{\text{crit}}$ , at which total internal reflection occurs can be derived from Snell’s law (Riedl, 2001):

$$n \cdot \sin(\alpha) = n_{\text{air}} \cdot \sin(\beta). \quad (31)$$

Here,  $n$  and  $n_{\text{air}}$  denote the index of refraction of the Fresnel lens material and air,

Parameter	Value	Description
MIRROR_CLASS	3	Defines use of spherical lens.
MIRROR_LIST	DACT_lens.dat	Position and diameter of lens.
FOCAL_LENGTH	51.32	Focal length of the lens in [cm].
MIRROR_OFFSET	-51.32	Distance of camera from the lens [cm]. A negative value means the camera is behind the lens.
FOCUS_OFFSET	0.0	Distance of starlight focus from the camera pixel entry plane.
MIRROR_ALIGN_RANDOM_*	0.0	Disables all random optical variation parameters, including vertical and horizontal variations.
CAMERA_TRANSMISSION	filter.dat	Contains the wavelength-dependent transmittance values.

Table 3: Initial *sim.telarray* parameters used in the optics simulation for DesertACT, with both values and a short description (Bernlöhr, 2022b).

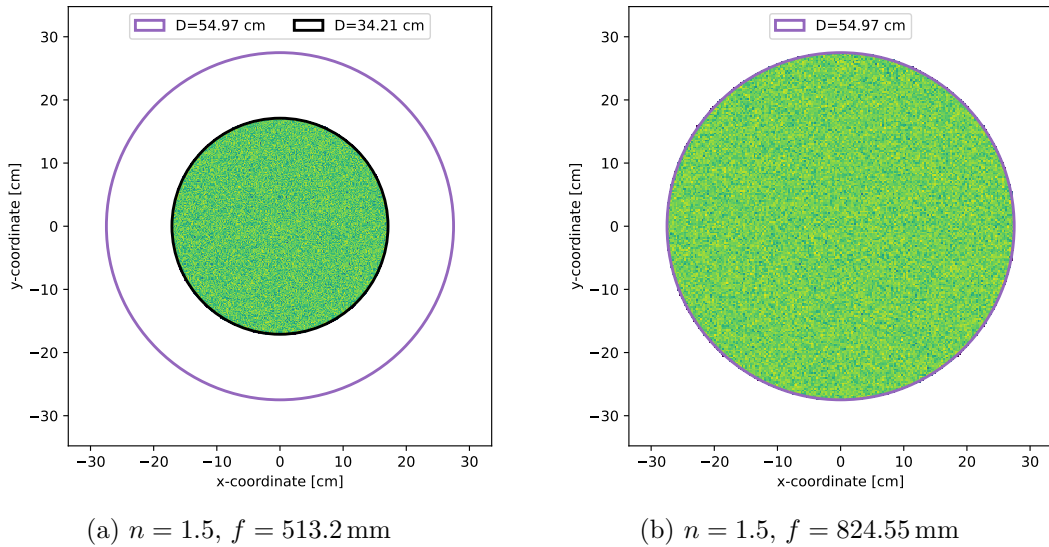


Figure 37: The distribution of tracked photons on the Fresnel lens for the original focal length (a) and the new focal length, mitigating the effect of total internal reflection (b). The physical lens diameter was set to  $D = 2R = 549.7$  mm (highlighted in purple). In addition, (a) shows the expected effective diameter limited by total internal reflection in black.

respectively. The latter can be approximated with  $n_{\text{air}} \approx 1$  (Laufer, 1996). Total internal reflection occurs when incoming light is refracted back into the lens instead of refracted to the bordering media. This, in turn, requires an angle of refraction  $\beta \geq 90^\circ$  (compare Figure 36). The critical angle of incidence  $\alpha_{\text{crit.}} = \arcsin(n^{-1})$  is calculated from Snell's law. The critical distance to the optical axis after which total internal reflection occurs is

$$h_{\text{crit.}} = r_{\text{curve}} \cdot \sin(\alpha_{\text{crit.}}) = \frac{r_{\text{curve}}}{n}$$

$$\stackrel{(30)}{=} f \cdot \frac{n-1}{n}. \quad (32)$$

For the simulation parameters shown in Table 3, the critical distance is  $h_{\text{crit.}} \approx 171.07$  mm. This informs an effective lens diameter of  $D = 2h_{\text{crit.}} = 342.14$  mm, which is highlighted in Figure 37a. The calculated critical distance fits the simulation result perfectly.

Since the direct implementation of the optical parameters does not produce the required output, new parameters for the optic simulation are derived to mimic the behaviour of the Fresnel lens without using its physical parameters directly. This can be done as long as the light-capturing area of the telescope (lens diameter) is not altered and the real telescope's optical PSF is replicated. The internal reflections limiting the effective diameter are absent in the actual Fresnel lens. Hence, new simulation parameter values for the focal distance and refractive index must satisfy

$$R \leq h_{\text{crit.}} = f \cdot \frac{n-1}{n} \quad (33)$$

to prohibit total internal reflection for photons spread over the entire lens diameter. One could use the refractive index alone to satisfy this requirement, with  $n = (1 - R/f)^{-1} \approx 2.15$  for  $R/f \neq 1$ . In this case, the valid parameter range ( $1.001 \leq n \leq 5.0$ ) in *sim\_telarray* (Bernlöhr, 2022b) would not suffice to replicate the measured  $R_{90\%}$  values seen in Table 2. Consequently, a new focal length  $f_{\text{new}}$  is selected instead to satisfy the requirement in Equation 33. Using the Fresnel lens parameters, a new minimum focal length of  $f_{\text{new}} \gtrsim R(n/n-1) = 824.55$  mm is calculated, resulting in a ratio of  $f_{\text{new}}/f \gtrsim 1.61$  between the new and old focal lengths. The tracked photon distribution of a ray tracing simulation with the new focal length parameter is shown in Figure 37b. As expected, tracked photons are found over the entire Fresnel lens area, and no total internal reflection occurs.

The newly calculated value for the focal length is the lower limit for focal lengths that can be chosen to mitigate the effects of total internal reflections. In general, the longer the focal length, the closer the behaviour of the spherical lens will be to that of an ideal lens. With wise foresight, a ratio of  $f_{\text{new}}/f = 3$  between the new and old focal length is selected, as this allows for sufficient adjustment of the PSF size in the valid parameter range of  $n$  to replicate the measured  $R_{90\%}$  values in Table 2. Increasing the focal length and keeping all other parameters constant will also change the image on the focal plane. To ensure that the image of the simulation also corresponds to that of the actual Fresnel lens, the size of the pixels and their positions must be scaled as well.

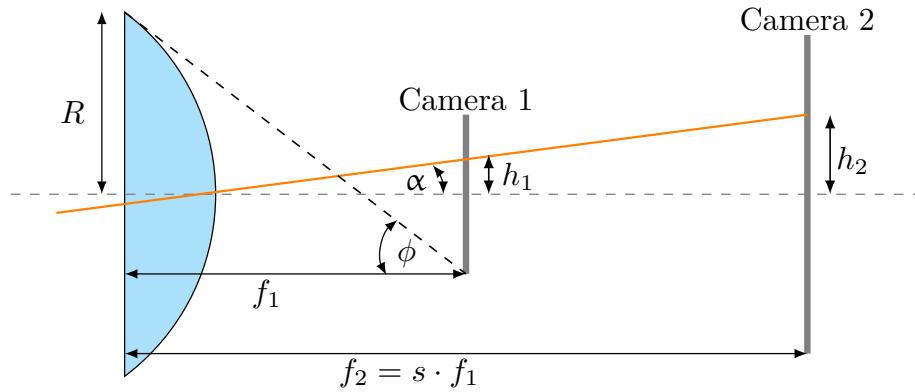


Figure 38: Illustration of a spherical lens of radius  $R$  for an incoming central light ray with an offset  $\alpha$  to the optical axis (orange) for two different camera image planes at distances  $f_1$  and  $f_2$ . The focal length  $f_2$  is connected to  $f_1$  with a scaling factor  $s$ . The heights  $h_1$  and  $h_2$  are the radial distance of the light ray’s impact point on camera 1 and camera 2, respectively. The largest possible incidence angle  $\phi$  is highlighted for camera 1.

A schematic view illustrating this scaling is shown in Figure 38. A central ray under incident angle  $\alpha$  hits the lens, and its image is projected on camera 1 at focal distance  $f_1$  at height  $h_1$ . Let  $h_1$  be the position of a pixel in the camera layout shown in Figure 34. Changing the focal length to  $f_2$ , the new position for this pixel is now  $h_2$ . Using simple trigonometry, the corresponding pixel position  $h_2 = h_1(f_2/f_1)$  for the focal length  $f_2$ . This expression is valid for both spatial directions on the camera plane (X-Y-Coordinates). Therefore, each pixel centre’s coordinates shown in Figure 34 is scaled by a factor of  $s = f_{\text{new}}/f = 3$ . Likewise, the pixel size needs to be scaled by this factor to maintain the established camera geometry. It should be noted that the increase in the pixel size and scaling of coordinates only corrects for the change in lens image and does not increase the light yield per pixel as the light collection area (Fresnel lens diameter) is not altered.

This increase in focal length also changes the maximum incidence angle  $\phi$  (see Figure 38). Following Koschinsky (2017), this angle can be calculated using the camera radius of  $R_{\text{cam}} = 60$  mm, the focal length of  $f = 513.2$  mm, and a focal length scaling

factor of  $s$ :

$$\phi(s) = \arctan\left(\frac{R + R_{\text{cam}} \cdot s}{f \cdot s}\right). \quad (34)$$

For the original telescope parameters, one finds  $\phi(s = 1) \approx 33.12$  deg, and for the new telescope parameters  $\phi(s = 3) \approx 16.78$  deg. Consequently, the angular acceptance for the Winston cones shown in Figure 33 must be rescaled. This is done by multiplying the incidence angles in the acceptance table (*cone\_acceptance.dat*) with a factor of  $\phi(s = 3)/\phi(s = 1) = 0.51$ . This way, the new maximum incidence angle is assigned the same transmittance value as before.

These changes are implemented, and a new ray tracing simulation is performed. In addition to the photon distribution on the Fresnel lens, the stored photon positions on the pixel plane are now utilised to create an overview of the ray tracking results shown in Figure 39.

To create an X-Y plane side view of the ray tracing simulation, the central line of the Fresnel lens along the X-direction is divided into 25 equidistant points, and the closest photon to these points is identified. The path of these photons is extracted and displayed with the position and size of the Fresnel lens and the camera as implemented in the simulation. Since an upscaling of the camera is required to mimic the imaging behaviour of the actual Fresnel lens, the optic simulation must be treated as a black box, such that the coordinates of each photon on the pixel plane must be scaled back by the same factor of  $s = 3$  that is used to upscale the camera.

The  $R_{90\%}$  is determined following the algorithm presented in Niggemann (2016), enabling easy comparison of the measured results (Table 2) to the simulation results. Let  $N$  be the total number of photons in the PSF distribution on the pixel plane. Each photon  $i = 1 \dots N$  is associated with a coordinate pair  $(x_i, y_i)$  on the pixel plane. The coordinates of the PSF's CoG on the pixel plane are calculated as

$$x_{\text{CoG}} = \frac{\sum_i^N x_i}{N} \quad \text{and} \quad y_{\text{CoG}} = \frac{\sum_i^N y_i}{N}. \quad (35)$$

For each photon, the radial distance  $R_i = \sqrt{(x_i - x_{\text{CoG}})^2 + (y_i - y_{\text{CoG}})^2}$  relative to the CoG is calculated and stored in an ordered set of the form

$$R = \{R_1, R_2, \dots, R_i, R_{i+1}, \dots, R_{N-1}, R_N | R_i \leq R_{i+1}\}. \quad (36)$$

The  $R_{90\%}$  is determined by finding a newly chosen radial distance  $R_{90\%}$  in which 90 % of the total number of photons are contained

$$\sum_{R_1}^{R_{90\%}} 1 \approx 0.9 \cdot N. \quad (37)$$

The accuracy of this method is evaluated using a two-dimensional Gaussian distribution of the form shown in Equation 38. In this case, the expected  $R_{90\%}^{\text{Theory}}$  can be calculated directly and compared to the result of the algorithm described above.

$$G(x, y) = \frac{1}{2\pi\sqrt{\sigma_x^2\sigma_y^2}} \exp\left[-\left(\frac{(x - \mu_x)^2}{2\sigma_x^2} + \frac{(y - \mu_y)^2}{2\sigma_y^2}\right)\right]. \quad (38)$$



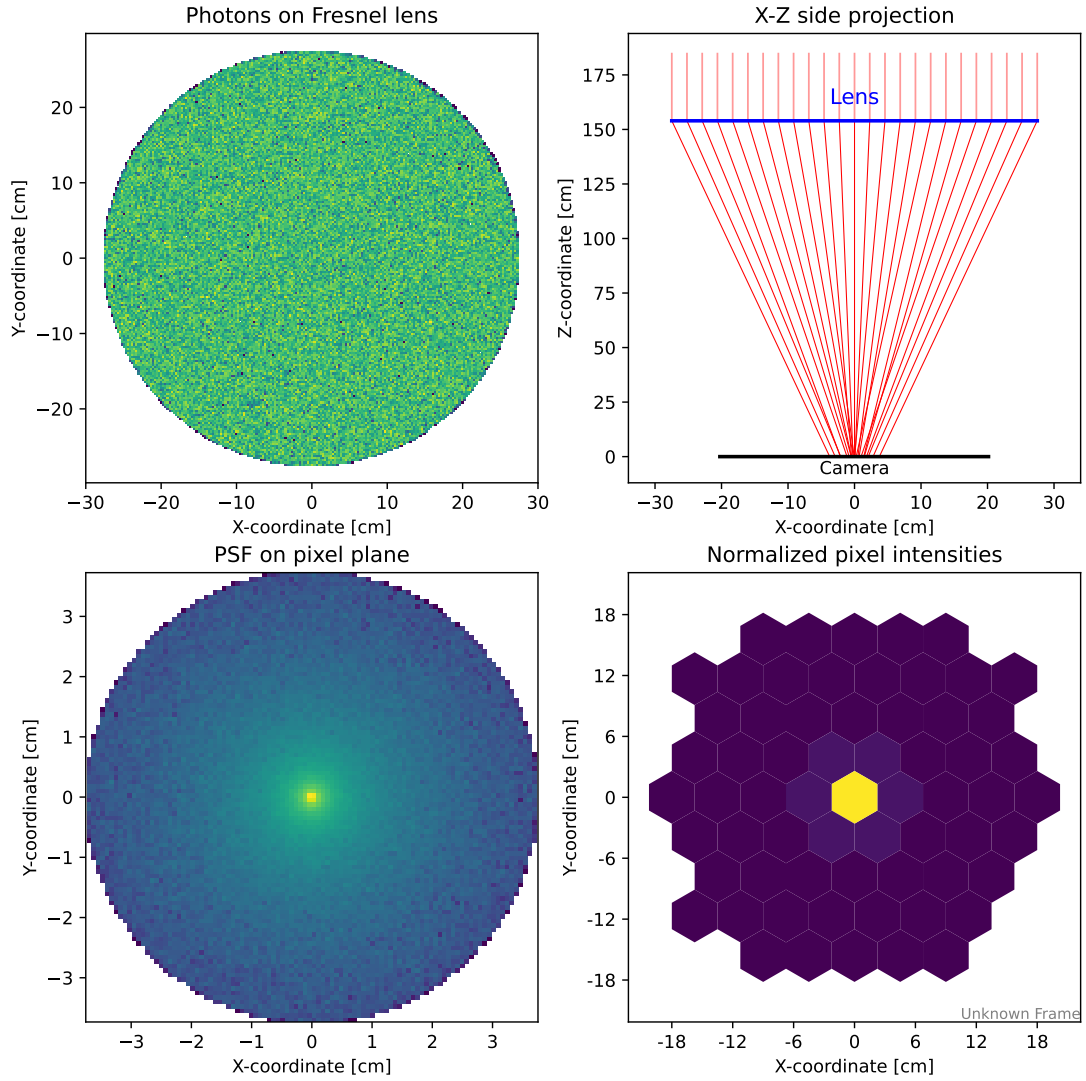


Figure 39: Ray tracing overview containing the photon distribution on the Fresnel lens (top left) and on the pixel plane (bottom left), the X-Z side projection of the optical setup as well as the normalised pixel intensities of the pixels that are hit by a photon. The simulation is performed for a focal length of  $f = 153.96$  cm, index of refraction  $n = 1.5$  and a camera scaling factor of three. All intensities are normalised.

For ease of calculation it is assumed that  $\mu_x = \mu_y = 0$  and  $\sigma_x = \sigma_y = 1$ , resulting in a simplified expression:

$$G(x, y) = \frac{1}{2\pi} \exp \left[ -\frac{x^2 + y^2}{2} \right]. \quad (39)$$

The integral of Equation 39 can be easily obtained in polar coordinates ( $r = x^2 + y^2$ ):

$$\begin{aligned} I_G(R) &= \frac{1}{2\pi} \int_0^R \int_0^{2\pi} e^{-\frac{r^2}{2}} r \, dr \, d\varphi \\ &= \int_0^R e^{-\frac{r^2}{2}} r \, dr. \end{aligned} \quad (40)$$

With the use of substitution ( $u = r^2/2$  and  $du = r \, dr$ ) the integral is solved

$$\begin{aligned} I_G(R) &= \int_0^{\frac{R^2}{2}} e^{-u} \, du \\ &= [-e^{-u} + C]_0^{\frac{R^2}{2}} \\ &= 1 - e^{-\frac{R^2}{2}}. \end{aligned} \quad (41)$$

Using the limit  $\lim_{R \rightarrow \infty} I_G(R) = 1$ ,  $R_{90\%}^{\text{Theory}}$  can be calculated:

$$I_G(R_{90\%}^{\text{Theory}}) = 0.9 \stackrel{!}{=} 1 - e^{-\frac{R_{90\%}^{\text{Theory}2}}{2}} \quad (42)$$

$$R_{90\%}^{\text{Theory}} = \sqrt{-2 \ln(1 - 0.9)} \approx 2.14597. \quad (43)$$

To test the algorithm described above, the distribution in Equation 39 is sampled one million times. The algorithmically determined result  $R_{90\%} \approx 2.14597 = R_{90\%}^{\text{Theory}}$  agrees with the expected value.

This accuracy, however, requires an adequate number of photons to be simulated. The comparison between the algorithm's result and the expected theoretical value can be used to estimate the minimum amount of simulated photons required. To this end, increasing sample sizes are taken from the distribution described in Equation 39 and the  $R_{90\%}$  algorithm applied. For each sample size, the random sampling and subsequent application of the algorithm are repeated 100 times, and the relative difference  $(R_{90\%}^{\text{Theory}} - R_{90\%})/R_{90\%}^{\text{Theory}}$  is calculated. The mean and standard deviation of the distribution for each sample size are shown Figure 40.

A relative difference of 1 %, highlighted in orange in Figure 40, is deemed acceptable. This threshold is reached for sample sizes  $> 2 \cdot 10^4$ . Thus, the previously chosen number of 50 k photons for ray tracing simulations is justified and is used in the following unless stated otherwise.

This validated method to determine  $R_{90\%}$  is applied to a ray tracing simulation with the current simulation settings used in Figure 39. The result is shown in Figure 41. As seen in Figure 41a, the resulting containment radius produced by the current simulation parameters and no offset to the optical axis is  $R_{90\%} = 10.40$  mm. To approach the reference value of 3.24 mm (see Table 2), the index of refraction  $n$  is increased until the best match is found, which is shown in Figure 41b. For an index of refraction of  $n = 2.2448$ , a perfect match is established between the measured and simulated value at zero offset to the optical axis.

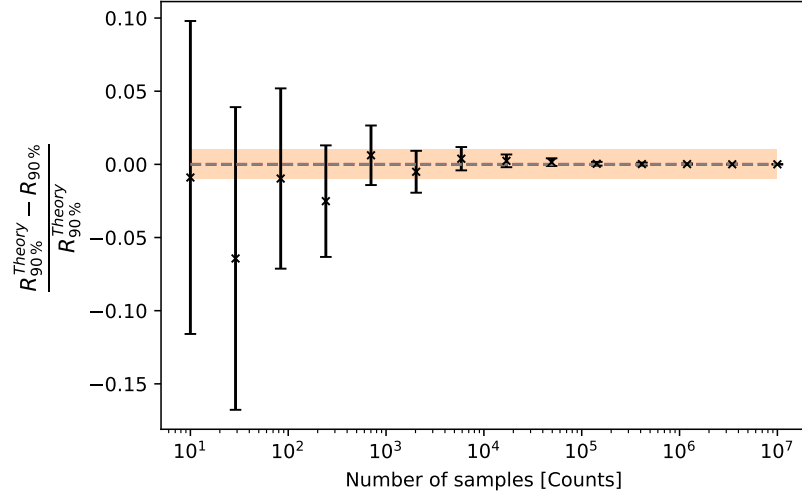


Figure 40: The relative difference between the expected and simulated containment radius, denoted with  $R_{90\%}^{\text{Theory}}$  and  $R_{90\%}$  respectively, for varying amounts of random samples taken from the simplified two-dimensional Gaussian in Equation 39. The calculations for each sample size are repeated 100 times with the mean shown as the datapoint and the standard deviation as error bars. The 1% band around zero relative deviation is highlighted in orange.

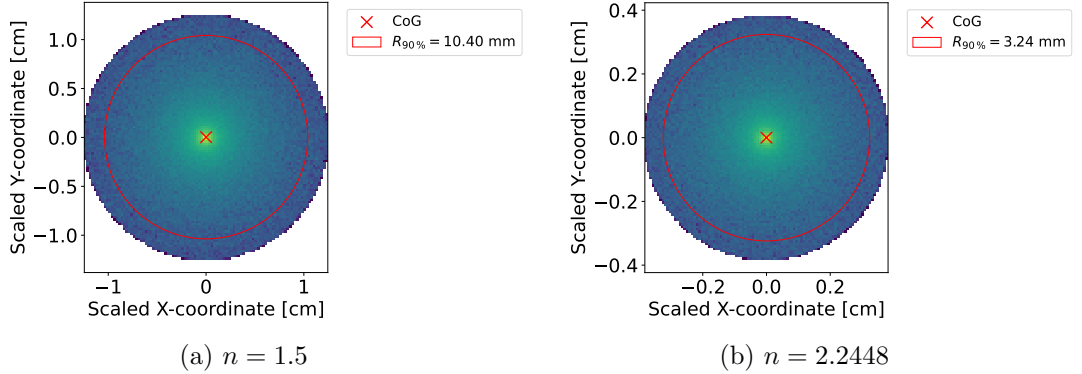


Figure 41: Applied  $R_{90\%}$  algorithm on photon coordinates on the pixel plane for a focal length of  $f = 153.96$  cm and two different indices of refraction. The photon position coordinates are scaled down by the camera scaling factor of three to correct for the increased camera size in the simulation.

The 90% containment radius with the newly selected index of refraction is also evaluated at non-zero optical axis offsets and compared to the measurement results shown in Table 2. This comparison is shown in Figure 42.

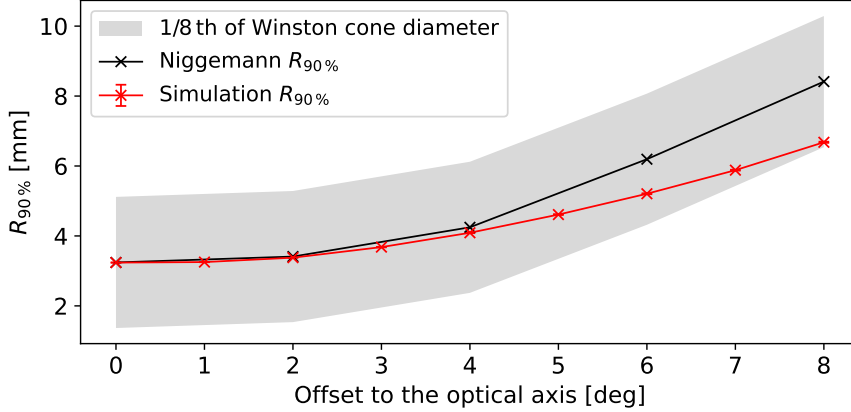


Figure 42: Measured  $R_{90\%}$  of the Orafol SC 943 Fresnel lens (Niggemann, 2016) at a distance of  $f = 513.2$  mm for incoming parallel light at different offsets to the optical axis together with the simulation results. Variance around the measured values of 1/8 th of the Winston cone flat-edge diameter (1.875 mm) is highlighted in grey. Measurements are taken from Niggemann (2016) and extracted with the polynomial fit (see Figure 35).

Here, an interval of 1/8 th of the Winston cone flat-edge diameter ( $\pm 1.875$  mm) is highlighted. While the deviations between the measured and simulated  $R_{90\%}$  values increase with increasing offset to the optical axis, they remain small even compared to a fraction of the pixel size. Therefore, the differences are considered negligible. It is concluded that the newly determined Fresnel lens simulation parameters reproduce the behaviour of the actual Fresnel lens on the scales of the DesertACT pixels.

During the production of DesertACT, however, the telescope body was constructed 3 cm too short. Therefore, the camera is out of focus by this amount. This is implemented with the `FOCUS_OFFSET` parameter (Table 3). The introduced scaling of  $s = 3$  for the simulated focal length must also be taken into account, resulting in a `FOCUS_OFFSET` setting of 9 cm. The final parameters that specify the optics of DesertACT are shown in Table 4

With the newly implemented and validated optic parameters, the simulation can be used to determine the optical properties of DesertACT. One such property is the relative optical acceptance, which later informs other simulation parameters. Again, ray tracing simulations are carried out for incoming parallel light with increasing offset to the telescope's optical axis. An example ray tracing overview for a  $5^\circ$  offset is shown in Figure 43. Such simulations are carried out for offsets between 0 deg to 10 deg zenith. The CoG of the PSF moves away from the camera centre in the X-direction with increasing offset to the optical axis (Figure 43). This movement represents the longest valid linear path through the active pixels of the camera. From these simulations, the so-called relative optical acceptance curve is determined. It is the ratio between the number of photons that hit the camera  $N_{\text{cam}}$  and the number of simulated photons  $N$  for a given offset of incoming parallel light to the optical axis. The result is shown in Figure 44. The point at which the relative acceptance falls to zero is identified as the angular acceptance  $\theta_{\text{max}} = 7.54^\circ$  of the telescope. For this point, the PSF has fully traversed all 4.5 pixels to reach the edge of the camera. From this, the pixel FoV of

Parameter	Value	Description
MIRROR_CLASS	3	Defines use of spherical lens.
MIRROR_LIST	DACT_lens.dat	Position and diameter of lens.
FOCAL_LENGTH	153.96	Focal length of the lens in [cm].
MIRROR_OFFSET	-153.96	Distance of camera from the lens [cm]. A negative value means the camera is behind the lens.
FOCUS_OFFSET	9	Distance of starlight focus from the camera pixel entry plane.
MIRROR_ALIGN_RANDOM_*	0.0	Disable all random optical variation parameters including vertical and horizontal reflection variations.
CAMERA_TRANSMISSION	filter.dat	Contains wavelength dependant transmittance values, scaled to account for the increased focal length and camera size.

Table 4: Final *sim.telarray* parameters used in the optics simulation for DesertACT, with both values and a short description (Bernlöhr, 2022b).

$\varphi_{\text{pix.}} \approx 1.68^\circ$  is calculated.

This is consistent with the expected pixel FoV of the initial IceACT design, adjusted for the increased Winston cone size. Contrary to the hexagonal Winston cones used for DesertACT, the initial IceACT design used round hollow funnels with a diameter of 13.42 mm and an expected pixel FoV of 1.5 deg (Aartsen et al., 2020b). As this initial prototype used the same Fresnel lens with near identical focal distance to the funnel entrance plane and identical pixel tiling, the equivalent pixel FoV expected for the hexagonal Winston cones can be estimated as  $1.5 \text{ deg} \cdot (15 \text{ mm}/13.42 \text{ mm}) \approx 1.68 \text{ deg}$ . This, in turn, is consistent with the presented simulation.

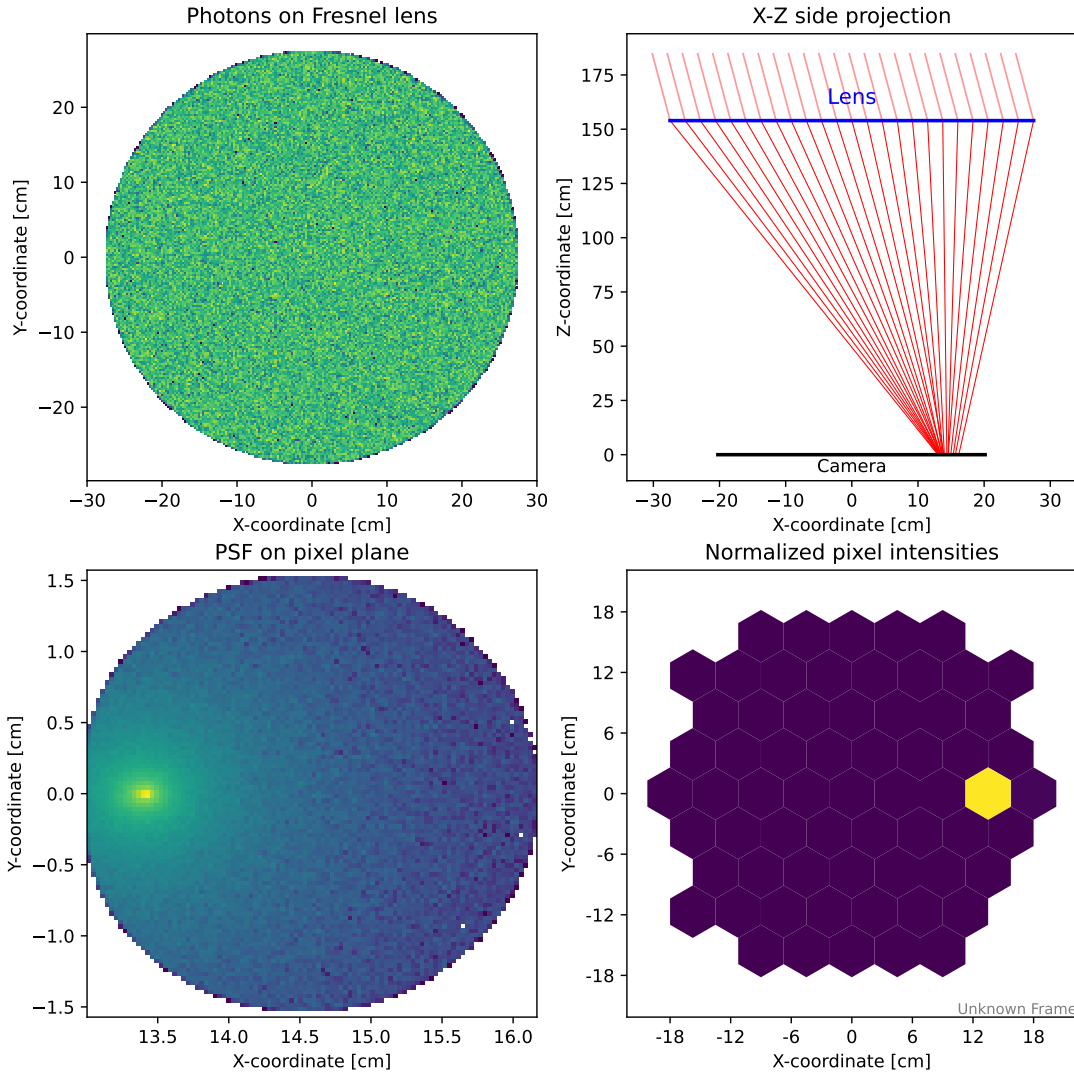


Figure 43: Ray tracing overview with the photon distribution on the Fresnel lens (top left) and on the pixel plane (bottom left), the X-Z side projection of the optical setup as well as the normalised pixel intensities of the pixels that are hit by a photon. Simulated for the new simulation parameters in table Table 4 and a zenith offset of  $5^\circ$  to the artificial star.

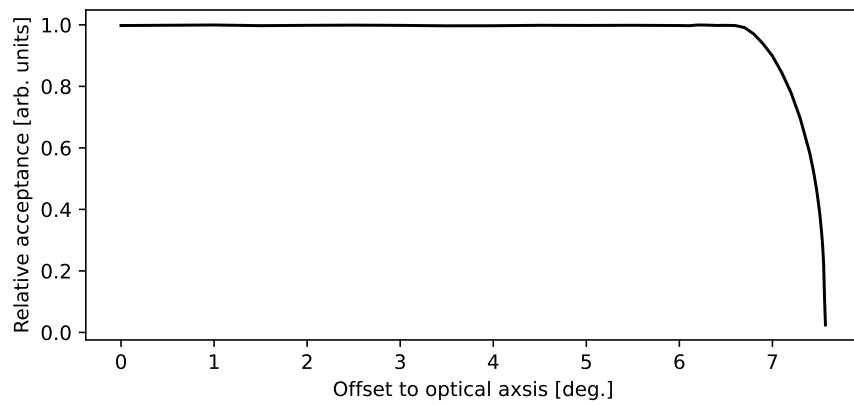


Figure 44: Relative acceptance of the simulated DesertACT optics for final optic simulation parameters (Table 4) over the offset of incoming parallel light to the optical axis.

### 3.5.5 Modification of the Electronic Signal Chain Based on TARGET

With the successfully implemented optical components in the previous section, the next step is to add the electronic components. As mentioned in section 3.3, DesertACT adapts the TARGET-Module (TM) for sampling, triggering and signal readout. The TARGET-Module (TM) is already part of the CHEC-S simulation in *sim\_telarray*, with a copy of the configuration file *CTA-PROD4-SST-CHEC-S-camera.cfg* being part of the *sim\_telarray* base installation. A copy of this configuration file and subsequently included files is the basis for DesertACT’s camera configuration file *camera.cfg*. As the original CHEC-S simulation configuration file contains an extensive list of parameters, only those modified are mentioned. However, trivial configuration parameters such as the camera name and output filenames are excluded, as these are of no consequence for the simulation output.

The signal shaping electronics for the used SiPMs were modified for the use in DesertACT compared to what is used for CHEC-S. This, in turn, results in a different shape of the input signal pulse. The new pulse shape provided by (Zink, 2021) is sampled in 1 ns steps and is shown in Figure 45 together with the original CHEC-S SiPM pulse.

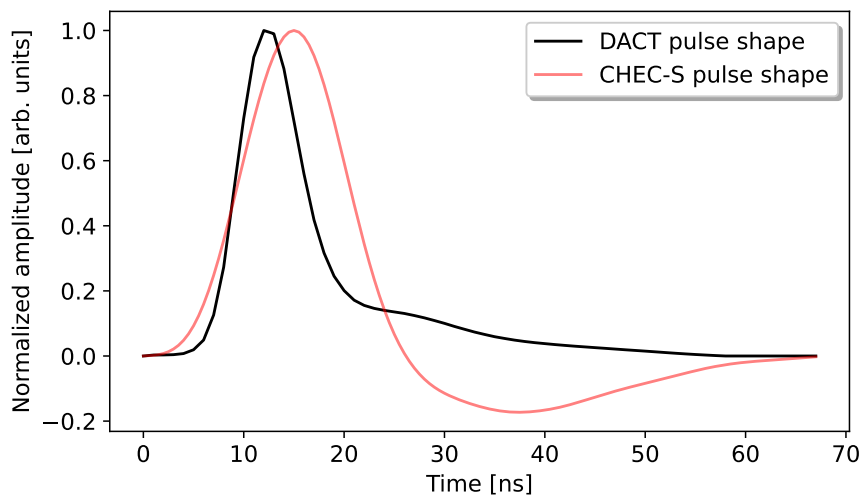


Figure 45: Shaped and amplitude normalized DesertACT SiPM pulse sampled in 1 ns steps and previously used pulse shape for CHEC-S as implemented in *sim\_telarray*. The DesertACT SiPM pulse was provided by Zink (2021)

The sampled pulse is again used to create a two-column table stored in the *dact\_pulse.dat* configuration file, with the time and normalized amplitude in each row. This pulse can characterize both the discriminator and the FADC pulse shape. Furthermore, *sim\_telarray* requires a parameter for the FADC amplitude, which defines the mean signal amplitude of a single p.e.. This is set to  $\approx 6$  ADC-counts (Zink, 2021).



Another parameter that needs to be considered is the quantum efficiency or PDE of the used SensL MicroFJ-60035-TSV SiPM modules. The manufacturer’s datasheet (SCI, 2021) provides such a PDE curve for two different Over Voltages (OVs) of 6.0 V and 2.5 V, shown in Figure 46. The  $OV = V_{op} - V_{br}$  is the difference between the breakdown and

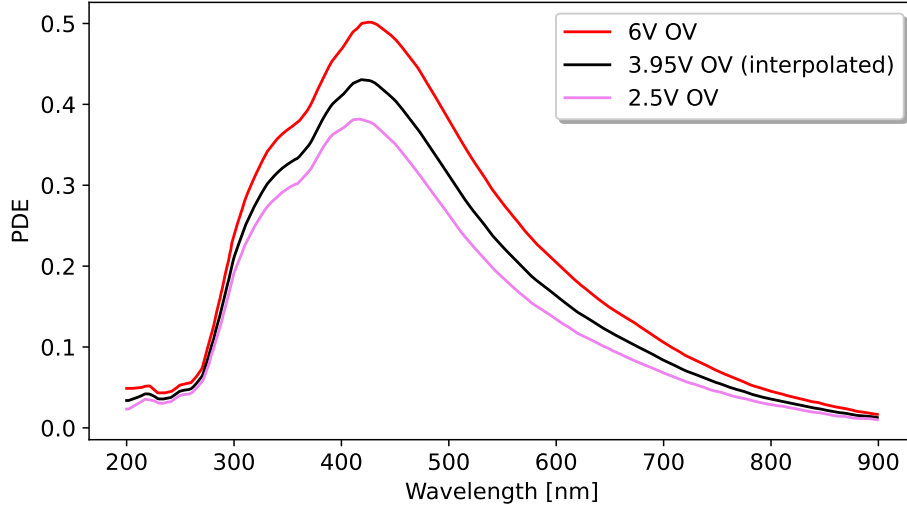


Figure 46: Manufacturer provided PDE curve of the SensL MicroFJ-60035-TSV SiPM (SCI, 2021) for  $OV = 2.5$  V and  $OV = 6.0$  V. The PDE curve at  $OV = 3.95$  V is created by linear interpolation between the two provided curves. The data is taken from manufacturer’s datasheet (SCI, 2021) and extracted using the webplotdigitizer (Rohatgi, 2022).

operating voltage of the SiPM. The SiPM’s datasheet provides a minimal and maximal breakdown voltage  $V_{br} = 24.2$  V – 24.7 V. For further calculations, the arithmetic mean  $V_{br} = 24.45$  V is used. During the Namibia campaign, an operating voltage of  $V_{op} = 28.4$  V was used, resulting in an  $OV = 3.95$  V (Dietz, 2018). Since no PDE curve is provided for this OV, it is created by linearly interpolating between the two provided PDE curves. Let  $PDE(OV_i, \lambda)$  be the PDE curve for an overvoltage  $OV_i$  for  $(i = a, b, c)$ . Further, let  $OV_a \leq OV_b \leq OV_c$ . The interpolated PDE curve for an overvoltage  $OV_b$  is calculated as

$$PDE(OV_b, \lambda) = \frac{(OV_b - OV_a) \cdot PDE(OV_c, \lambda) - (OV_b - OV_c) \cdot PDE(OV_a, \lambda)}{OV_c - OV_a}. \quad (44)$$

Using Equation 44 with  $OV_a = 2.5$  V,  $OV_b = 3.95$  V, and  $OV_c = 6.0$  V the interpolated PDE curve is calculated and shown in Figure 46.

The manufacturer also provides a graph, seen in Figure 47, detailing the relationship between the maximum PDE curve peak value and the overvoltage (SCI, 2021). A linear fit of the form  $f(OV) = m \cdot OV + t$  is made to the data, and the PDE peak value at the required OV  $f(OV = 3.95$  V) = 0.4398 is extracted.

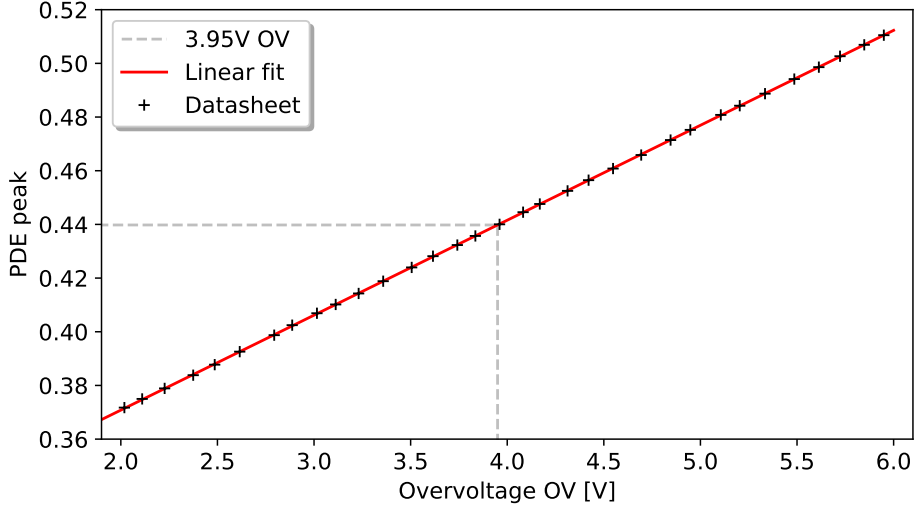


Figure 47: The PDE curve maximum for varying overvoltage settings with a linear fit from which the PDE peak value at 3.95 V OV is extracted. Data taken from manufacturer datasheet (SCI, 2021) and extracted with the webplotdigitizer (Rohatgi, 2022).

The linear interpolated PDE curve calculated with Equation 44 predicts a value of  $\text{PDE}^{\max}(\text{OV} = 3.95 \text{ V}) = 0.4305$  at the same OV. The interpolation prediction and the manufacturer’s expectation match within 2.2%, deemed acceptable. Furthermore, the linear relationship between the PDE peak value and the selected overvoltage validates the linear interpolation approach chosen for the PDE curves. Again, the interpolated PDE curve is sampled in 1 nm intervals and tabulated in the *dact.PDE.dat* configuration file, with each row containing a wavelength and the corresponding PDE value.

*Sim\_telarray* further allows specifying the minimum number of photons and photo-electrons required to run a simulation. This way, no CPU time is wasted on telescope response simulations that do not result in data output. One of the telescope properties that should be derived from this simulation is the proton energy threshold. Hence, the simulation is run for every simulated event. These modified parameters for the electronic simulation are shown in Table 5. Here, the number of camera pixels also needs to be explicitly specified.

Parameter	Value	Description
DISCRIMINATOR_PULSE_SHAPE	dact_pulse.dat	Pulse shape of the discriminator.
FADC_PULSE_SHAPE	dact_pulse.dat	Pulse shape of the FADC.
FADC_AMPLITUDE	8	ADC amplitude of a single p.e.
CAMERA_PIXELS	64	Number of defined camera pixels.
MIN_PHOTONS	-1	Least amount of photons required to run a simulation.
MIN_PHOTOELECTRONS	0	Least amount of p.e. required to run a simulation.
QUANTUM_EFFICIENCY	dact_PDE.dat	PDDE curve of the specified camera pixels.

Table 5: Modified *sim\_telarray* parameters and values for DesertACT’s electronic simulation based on the *CTA-PROD4-SST-CHEC-S-camera.cfg* configuration file for CHEC-S. The parameter descriptions are adapted from (Bernlöhner, 2022b).

### 3.5.6 First Cherenkov Shower Simulations

With the implemented *sim\_telarray* telescope response simulation of DesertACT, coupled Cherenkov shower simulations with CORSIKA can be produced. In the following, Cherenkov showers will be referred to as showers. As introduced in section 2.7.1, the simulation of hadronic showers is complex and requires extensive configuration for a specific location. The default installation of the CORSIKA software already provides a H.E.S.S.-site specific companion script (*hess2d\_run*) that creates the required CORSIKA-input parameters file based on simple user input.

The user must specify the primary particle type inducing showers, zenith, and azimuth direction of the showers, simulated energy range, number of simulated showers, simulation multiplicity, and the simulation date. The latter is essential to calculate the earth’s magnetic field strength at the H.E.S.S.-site. With this information, a template CORSIKA-input file containing the simulation parameters is modified accordingly.

DesertACT-standalone proton simulations are conducted using the default QGSJET II-04 high-energy interaction model (see section 2.7.1). The H.E.S.S. simulation template is modified to simulate a single telescope of DesertACT’s size. An X-Y-Z-coordinate specifies the telescope positions with a radius of a sphere encompassing the telescope.

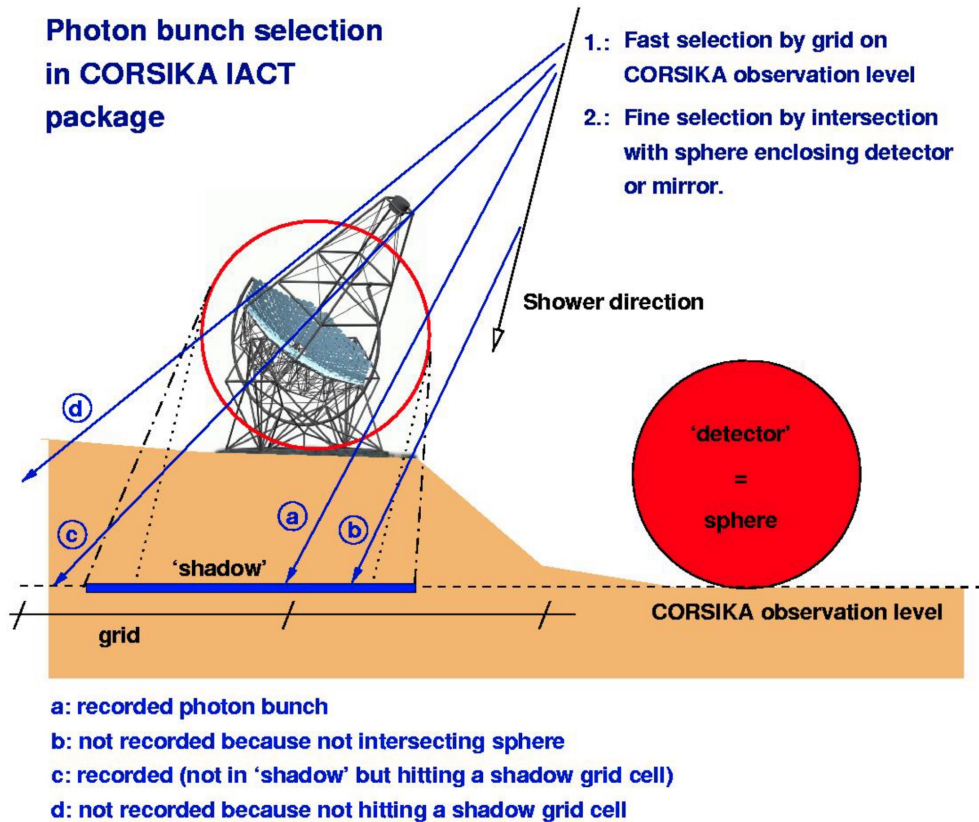


Figure 48: Illustration of the photon bunch selection method in the CORSIKA-IACT package. The illustration is taken from Bernlöhner (2022b).

These coordinates are relative to the array centre and CORSIKA observation level, equivalent to the altitude above sea level (1835 m). The radius defines a sphere around the telescope, which is part of a fast algorithm that selects which photons are stored and forwarded to the telescope response simulation done with *sim\_telarray*. This way, photons that do not hit the primary optical element (i.e. mirror or lens) are not considered in the later simulation. An illustration is shown in Figure 48. Due to the increased focal length in the DesertACT optic simulation (section 3.5.1), the simulated telescope frame now has a length of  $\approx 1.6$  m, which is also chosen as the telescope sphere radius. It should be noted that a larger-than-necessary sphere radius is not detrimental to the simulation output itself. However, it might add computational time since photon bunches that do not hit the primary optical element are forwarded to the instrument response simulation. As mentioned in section 3.4, DesertACT was located on the roof of an instrument container of 8 m height during the Namibia measurement campaign, which is set as the Z-coordinate. Since DesertACT is the only simulated telescope, its X-Y-position is set to the array centre at zero.

The simulated events follow a power law with an index of  $\gamma = -2.0$ , within a fixed energy range from 1 TeV to 1 PeV. The low-energy boundary is informed by the initial analysis of the Namibia campaign data in Dietz (2018), estimating DesertACT's proton trigger threshold as  $\approx 11$  TeV (Dietz, 2018). Showers can be reused multiple times

without additional CPU-intensive simulation to improve the simulation performance. For each reuse, the array is repositioned randomly in a circular area limited by the user-specified radius `RSCAT`. How often the array is repositioned for each shower is specified with the `NSCAT` parameter. The default values for H.E.S.S.-simulations at the time of writing are `NSCAT` = 10, and `RSCAT` = 800 m. Whilst chosen as initial values for the DesertACT simulation, they are subject to validation later in this section. Therefore, showers capable of triggering DesertACT with an impact distance far from the array centre must be considered. As the brightness of the Cherenkov emission is proportional to the primary particle’s energy (section 2), such showers are predominantly initiated by higher-energy particles. The terminology of bright and dim showers is commonly used in this context. To not bias the validation of the maximum shower distance `RSCAT`, the upper energy limit of the simulation is chosen generously as 1 PeV.

The primary particle’s direction is selected as arriving from the south, which will be the dominant direction in the later analysis. Per default, the selected primary particles originate from a single source at the specified pointing direction. Diffuse simulations can be enabled by specifying a view cone, which defines the half-opening angle of a cone around the pointing direction from which primary particles can originate. The simulated view cone should be larger than the telescope’s FoV, as showers that are initiated outside the telescope FoV can still contribute observable Cherenkov emission inside the telescope FoV. Due to the radial 7.5 deg FoV of DesertACT (section 3.5.1), an initial view cone setting of 10 deg is chosen for the simulation. This setting is also subject to validation later in this section.

DesertACT’s trigger threshold is set in units of p.e. using the `DISCRIMINATOR.THRESHOLD` parameter in `sim_telarray`. Furthermore, a per-pixel NSB rate can be specified. A discriminator threshold of 10 p.e. and a NSB rate of 450 MHz is chosen for the initial simulation used to validate the CORSIKA simulation parameters. The chosen discriminator threshold and NSB rate are informed by final simulation parameters obtained in section 3.5.7 and represent lower and upper bounds, respectively. Initial proton-induced air shower simulations are performed with the introduced settings at zenith angles of 15 deg, 25 deg, 35 deg, and 45 deg. The output of `sim_telarray` is written in the eventio (Bernlöhr, 2005) format and contains both the simulation parameters of the simulated showers and waveform-level data output of the telescope. The `ctapipe v0.17.0` python package (Noethe et al., 2021) is used to read data from the simulation files.

As a first step, the chosen `RSCAT` setting can be validated by looking at the impact point distribution of all triggered events. At zenith, the `RSCAT` directly corresponds to the farthest radial distance to the array centre, at which an event can still result in a trigger. For non-zero zenith angles  $\theta$ , however, a projection effect of the impact point distribution occurs along the X-coordinate (South-North) due to the difference between the shower and array coordinate system. The impact point distribution, expected to be radially symmetric, forms an ellipse with a zenith angle dependant ratio of  $a/b = \cos(\theta)$  between the minor axis  $a$  and major axis  $b$ . To create a combined impact point distribution of all produced simulations, the X-coordinates of the impact points are corrected using this factor with  $\theta$ , the corresponding zenith angle of the simulation.

The resulting combined impact point distribution for the simulated zenith angles of 15 deg, 25 deg, 35 deg, and 45 deg with a maximum impact distance of  $RSCAT = 800$  m is shown in Figure 49.

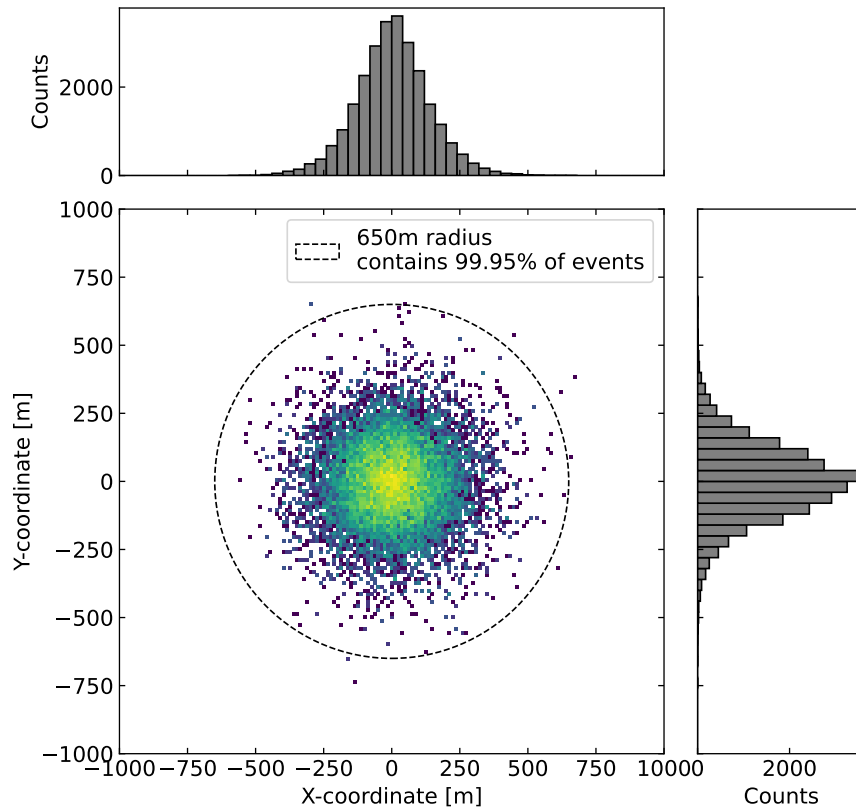


Figure 49: Zenith angle corrected impact point distribution for a combination of simulations performed for zenith angles of 15 deg, 25 deg, 35 deg, and 45 deg with a maximum impact distance of  $RSCAT = 800$  m. A theoretical  $RSCAT = 650$  m value and the percentage of contained showers are highlighted.

Only a comparably small fraction of events is detected close to the maximum radial distance of 800 m, resulting in the loss of CPU time during the simulation. Using the impact point distribution shown in Figure 49, a new  $RSCAT$  value of 650 m is selected, reducing the simulated area by  $\approx 34\%$  while still containing  $> 99.9\%$  of all events.

Similarly, the viewcone setting is validated by observing the event distribution inside the viewcone. The simulation output provides the impact point, shower direction  $S$ , and telescope pointing  $P$  in the array coordinate system. These vectors consist of an azimuth and zenith component  $\phi$  and  $\theta$ , respectively. An illustration of the CORSIKA-coordinate system together with these vectors are shown in Figure 50

To determine the position of the shower inside the specified viewcone, only the angular offset  $d\varphi$  and its components are important. Expressing these vectors in a

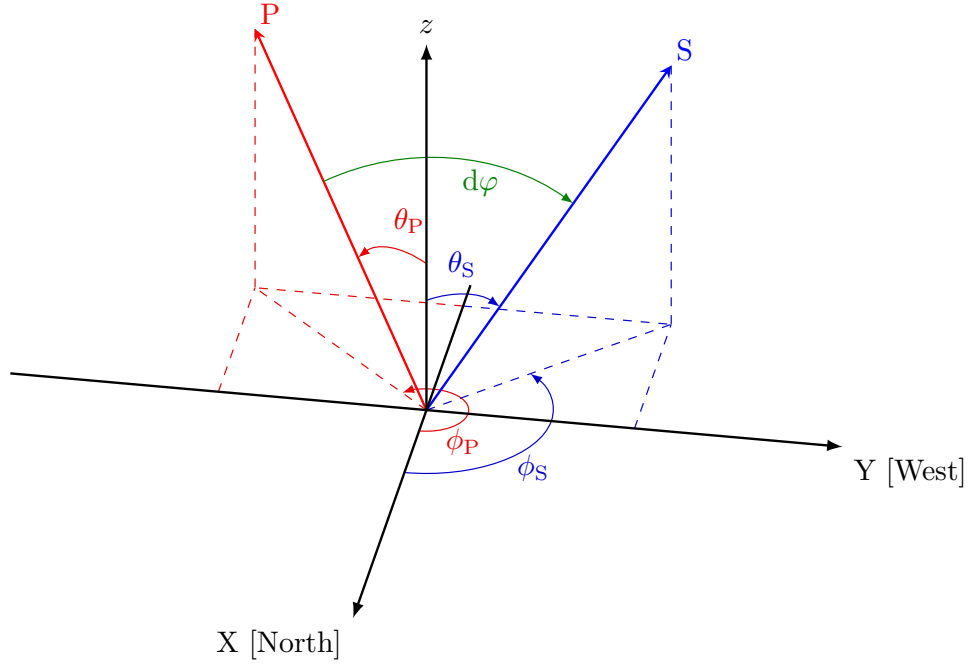


Figure 50: CORSIKA-coordinate system with telescope pointing direction  $P$  and shower direction  $S$ .  $\theta$  and  $\phi$  denote the zenith and azimuth angles, respectively.  $d\varphi$  is the angular offset between the shower direction and telescope pointing.

spherical coordinate system yields:

$$\hat{P} = \begin{pmatrix} \sin(\theta_P) \cos(\phi_P) \\ \sin(\theta_P) \sin(\phi_P) \\ \cos(\theta_P) \end{pmatrix} \quad \hat{S} = \begin{pmatrix} \sin(\theta_S) \cos(\phi_S) \\ \sin(\theta_S) \sin(\phi_S) \\ \cos(\theta_S) \end{pmatrix} \quad (45)$$

With this, the angular offset  $d\varphi$  is calculated as

$$\begin{aligned} \cos(d\varphi) &= \hat{P} \cdot \hat{S} \\ &= \sin(\theta_P) \cos(\phi_P) \cdot \sin(\theta_S) \cos(\phi_S) \\ &\quad + \sin(\theta_P) \sin(\phi_P) \cdot \sin(\theta_S) \sin(\phi_S) \\ &\quad + \cos(\theta_P) \cdot \cos(\theta_S). \end{aligned} \quad (46)$$

$d\varphi$  can now be decomposed into its azimuth  $d\varphi_{az}$  and altitude component  $d\varphi_{alt}$ . An illustration of which is shown in Figure 51. Since the viewcone is centred around the telescope pointing direction, the azimuth and altitude component description of the angular offset, as shown in Figure 51, is adapted. By this definition, the altitude component is equivalent to the angular offset when the azimuth coordinate of  $S$  is set equal to the one of  $\hat{P}$  such that  $d\varphi_{alt} = d\varphi(\phi_S = \phi_P)$ . Using Equation 46, the altitude

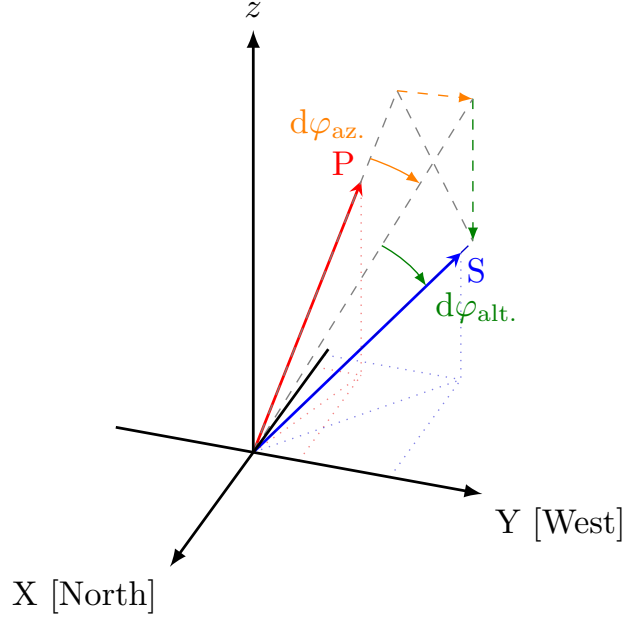


Figure 51: CORSIKA-coordinate system with the telescope pointing direction  $P$  and shower direction  $S$ .  $d\varphi_{\text{az}}$  and  $d\varphi_{\text{alt}}$  denote the azimuth and altitude component of the shower's position inside the simulated viewcone.

separation between the telescope pointing and shower direction is calculated as

$$\begin{aligned}
 \cos(d\varphi_{\text{alt}}) &= \sin(\theta_P) \sin(\theta_S) \cdot \cos^2(\phi_P) \\
 &\quad + \sin(\theta_P) \sin(\theta_S) \cdot \sin^2(\phi_P) \\
 &\quad + \cos(\theta_P) \cos(\theta_S) \\
 &= \sin(\theta_P) \sin(\theta_S) + \cos(\theta_P) \cos(\theta_S) \\
 &= \cos(\theta_S - \theta_P).
 \end{aligned} \tag{47}$$

From this, the altitude component of the angular offset can be expressed as is  $d\varphi_{\text{alt}} = \theta_S - \theta_P$ . The azimuth component is identified similarly, and  $d\varphi_{\text{az}} = d\varphi(\theta_P = \theta_S)$  is calculated by setting the zenith component of  $\hat{S}$  equal to the one of  $\hat{P}$  in Equation 46.

$$\begin{aligned}
 \cos(d\varphi_{\text{az}}) &= \left( \underbrace{\cos(\phi_P) \cos(\phi_S) + \sin(\phi_P) \sin(\phi_S)}_{=\cos(\phi_S - \phi_P)} \right) \cdot \sin^2(\theta_P) + \cos^2(\theta) \\
 &= \cos(\phi_S - \phi_P) \cdot \sin^2(\theta_P) + \cos^2(\theta_P)
 \end{aligned} \tag{48}$$

$$\implies d\varphi_{\text{az}} = \underline{\underline{\arccos(\cos(\phi_S - \phi_P) \cdot \sin^2(\theta_P) + \cos^2(\theta_P))}} \tag{49}$$

Using Equation 46, Equation 47, and Equation 49, the angular offset  $d\varphi$  and its components are calculated for each simulated event. A 2D-Histogram of the shower positions inside the viewcone is shown in Figure 52.



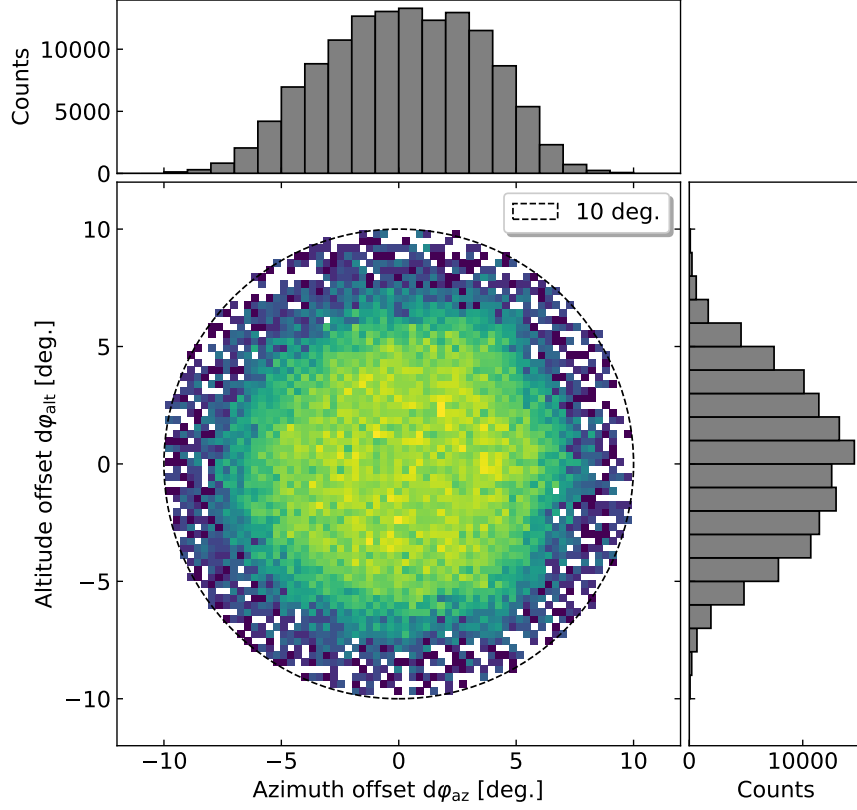


Figure 52: Event distribution inside the simulated 10 deg viewcone. Input data is a combination of simulations performed for zenith angles of 15 deg, 25 deg, 35 deg, and 45 deg with a maximum impact distance of  $RSCAT = 800$  m.

As expected, the distribution is close to uniform for small angular offsets. The distribution shows a rapid falloff towards the viewcone edges due to the telescope’s decreasing angular acceptance (Figure 44). This can also be seen in Figure 53, where the number of events per angular offset bin is shown. The linear rise between 0 deg to 4.35 deg is consistent with a constant radial event density per angular offset  $d\varphi$ . Moreover, Figure 53 also shows two different methods to calculate the angular offset. The first method is the direct calculation described in Equation 46 (shown in blue). The second method uses the azimuth and altitude component of the angular offset to calculate  $d\varphi = \sqrt{d\varphi_{alt}^2 + d\varphi_{az}^2}$ . Both methods show agreement, with residuals below  $1.5\sigma$ . The small deviations are attributed to rounding errors in the calculation and subsequent bin assignment.

The chosen 10 deg viewcone setting is validated by calculating the fraction of contained events within a specified angular offset  $d\varphi$ , which is defined as the ratio between the number of events with an angular offset  $\leq d\varphi$  and the total number of events. As shown in Figure 54, an angular offset of  $d\varphi = 9.5$  deg encloses 99.68 % of all simulated runs. It should be noted that only a viewcone of 10 deg was simulated, and indeed, events can be found for larger offsets. However, the increasing flattening of the curve towards larger angular offsets in Figure 54 suggests that larger viewcone settings

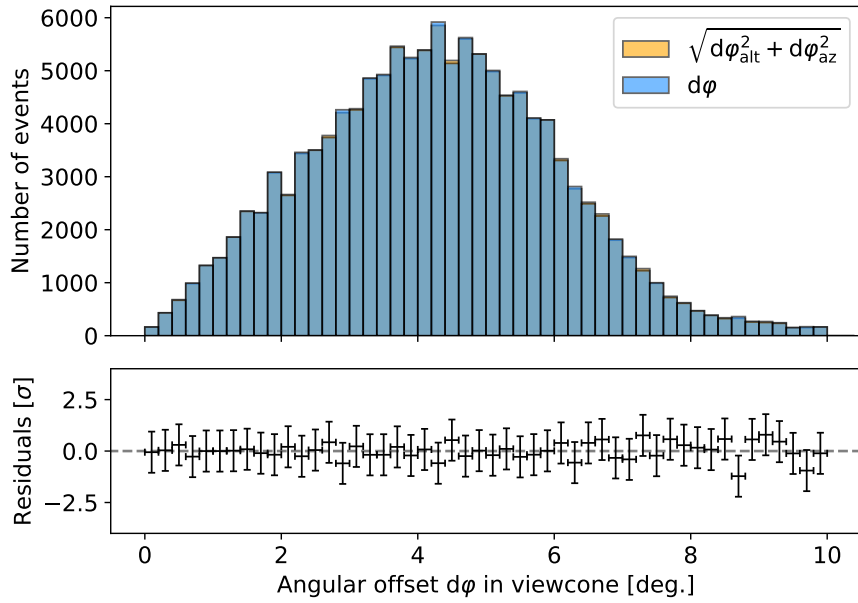


Figure 53: The number of events per angular offset  $d\varphi$  inside the viewcone calculated directly using Equation 46 (blue) as well as utilizing the altitude and azimuth component of the angular offset  $d\varphi_{\text{alt}}$  and  $d\varphi_{\text{az}}$  respectively (orange). Both distributions are made transparent to make the deviations more visible. Assuming Poissonian errors for each bin.

are entering the regime of diminishing returns. Hence, the viewcone setting of 10 deg is adapted for further simulations.

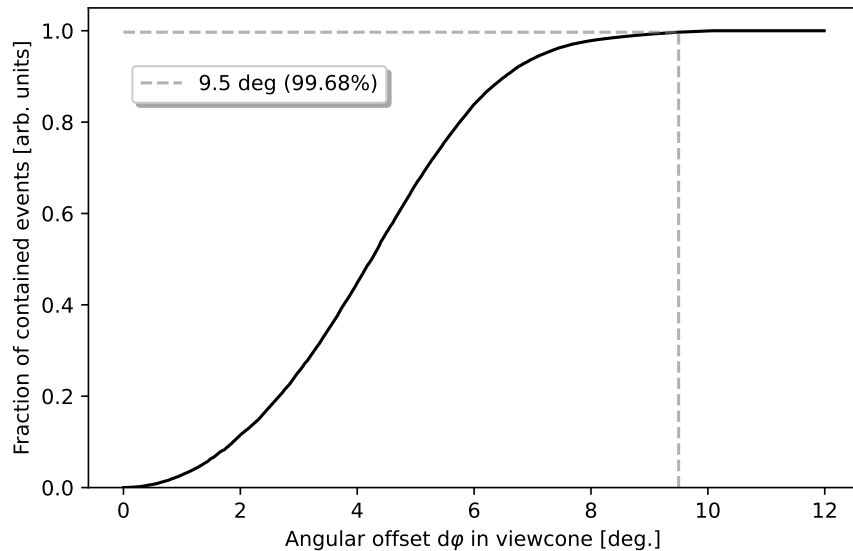


Figure 54: Fraction of events contained within a given angular offset  $d\varphi$  within the viewcone. The fraction for 9.5 deg is highlighted.

### 3.5.7 Recreation of the Namibia Measurement Campaign

To validate that the new telescope simulation indeed produces DesertACT-like output, the available data from the Namibia campaign (see section 3.4) is used. The Namibia campaign data and the simulation results can only be compared when the simulation mimics the same observation conditions. These conditions include the telescope location, pointing, NSB rate, and set discriminator threshold of DesertACT. All location-specific settings have already been implemented in section 3.5.6 and follow the example of existing simulations at the H.E.S.S.-site. The remaining pointing positions, NSB rate and the discriminator threshold of DesertACT are deduced from H.E.S.S.-data during the time of the Namibia campaign. As mentioned in section 3.4, DesertACT followed the planned observation schedule of the H.E.S.S. array.

The H.E.S.S. observation schedule consists of single runs scheduled throughout the night with DesertACT observations grouped similarly. As single telescope events in DesertACT are matched up to corresponding H.E.S.S. events using the event time-stamp in Dietz (2018), the DesertACT runs can be correlated to H.E.S.S. runs. It should be noted that each DesertACT can contain multiple H.E.S.S. runs, mostly at similar pointing positions but not vice versa. The NSB rates for each H.E.S.S.-telescope and the pointing position in the zenith-azimuth coordinate system are extracted from the H.E.S.S.-database. Average values for the pointing direction and the NSB are calculated for all H.E.S.S. runs in a DesertACT run over all small H.E.S.S. telescopes (CT1-4). For this average, all H.E.S.S. runs are weighted equally, as all observations are of similar length and general pointing direction. However, each DesertACT run is of varying length, and the number of contained events fluctuates drastically. To account for this in later results, the relative contribution of each DesertACT run is calculated as the fraction of the contained events to the total number of events over all DesertACT runs. The results are tabulated in Table 6.

Ideally, each DesertACT run in Table 6 would be replicated in the later simulation in a so-called run-wise simulation. However, this would increase the simulation time significantly. To run a more efficient simulation, the run list shown in Table 6 is first binned concerning the observed zenith angles. A bin width of 10 deg from 10 deg to 50 deg is chosen as a compromise between the accurate replication of the original run list and the required simulation time. The relative contribution of each zenith bin is shown in Figure 55.

DesertACT run number	Relative contribution	H.E.S.S. run numbers	Zenith angle [deg]	Azimuth angle [deg]	NSB [MHz]
190403_215	0.076	147805 - 147810	$35 \pm 11$	$108.6 \pm 1.2$	$152 \pm 9$
190407_100	0.014	147945	$41.34 \pm 0$	$200.73 \pm 0$	$223.2 \pm 2.7$
190402_105	0.010	147758	$31.22 \pm 0$	$67.98 \pm 0$	$99.1 \pm 1.0$
190405_100	0.014	147874 - 147875	$40.0 \pm 2.9$	$72.39 \pm 0$	$90.4 \pm 0.8$
190402_200	0.002	147759	$24.84 \pm 0$	$58.92 \pm 0$	$99.5 \pm 0.8$
190406_2000	0.117	147901 - 147910	$39.4 \pm 2.7$	$177 \pm 14$	$219 \pm 8$
190405_2140	0.012	147869 - 147870	$37.3 \pm 0.8$	$169.3 \pm 2.1$	$232 \pm 5$
190406_350	0.015	147917	$16.56 \pm 0$	$323.6 \pm 0$	$87.9 \pm 0.9$
190407_2000	0.012	147933	$24.99 \pm 0$	$236.77 \pm 0$	$92.8 \pm 0.8$
190404_2005	0.002	147834	$23.26 \pm 0$	$235.05 \pm 0$	$107.9 \pm 0.9$
190407_2200	0.082	147938 - 147944	$37.4 \pm 0.9$	$181 \pm 9$	$228 \pm 6$
190405_2215	0.051	147870 - 147873	$37.0 \pm 0.5$	$181 \pm 7$	$235 \pm 7$
190407_350	0.041	147955 - 147956	$9.2 \pm 2.8$	$121.5 \pm 1.7$	$123.7 \pm 1.3$
190407_250	0.043	147953 - 147954	$18.5 \pm 1.9$	$319 \pm 8$	$85.0 \pm 1.2$
190402_210	0.020	147760	$23.69 \pm 0$	$55.14 \pm 0$	$98.0 \pm 0.7$
190407_150	0.065	147949 - 147952	$49 \pm 5$	$315 \pm 8$	$78.9 \pm 1.5$
190405_130	0.053	147876 - 147879	$50 \pm 7$	$109.6 \pm 1.3$	$165 \pm 11$
190404_2015	0.135	147840 - 147849	$36 \pm 17$	$112 \pm 6$	$159 \pm 11$
190402_250	0.066	147761 - 147763	$15.5 \pm 1.0$	$133 \pm 150$	$98.3 \pm 1.3$
190407_130	0.023	147947	$39.04 \pm 0$	$336.74 \pm 0$	$74.0 \pm 0.7$
190406_420	0.008	147918	$16.82 \pm 0$	$115.11 \pm 0$	$132.0 \pm 1.1$
190403_2320	0.030	147799 - 147801	$37.8 \pm 1.2$	$190 \pm 4$	$226 \pm 6$
190406_300	0.030	147915 - 147916	$14.5 \pm 0.7$	$183 \pm 166$	$85.9 \pm 1.0$
190406_100	0.080	147911 - 147914	$40 \pm 3$	$333 \pm 11$	$76 \pm 3$

Table 6: DesertACT run numbers and corresponding H.E.S.S. run numbers identified using the run time stamp during the Namibia campaign. The mean pointing direction in zenith and azimuth are calculated over all H.E.S.S. runs in a DesertACT run with the error representing the standard deviation of these values. Mean NSB is calculated over all mono NSB entries for the small H.E.S.S. telescopes CT1-4. The relative contribution is the number of events relative to the total number of events a single DesertACT run contributes.

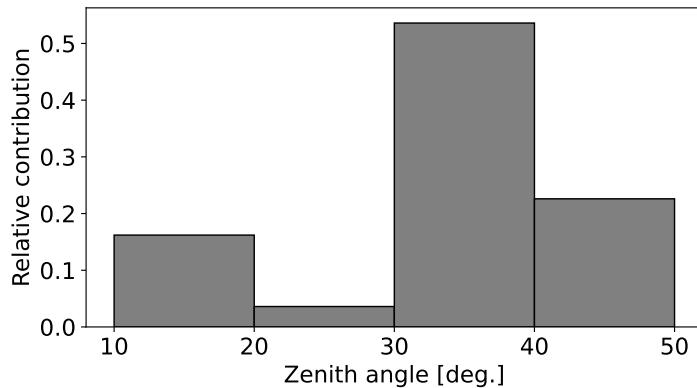


Figure 55: Relative contribution of DesertACT runs in Zenith bins from 10 deg to 50 deg with a bin-width of 10 deg.

This process could be repeated with the azimuth angles in the run list. However, as seen in Figure 56, most runs are taken towards the south, and additional binning would further increase the required computing time. Thus, the average azimuth angle over all runs, weighted with the relative contribution of each run, is calculated as  $\approx 183$  deg

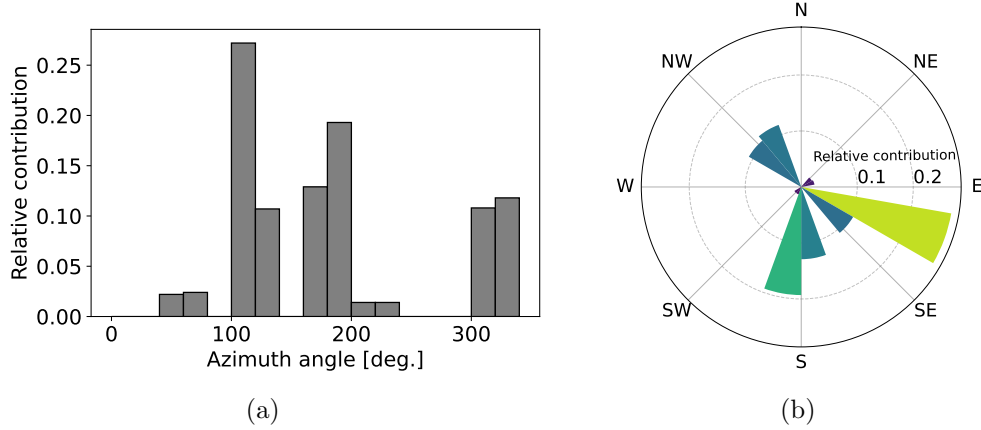


Figure 56: The relative contribution of DesertACT runs in azimuth bins from 0 deg to 360 deg with a bin-width of 20 deg. This distribution is illustrated as a plain histogram in (a) and in polar coordinates with the respective CORSIKA-coordinate cardinal and ordinal directions (b).

As mentioned in section 3.5.6, the H.E.S.S.-site specific companion script that creates the CORSIKA-input parameters file allows specifying the azimuth angle of incoming showers in terms of cardinal directions (N, E, S, W) only. Due to the near-perfect match with the average run azimuth angle, all runs will be simulated arriving from the south.

To reduce the number of simulated configurations further, a NSB binning is introduced, which is informed by the NSB distribution of the run list. This distribution can be seen in Figure 57. Here, three NSB regions  $R_1 = 70$  MHz – 115 MHz,  $R_2 = 115$  MHz – 200 MHz,  $R_3 = 200$  MHz – 260 MHz are identified and will later be used to initially group the DesertACT runs.

Initially, runs are preselected based on the zenith-angle bin assignment, shown in Figure 55. Within this selection, DesertACT runs are further grouped into one of the three NSB regions  $R_1$ ,  $R_2$ , and  $R_3$ . For each such region, the mean NSB of selected runs, weighted with the relative contribution of each run, is calculated. This yields a new binned run list, shown in Table 7, later used for the simulations.

The only parameters not yet determined are the NSB rate as seen by DesertACT and the set discriminator threshold for each run in the simulation run list. Both will be determined in the following.

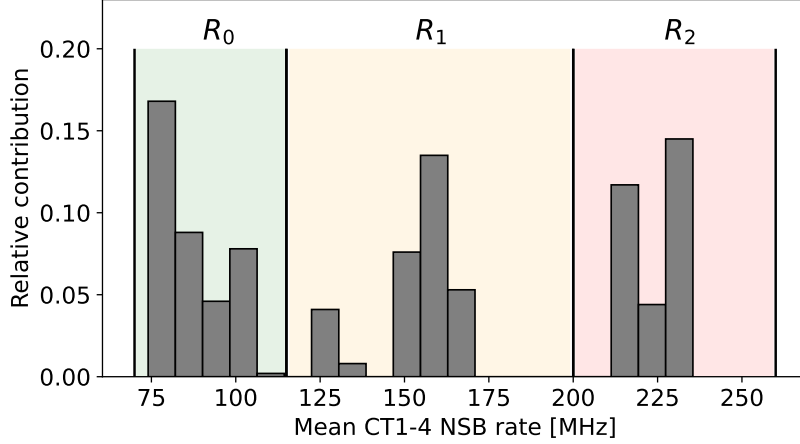


Figure 57: Relative distribution of mean CT1-4 NSB of DesertACT runs to mean H.E.S.S. CT1-4 NSB bins. Identified NSB regions  $R_1$ ,  $R_2$ , and  $R_3$  are highlighted in colour.

### Determining the DesertACT NSB Setting for *Sim\_telarray*

Since the detected NSB rate of DesertACT during the Namibia campaign is unknown, it must be calculated based on the mean H.E.S.S. CT1-4 NSB values. Following Preuß et al. (2002), the wavelength-dependent NSB flux  $\phi(\lambda)$  can be calculated based on a measured NSB rate  $R$  as

$$\phi(\lambda) = \frac{R}{A \cdot \Omega \cdot \int S(\lambda) \cdot T(\lambda) \cdot PDE(\lambda) d\lambda}, \quad (50)$$

with  $A$  the collection area,  $T(\lambda)$  the wavelength-dependent transmission, and  $PDE(\lambda)$  the wavelength-dependent photon detection efficiency of the instrument.  $S(\lambda)$  is the normed shape of the NSB spectrum such that  $\int S(\lambda) d\lambda = 1$ , which is shown in Figure 58. It is a simplification of the measured NSB spectrum in La Palma presented in Benn and Ellison (1998). As of the time of writing, no full-spectrum measurements of the NSB spectrum are available for the H.E.S.S.-site in Namibia.

Since the total NSB flux  $\phi(\lambda)$  is instrument-independent, it is the same for both DesertACT and the small H.E.S.S. telescopes. This is used to calculate a conversion factor

$$\omega = \frac{R_{\text{DesertACT}}}{R_{\text{H.E.S.S.}}}, \quad (51)$$

that translates a measured H.E.S.S. NSB rate  $R_{\text{H.E.S.S.}}$  to the NSB rate  $R_{\text{DesertACT}}$  that is set for DesertACT in *sim\_telarray*.

It is important to distinguish between the measured NSB rate and the NSB setting in *sim\_telarray*. The latter does not include all transmittance effects of the optical telescope elements, such as the mirror degradation, as they are simulated at runtime. These effects, however, are included in the measured NSB rate of the small H.E.S.S. telescopes.

Zenith angle bin [deg.]	Mean Hess NSB in bin [MHz]	Relative contribution
15	91	0.164
	132	0.008
25	97	0.036
35	82	0.033
	157	0.231
	226	0.302
45	79	0.159
	165	0.053
	224	0.014

Table 7: Zenith and NSB binned run list with the relative contribution to the total number of simulated runs.

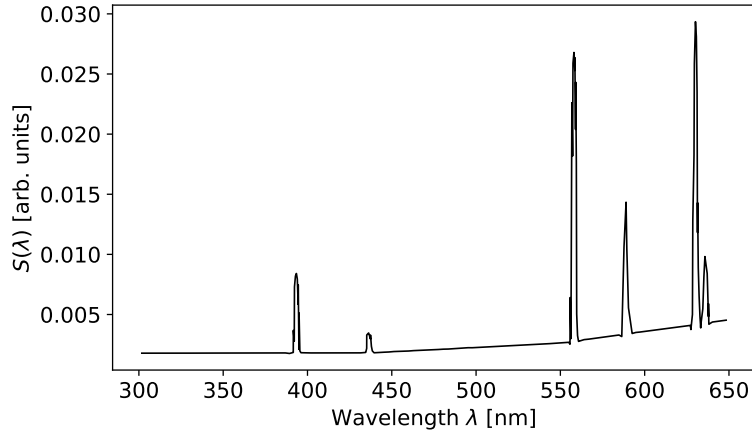


Figure 58: Simplified shape  $S(\lambda)$  of the NSB spectrum in La Palma. The data is taken from Preuß et al. (2002) and extracted with the webplotdigitizer (Rohatgi, 2022).

The Namibia campaign (section 3.4), took place in April 2019. During this timeframe, the *sim\_telarray* configuration for the *phase2b5* H.E.S.S. muon phase (section 2.5) was used, from which the now discussed values are taken.

The PDE curve of the small H.E.S.S. telescopes used in *phase2b5* is specified in the *hess\_qe2.dat* configuration file, which is part of the standard *sim\_telarray* installation. The PDE curve is shown in Figure 59a. The default wavelength range of the PDE from 300 nm to 600 nm is extended to 650 nm with the value zero to fit the wavelength range that is provided by  $S(\lambda)$ .

The mirror reflectivity is specified in the *hess\_reflect.dat* configuration file and is referred to as transmittance to comply with the established terminology. This transmittance is further modified by a mirror degradation parameter<sup>8</sup> that acts as a multiplicative scaling factor for the entire transmittance curve. Each of the four small H.E.S.S. telescopes

<sup>8</sup>The mirror degradation parameter is based on the muon efficiency introduced in section 2.5

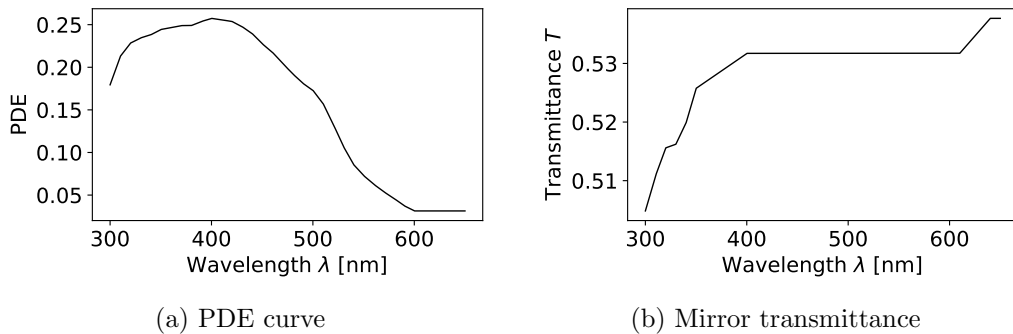


Figure 59: PDE curve (a) and mirror transmittance (b) of the small H.E.S.S. telescopes as specified in *sim\_telarray* during the time of the DesertACT Namibia campaign (phase2b5). Both are shown in the wavelength range from 300 nm to 650 nm predetermined by the available NSB spectrum range. The PDE curve has been extended from 600 nm to 650 nm with the value of zero. Data is taken from stock H.E.S.S. configuration files in *sim\_telarray*.

has such a unique mirror degradation assigned to them. With a standard deviation of  $\approx 4\%$  between all four telescopes, the mean degradation of  $\epsilon_{\text{deg.}} = 63.3\%$  is adapted and added to the transmittance curve. The result can be seen in Figure 59b.

The PDE (see Figure 46) and transmittance curve (see Figure 30) of DesertACT have been discussed extensively in previous sections. The remaining geometric properties, such as mirror area and pixel FoV, can be found in Table 8. It should be noted that

	CT1-4	CT5	DesertACT
Mirror area $A$ [m <sup>2</sup> ]	94	567.95	0.24
Pixel FoV [deg.]	0.16	0.067	1.68
Solid angle $\Omega \cdot 10^6$ [sr]	6.13	1.074	667.22

Table 8: the Mirror area and single-pixel FoV for all H.E.S.S. telescope types and DesertACT. Values for H.E.S.S. telescopes are taken from Bernlöhr (2022a).

Table 8 lists the effective mirror area, taking into account the curvature of the telescope support structure (section 2.5). The solid angle of a single pixel is the area on a unit sphere taken up by the pixel FoV  $\alpha$ . The latter is the opening angle of a cone, with the apex located at the centre of the unit sphere. The solid angle of a pixel is calculated as

$$\begin{aligned}
 \Omega(\alpha) &= \int_0^{2\pi} \int_0^{\frac{\alpha}{2}} \sin(\theta) d\theta d\phi \\
 &= 2\pi \left(1 - \cos\left(\frac{\alpha}{2}\right)\right)
 \end{aligned} \tag{52}$$



Inserting Equation 50 into Equation 51, the conversion factor is calculated as

$$\begin{aligned}
\omega &= \frac{R_{\text{DesertACT}}}{R_{\text{H.E.S.S.}}} \\
&= \frac{A_{\text{DesertACT}} \cdot \Omega_{\text{DesertACT}} \cdot \int S(\lambda) \cdot T_{\text{DesertACT}}(\lambda) \cdot PDE_{\text{DesertACT}}(\lambda) d\lambda}{A_{\text{H.E.S.S.}} \cdot \Omega_{\text{H.E.S.S.}} \cdot \epsilon_{\text{deg.}} \cdot \int S(\lambda) \cdot T_{\text{H.E.S.S.}}(\lambda) \cdot PDE_{\text{H.E.S.S.}}(\lambda) d\lambda} \quad (53) \\
&= 1.573.
\end{aligned}$$

This factor can be used to convert the mean H.E.S.S. CT1-4 NSB-rate to the one that needs to be specified in the DesertACT *sim\_telarray* configuration.

This method is validated by determining a conversion factor translating the H.E.S.S. CT5 NSB rate to the corresponding CT1 rate. The former is also available from the H.E.S.S.-database and is used for comparison. During the Namibia campaign, CT5 still utilised the original camera before the FlashCam upgrade (section 2.5). It used the same pixel type and transmittance curve as the H.E.S.S. phase-I telescopes, with an altered mirror degradation of  $\epsilon_{\text{deg.}} = 73.8\%$ . Further, the *sim\_telarray* configuration specifies an additional degradation  $\epsilon_{\text{shadow}} = 92.5\%$  due to the shadowing of the primary mirror by the camera structure for CT5. From this, the rate fraction between CT5 NSB rate  $R_{\text{CT5}}$  and CT1 NSB rate  $R_{\text{CT1}}$  is calculated as

$$\frac{R_{\text{CT5}}}{R_{\text{CT1}}} = \frac{A_{\text{CT5}} \cdot \Omega_{\text{CT5}} \cdot \epsilon_{\text{deg.}}^{\text{CT5}} \cdot \epsilon_{\text{shadow}}^{\text{CT5}}}{A_{\text{CT1}} \cdot \Omega_{\text{CT1}} \cdot \epsilon_{\text{deg.}}^{\text{CT1}}} \quad (54)$$

$$= 1.14. \quad (55)$$

The NSB rates of CT5 are binned from 60 deg to 280 deg in 20 deg steps. The mean NSB value for CT1 and CT5 is calculated for each such bin, with the standard deviation used as an error. In Figure 60, the calculated conversion factor of 1.14 is used to calculate the expected CT1 NSB rate based on a given CT5 NSB rate. This conversion factor yields good agreement between the predicted and actual CT1 NSB rate, with residuals well below  $2\sigma$ . Without any correction factor, the CT1 and CT5 NSB rates show a difference exceeding  $4\sigma$ . From this, it is concluded that the described method produces reasonable results in converting NSB rates between telescopes and the calculated conversion factor in Equation 54 is adapted for further use.

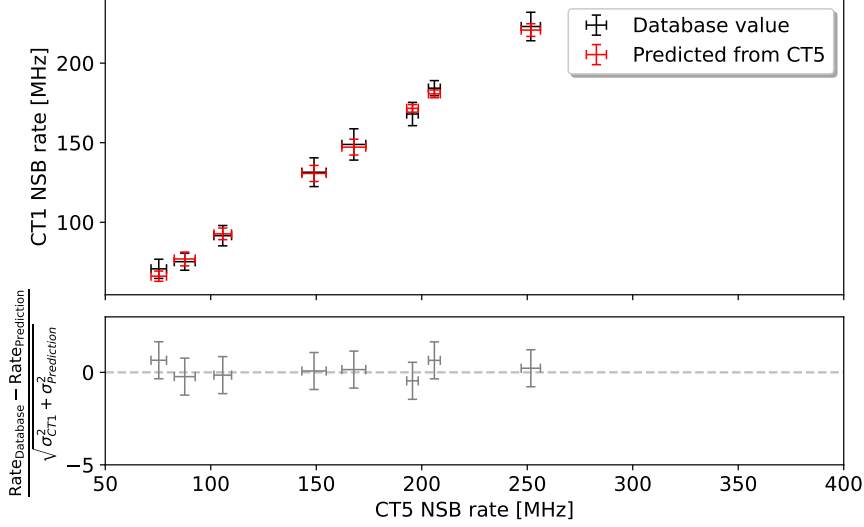


Figure 60: Correlation between the NSB values of CT5 and CT1 of H.E.S.S. runs in Table 6 (black) with predicted CT1 NSB values (red) based on the CT5 NSB rate with a conversion factor of 1.14.

### Determining the Discriminator Threshold of DesertACT

Using Equation 54, the NSB of DesertACT can be estimated based on the mean H.E.S.S. CT1-4 NSB rate. With this, the corresponding discriminator threshold setting for DesertACT must be determined, as the related data on the thresholds set during the Namibia campaign is no longer available (section 3.4). As stated in section 3.4, the DesertACT discriminator threshold was set such that a stable single trigger group trigger rate of 3 kHz was maintained, with NSB events dominating the trigger rate. This is used to determine the DesertACT discriminator threshold with a simplified baseline simulation of the trigger group signal.

The single-pixel baseline is the pixel-signal waveform without any applied signal. Without considering electronic noise or NSB, the single-pixel baseline is constant over time. However, NSB photons induce a signal in the SiPM pixels, resulting in baseline fluctuations. In the case of the TARGET, four AC-coupled single-pixel baselines are summed together, forming the trigger group baseline. This waveform-like signal is compared to a set trigger threshold. Given an initial NSB rate, the trigger threshold can be determined by simulating the trigger group baseline.

To simulate the single-pixel baseline, an ordered list

$$T = (dt_1, \dots, dt_i, dt_{i+1}, \dots, dt_N) \quad (56)$$

of  $N$  time slices  $dt_i$  of duration  $dt = 0.1$  ns is created. For each such time slice, a NSB event can take place with a probability of  $P_{\text{NSB}}(dt) = R_{\text{DesertACT}} [\text{GHz}] \cdot dt$  [ns]. Here,  $R_{\text{DesertACT}} = R_{\text{H.E.S.S.}} \cdot \omega$  is the single pixel NSB rate as calculated using Equation 54. To guarantee  $P_{\text{NSB}}(dt) \leq 1$ , the time slice duration is chosen such that  $dt \leq 1/R_{\text{DesertACT}}$ . Using the H.E.S.S. NSB rates in Table 7 with the conversion factor in Equation 54 it can

be shown that the expected DesertACT NSB values show an upper bound of  $< 400$  MHz. Therefore, the selected  $dt = 0.1$  ns is well within the aforementioned requirement.

For each NSB event, a varying number of additional photo-electrons  $C$  (referred to as the order) can be produced in the SiPM substrate, commonly called optical crosstalk. Here,  $C$  is determined by the crosstalk probability  $P_{\text{ct}} = 0.25$  (Zink, 2021) of the SiPM used in DesertACT, such that the probability of producing  $C$  crosstalk photons for a given NSB event is  $P(C) = (P_{\text{ct}})^C$ .

For each time slice  $dt_i$  containing a NSB event,  $C$  is calculated by repeatedly dicing with a success chance of  $P_{\text{ct}}$  and counting the number of consecutive successful dices until the first unsuccessful iteration, considering up to the 30th order. The total number of p.e. in a given time slice  $dt_i$  is then  $K_i = C + 1$ .

For each time slice  $dt_i$  with a total number of p.e.  $K_i > 0$ , a signal pulse of amplitude  $K_i$  is produced. This is implemented by resampling the DesertACT pulse, shown in Figure 45, in steps of  $dt$  and scaling it by the number of produced p.e.  $K_i$ . The resulting pulse is added element-wise to the Baseline list

$$B = (b_1, \dots, b_i, b_{i+1}, \dots, b_N), \quad (57)$$

starting at  $b_i$ . The latter is the baseline value in the time slice  $dt_i$ . The result is a simulated baseline of a single pixel with a total duration of  $t_{\text{tot}} = N \cdot dt$  which can be seen in Figure 61a.

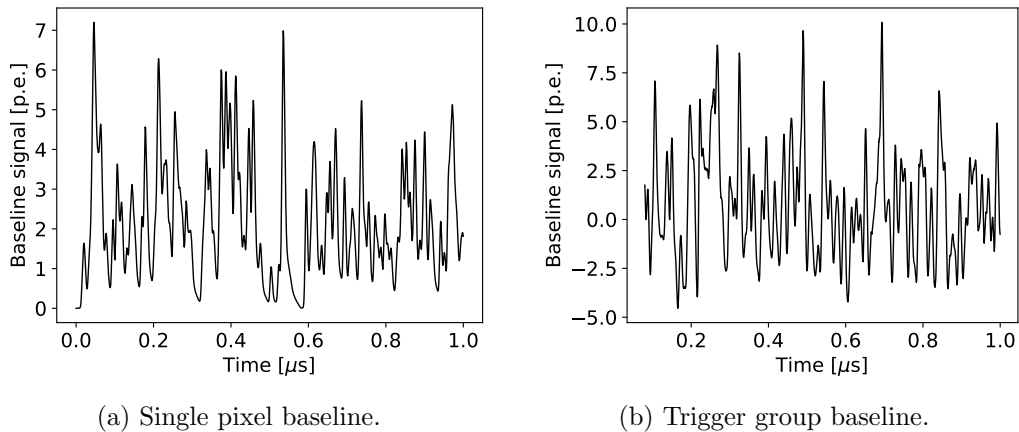


Figure 61: The simulated baseline for a single pixel (a) and a four-channel trigger group (b). Both baselines simulated for  $R_{\text{H.E.S.S.}} = 100$  MHz and a total duration of  $1 \mu\text{s}$ .

These single-pixel signals are AC-coupled in the TARGET signal path before the analogue sum of four single-pixel signals is created. This is realised by subtracting the mean baseline signal from each of the four single-pixel baselines and creating the element-wise sum of the results such that

$$B_{\text{group}} = \sum_{i=1}^4 B_{\text{bc}}^i \quad \text{with} \quad B_{\text{bc}}^i = B^i - \frac{\sum_{j=1}^N b_j^i}{N}. \quad (58)$$

An example trigger group baseline  $B_{\text{group}}$  is shown Figure 61b. From this, the discriminator threshold can be determined by identifying a baseline signal threshold such that the number of signal peaks above this threshold  $N_{\text{peaks}}$  results in a trigger rate of

$$R_{\text{peaks}} = \frac{N_{\text{peaks}}}{N \cdot dt} \stackrel{!}{=} 3 \text{ kHz}. \quad (59)$$

For this method to be accurate, the total simulated time  $t_{\text{tot}}$  must be chosen sufficiently long to accommodate low NSB rates and reach a good rate resolution. The latter is determined by the influence of a  $\pm 1$  fluctuation in the number of peaks  $N_{\text{peaks}}$  and the subsequently calculated rate. This rate change is calculated as

$$\Delta R = \pm (t_{\text{tot}})^{-1}. \quad (60)$$

To satisfy a variation of  $\Delta R = 2.5 \text{ Hz}$  a total integration time of  $t_{\text{tot}} = 400 \text{ ms}$  is chosen for the final threshold simulations. These simulations are performed for all H.E.S.S. NSB values in the created run list (see Table 7) and some additional, lower NSB values. The resulting discriminator thresholds can be seen in Figure 62.

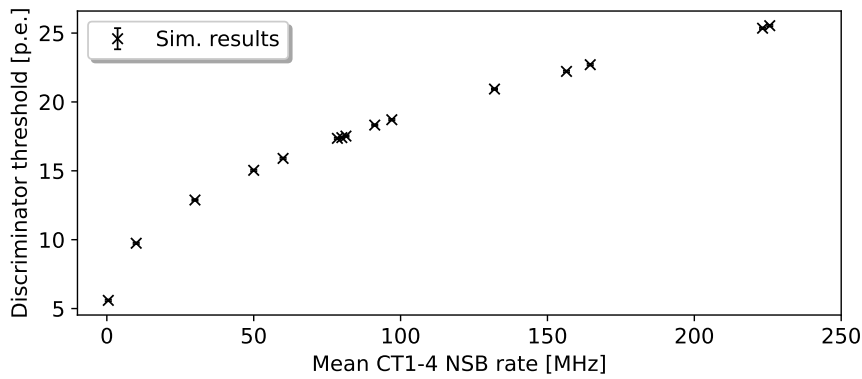


Figure 62: Simulated DesertACT discriminator threshold for different mean CT1-4 NSB rates.

The error bars show the simulation-to-simulation variation introduced by the aforementioned accepted variation of  $\pm 2.5 \text{ Hz}$ , which is on the order of 0.06 p.e. and assumed to be symmetrical. With the conversion factor  $\omega$  to estimate the NSB rate in DesertACT based on the mean CT1-4 NSB rate and the discriminator threshold simulation, the run list in Table 7 is appended with the missing DesertACT NSB rates and discriminator thresholds. The resulting run list is shown in Table 9.

Zenith angle bin [deg.]	Mean H.E.S.S. NSB rate [MHz]	Estimated DesertACT NSB rate [MHz]	Estimated DesertACT discriminator threshold [p.e. ]	Relative contribution
15	91	143	18.13	0.164
	132	208	20.66	0.008
25	97	153	18.52	0.036
35	82	128	17.43	0.033
	157	246	22.00	0.231
	226	355	25.27	0.302
45	79	123	17.22	0.159
	165	259	22.40	0.053
	224	351	25.16	0.014

Table 9: Zenith and NSB binned run list of the Namibia campaign with relative contribution to the total number of simulated runs, estimated *sim\_telarray* NSB settings, and discriminator thresholds.

### 3.5.8 Validation of the Simulation

A set of simulations is created based on the parameters of the created run list in the previous section, shown in Table 9. For each entry in this run list, 100 runs are simulated with  $\approx 140$  k events each.

The DesertACT data in both the simulation and during measurements is stored on a per-pixel waveform level. As mentioned before, none of the unprocessed waveform-level Namibia campaign data is available at the time of writing due to a data loss incident. However, data processed in Dietz (2018) is still accessible, with the pixel waveform information being reduced to pixel amplitude values and peak time within the waveform. In the simulation, NSB signal is diced on top of existing camera images that triggered the camera. Therefore, the simulation does not contain triggered events caused by pure NSB fluctuations, which dominate the DesertACT data taken during the Namibia campaign. Since H.E.S.S. uses a stereo coincidence trigger (section 2.5), such pure NSB events are strongly suppressed. Consequently, only DesertACT events that have been timestamp-matched with a H.E.S.S. event (Dietz, 2018) are used for the validation of the simulation.

The same signal analysis chain must be applied to the simulation output to enable a comparison between the reduced Namibia campaign and the simulated data. This analysis chain is outlined in Dietz, 2018 and is adapted for use with the simulation data from the used source code. The single pixel waveform data consists of 128 Samples (1 ns each) with the sample's value represented in ADC-counts. In the simulation, these ADC-Values are linear with the input signal and without an upper bound. As mentioned in section 2.6.2, the ADC of the TARGET-Module only allows for a 12 bit (4096 ADC-counts) value when digitizing a waveform. Moreover, the ADC exhibits a significant non-linearity between the input signal and digitized value, characterized by TF (section 2.6.2). The output of the saturating ADC can be emulated by applying the TF to the simulation data. TFs are unique to every TARGET-Module but generally exhibit similar behaviour. As the exact TF of the TARGET-Module used in DesertACT during the Namibia campaign is not available, the TF of the TARGET-Module with the serial number SN0007 is used in the following.

However, a per-storage-cell TF cannot be applied as the simulation does not consider single cells. Instead, the mean TF over all storage cells and channels in the TARGET-Module is calculated, shown in Figure 63a.

It should be noted that as a second-order effect, the TF also exhibits dependents on the ambient temperature, resulting in an up to 5% shift<sup>9</sup> for the resulting ADC-Values (Schaefer, 2019). Temperature dependant effects, however, cannot be considered in the *sim\_telarray* simulation at the time of writing.

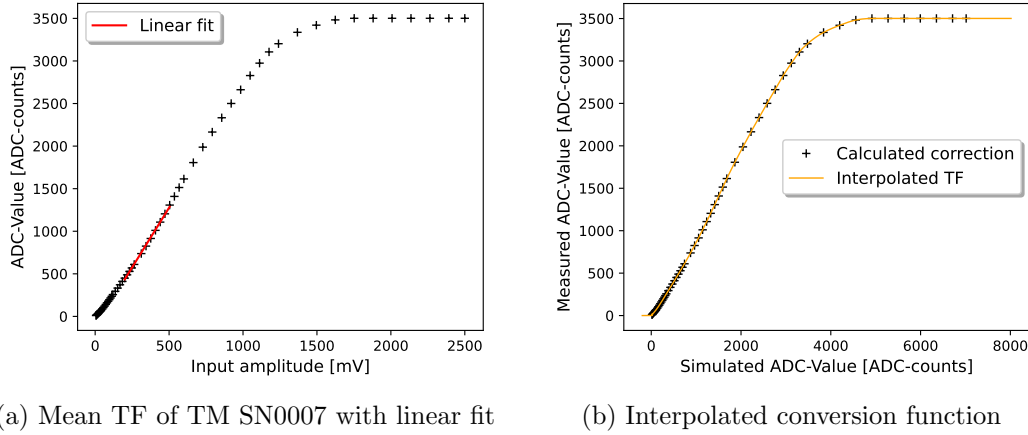


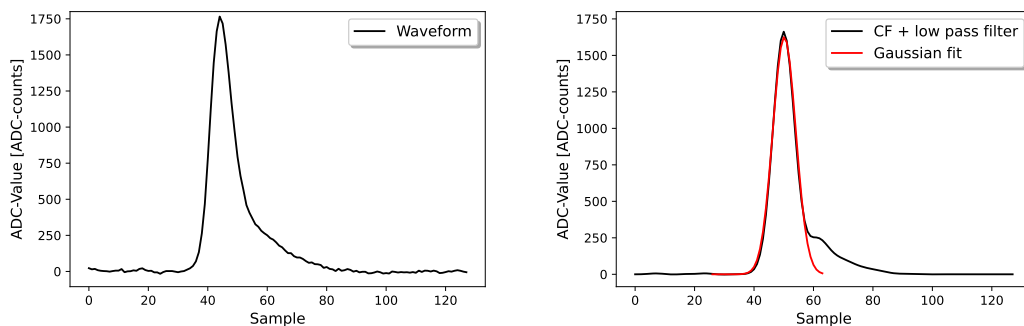
Figure 63: Mean TF of TARGET-Module SN0007 over all storage cells and channels with a linear fit to TF values between 200 mV to 500 mV (a) and subsequently calculated conversion function from simulated ADC-Value to the corresponding measured value (b) with linear interpolation between data points.

A linear fit is applied to the linear region in the input amplitude range of 200 mV to 500 mV with a calculated slope of  $(2.81 \pm 0.04) \text{ ADC-counts} \cdot \text{mV}^{-1}$ . Since the simulated ADC-Values are linear with the input voltage, this slope converts the input amplitude to an equating simulated ADC-Value. The resulting Conversion Function (CF) equates a given simulated ADC-Value to a corresponding measured ADC-Value equivalent, as shown in Figure 63b. Further, the CF is interpolated linearly between each data point for easy application to simulated data.

The simulated data is read using *ctapipe v0.17.0* (Noethe et al., 2021), and the pixel-level waveform data is extracted. Initially, the pedestal  $P$  is subtracted from the raw waveform  $W$ . It is determined by forming the mean over the first ten samples of the deactivated pixels 44, 45, and 46 waveforms. An example of the resulting pedestal corrected waveform  $W_{\text{ped}} = W - P$  is shown in Figure 64a.

To replicate the real ADCs non-linearity, the CF is applied to the pedestal corrected waveform  $W_{\text{ped}}$ . This represents the only deviation from the signal analysis chain presented in Dietz (2018). A low pass filter of order 5 and cut-off 100 MHz (Dietz, 2021) is applied to the pedestal-corrected waveform, and a Gaussian is fitted to the peak with an expected peak position at sample 45. This Gaussian is used to determine the

<sup>9</sup>A shift of 5% was observed for an ambient temperature increase from 20 °C to 50 °C



(a) Pedestal corrected simulated waveform (b) Simulated waveform after applying CF and a low pass filter

Figure 64: Example simulated pixel waveform after pedestal correction (a) and after applying the CF and a low pass filter (Dietz, 2021) (b). A Gaussian fit is made to the peak to determine the peak position.

peak position  $\mu_0$  within the waveform. The pixel's amplitude  $A = CF(W_{\text{ped}})(\mu_0)$  is extracted from the pedestal-corrected waveform with applied CF. This procedure is applied to all simulated data to reduce the dataset to pixel amplitude values.

If the original data were available, a full waveform fit could be performed to reduce artefacts introduced by the method used by Dietz (2018). It should be noted that the presented method is only applied to enable a comparison to the remaining Namibia campaign data.

As mentioned in section 3.4, the H.E.S.S. FoV is always contained within the larger DesertACT FoV during the Namibia campaign and further kept in approximately the same location inside the DesertACT camera. Following the example presented by Dietz (2018), the position of each shower inside a camera image is estimated by identifying the pixel with the largest amplitude. The resulting event fraction of each pixel is shown in Figure 65. Pixel numbers with a ratio of events  $> 3\%$  are identified as within the H.E.S.S. FoV. One would expect a  $\approx 3 \times 3$  pixel region containing the  $\approx 5^\circ$  FoV of the H.E.S.S. telescopes when considering the  $1.68^\circ$  single-pixel FoV DesertACT (section 3.5.1).

The pointing accuracy achieved during the Namibia campaign was  $< 1^\circ$  Root Mean Square (RMS). These pointing fluctuations extend the expected  $\approx 3 \times 3$  pixel region due to spillover to neighbouring pixels. Furthermore, the H.E.S.S. FoV is not centred in the DesertACT FoV as the used guiding camera was mounted with an offset to DesertACT's optical axis (section 3.3).

A cut must be applied to the simulated dataset to imitate this H.E.S.S.FoV effect present in the campaign dataset. Only events where the largest amplitude  $\hat{p}$  or an amplitude value  $> 40$  ADC-counts is within the highlighted pixel region in Figure 65 pass this so-called H.E.S.S. FoV cut. The latter value represents the smallest  $\hat{p}$  in a camera image that resulted in a telescope trigger. The H.E.S.S. FoV cut is also applied to the campaign data. For the remaining analysis, it is implied that only camera images

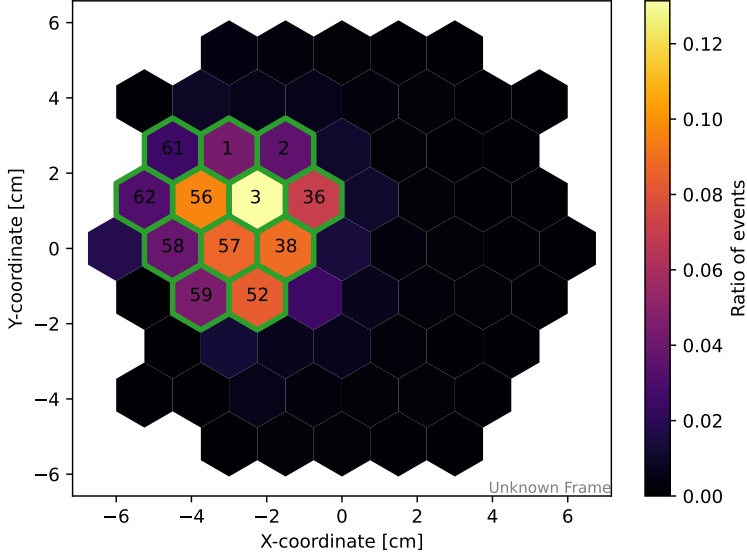


Figure 65: The ratio of camera images in which a given pixel is identified as possessing the largest amplitude. Pixels with ratios  $\geq 0.03$  are outlined in green with the corresponding pixel number shown and identified as within the H.E.S.S. FoV.

passing this H.E.S.S. FoV cut are used.

As a first step, the size spectrum of both the campaign and simulated data is computed and compared. The size of an event is defined as the sum of all pixel amplitudes in the camera image<sup>10</sup>. However, further steps need to be introduced for the simulated data to account for the simulated spectral index and the relative participation of each run. As mentioned in section 3.5.6, the simulated primary proton energies are distributed according to a power law  $\Phi_{\text{sim}}$  of index  $\gamma_{\text{sim}} = -2.0$ . The cosmic proton spectrum, however, approximately follows a power law  $\Phi_{\text{meas}}$  of index  $\gamma_{\text{meas}} = -2.7$  (section 1). The contribution of each event  $i$  towards the size spectrum is weighted with the simulated MC energy according to

$$\begin{aligned} \omega_i^{\text{E}} &= \frac{\Phi_{\text{meas}}}{\Phi_{\text{sim}}} \\ &= \left( \frac{E_i}{E_0} \right)^{\gamma_{\text{meas}} - \gamma_{\text{sim}}}. \end{aligned} \quad (61)$$

Here  $E_0 = 0.1$  TeV is the reference energy, chosen to be smaller than the lower energy bound of the simulated energy range. Further, the relative contribution  $\omega_i^{\text{rc}}$  of each simulated run set as listed in Table 9 is considered for each event individually with events in a given run set sharing the same  $\omega_i^{\text{rc}}$ . Lastly, the number of weighted simulated events  $N_{\text{sim}} = \sum_i \omega_i^{\text{E}} \cdot \omega_i^{\text{rc}}$  is rescaled to the number of measured events  $N_{\text{meas}}$  resulting in a final weight for a given event  $i$  of

$$\omega_i^{\text{tot}} = \omega_i^{\text{E}} \cdot \omega_i^{\text{rc}} \cdot \frac{N_{\text{meas}}}{\sum_i \omega_i^{\text{E}} \cdot \omega_i^{\text{rc}}}. \quad (62)$$

<sup>10</sup>At this step, no camera image cleaning is applied, and all camera pixels are included in the sum.



The size spectrum is computed using these weights and shown in Figure 66.

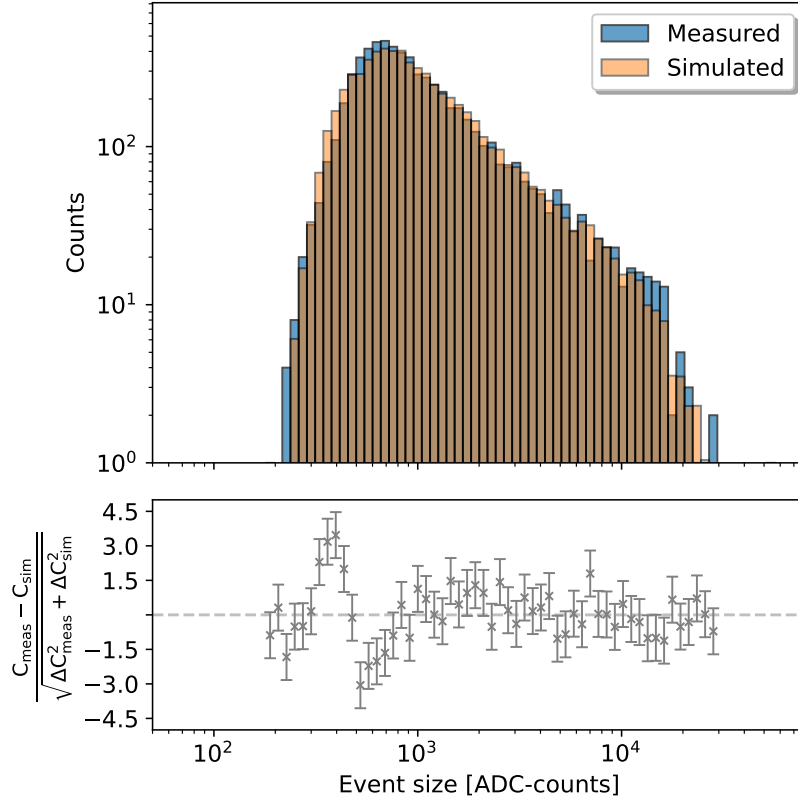


Figure 66: Size spectrum of the campaign and reweighted simulation data with the significance of deviation.

The distribution's peak position, as well as the slope change at  $\approx 10^4$  ADC-counts, are matched well with a significance between the simulated and measured distribution staying within  $\pm 1.6\sigma$  for event sizes  $> 700$  ADC-counts. A larger deviation can be observed at the peak ( $-3.1\sigma$ ) and in the region immediately before ( $+3.5\sigma$ ). This is likely caused by the choice of TF used to create the CF. The event sizes in this region consist predominantly of small amplitude events. As mentioned before, the TF's non-linearity for such small events is subject to change depending on the choice of the TM, used storage cell, and ambient temperature. Such a change in the TF behaviour for small amplitudes that results in an effective count shift towards larger event sizes can be accounted for by TARGET-Module-to-TARGET-Module variation alone (Schaefer, 2019).

Further confirmation for this is found in the pixel amplitude distribution, shown in Figure 67. Here, deviations exceeding  $9\sigma$  are observed for small amplitudes, which could be explained by incorrect modelling of the TF's non-linearity. In addition, the amplitude distribution shows deviations for the largest pixel amplitudes within the saturation regime of the TF. Again, this part of the TF is subject to change between TM's. Furthermore, a mean TF was implemented for the simulation instead of a per-pixel TF, leading to further inaccuracies. However, taking into account this and the simplified simulation run list (see Table 9), both distributions show a good match

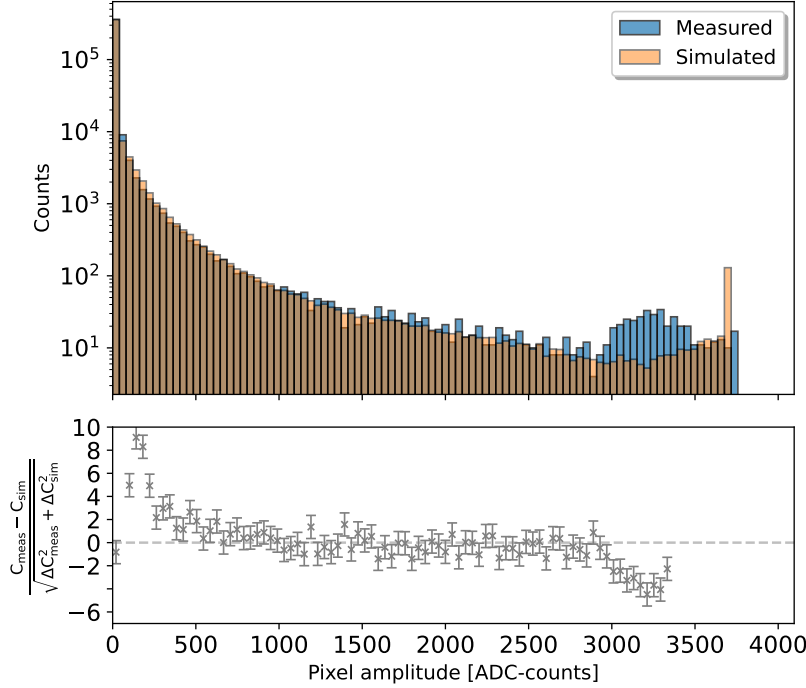


Figure 67: Distribution of pixel amplitudes for the measured campaign and simulation data with the significance of the deviation between them.

for intermediate pixel amplitudes and event sizes.

The effect of the deviations shown in Figure 67 and Figure 66 on the shower image are further studied by using the Hillas parametrization (section 2.5.7). These resulting Hillas parameters include width, length, and amplitude. The width and length can be interpreted as the minor and major axis of an approximated elliptical shape, respectively. The amplitude is the signal sum of all pixels that approximate the elliptical shape. Before this parametrization can be applied, the camera images must be cleaned by excluding pixels that do not contain a significant amount of shower signal. To this end, the tail cut cleaning algorithm (section 2.5.7), as implemented in ctape, is used. This algorithm requires the following:

- A picture threshold describing a pixel amplitude over which a pixel will be considered a signal pixel containing relevant shower information.
- A boundary threshold determining the pixel amplitude a next neighbour to a signal pixel must possess to be retained.

Further, identified signal pixels that do not possess a neighbouring signal pixel are discarded.

The initial peak in the pixel amplitude distribution shown in Figure 67 is dominated by NSB, which is the background that needs to be rejected. The measured dataset is used to determine the required tail cut cleaning parameters, as to not introduce a bias based on the simulated results. The pixel amplitude distribution in log-binning for small

amplitudes is shown in Figure 68. As expected, a NSB peak around 10 ADC-counts can be observed with a clear population change above 30 ADC-counts. Due to

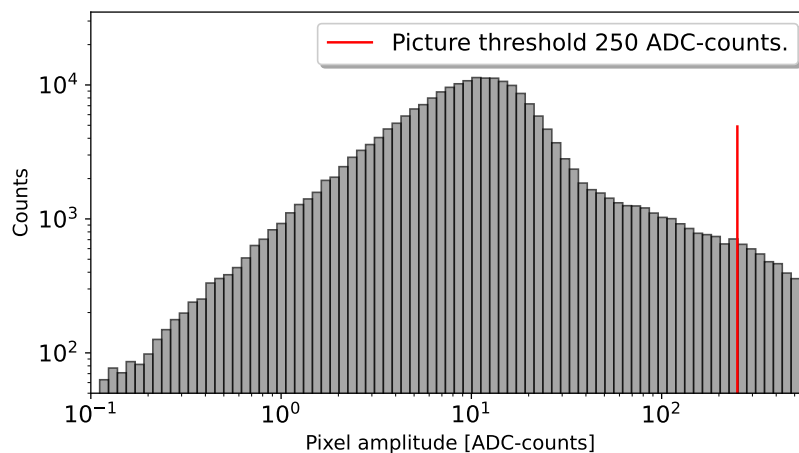


Figure 68: Pixel amplitude distribution of the measured data set for amplitudes up to 500 ADC-counts. The chosen Hillas picture threshold is highlighted in red.

the large pixel size, the image of a proton shower usually consists of only a few pixels, with smaller showers consisting mainly of a single pixel. Hillas parametrization proves difficult for such images even before reducing the number of available pixels by tail cut cleaning. Therefore, the picture threshold must not be chosen too large to make Hillas parametrization impossible but large enough to clear the NSB peak seen in Figure 68. A picture threshold of 250 ADC-counts is chosen as a compromise.

To identify the boundary threshold setting, camera pixels with an amplitude of  $(250 \pm 5)$  ADC-counts around the picture threshold and their subsequent next neighbours with smaller amplitudes are identified. Given the picture signal amplitude of  $p_P$  and the amplitude of a neighbouring pixel  $p_N$ , the relative amplitude reduction  $\frac{p_P - p_N}{p_P}$  is calculated. The resulting distribution is shown in Figure 69.

Most next neighbours tend towards larger relative amplitude reductions, attributed to the relatively large pixel size of DesertACT and the subsequent abrupt intensity falloff from a signal pixel to its next neighbour. Especially the NSB contribution peak between 0.8 and 0.95 relative amplitude reduction needs to be avoided for the tail cut cleaning to work effectively. To this end, a relative amplitude reduction of 0.5 is allowed from a signal pixel to its next neighbour, resulting in a boundary threshold of 125 ADC-counts.

Tail cut cleaning with the determined parameters is applied to the Namibia campaign, and simulated data and the Hillas parameters are calculated. The Hillas parameter distributions for the simulation results are again reweighted (Equation 62) and are compared to the parameter distributions of the Namibia campaign data. The results are shown in Figure 70.

The simulated Hillas length distribution in Figure 70a shows a good agreement with results from the Namibia measurement, with the means of the distributions matching

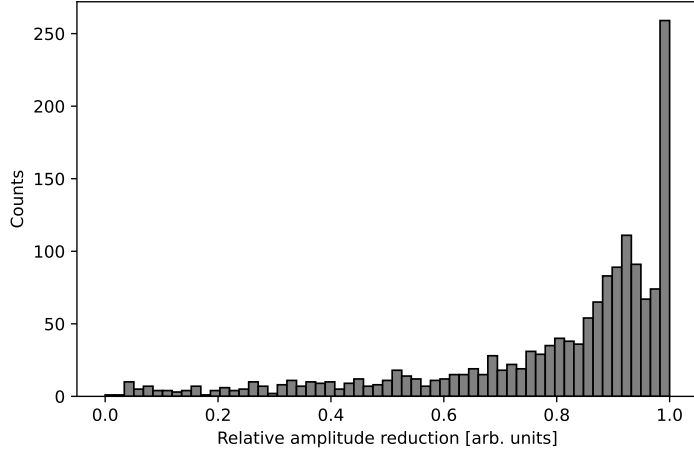


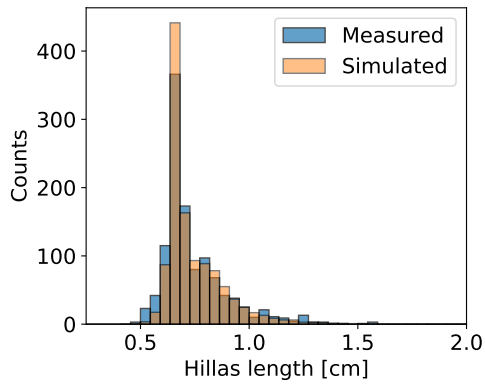
Figure 69: Relative amplitude reduction from a pixel with an amplitude of  $(180 \pm 3)$  ADC-counts to its next neighbors with smaller amplitudes.

within 0.5% and the overall shape of the distribution being reproduced.

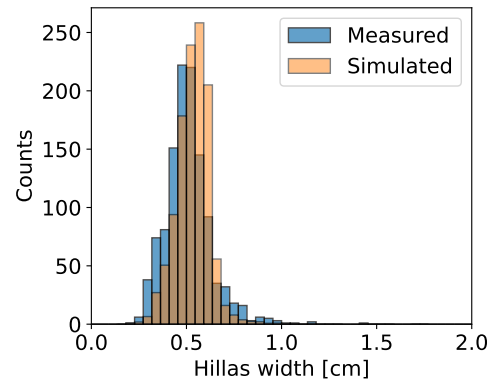
The simulated Hillas width distribution in Figure 70b shows an approximately 25% smaller spread with the means of the distributions matching within 5%. These deviations, however, are small compared to the pixel width of 1.5 cm falling with 2% of the pixel width at worst. Hence, the observed deviations are sub-pixel effects and unlikely to be of extensive significance.

Proton-induced Cherenkov air showers are less effective at producing Cherenkov light than a Cherenkov air shower induced by a gamma-ray of the same energy but show a larger spatial dimension in the camera. As most simulated proton showers fall below a Hillas width and length of 1.5 cm, this implies the inability of DesertACT to differentiate between gamma and proton-induced cosmic ray showers through conventional Hillas parametrization. This has been investigated and verified by Celic (2021) using a preliminary version of the presented simulation.

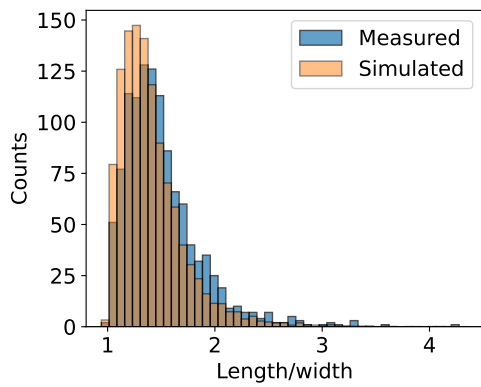
The Hillas amplitude distributions, shown in Figure 70d show agreement with each other within  $2.2\sigma$  with an excess of Hillas amplitudes above  $4 \cdot 10^3$  ADC-counts. Similarly to the size distribution in Figure 66, this could be caused by using a mean TF of a different TM, leading to an incorrect saturation behaviour for large amplitudes (compare Figure 67) and non-linearity for smaller amplitudes. More low-level comparisons between the Namibia measurement could be made if the original, unprocessed data were still available. Given the necessary simplifications and assumptions made for the telescope simulation and subsequent signal processing, the size spectrum in Figure 66 and the Hillas parameter distributions in Figure 70 show good agreement between the Namibia measurements and the presented simulation. It is concluded that the presented telescope response simulation reproduces the behaviour of DesertACT.



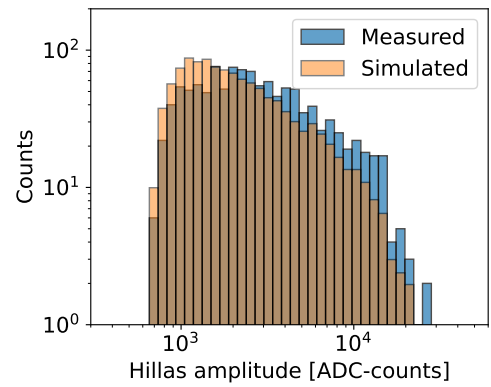
(a) Hillas length distribution



(b) Hillas width distribution



(c) Hillas length/width distribution



(d) Hillas amplitude distribution

Figure 70: Distributions for Hillas length, width, length/width, and amplitude of both the measured and simulated DesertACT runs.

### 3.5.9 Determining Simulated Telescope Properties

The previous section established the match between the simulation and the Namibia measurements by comparing the shower geometry using Hillas parametrization and the shower size distributions. This new simulation allows telescope-specific properties, such as the effective aperture and the telescope's energy threshold, to be determined.

#### Effective Aperture

The effective aperture  $A_{\text{eff}}(E)$  provides information about the energy-dependent cosmic ray proton detection efficiency of a telescope or telescope array. To calculate  $A_{\text{eff}}(E)$ , the number of triggered showers  $N_{\text{trig}}(E)$  and simulated showers  $N_{\text{sim}}(E)$  in an energy bin  $E$  are extracted from the simulated data. Considering the simulated area  $A_{\text{sim}}$  and the solid angle  $\Omega_{\text{view}}$  of the simulated viewcone, the effective aperture is given as

$$A_{\text{eff}}(E) = \left( \frac{N_{\text{trig}}(E)}{N_{\text{sim}}(E)} \right) \cdot A_{\text{sim}} \cdot \Omega_{\text{view}}. \quad (63)$$

The number of triggered and simulated showers in an energy bin is determined with the *read\_hess* program included in the *hessio* package of the *sim\_telarray* installation. The simulated area  $A_{\text{sim}} = \pi \cdot \text{RSCAT}^2$  is defined by the  $\text{RSCAT} = 650$  m parameter value. The solid angle of the simulated viewcone  $\varphi = 10$  deg (section 3.5.6) is calculated following Equation 52 as  $\Omega_{\text{view}}(2\varphi)$ .

As the simulated population of cosmic ray protons follows a power law distribution in energy with user-defined spectral index  $\gamma$  (section 2.7.1), the number of simulated events  $N_{\text{sim}}(E) \propto E^{-\gamma}$  follows the same distribution. Consequently, the number of  $N_{\text{trig}}(E)$  shows the same dependency. However,  $N_{\text{trig}}(E)$  also encodes the detection efficiency  $\epsilon_{\text{D}}(E)$  of the simulated telescope such that

$$N_{\text{trig}}(E) \propto \frac{\epsilon_{\text{D}}(E) \cdot E^{-\gamma}}{A_{\text{sim}} \cdot \Omega_{\text{view}}}, \quad (64)$$

for sufficiently large values of  $A_{\text{sim}}$  and  $\varphi$ . Therefore,  $A_{\text{eff}}(E)$  is independent of the simulated power law spectral index, area, and viewcone and can be used to compare detection efficiencies between different telescopes.

To illustrate zenith-dependent effects on the effective aperture, a new simulation is created for telescope pointing of 15 deg and 45 deg zenith. In both cases, an identical NSB rate of 200 MHz and a discriminator threshold of 18 p.e. is used, resulting in a total of  $\approx 22 \cdot 10^4$  triggered showers at 15 deg zenith and  $\approx 13 \cdot 10^3$  triggered showers at 45 deg zenith. The calculated effective apertures are shown in Figure 71.

The difference in the number of triggered showers can be explained by considering the expected location of the shower maximum. The slant depth at which the cascade maximum is expected is similar for primary particles of a given energy (section 2). However, this slant depth is reached further up in the atmosphere for increasing zenith angles, as a larger air mass lies between the telescope on the ground and the primary particle. Consequently, a larger fraction of the Cherenkov emission is absorbed or scattered by the atmosphere, reducing the Cherenkov photon density on the ground.

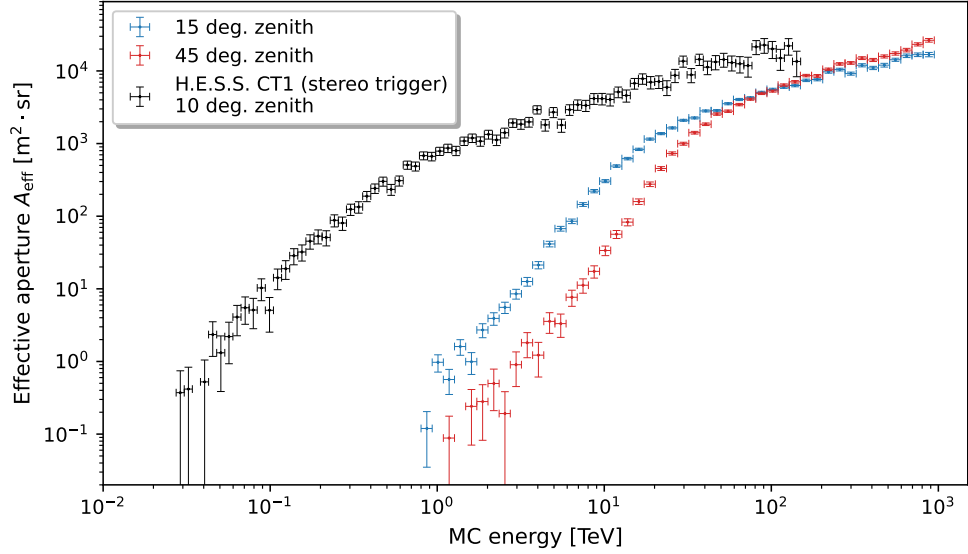


Figure 71: Effective aperture  $A_{\text{eff}}$  for a DesertACT simulation run set 1 (blue) and run set 2 (red) with shower directions of 15 deg and 45 deg zenith and for a simulation of the H.E.S.S. CT1 telescope operated with a stereo trigger at a zenith angle of 10 deg. The DesertACT simulation sets 1 and 2 are selected from the simulation run list in Table 9 with similar NSB rate and discriminator threshold and binned with 15 bins per decade. The effective aperture of the simulated H.E.S.S. CT1 telescope was created as part of the H.E.S.S. Monte-Carlo validation effort described in section 4.

This reduces the fraction of triggered showers for lower primary particle energies as the total signal detected by the telescope falls below the trigger threshold. As the effective aperture is proportional to the triggered shower fraction, this effect is seen in Figure 71, resulting in a decreased effective aperture for the larger zenith angle for energies between 1 TeV and 10 TeV.

For rising primary particle energies, the location of the cascade maximum moves further into the atmosphere and a larger number of Cherenkov photons is emitted (section 2), increasing the Cherenkov photon density on the ground and a subsequent increase in the fraction of triggered showers. A further gain in the fraction of triggered events is expected due to projection effects of the Cherenkov light pool for non-zero zenith angles (section 2.3). For increasing zenith angles, the Cherenkov light pool becomes increasingly elongated, with air showers at larger impact distances able to trigger the telescope. When comparing the effective apertures of the two simulated zenith angles, this effect dominates for primary particle energies above 100 TeV, increasing the effective aperture of the simulation at 45 deg zenith above the one at 15 deg zenith. For reference, Equation 63 also shows the simulated effective aperture of the H.E.S.S. CT1 telescope simulated using the default stereo trigger configuration (section 2.5) at default simulation parameters. The calculation of effective aperture for H.E.S.S. telescopes is outlined as part of the H.E.S.S. Monte Carlo validation effort, discussed in a later section (section 4). It should be noted that no cuts on the event size or impact distance are imposed on the data of the simulated telescopes.

## Proton Energy Threshold

The average proton energy threshold during the Namibia campaign can be determined from the recreated campaign simulation data by calculating the energy-binned differential count spectrum  $\left(\frac{dN_{\text{trig}}}{dE}\right)(E)$ . The energy at which the differential count spectrum reaches a maximum is the proton energy threshold  $E_{\text{th}}^{\text{p}}$  of DesertACT.

All events within an energy bin are identified following the method used to calculate the effective aperture. The contribution of each event to the number of triggered showers is reweighted following Equation 62, again taking into account the contribution of the simulated run to the recreated Namibia campaign and the simulated spectral index. To calculate the differential count spectrum in each energy bin, the number of weighted triggered showers is divided by the width of the logarithmic energy bins. The result is shown in Figure 72.

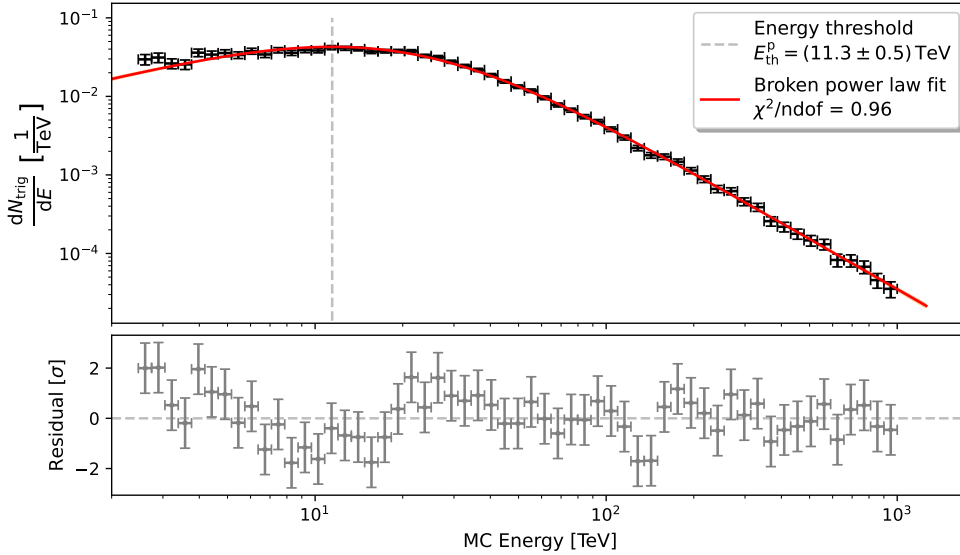


Figure 72: Differential count spectrum for the simulated Namibia campaign run list with broken power law fit and highlighted mean proton energy threshold. The contribution of each simulated triggered event is rescaled to account for the simulated spectral index and the run contribution.

To determine the proton energy threshold, a smoothly broken power law (Equation 65) is fit to the data. Here,  $A$  is the amplitude,  $E_0$  the reference energy,  $\alpha_1$  the spectral index before and  $\alpha_2$  after the spectral break, and  $\beta$  the spectral index of the crossover.

$$\Phi^{\text{fit}}(E) = A \left(\frac{E}{E_0}\right)^{-\alpha_1} \left(\frac{1}{2} \left[1 + \left(\frac{E}{E_0}\right)^{1/\beta}\right]\right)^{(\alpha_1 - \alpha_2) \cdot \beta} \quad (65)$$

The fit resulted in a good reduced  $\chi^2$  value of  $\chi^2/(\text{ndof}=72) = 0.96$  and residuals within  $\pm 2\sigma$ . The fit parameters are shown in Table 10. The value and error of  $E_{\text{th}}^{\text{p}}$  are determined with a numerical approach. Let  $PN(\mu, \sigma)$  be a function returning a sample of a normal distribution with the specified parameters. For each iteration, the parameters



Parameter	$A$ [ $\text{TeV}^{-1}$ ]	$E_0$ [ $\text{TeV}$ ]	$\alpha_1$	$\alpha_2$	$\beta$
Fit value	$195 \pm 3$	$20.00 \pm 0.21$	$-0.92 \pm 0.06$	$-2.13 \pm 0.05$	$0.67 \pm 0.05$

Table 10: Fit parameters for the broken power law (Equation 65) fit to the simulated differential count spectrum in Figure 72.

$P$  of  $\Phi^{\text{fit}}$  are perturbed according to their error following  $P_{\text{pert}} = PN(\mu = P, \sigma = \sigma_P)$  and the energy threshold is determined as the location of the maximum of  $\Phi_{\text{pert}}^{\text{fit}}$ . The number of iterations is increased, and the means and standard deviations of the determined energy thresholds are calculated. As shown in Figure 73, the standard deviation of the energy threshold distribution converges after  $10^5$  iterations. After  $10^6$  iterations, the mean and standard deviation of the threshold distribution are identified as the proton energy threshold  $E_{\text{th}}^{\text{p}}$  and the corresponding error  $\sigma_{\text{th}}$ .

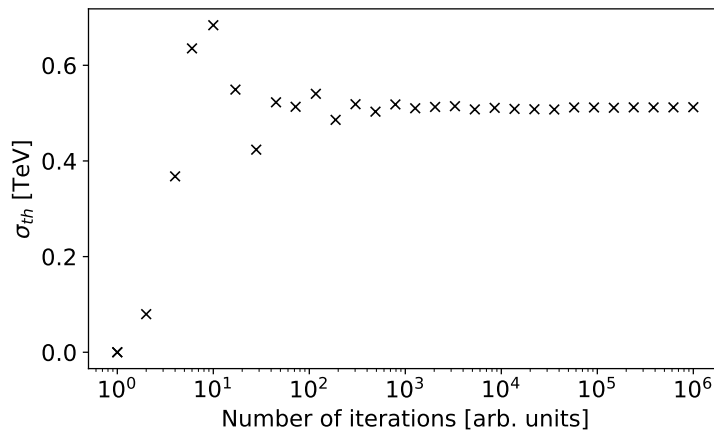


Figure 73: Numerically determined error  $\sigma_{\text{th}}$  of proton energy threshold for different numbers of numerical iterations.

The average proton energy threshold of DesertACT during the recreated Namibia campaign in simulation is determined as  $E_{\text{th}}^{\text{p}} = (11.3 \pm 0.5) \text{ TeV}$ . This value is consistent within statistical errors with the estimated proton energy threshold of  $(10.84 \pm 0.21) \text{ TeV}$  presented in Dietz (2018) using the gamma energy reconstruction of H.E.S.S. and estimating an equivalent proton energy threshold. Further, the simulated proton energy threshold is within  $2.6\sigma$  of initial IceCube results using an IceACT with TARGET trigger electronics showing a proton energy threshold of 10 TeV (Paul et al., 2021). As the average threshold during the Namibia campaign is presented, small deviations to the IceCube measurements are expected.

It should be noted that although the events are reweighted to resemble an observation of a power law spectrum with spectral index  $\gamma = -2.7$ , the spectral index of the fit smoothly broken power law only approaches  $\alpha_2 = (-2.13 \pm 0.05)$ . As seen in Figure 71, the effective aperture of DesertACT does not yet reach a constant value for energies above 60 TeV but follows a power law of spectral index  $\gamma_A \approx 0.5$ . The simulated spectrum defines the number of protons per unit of energy, area, time, and solid angle. The latter four are not considered in calculating the differential count spectrum

of DesertACT. Therefore, the expected energy dependence of the differential count spectrum of DesertACT at high energies is

$$\frac{dN_{\text{trig}}}{dE} \propto \frac{dN_{\text{sim}} dA_{\text{eff}}}{dE} \propto E^{\gamma+\gamma_a} \approx E^{-2.2} \quad (66)$$

This expectation is consistent with the fit result  $\alpha_2 = (-2.13 \pm 0.05)$  within the statistical error.

### 3.6 Summary and Outlook

This chapter presents a simulation for DesertACT and by extension IceACT with TARGET using CORSIKA for the simulation of air showers and *sim\_telarray* for the telescope response simulation.

The optical properties of DesertACT are implemented in *sim\_telarray* using an extensive list of available parameters. Whilst a direct simulation of a Fresnel lens is not possible, its imaging behaviour can be approximated with a spherical lens. However, total internal reflections restrict the effective diameter of the spherical lens. This is counteracted by tripling the original focal length of DesertACT to reduce the radius of curvature of the simulated spherical lens. Consequently, the camera dimensions are scaled by the same factor to account for the change in the angular behaviour of the simulated lens. The performance of the simulated lens is evaluated by comparing the incidence-angle-dependant 90% containment radius  $R_{90\%}$  to measurements performed by Niggemann (2016). Tuning the refractive index of the simulated lens, a match between the simulated and measured containment radii within  $\approx 1.9$  mm (1/8th of DesertACT's pixel size) could be established. For all incidence angles,  $R_{90\%}$  is smaller than a single DesertACT pixel, rendering the remaining deviation insignificant.

However, the measurements presented by Niggemann (2016) were performed using a small CMOS camera with an approximate size of 2 cm times 1.5 cm capturing the highest intensity part of the optical PSF. Due to the physical structure of the Fresnel lens, however, incoming photons get scattered to positions far away from the optical PSF CoG, producing a large so-called photon carpet. The measurement does not capture the photon carpet, resulting in an underestimation  $R_{90\%}$ . Further, the measurement was only conducted with a light of 550 nm wavelength. Hence, the resulting measurements and subsequent implementation in *sim\_telarray* are wavelength-agnostic.

At the time of writing, plans to modify an existing test stand (initially developed for CHEC-S by Herrmann (2019)) to perform optical measurements with the DesertACT Fresnel lens are underway. Here the lens is fixed using a holding mechanism (see Figure 74a) with a robotic arm (UNIVERSAL ROBOTS UR5e) able to position a test laser. The attachment for the robotic arm carrying the laser with a beamsplitter forwarding a fraction of the light to a controlling photodiode is shown in Figure 74b. The lens image can be rastered with a large-scale X-Y-axis scanner carrying a photodiode for any laser position. This allows measuring the lens image far from the optical PSF's CoG. This measurement is planned to be repeated for different wavelengths using different lasers.

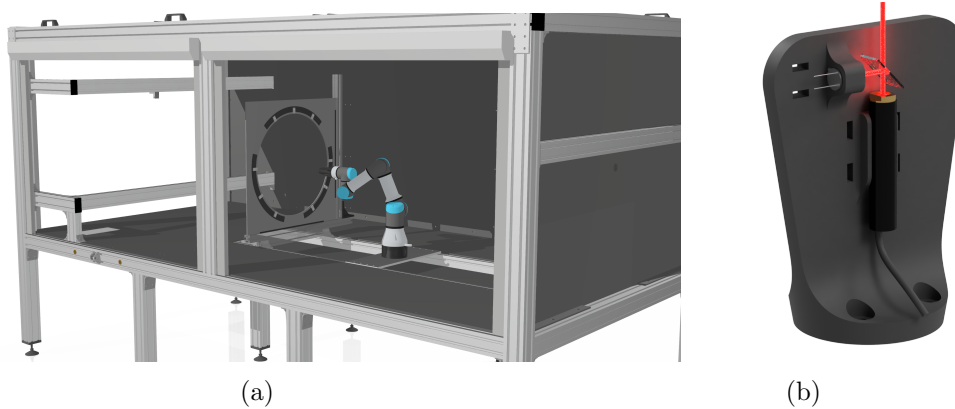


Figure 74: CAD model of the modified CHEC-S test stand with a robotic arm (UNIVERSAL ROBOTS UR5e) and Fresnel lens holder (a) and robotic arm laser attachment with laser and photodiode for intensity measurements (b). The CAD model of the original CHEC-S test stand taken from Herrmann (2019).

The Winston cone’s angular acceptance is based on simulations performed by (Koschinsky, 2017) and adjusted to maintain the proper angular response for the new focal length and camera size in the simulation. A PLEXIGLAS plate protects the Fresnel lens from environmental influences and offers scratch resistance. The PLEXIGLAS and Winston cone materials transmittance curves are subject to change with continued UV-A exposure. The transmittance curves of both materials stabilize after initial UV-A exposure and remain unchanged afterwards. Both curves are combined to form a joined transmittance curve of the optical system, considering the altered Fresnel loss.

The electronic simulation is based on a pre-existing *sim\_telarray* configuration for CHEC-S (PROD4) with modified parameters to adjust for changes introduced in DesertACT. These changes include a new SiPM pulse to account for capacity changes in the signal-shaping electronics and a new PDE curve for the SiPM pixels. Further changes include the number of pixels (64), a `FADC_AMPLITUDE` of 8 p.e., and the implementation of the two-superpixel majority trigger.

Initial proton-induced Cherenkov air shower simulations are used to validate the simulated viewcone (10 deg), and maximum impact distance of 650 m with remaining CORSIKA and location-specific settings adapted (i.e. geolocation of the telescope, local magnetic field, and number of reused Cherenkov air showers) from the existing H.E.S.S. simulation<sup>11</sup>.

The presented simulation is validated by recreating a measurement campaign in Namibia (Dietz, 2018) during which DesertACT followed the observation schedule of H.E.S.S. However, the raw waveform-level data and information about the set telescope trigger threshold is no longer available due to a data-loss incident occurring shortly after the Namibia campaign (Dietz, 2021), with only the pixel amplitude and amplitude

<sup>11</sup>The validated H.E.S.S. simulation configuration for *phase2d3* was used as a basis for these settings (see section 4)

timing information remaining. This lost information also includes the exact trigger threshold settings for each DesertACT observation. However, the trigger threshold setting was chosen to achieve a 3 kHz super-pixel trigger rate. As the trigger rate of DesertACT was dominated by NSB events during the Namibia measurement campaign, a simulation of the super-pixel baseline is created and used to estimate the telescope’s trigger threshold settings. As a first step, the NSB rate seen by DesertACT is calculated based on the mean H.E.S.S. CT1-4 NSB rate using geometric parameters such as the mirror area and angular pixel size. The expected super-pixel baseline is simulated with the crosstalk probability of the SiPMs used by DesertACT, and the trigger threshold setting is approximated for every DesertACT observation run.

To validate the telescope response simulation, the Namibia measurement campaign is recreated in simulation, with the original run list being simplified with a NSB and zenith angle binning. The same basic pixel amplitude and peak time extraction algorithm used by Dietz (2018) were applied to the raw waveform level simulation data to enable a comparison to the campaign data. The nonlinearity and saturation of the digitization electronics of the TARGET-Module (TM) is approximated using the mean TF of a different TARGET-Module (TM) than that used during the Namibia campaign, as the TF of this module is not available. TARGET-Module (TM)-to-TARGET-Module (TM) variations in the used TF result in deviations of nonlinearity for small ADC signals and those in the saturation regime resulting.

The simulated Namibia campaign data is compared to the data obtained by Dietz (2018) using the size spectra and Hillas parametrization. The size spectra show good agreement within  $1.5\sigma$  for image sizes above 700 ADC-counts. A deviation of approximately  $3.3\sigma$  is observed for smaller image sizes but can be explained with TARGET-Module (TM)-to-TARGET-Module (TM) variations in the used TF. Considering the limitations, however, the overall simulated size spectrum matches the one of the Namibia campaign data.

Another comparison between the simulation and observation data is performed based on the Hillas parametrization of the camera images. Identical tail cut cleaning is applied to simulated images, and those of the Namibia campaign data, and the Hillas parametrization is applied. The comparison of the Hillas parameters generally shows good agreement between the respective distributions. The Hillas length and width distributions mean values match within 0.5 % and 5 %, respectively. The shape of both distributions is well captured by the simulation, with the Hillas width distribution showing approximately 25 % smaller standard deviation in the simulation. However, both distributions fall within the width of a single pixel, with the aforementioned deviations only representing a percent-level fraction of the pixel size.

Using the presented simulation, the effective aperture and the proton energy threshold  $E_{\text{th}}^{\text{P}} = (11.3 \pm 0.5)$  TeV of DesertACT during the Namibia campaign is determined. This result is consistent with estimates from Dietz, 2018, further validating the simulation. Moreover, these results show agreement with an initial IceCube result within  $2.6\sigma$  (Paul et al., 2021).

With additional future measurements, the simulation parameters can be further refined and systematic influences introduced by the TF variation could be accounted for. As mentioned, the measurement of the wavelength dependant Fresnel lens image is currently underway. Further studies could be conducted using the presented simulation, including alternative majority trigger configurations and hardware changes to the optical system. Since *sim\_telarray* is already the host to CTA and H.E.S.S. simulations, the validity of an IceACT array extension for these projects could be investigated. Such an extension could offer coverage for Cherenkov showers with impact distances far from the array centre. With multiple IceACTs, event reconstruction becomes feasible, as shown by Baden (2023) using a neural network approach. The low system cost of IceACT makes it a valid option for single-institute projects, student projects, and scientific outreach.

## 4 Validation of the H.E.S.S. Monte Carlo Simulation Chain

Monte Carlo simulations are fundamental for many modern Cherenkov shower reconstruction techniques. Cherenkov shower camera images of multiple telescopes are used to reconstruct the primary particle's origin and energy using the stereoscopic technique (section 2.4). For the H.E.S.S. array, the primary particle's energy reconstruction is based on simulated lookup tables, correlating the Hillas size and impact distance to the reconstructed energy (section 2.5.7). These reconstructed values still contain biases specific to the telescopes used for the reconstruction. The Instrument Response Functions (IRFs) assign a true value to a reconstructed value. IRFs contain instrument-specific properties such as the effective area, PSF, and energy dispersion matrix and are created again created using simulations. As the primary shower particle's properties are known in the simulation, they are referred to as the true properties.

Consequently, any deviation between the simulated and actual telescope response results in the assumed true parameters no longer being correct. This, in turn, has broad implications for all further analyses done with this data, including the high-level results, such as the spectra and significances of detected sources. Therefore, it is of particular importance that a match between the simulated and actual telescope response is maintained.

For the H.E.S.S. telescopes, this match is subject to an investigation presented in this work, as recent analysis implied possible discrepancies in the H.E.S.S. telescope simulations. The simulation configurations for the H.E.S.S. telescopes are grouped into hardware phases (section 2.5) and muon phases (section 2.5.5), considering changes in the optical efficiency of the telescopes. A joint naming scheme for the simulation configuration describes both the hardware and muon phases. This work is concerned with the so-called *phase2d3* simulation configuration, spanning a time interval from the 6th of June 2020 to the 28th of August 2020. During *phase2d3*, the large central telescope of H.E.S.S. is equipped with FlashCam and the small telescopes with the upgraded HESS1U cameras (see section 2.5). The discrepancies between the simulated and real telescope response become especially apparent when observing one of the brightest and, subsequently, most studied sources of Very High Energy (VHE) gamma rays, the Crab nebula.

The reconstructed spectrum based on CT5 data in the *phase2d3* era is shown in Figure 75. For comparison, an older H.E.S.S. Crab spectrum of H.E.S.S. (Aharonian et al., 2006) together with the derived spectrum by Meyer et al. (2010) is shown. The flux normalization (at 1 TeV) using CT5 is determined to be  $(5.04 \pm 0.08) \cdot 10^{-11} \text{TeV}^{-1} \text{cm}^{-2} \text{s}^{-1}$ , compared to the previous result of  $(3.45 \pm 0.05) \cdot 10^{-11} \text{TeV}^{-1} \text{cm}^{-2} \text{s}^{-1}$  (Aharonian et al., 2006) from Aharonian et al. (2006). This mismatch of  $\approx 46\%$  cannot be explained by the 20% systematic error currently estimated for the H.E.S.S. Crab flux (Aharonian et al., 2006) and represents a total deviation<sup>12</sup> of  $\approx 2.4\sigma$ .

---

<sup>12</sup>The significance is calculated for the systematic errors only as the statistical errors are of lesser magnitude for Crab observations.

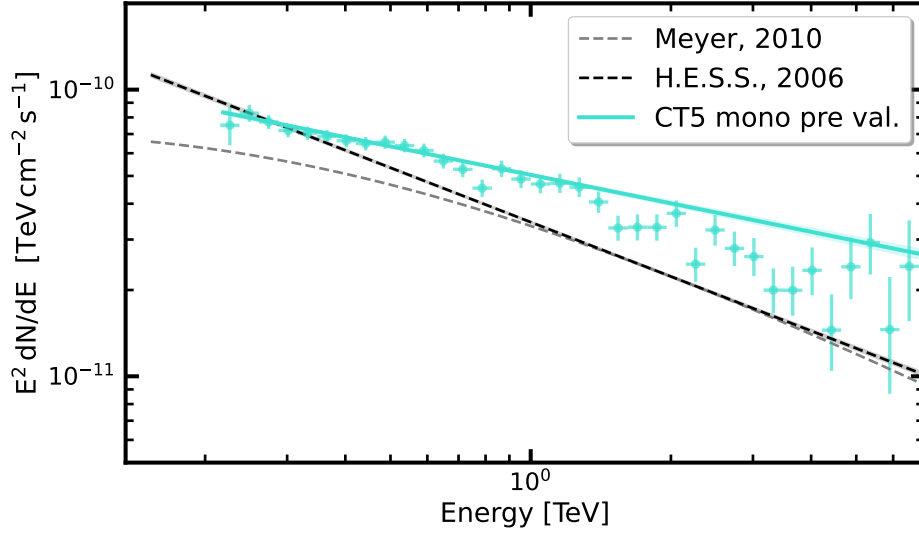


Figure 75: Reconstructed Crab flux for CT5 mono using the most recent simulation configuration *phase2d3* together with previous H.E.S.S. results (Aharonian et al., 2006) and the spectrum presented by Meyer et al. (2010). The plot is taken from Steinmassl (2023).

Further, the Crab flux determined using CT1-4 in their default hybrid trigger configuration does not match the Crab flux determined using CT5 (see Figure 102). Such discrepancies are likely caused by the incorrect representation of the telescope within MC simulations used for Cherenkov shower reconstruction, proving fatal to scientific studies.

This section presents the author’s significant contributions in identifying and rectifying major sources of discrepancies between the actual and simulated telescope response in the H.E.S.S. telescope simulation chain. This work is part of the MC validation group effort led by the author, Simon Steinmassl, Tim Lukas Holch, and Fabian Leuschner. In the following, a summary of the entire investigation is presented, focusing on the author’s results. Attribution is given in the beginning for parts in which someone besides the author leads the effort. The intermediate results of this investigation and a brief summary of the presented work have been published in Leuschner et al. (2023).

## 4.1 Basic Monte Carlo Consistency

As a first step, basic Monte Carlo consistency checks are performed. These concern the basic implementation of the H.E.S.S. telescopes in *sim\_telarray* and the chosen settings for the CORSIKA Cherenkov air shower simulation. The latter uses the QGSJET-II-4 high energy and UrQMD low-energy interaction model. As mentioned, the validation is performed for the latest H.E.S.S. simulation configuration *phase2d3* at the time of writing. The *phase2d3* timeframe corresponds to the H.E.S.S. run range of 160051 – 162824, containing 1174 observation runs used to compare the simulation against.

### 4.1.1 Telescope Optics

Initially, the optics of the H.E.S.S. telescopes are validated. Following the procedure outlined in section 3.5.1, the internal ray tracing of *sim\_telarray* with a parallel light source is used to assess the behaviour of the telescope’s optical system. The H.E.S.S. telescopes adapt large mirrors, segmented into smaller mirror facets, with a total mirror diameter of 12 m for CT1-4 and 28 m for CT5. Further, the Cherenkov cameras of the H.E.S.S. telescopes feature a camera lid that can be closed for protection or to measure the telescope’s optical PSF.

For this measurement, the camera lid is closed, so starlight reflected by the primary mirror produces an image on the lid, which is captured using a secondary CCD Lid pointing camera (further referred to as the pointing camera). This pointing camera is positioned at the centre of the primary mirror, pointing towards the telescope’s Cherenkov camera. An example image for CT1 taken on January 2023 is shown in Figure 76.

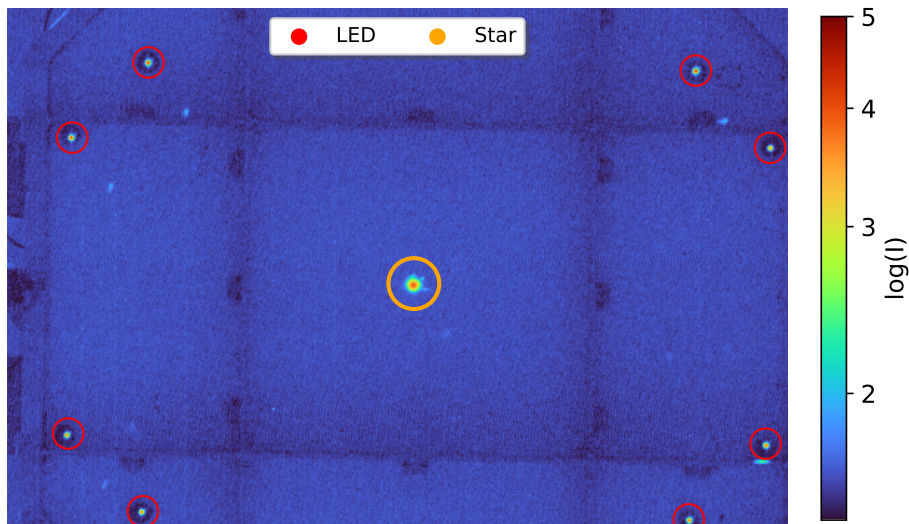


Figure 76: Pointing camera image of CT1 pointing towards the star Sirius. The locations of the Cherenkov camera’s pointing LEDs and Sirius (centre) on the lid are highlighted with red and orange ring indicators, respectively. The image data is provided by Salzmann (2023).



The indicated LED positions (red rings) are the pointing LEDs on the Cherenkov camera’s focal plane that shine through openings in the camera lid. Since their location is known precisely, they are used to measure the misalignment between the primary mirror’s optical axis and the telescope camera caused by the bowing of the telescope structure. Still, they are of no further concern for the presented investigation. In Figure 76, CT1 is pointed towards the star Sirius, the position of which on the camera lid is highlighted with an orange ring. The star’s photon distribution is isolated, and the 80 % containment radius  $R_{80\%}$  is determined following the method introduced for DesertACT in section 3.5.1 for 80 % signal containment instead of 90 %. Multiple such measurements are made for different telescope elevations  $\alpha$  to include statistical fluctuations. Following Cornils et al. (2003) and Gottschall (2018), the resulting data points are fitted with a telescope-dependent function of the form

$$R_{80\%}^{\text{CT1-4}}(\alpha) = \sqrt{R_{\min}^2 + d_1^2 \cdot [\sin(\alpha) - \sin(\alpha_0)]^2} \quad (67)$$

$$R_{80\%}^{\text{CT5}}(\alpha) = \sqrt{R_{\min}^2 + d_1^2 \cdot [\sin(\alpha) - \sin(\alpha_0)]^2 + d_2^2 \cdot [\cos(\alpha) - \cos(\alpha_0)]^2} \quad (68)$$

for CT1-4 and CT5 respectively. In Equation 67 and Equation 68,  $\alpha_0$  is the elevation angle at which the minimum  $R_{\min}$  is reached, such that  $R_{80\%}(\alpha = \alpha_0) = R_{\min}$ . The parameters  $d_1$  and  $d_2$  are scaling factors for the angular dependencies. The additional angular dependency term in Equation 68 is required for CT5 due to the more complex telescope structure bowing behaviour (Salzmann, 2020). Only the resulting fit parameters for the function shown in Equation 68 and Equation 67 are available for later comparison, but not the covariance matrix, as its storage is not part of the standard analysis chain. Therefore, the fit errors cannot be considered for the presented analysis. An investigation is currently underway to solve this issue (Salzmann, 2023).

This type of observation is recreated in the simulation utilizing internal ray tracing simulation of *sim\_telarray*. Following the optical simulation of DesertACT (section 3.5.1), an artificial star at an infinite distance is used to create parallel light, which is traced through the telescope’s optical system. The photon positions on the primary mirror, the camera lid and the pixel plane are provided as an output of this simulation. The photon distributions on these optical elements for an elevation of  $\alpha = 90$  deg are shown in Figure 77 for the CT5 telescope and in Figure 78 for the CT1 telescope. The distributions for CT2-4 are shown in section A.1 (Appendix A).

The  $R_{80\%}$  is obtained from the photon distribution on the camera lid using the algorithm presented in section 3.5.1 for the case of 80 % containment. For each telescope elevation, this ray tracing simulation and subsequent determination of  $R_{80\%}$  is repeated 50 times to form a mean and standard deviation value for  $R_{80\%} = \bar{R}_{80\%} \pm \Delta R_{80\%}$ . These values are converted into an angular size using the focal length  $f_{\text{CT5}} = 36$  m of CT5 and  $f_{\text{CT1-4}} = 15$  m of CT1-4 as

$$R_{80\%} [\text{rad}] = \tan \left( \frac{R_{80\%}}{f} \right) \quad (69)$$

with corresponding error propagation. The simulated elevation angle dependant  $R_{80\%}$  for CT1 and CT5, together with the fit to the measured  $R_{80\%}$  values, is shown in Figure 79.

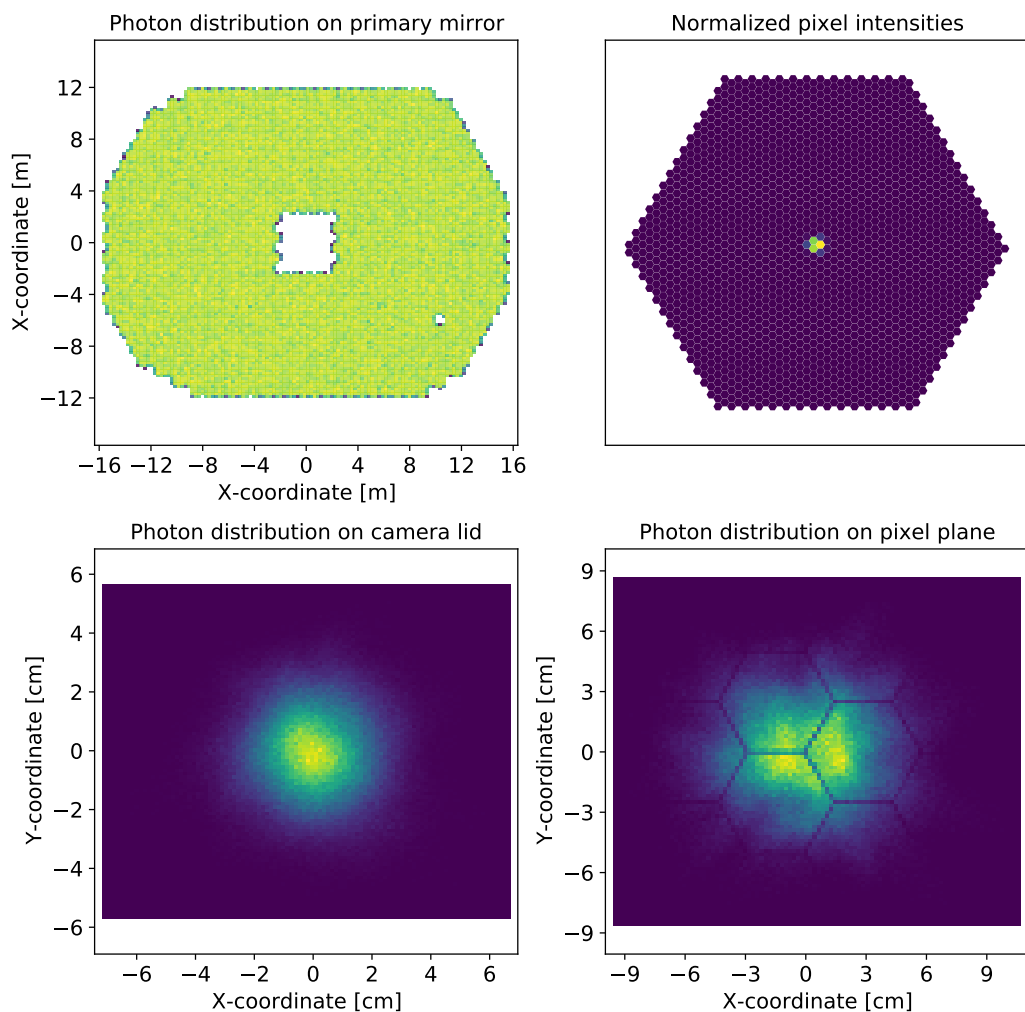


Figure 77: Ray tracing overview plot for the H.E.S.S. CT5 telescope pointing towards the zenith for incoming parallel light with an incidence angle of 0 deg to the telescope’s optical axis. The overview contains the normalized photon distributions on the primary mirror (top left), camera lid (bottom left), pixel plane (bottom right), and the normalized pixel amplitudes (top right).

The relative deviations between the simulated and real  $R_{80\%}$  values can exceed 20% with CT1 and CT5 showing relative deviations  $\gtrsim 10\%$ . The results for CT1-4 are shown in Figure 113 (Appendix A).

The elevation dependant  $R_{80\%}$  value in the *sim\_telarray* simulation is specified with the so-called mirror-alignment component settings `MIRROR_ALIGN_RANDOM_HORIZONTAL` and `MIRROR_ALIGN_RANDOM_VERTICAL`, defining the behaviour of the horizontal and vertical component respectively. Each mirror-align component setting requires four parameters defining a function similar to the one shown in Equation 68 with the dependence on the elevation angle  $\alpha$  being replaced by the zenith angle  $\Theta$ , following the parameter assignment shown in Configuration 5.

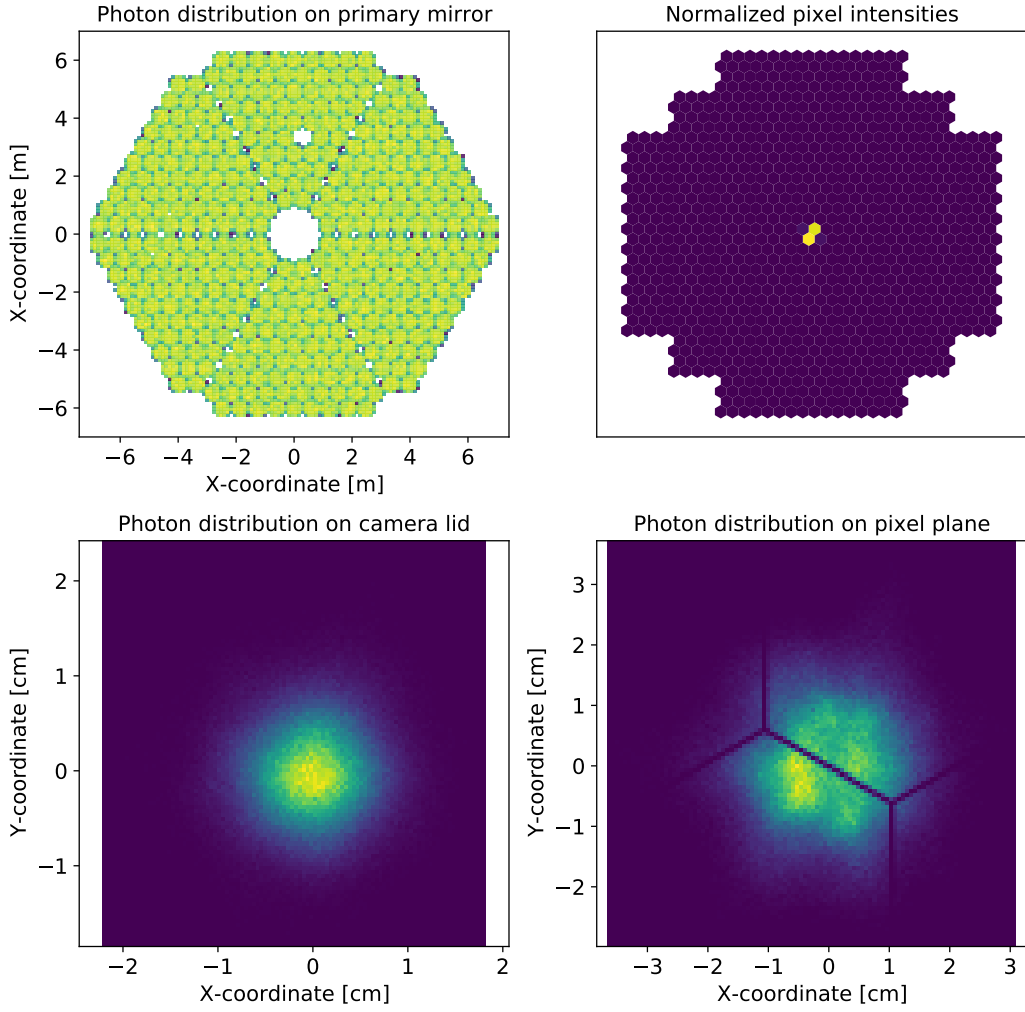


Figure 78: Ray tracing overview plot for the H.E.S.S. CT1 telescope pointing towards the zenith for incoming parallel light with an incidence angle of 0 deg to the telescope’s optical axis. The overview contains the normalized photon distributions on the primary mirror (top left), camera lid (bottom left), pixel plane (bottom right), and the normalized pixel amplitudes (top right).

```

1 mirror_align_random_horizontal/vertical= Rmin [deg], Θ0 [deg], d2, d1
2

```

Configuration 5: Definition of horizontal/vertical mirror-alignment component setting in *sim\_telarray* based on the parameters introduced in Equation 68. Parameter assignment is adapted from Bernlöhr (2022b).

In the current simulation configuration of *phase2d3*, all small H.E.S.S. telescopes (CT1-4) share the same parameter values for both mirror align components, resulting in identical  $R_{80\%}$  values. To reduce the relative deviation between the simulated and measured  $R_{80\%}$ , both mirror-align component settings are adjusted on a per-telescope basis.

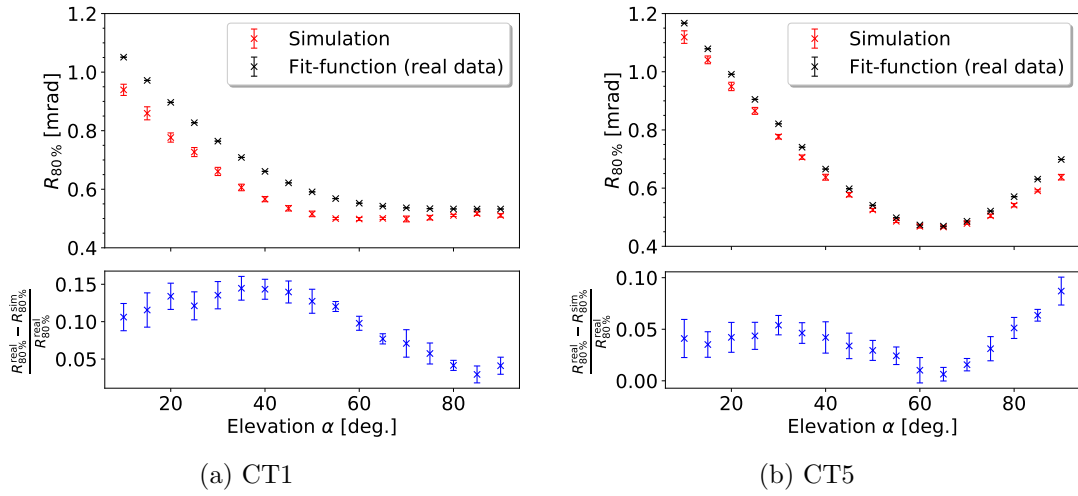


Figure 79: The elevation dependant 80% containment radius  $R_{80\%}$  of CT1 (a) and CT5 (b) for the simulation and the fit function made to the real values, with the relative deviation between them.

The simulated photon distribution on the camera lid is a function of the vertical and horizontal mirror-alignment component settings in *sim.telarray*. As this distribution is not necessarily radially symmetric, the contributions of each component are different. Consequently, none of the remaining fit parameters for the measured data besides  $\alpha_0$  can be directly used for the mirror-alignment component settings as both components contribute to the  $R_{80\%}$  value.

At the time of the validation, a manual tuning approach was selected. The simulation parameters of both the horizontal and vertical components were adjusted individually, with the parameter ratios of both components being maintained to reduce the resulting  $R_{80\%}$  value but maintain the shape of the simulated photon distribution on the camera lid. The resulting  $R_{80\%}$  values for CT1 and CT5 are shown in Figure 80. The results for CT1-4 are shown in Figure 114 (Appendix A). The initial mismatch of up to 20% between the measured and simulated  $R_{80\%}$  is reduced to within 5% for all telescopes. Whilst additional adjustments could be made to improve the match further, the adjusted  $R_{80\%}$  values are already below the scale of a single pixel. Adjustments on a sub-pixel level are unlikely to affect the telescope's performance significantly, with the remaining 5% deviation deemed acceptable. The performance of the telescopes is evaluated in a later section using the trigger rates (section 4.2.3), with the results confirming this assumption.

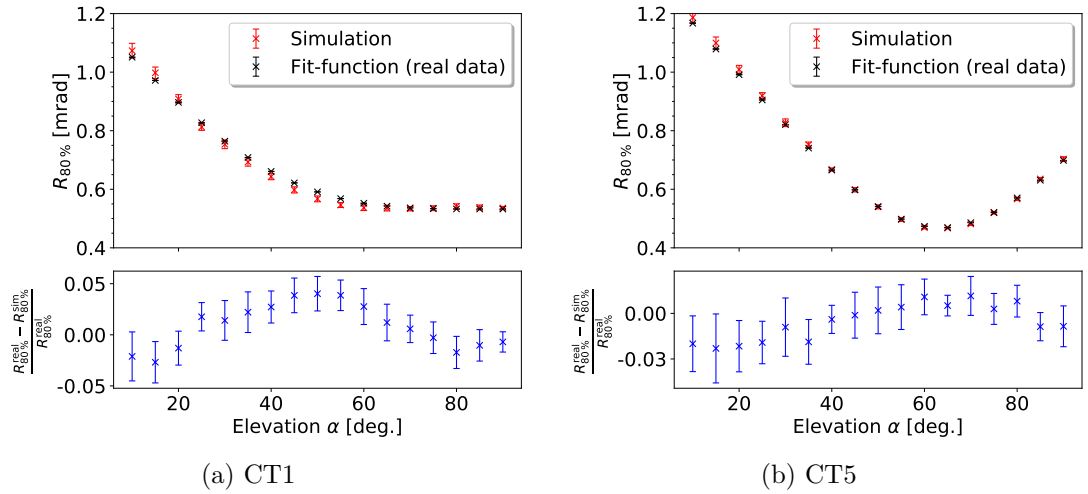


Figure 80: The elevation dependant 80 % containment radius  $R_{80\%}$  of CT1 (a) and CT5 (b) for the telescope-dependant adjusted simulation and the fit function made to the real values, with the relative deviation between them.

#### 4.1.2 Waveform-Level validation

Another important validation step concerns the single-pixel waveforms. More specifically, the correct handling of the waveform amplitude and peak position within the readout window for different input parameters. This investigation was led by Simon Steinmassl as part of the MC validation efforts, and more details can be found in Steinmassl (2023). The position and amplitude response is initially evaluated using the laser pulse simulation feature of *sim.telarray*. Each camera pixel is illuminated with exactly 300 photons of 400 nm wavelength. The duration of each laser pulse is of the same nanosecond timescale as those of Cherenkov showers. The resulting camera events and subsequent pixel waveforms after 500 such simulations of fixed intensity are extracted using *ctapipe*, and the mean pixel waveform is calculated. The results for CT1 and CT5 are shown in Figure 81.

As the laser photons all arrive simultaneously, the waveform peaks are expected to be located approximately at the same position within the readout window, which is indeed observed in Figure 81. The containment of most of the pulse signal in the readout window is essential for the later signal integration. Altering the illumination intensity and the time offset within the readout windows yields the expected results. The peak timing and signal containment are further evaluated by switching from laser pulse simulations to photons from gamma ray-induced Cherenkov air showers. The resulting pulses are the same shape as the laser pulses and are contained within the readout window of CT1-5, with the peak positions more spread out compared to the laser simulations. This procedure validates the proper scaling and positioning of the simulated signal pulse for parameter changes.

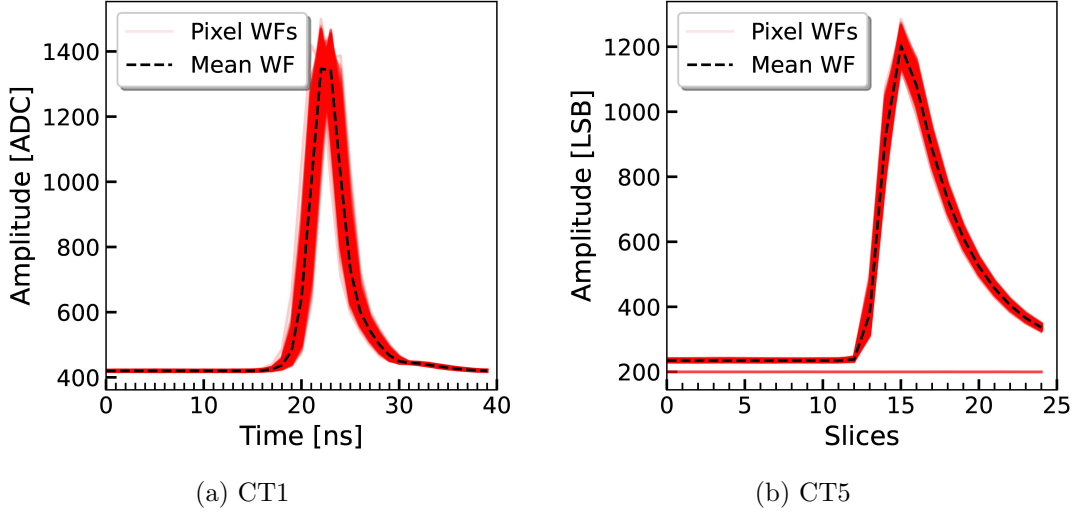


Figure 81: Mean pixel waveforms (WFs) for CT1 (a) and CT5 (b) with highlighted mean waveform for 500 simulated laser events with a fixed laser intensity of 300 photons/pixel at 400 nm wavelength. The plots are adapted from Steinmassl (2023).

### 4.1.3 Atmospheric Transmission

In *sim\_telarray*, the atmospheric light attenuation is specified in atmospheric transmission tables. These contain the Atmospheric Optical Depth (AOD) for different heights above ground and wavelengths of light. These transmission tables are produced using the Moderate resolution atmospheric Transmission software (MODTRAN) (Bernlöhr, 2022a).

The total AOD values contained in the transmission tables can be decomposed into two factors,  $AOD^{\text{aero}}$  and  $AOD^{\text{mol}}$ , representing the contribution of aerosols and gaseous molecules, respectively. Whilst the molecular contribution  $AOD^{\text{mol}}$  to the total AOD remains constant over long timescales, the aerosol contribution  $AOD^{\text{aero}}$  can vary on comparably short timescales. These changes are especially prominent during the local biomass burning season in Namibia, during which the concentration of aerosols drastically increases.

As the currently used  $AOD^{\text{mol}}$  contributions have been separately validated to show agreement with atmospheric measurements (Holch, 2022), the  $AOD^{\text{aero}}$  component is for adjustments of the total AOD values in the transmission tables. The magnitude of these adjustments can be determined using data from a local station of the Aerosol Robotic Network (AERONET) (Holben et al., 1998). A photograph of this station with the H.E.S.S. array in the background is shown in Figure 82.

The AERONET installation features a multispectral radiometer performing atmospheric measurements every 2 min to 15 min in a wavelength range from 340 nm to 1020 nm by tracking the sun during the day and the moon at night. Resulting data is accessible online, with multiple derived quantities such as the aerosol contribution  $AOD^{\text{aero}}$  and molecular composition (*Aerosol Robotic Network (AERONET) website* 2022; Holben et al., 1998). First, the difference between the simulated AOD values in



Figure 82: Photograph of the AERONET station (top right) close to the H.E.S.S. site in Namibia (lower left) taken in 2022. Image credit: Tim Lukas Holch.

the transmission tables and the AERONET results is investigated. This is done by estimating the detected Cherenkov photon spectrum of air showers for the observed and simulated AOD values. The atmospheric transmission between a height  $h_1$  and  $h_2$  above sea level can be written as an exponential function

$$T_{\text{atm}}(\lambda, h_1, h_2) = e^{-\int_{h_1}^{h_2} \text{AOD}(\lambda, h) dh}, \quad (70)$$

with  $\text{AOD}(\lambda, h)$  the total AOD at a specific wavelength  $\lambda$  and height above sea level  $h$ . Considering a generic Cherenkov emission spectrum  $\Phi_{\text{cher}}(\lambda)$  (Fink et al., 2016), shown in Figure 83, the detected Cherenkov spectrum by the CT5 camera can be written as

$$\Phi_{\text{det}}(\lambda, h_1, h_2) \propto T_{\text{atm}}(\lambda, h_1, h_2) \cdot \text{PDE}_{\text{CT5}}(\lambda) \cdot \Phi_{\text{cher}}(\lambda). \quad (71)$$

The mirror reflectivity is not included in Equation 71, as its wavelength dependence is negligible compared to the one of the PDE (compare Figure 59b).

The observation height of H.E.S.S. at  $h_1 \approx 1.8$  km and the expected location of electromagnetic air shower maxima is at  $h_2 \approx 15$  km (section 2.1). The transmission tables directly list the  $\text{AOD}(\lambda, h)$  in tabulated form. For the AERONET observations, the  $\text{AOD}(\lambda, h)$  has been calculated by Tim Lukas Holch using the derived quantities provided by AERONET as input to the *Py6s* atmospheric radiative transfer model (Wilson, 2013). The results are shown in Figure 84.

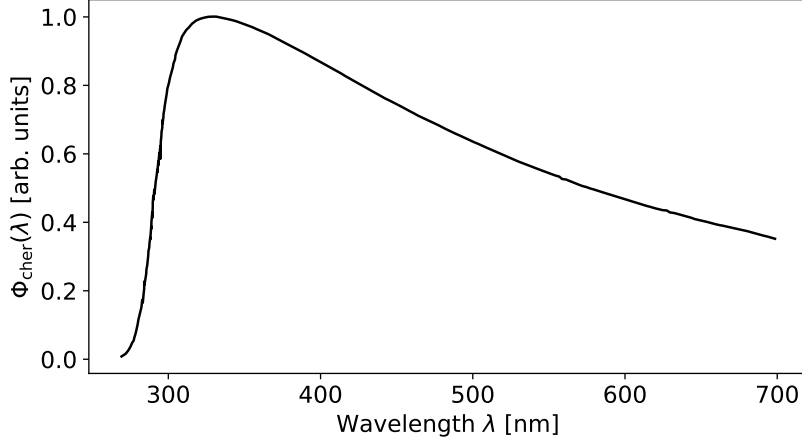


Figure 83: The Cherenkov emission spectrum in arbitrary units. Data is taken from Fink et al. (2016).

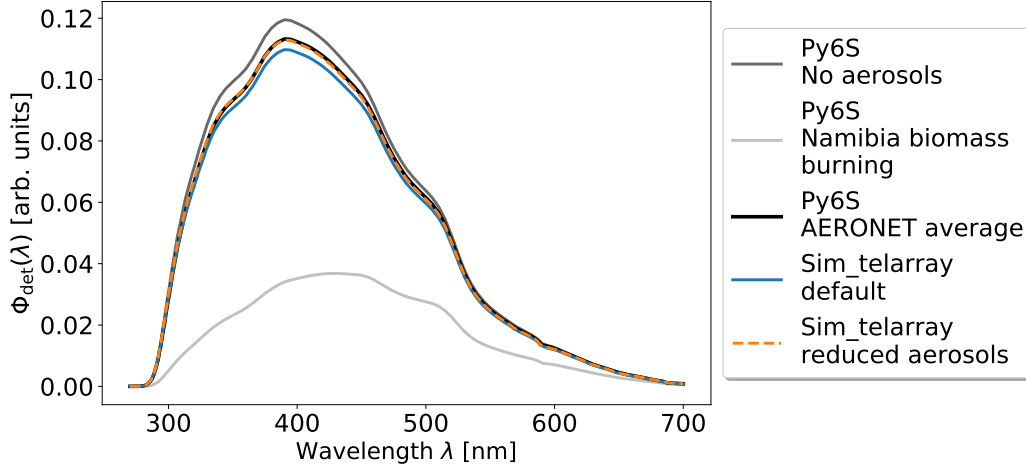


Figure 84: The  $\Phi_{\text{det}}$  curve for Cherenkov photons originating at 15 km height above sea level and arriving at the H.E.S.S. observation height of 1835 m for CT5 and varying AOD levels.

In addition to the no-aerosol contribution scenario, the  $\Phi_{\text{det}}$  curve during the biomass burning season in Namibia and the AERONET average during the timeframe of phase2d3 are shown together with the  $\Phi_{\text{det}}$  curve produced by the default transmission table<sup>13</sup> used in *sim\_telarray*. Comparing the integral of  $\Phi_{\text{det}}$  between different scenarios provides information about the percentile reduction in the number of detected Cherenkov photons. Comparing the *Py6s* AERONET average (black) and the *sim\_telarray* default (blue) in Figure 84, the number of detected Cherenkov photons is reduced by  $\approx 3\%$ .

This slight reduction in the number of detected Cherenkov photons can yield drastic changes in the telescope trigger rates, as they are dominated by the emission of Cherenkov showers close to the telescope’s trigger threshold. A reduction in the detected

<sup>13</sup>The default transmission table file for H.E.S.S. simulations is *atm\_trans\_1835\_1\_10\_0\_0\_1835*.



number of photons effectively increases the telescope’s trigger threshold, significantly reducing the trigger rate. This is also highlighted when the telescope trigger rates are validated in section 4.2.3. Furthermore, this also impacts the energy reconstruction. As fewer Cherenkov photons are detected, the Hillas size of Cherenkov showers is reduced. The latter is an essential part of the lookup tables used for energy reconstruction (section 2.5.7). Therefore, a deviation in the number of detected photons in the simulation relative to the observation conditions results in an incorrect energy reconstruction.

To reduce this deviation, the aerosol contribution  $\text{AOD}^{\text{aero}}$  in the used transmission table is altered. As shown in Figure 84, a reduction in  $\text{AOD}^{\text{aero}}$  results in an enhanced  $\Phi_{\text{det}}$ . Therefore, to reduce the deviation, the  $\text{AOD}^{\text{aero}}$  in the transmission table must also be reduced.

Besides the default transmission table, *sim\_telarray* provides another table<sup>14</sup> without the aerosol contribution to the total AOD. For each entry in the transmission table, the new AOD value is calculated using

$$\text{AOD}^{\text{mix}} = \text{AOD}^{\text{no aero}} \cdot \nu + \text{AOD}^{\text{default}} \cdot (1 - \nu), \quad (72)$$

With  $\nu$  as the new fractional reduction in aerosol concentration relative to the default transmission table. The deviation of the simulation and the observations based on AERONET is reduced to  $\approx 0.1\%$  by reducing the aerosol contribution in the default transmission table by 50% ( $\nu = 0.5$ ). From this, a new atmospheric transmission table<sup>15</sup> is created, hereafter referred to as ”mix transmission”. It should be noted that the observed deviation in the number of detected Cherenkov photons is only valid for the mean atmospheric conditions during the *phase2d3* era, and variations on the scale of  $\approx 10\%$  are observed on timescales of a few days. Phenomenologically, these variations can be observed using the transparency coefficient derived by H.E.S.S. (Figure 16). Such variations could be accounted for in simulations on a run-by-run basis. This, however, proves to be impractical due to the required number of simulations and subsequent computing time. An alternative approach is presented by the MC validation group in Holch et al. (2022), using an estimate of momentary atmospheric conditions to correct existing lookup tables and energy dispersion matrices without the need for resimulation.

#### 4.1.4 Telescope Trigger Threshold

The telescope trigger threshold is one of the most critical parameters for the telescope’s low-energy performance. The CT5 trigger threshold setting has been investigated in Steinmassl (2023) as part of the MC validation effort. In the following, a summary of this investigation is presented. Initially, the simulated trigger threshold of FlashCam used in CT5 is investigated. As outlined in section 2.5, the pixels of FlashCam are grouped into 588 overlapping camera sectors of nine pixels each. The trigger decision is made using the sum of three sectors. Hence, the brightest sector in any given camera image is a good indicator of the trigger behaviour. The brightest sector intensity distribution for proton simulations with the default simulation configuration (def.) is compared to

<sup>14</sup>The transmission table file without the aerosol contribution for H.E.S.S. simulations is *atm\_trans\_1835\_1\_0\_0\_0.1835*.

<sup>15</sup>The assigned configuration file name is *atm\_trans\_1835\_mix\_atm\_1835.dat*

the distribution of observation runs<sup>16</sup> in the previously specified *phase2d3* period. The chosen observation runs were taken during nights with typical NSB, good atmospheric conditions and no bright gamma-ray source in the telescope’s FoV. The results are shown in Figure 85. The point at which the distribution reaches the 50% point on the

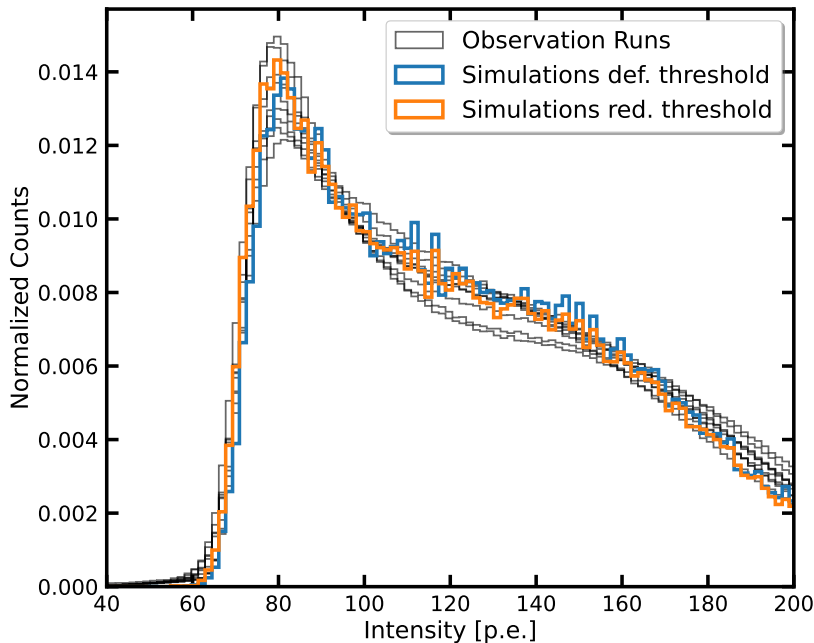


Figure 85: The intensity distribution of the brightest sector in FlashCam for simulated proton showers using the default (def.) *sim\_telarray* configuration (blue) and nine example observation runs (selection criteria are explained in the text). The distribution for the reduced (red.) threshold setting is shown in orange. The plot is taken from Steinmassl (2023).

rising edge characterises the trigger setting. For this point, a significant deviation of 3.8% is observed between the observation runs and the default simulation. As described in section 4.1.3, even a percentile deviation in the trigger threshold setting can yield a significant change in the telescope’s trigger rate (section 4.2.3). Therefore, this deviation must be reduced. The telescope’s trigger threshold is set with the `DSUM.THRESHOLD` parameter in the *sim\_telarray* definition of CT5. It specifies the ADC-Count threshold beyond the sector pedestal above which a telescope trigger is issued (Bernlöhr, 2008). Its default value of 79 ADC-counts is adjusted by the observed percentile deviation to the next integer value of 76 ADC-counts. The simulation for this reduced threshold now fits the observation distribution with a 2% remaining uncertainty limited by the used binning.

The smaller H.E.S.S. telescopes feature 960 pixel cameras and are grouped into 60 drawers with 16 pixels each. At least three pixels above the pixel trigger threshold are required to issue a camera-level trigger (Bernlöhr, 2008). Therefore, the third-brightest pixel intensity distribution is a good measure of the telescope’s trigger behaviour for

<sup>16</sup>Off runs are used for the comparison to proton simulations

small-intensity camera images. These distributions for simulation and observation can be seen in Figure 86. The observation runs are selected identically to the ones used for CT5. The distributions show a mismatch of  $\approx 27\%$  for the 50% point on the distribution's

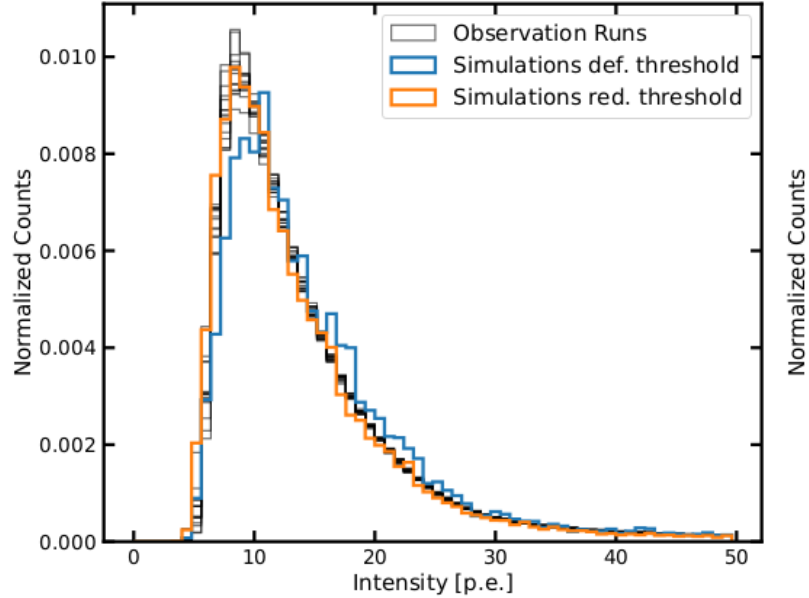


Figure 86: The intensity distribution of the third-brightest pixel in the camera of CT1 for observation runs and simulations. The distributions for the default *phase2d3* and redefined *sim\_telarray* configuration are highlighted in blue and orange, respectively. Taken from Steinmassl (2023).

rising edge. The telescope threshold for the small H.E.S.S. telescopes is set using the `DISCRIMINATOR_THRESHOLD` setting in *sim\_telarray* and, per default, is set to 3.24 for all four telescopes<sup>17</sup>. The author calculates the new telescope-dependent threshold values to match the mean observation distribution better. These newly adopted discriminator threshold settings are in Table 11. The resulting simulated distribution for the new

Telescope	Discriminator threshold setting [p.e.]	
	Original	Adjusted
CT1	3.24	2.63
CT2	3.24	2.67
CT3	3.24	2.66
CT4	3.24	2.74

Table 11: Discriminator threshold setting in *sim\_telarray* in the original *phase2d3* and adjusted simulation configuration for CT1-4.

discriminator threshold setting can be seen in orange in Figure 86 and results in an acceptable match.

<sup>17</sup>The discriminator threshold *sim\_telarray* setting for the CT1-4 Cherenkov cameras does not have a particular unit.

### 4.1.5 Mirror Reflectivity

A measure for the absolute mirror reflectivity of a telescope can be derived from the measured muon efficiency (section 2.5.5). The CT5 muon efficiency distributions for simulations and observations initially show a match. However, the previous muon analysis chain for the CT5 telescope simulation did not include corrections for the pedestal width and bias, which Simon Steinmassl implemented. The muon efficiency distributions before and after updating the muon analysis chain for CT5 were determined by Tim Lukas Holch and are shown in Figure 87. Adopting the new muon analysis

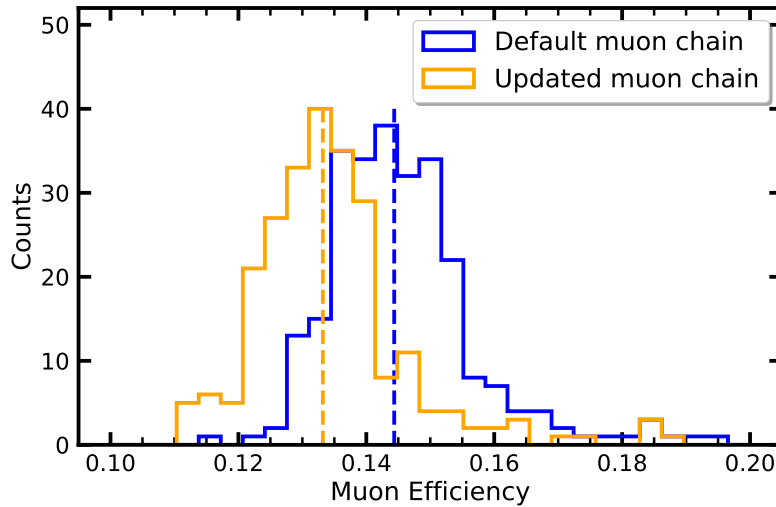


Figure 87: Simulated muon efficiency distribution of CT5 for the initial and updated muon chain. The latter now includes corrections for the pedestal width and bias of CT5. The plot is taken from Steinmassl (2023).

chain results in a  $\approx 8\%$  shift of the distribution's mean towards lower efficiencies. As the initial simulated muon efficiency was already matched to measurements, the mirror reflectivity of CT5 in simulation after adapting the new muon chain is increased by the same amount to account for the introduced shift.

The mirror reflectivity in *sim.telarray* is defined by the mirror transmittance curve and the mirror degradation parameter<sup>18</sup>. The former defines the default mirror reflectivity for different wavelengths of light (Figure 59), and the latter defines a multiplicative scaling factor for this curve (Bernlöhr, 2022b). The required shift is implemented by increasing the default mirror degradation parameter from 0.738 to 0.79, increasing the mirror reflectivity.

The muon efficiencies of CT1-4 have been previously validated in Zorn (2020). However, a new calibration scheme for observation data was adopted in November 2022. This scheme replaces the previously fixed PMT gain in *phase2d3* with a dynamic gain based on measurements during calibration runs. This change impacts the brightness of muon rings, resulting in a telescope dependant shift of the muon efficiency distribution towards smaller efficiencies. These shifts are again implemented by changing the mirror

<sup>18</sup>MIRROR\_DEGRADED\_REFLECTION (Bernlöhr, 2022b).

degradation parameter on a per-telescope basis. The original and adjusted mirror degradation parameters are shown in Table 12.

Telescope	Original degradation	Adjusted degradation
CT1	0.823	0.800
CT2	0.840	0.827
CT3	0.826	0.804
CT4	0.794	0.745
CT5	0.738	0.790

Table 12: Mirror degradation parameter settings for each H.E.S.S. telescope before and after adjustment.

#### 4.1.6 Simulated Viewcone

In addition to validating the *sim\_telarray* configuration parameters, the CORSIKA input parameters are critical for the simulation of Cherenkov showers. Similarly to the validation of the DesertACT CORSIKA parameters (section 3.5.6), the viewcone and the **RSCAT** setting, specifying the maximum allowed shower distance to the array centre, are subject to validation. The to-be-validated default proton simulation settings for the H.E.S.S. *phase2d3* period defines a simulated energy range from 30 GeV to 150 TeV, a viewcone of 5 deg, and a maximum impact distance of **RSCAT** = 1500 m.

To validate the viewcone setting, a larger than default viewcone of 10 deg is chosen, such that the performance of smaller viewcone settings can be evaluated. With these settings, proton-induced Cherenkov shower simulations are conducted at a zenith angle of 20 deg, resulting in  $\approx 10^4$  triggered showers. To determine a new value for the simulated viewcone, showers that are far away from the array centre or of low energy are specifically significant. Hence, data from CT5 is selected to evaluate the viewcone performance due to the larger effective aperture and mirror collection area. The used simulation configuration includes all adjustments introduced to the default *sim\_telarray* configuration up to now. The resulting distribution of triggered showers inside the simulated viewcone is determined using Equation 47 and Equation 49 introduced in section 3.5.6 and is shown in Figure 88.

As expected, the shower distribution inside the viewcone shows a central peak with fewer events towards larger angular offsets towards the viewcone centre. This is quantified by determining the fraction of triggered showers contained within a given total angular offset  $d\varphi = \sqrt{d\varphi_{\text{alt}}^2 + d\varphi_{\text{az}}^2}$ , shown in Figure 89.

From distribution, it can be determined that the default viewcone setting of 5 deg contains  $\approx 92\%$  all simulated showers. Increasing the viewcone setting, however, increases the CPU time spent on showers that do not result in a telescope trigger. Therefore, a new viewcone setting of 8 deg is selected as a compromise between the contained fraction of showers and computation time, such that the fraction of contained showers

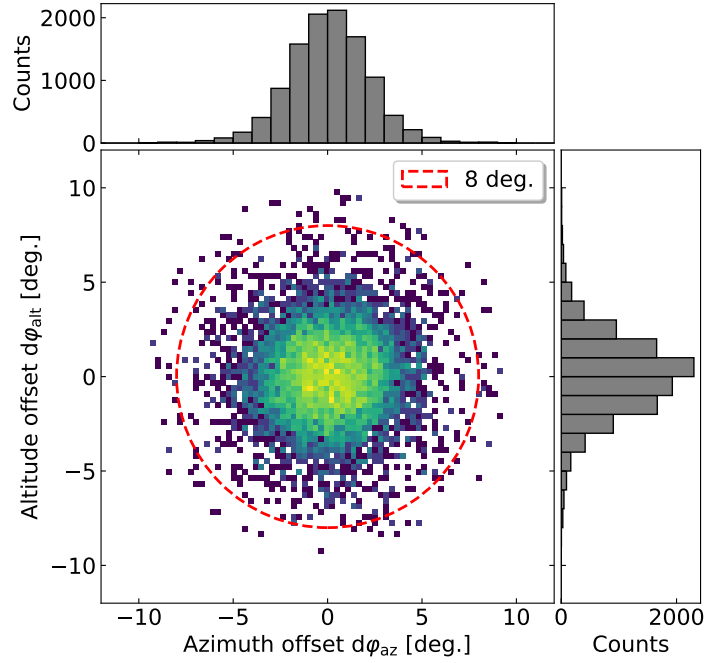


Figure 88: CT5 triggered proton shower distribution inside the simulated 10 deg viewcone, with the new setting of 8 deg highlighted in red. Showers were simulated at a zenith angle of 20 deg in the standard energy range from 30 GeV to 150 TeV with a maximum shower distance of  $RSCAT = 1500$  m.

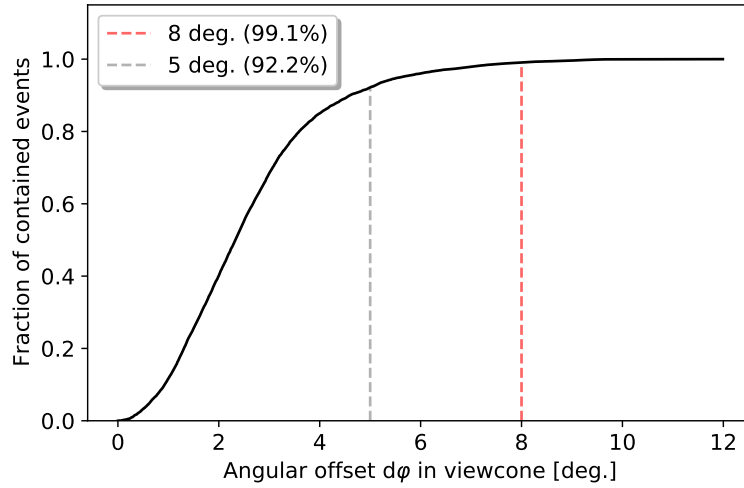


Figure 89: Fraction of triggered showers contained within a given total angular offset  $d\phi$  inside the viewcone relative to the telescope pointing direction. The default viewcone setting of the simulation (5 deg) and the newly chosen 8 deg setting, together with their respective total fraction of contained showers, are highlighted.

is  $\approx 99\%$ <sup>19</sup>. To evaluate that the shown percentile fractions are valid, a simulation with

<sup>19</sup>In reference to a simulated viewcone of 10 deg

a much bigger viewcone of 30 deg has been conducted, yielding sup-percent variations from the values given above. Therefore, the newly proposed viewcone setting of 8 deg is used.

From the original 10 deg viewcone simulation, one can further look at the zenith angle corrected impact point distribution of triggered showers (compare section 3.5.6), which is shown in Figure 90. As seen in Figure 90, the event distribution is well contained

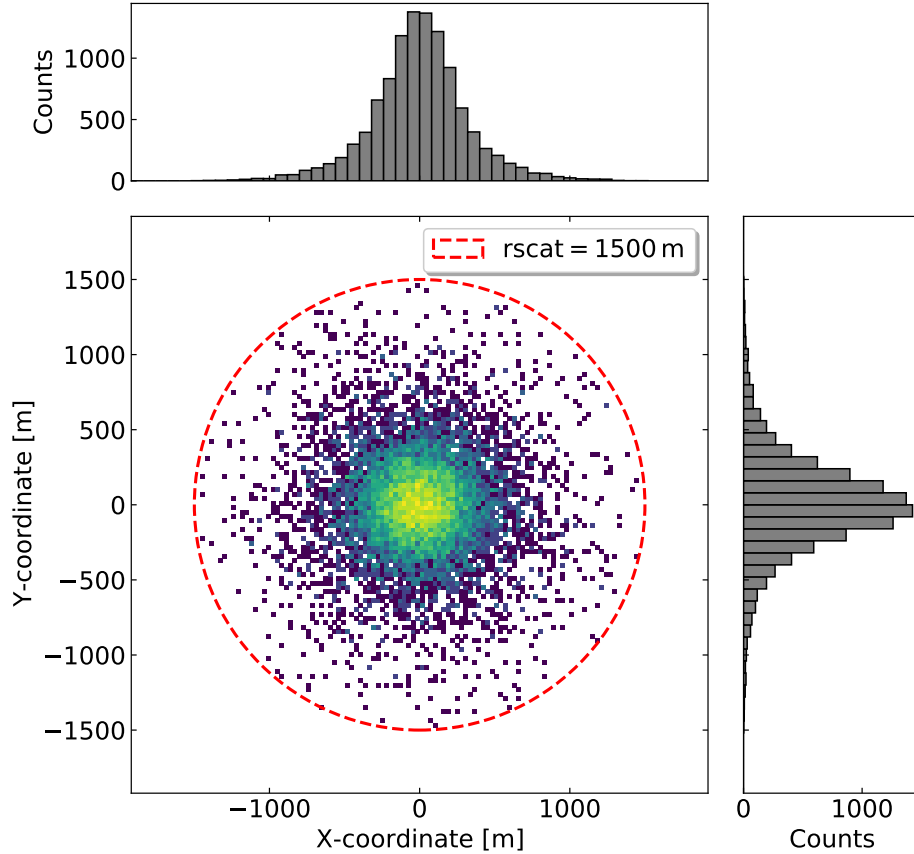


Figure 90: CT5 proton shower impact point distribution on the ground for a simulated viewcone of 10 deg viewcone, with the maximum shower distance of  $RSCAT = 1500$  m highlighted in red. Showers were simulated in the standard energy range from 30 GeV to 150 TeV.

within the area specified with the default  $RSCAT = 1500$  m value. The used viewcone setting influences the distribution of events, with a larger viewcone setting yielding more events towards larger impact distances. Since the simulation was conducted with the 10 deg for which the  $RSCAT = 1500$  m is deemed acceptable, this is valid for the smaller viewcone setting of 8 deg as well. The default  $RSCAT$  setting is maintained.

## 4.2 Single Telescope Consistency

The second stage of the validation is to establish the single telescope consistency, i.e. the match between the single telescope simulation and single telescope observations. All previous adjustments to the default *phase2d3* simulation configuration in *sim\_telarray* and CORSIKA are adapted for the upcoming investigations.

### 4.2.1 Photo Electron Definition

The consistency of the p.e. definition between the simulation and the HAP-analysis framework is essential for later analysis and must be consistent. For CT5, this consistency is established in Steinmassl (2023) as part of the MC validation effort. Here, the laser simulation of *sim\_telarray* was used with an intensity of 300 photons/pixel at a wavelength of 400 nm. *Sim\_telarray* provides the true number of photoelectrons  $I_{\text{true}} = 107.65$  p.e., which is compared to the arithmetic mean  $\mu_{\text{ar}}$  of the intensity distribution produced by HAP and the mean  $\mu_G$  of a fit Gaussian. This is shown in Figure 91.

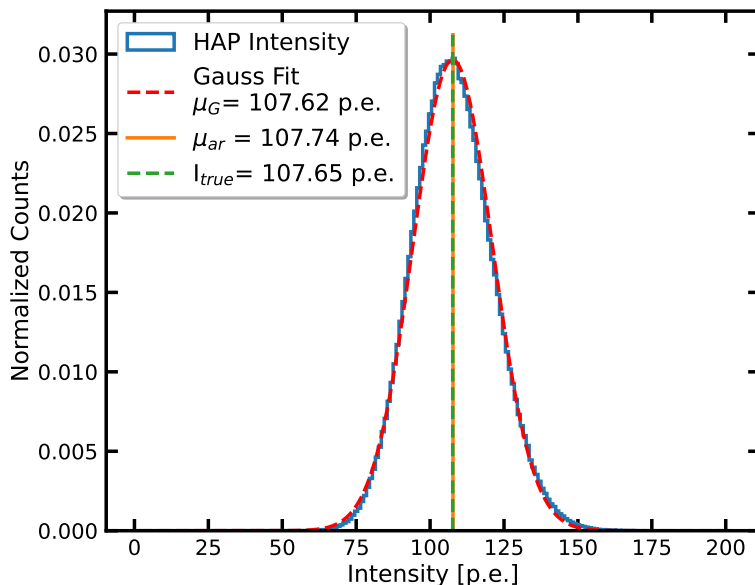


Figure 91: The intensity distribution of flat field measurements together with the laser simulation results (green). The plot is taken from Steinmassl (2023).

The deviation between the true photo electron value provided by *sim\_telarray* and the intensity calculated by HAP is consistent within 1%. Therefore, no adjustment is required. The photoelectron consistency for CT1-4 has previously been established in Zorn (2020).



### 4.2.2 Night Sky Background Setting

The NSB rate is another critical parameter in the *sim\_telarray* simulation. The NSB setting is validated in Leuschner (2023) as part of the MC validation effort.

Similarly to how the NSB setting for *sim\_telarray* is calculated for DesertACT in section 3.5.7, Equation 50 is used to the same effect for the H.E.S.S. telescopes as specified in *phase2d3*. This results in a NSB rate setting of 124.69 MHz and 316.01 MHz for CT1-4 and CT5, respectively. In addition, the H.E.S.S. database provides approximated values for the NSB rate during observations based on the observed baseline shift in the pixel waveforms of 134.22 MHz and 391.21 MHz for CT1-4 and CT5 respectively.

The best choice of NSB setting between the calculated and database values can be determined by simulating their effect on the pedestal and determining the resulting pedestal width. The resulting pedestal widths are shown in Table 13.

Source	Pedestal width [p.e.]	Source	Pedestal width [p.e.]
Simulation NSB=124.69 MHz	1.19	Simulation NSB=316.01 MHz	1.64
Simulation NSB=134.22 MHz	1.24	Simulation NSB=391.21 MHz	1.82
Database	1.27	Database	1.65

(a) CT1-4

(b) CT5

Table 13: The measured and simulated pedestal width for different NSB rate settings for the *sim\_telarray* simulation for CT1-4 (a) and CT5 (b). In both tables, the first-row NSB values are derived using Equation 50 and the second-row NSB values are taken from the H.E.S.S. database. Pedestal width values are taken from Leuschner (2023).

These values are compared to the pedestal width in the database. As the best match between the simulated and measured pedestal width, the NSB values of 134.22 MHz (60% increase) for CT1-4 and 316.01 MHz (44% increase) for CT5 are chosen as the new values for the simulation.

### 4.2.3 Mono Trigger Rates

The mono trigger rates are an excellent metric to evaluate the single telescope simulation of the H.E.S.S. telescopes. Usually, the H.E.S.S. telescopes are operated in hybrid mode, allowing a CT5 mono trigger and a stereo trigger between multiple H.E.S.S. telescopes, including CT5 (section 2.5). However, the mono trigger rates of each H.E.S.S. telescope during observation are also available. These rates are calculated before any cuts are applied to the data and are dominated by the more abundant proton-induced Cherenkov showers.

Hence, diffuse proton shower simulations are used to determine the simulated telescope mono-trigger rate. However, the simulation does not provide timing information between simulated showers, and a direct calculation of the trigger rate is impossible. The trigger rates can instead be calculated indirectly from the telescope's effective aperture, as defined in Equation 63. An example of the effective aperture for the original *phase2d3* configuration, with a simulated viewcone of 8 deg, and  $r_{\text{scat}} = 1500$  m is shown in Figure 92.

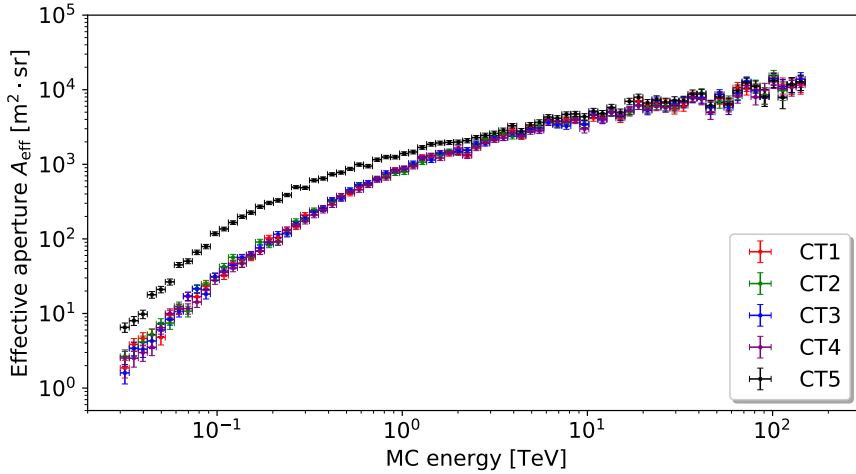


Figure 92: Simulated effective aperture of all H.E.S.S. telescopes pointing towards zenith using the original *phase2d3 sim\_telarray* configuration with a simulated viewcone of 8 deg, a maximum impact distance of 1500 m, and a simulated energy range from 30 GeV to 150 TeV. Each telescope is allowed to trigger by itself.

For each energy bin  $E_{\text{bin}}$ , the corresponding trigger rate is calculated as

$$R(E_{\text{bin}}) = A_{\text{eff}}(E_{\text{bin}}) \cdot \Phi_{\text{CR}}^{\text{P}}(E_{\text{bin}}) \cdot a_{\text{corr}}, \quad (73)$$

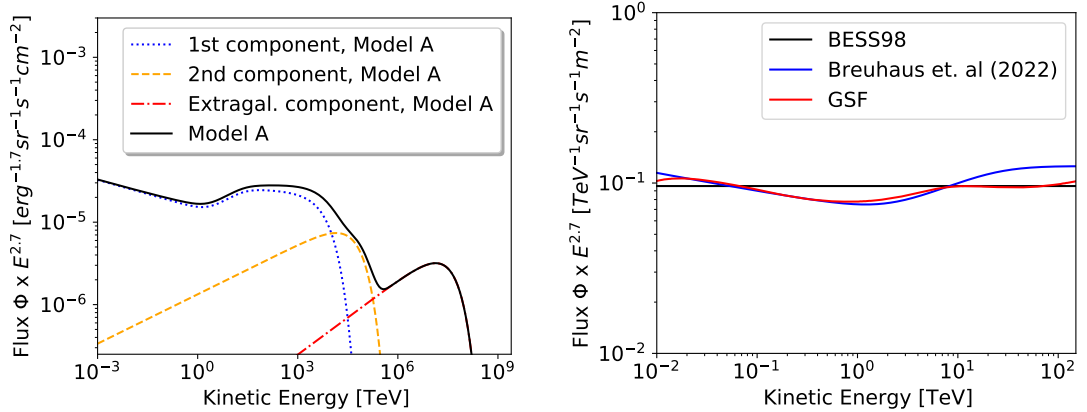
with  $A_{\text{eff}}$  the effective aperture,  $\Phi_{\text{CR}}^{\text{P}}(E_{\text{bin}})$  the integral cosmic proton flux and  $a_{\text{corr}}$  the heavy nuclei correction factor. The latter two are introduced in the following.

### Global Spline Fit Spectrum

Typically, two models are considered when describing the CR proton spectrum. The first model is the BESS98 spectrum presented in Sanuki et al. (2000), which describes

the CR proton spectrum as a simple power law. The second model is the Global Spline Fit (GSF) proton spectrum introduced in Dembinski et al. (2017), based on the cosmic ray flux measurements of multiple instruments such as AMS-02, PAMELA (Adriani et al., 2011), IceCube (IceCube Collaboration, 2013), and Auger (Sommers, 2005). The GSF spectrum shows more structure than the simple BESS98 power-law spectrum, with energy-dependant flux differences of up to 20 %.

Further, the GSF proton spectrum has been compared to the modelled proton spectrum presented in Breuhaus et al. (2022) to estimate the systematic differences in the resulting telescope mono trigger rates. In this publication, the cosmic ray proton spectrum is modelled using two galactic and an additional extra-galactic component, resulting in agreement with measurements of other experiments. Here, two different models are introduced, since experimental results above 10 TeV show inconsistencies. Either model can be selected, with resulting telescope trigger rates not changing significantly.



(a) Breuhaus et al. (2022) cosmic proton spectrum model A with corrected parameters.

(b) Comparison between the BESS98, GSF, and modelled cosmic ray proton spectrum.

Figure 93: Modelled cosmic ray proton spectrum with corrected model parameters from Breuhaus (2022) following Model-A, presented in Breuhaus et al. (2022) (a), with a comparison to the BESS98 and the GSF cosmic proton spectrum in (b). This comparison is made in the energy range of 10 GeV to 150 TeV used for the presented H.E.S.S. simulations. GSF proton spectrum data is taken from Dembinsky (2022), and BESS98 power law parameters are taken from Sanuki et al. (2000).

The spectral model presented in Breuhaus et al. (2022) could be replicated after correspondence with its author, working out inconsistencies between the provided model parameters and the shown model<sup>20</sup>. The result is shown in Figure 93a. The corresponding erratum has yet to be published at the time of writing. The comparison between this modelled spectrum, the BESS98, and GSF cosmic proton spectrum is

<sup>20</sup>The reference energy for the second galactic and the extra-galactic component is 1 TeV instead of 10 GeV with the corresponding plot for Model-A showing  $[\text{erg}^{-1.7} \text{sr}^{-1} \text{s}^{-1} \text{cm}^{-2}]$  instead of the shown  $[\text{erg}^{-1.7} \text{sr}^{-1} \text{s}^{-1} \text{m}^{-2}]$

shown in Figure 93b. The GSF and modelled spectrum show good agreement below 10 TeV, with the latter following closer to the BESS98 spectrum for the remaining shown energy range. For each proton spectrum, the total telescope mono trigger rate is determined following Equation 73, using the same simulated effective aperture to study the systematic differences. The heavy nuclei correction factor is not considered in this calculation. As expected, the resulting trigger rates for the GSF and modelled spectrum are consistent within  $1\sigma$ . As both spectra show good agreement below 10 TeV from which the majority of contributions to the total trigger rate originates (compare Figure 96b). In contrast, the BESS98 spectrum results in a  $(15.7 \pm 0.8)\%$  and  $(8.6 \pm 1.4)\%$  increase in the mono trigger rates of CT1-4 and CT5, respectively.

The GSF cosmic proton spectrum is used for the rest of the validation as there are no significant differences in the resulting telescope trigger rates compared to the modelling approach in Breuhaus et al. (2022), and both can replicate multi-instrument measurement results. Further, Dembinski et al. (2017) also provides spectra for heavier nuclei required to validate the heavy nuclei correction factor.

## Heavy Nuclei Correction Factor

While proton-induced Cherenkov showers dominate the observed telescope trigger rate before cuts, heavier nuclei contribute significantly to the total observed telescope trigger rate. However, Cherenkov air shower simulations of heavier nuclei become increasingly computationally expensive with increasing nucleon mass due to the increased kinetic energy and subsequent more extensive Cherenkov air showers. Consequently, only proton simulations are carried out, and a heavy nuclei correction factor  $a_{\text{corr}}$  is applied to the resulting telescope trigger rates to compensate for the missing contribution of heavier nuclei.

Traditionally, a heavy nuclei correction factor of  $a_{\text{corr}} = 1.34$  is used for H.E.S.S. simulations (Bernlöhner, 2022a). Heavy nuclei simulations are carried out to validate this factor, and their contribution to the telescope trigger rate is determined. Due to the time-intensive nature of these simulations, multiple nuclei are grouped based on the natural logarithm of their atomic number  $\ln(A)$ , to which hadronic air shower measurements are susceptible because of increased light yield (Dembinski et al., 2017) (section 2.2). Such a grouping is illustrated in Figure 94. Here, elements are grouped by approximately equal intervals in  $\ln A$ , with the heaviest element in a given group used as the group identifier. The marker size of each element indicates the CR flux contribution within a given element group.

However, the default *run\_hess* interface only offers proton, helium, nitrogen, silicon, and iron nuclei as primary cosmic ray particles. Hence, a new grouping is adapted following the mass ordering example. This grouping is shown in Table 14.

Simulations are carried out for each group  $G$  shown in Table 14 as the primary particle in an energy range from 30 GeV to 100 TeV and the resulting effective aperture of each telescope is calculated. The energy-dependent trigger rates are calculated from these effective apertures, following

$$R^G(E_{\text{bin}}) = A_{\text{eff}}^G(E_{\text{bin}}) \cdot \sum_{Z \in G} \Phi_{\text{CR}}^Z(E_{\text{bin}}), \quad (74)$$

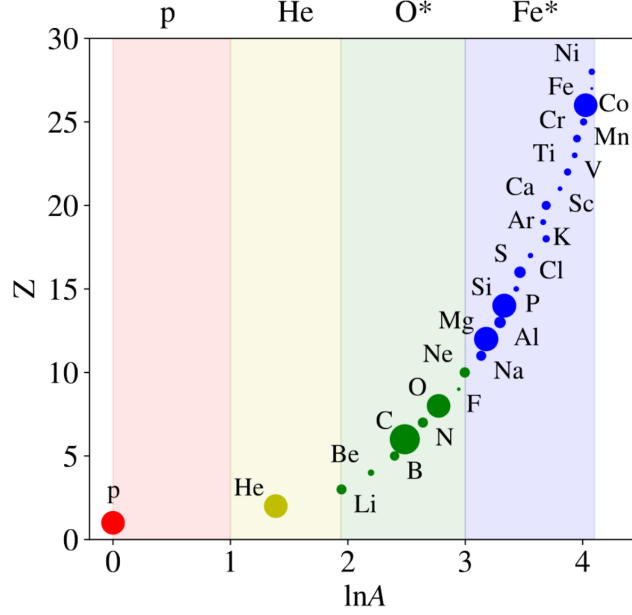


Figure 94: Mass ordering of different elements, with groupings based on the natural logarithm of their atomic mass highlighted in colour. The size of element markers represents the CR flux contribution of each element within a given group represented by the leading element in  $\ln A$  as p, He, O\* and Fe\*. The latter two are starred to indicate the presence of multiple elements in the group. Taken from Dembinski et al. (2017).

Group G	Included atomic numbers
p	$Z = 1$
He	$Z = 2$
N*	$3 \leq Z \leq 9$
Si*	$10 \leq Z \leq 14$
Fe*	$15 \leq Z \leq 29$

Table 14: Element grouping used to determine the heavy nuclei correction factor  $a_{\text{corr}}$ . Element groupings follow the nuclei presets in the default H.E.S.S. simulation configuration script.

with  $\Phi_{\text{CR}}^Z(E_{\text{bin}})$ , the integral flux of the element with atomic number  $Z$  in the energy bin  $E_{\text{bin}}$ . The required heavy nuclei CR spectra are taken from the online cosmic ray explorer tool (Dembinsky, 2022) and are based on the GSF spectra presented in Dembinski et al. (2017). The results for CT5 are shown in Figure 95. The results for CT1-4 are shown in Figure 115 to Figure 118 in Appendix A. The heavy nuclei correction factor is then calculated as the fraction between the total telescope trigger rate over all groups  $G$  and the proton trigger rate  $R^{\text{p}}$  as

$$a_{\text{corr}} = \frac{\sum_G R^G}{R^{\text{p}}}. \quad (75)$$

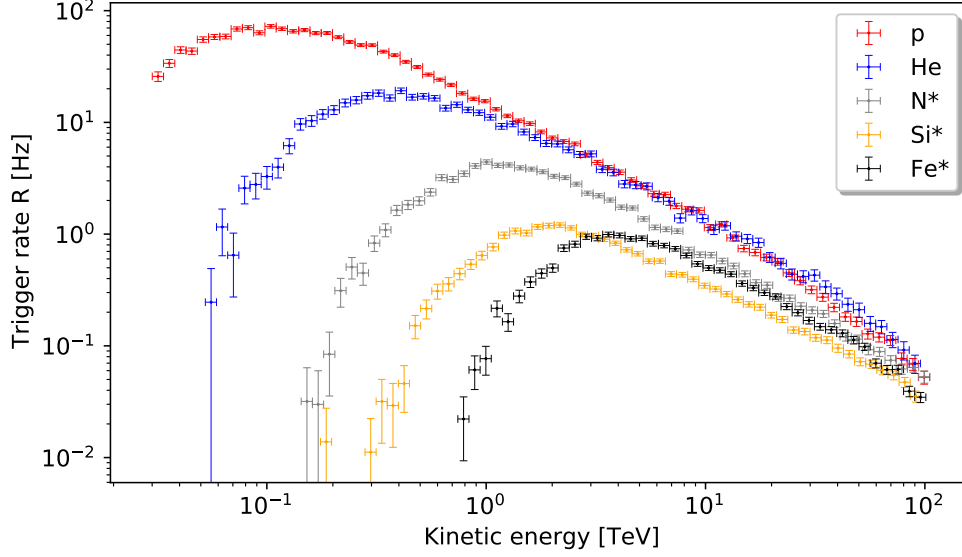


Figure 95: Simulated energy-dependant trigger rate of CT5 for different primary CR nuclei mass groups from 30 GeV to 100 TeV.

Telescope	CT1	CT2	CT3	CT4	CT5
$a_{\text{corr}}$	$1.40 \pm 0.04$	$1.40 \pm 0.04$	$1.40 \pm 0.04$	$1.40 \pm 0.04$	$1.33 \pm 0.03$

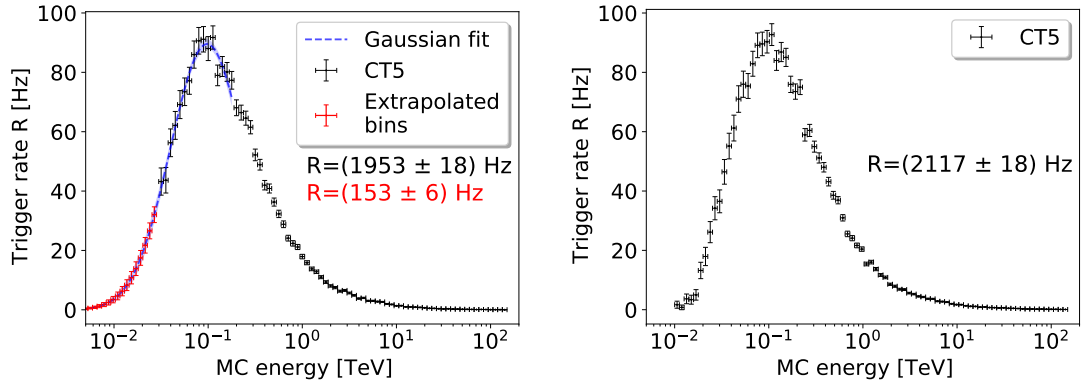
Table 15: Calculated heavy nuclei correction factors for CT1-5 based on heavy nuclei simulations.

This is repeated for all telescopes, and the results are shown in Table 15. The calculated heavy nuclei correction factors for CT1-4 are consistent with the original factor of  $a_{\text{corr}} = 1.34$  within  $1.5\sigma$  with CT5 showing a smaller deviation below  $1\sigma$ . Therefore, the original value is deemed validated and is used in further analysis. The  $1.4\sigma$  difference between the CT1-4 and CT5 result is explained by the larger effective aperture of CT5 at lower energies compared to CT1-4. At these lower energies, the composition of the total CR spectrum is increasingly dominated by protons (see Figure 95), resulting in a smaller required heavy nuclei correction factor.

### Simulated Energy Range

The energy-dependant trigger rates for the default *phase2d3* simulation configuration are calculated following Equation 73. The result for CT5 are shown in Figure 96a together with the total trigger rate of  $R = (1953 \pm 18)$  Hz.

Here, the distribution of trigger rates is cut off at the rising edge for the default simulated energy range with  $E_{\text{low}} = 30 \text{ GeV}$  and  $E_{\text{up}} = 150 \text{ GeV}$  the lower and upper<sup>21</sup> energy bound for the simulated protons respectively. A Gaussian fit is made to the rising edge of the trigger rate distribution, and the missing trigger rate bins are estimated using the same binning as the simulated data. For each new bin position, the Gaussian fit is evaluated, with the  $1 \sigma$  error shown as the error bar. The expected missing trigger rate is calculated as  $R = (153 \pm 6) \text{ Hz}$ , corresponding to  $(7.8 \pm 0.3) \%$  of the total trigger rate.



(a)  $E_{\text{low}} = 30 \text{ GeV}$  with Gaussian fit to the rising edge and estimated missing trigger rate bins.

(b)  $E_{\text{low}} = 10 \text{ GeV}$ .

Figure 96: Simulated energy dependant trigger rate of CT5 for the original *phase2d3 sim.telarray* simulation configuration with varying lower energy bound  $E_{\text{low}} = 30 \text{ GeV}$  (a) and  $E_{\text{low}} = 10 \text{ GeV}$  (b) for the simulated protons. For the default low-energy bound in (a), a Gaussian fit to the rising edge is shown together with the estimated missing trigger rate bins. The total trigger rate  $R$  is shown in black, and the expected missing trigger rate in (a) is shown in red.

The Gaussian fit is used to estimate a new lower energy bound  $E_{\text{low}} = 10 \text{ GeV}$ , below which the estimated trigger rate contribution  $\ll 1 \%$ . The simulation results for CT5 using the new lower energy bound are shown in Figure 96b. Here, the new total trigger rate  $R = (2117 \pm 18) \text{ Hz}$  is consistent with the predicted trigger rate  $R = (2106 \pm 19) \text{ Hz} = (1953 \pm 18) \text{ Hz} + (153 \pm 6) \text{ Hz}$  from Figure 96a. Further, one can identify that the trigger distribution's rising edge's slope is steeper than the Gaussian model predicted, with the trigger rate falling below zero at  $14 \text{ GeV}$ . As this lower energy bound yields a significant contribution to the total trigger rate, it is adapted for all simulations in upcoming sections.

<sup>21</sup>Contribution to total trigger rate above  $50 \text{ TeV}$  is  $< 1 \%$

## Observation Run Selection

The process of calculating the total trigger rate is repeated for multiple zenith angles from 0 deg to 70 deg and different stages of modifications to the original *phase2d3* simulation configuration, as discussed in previous sections. The simulated values are compared to the results of observations within the H.E.S.S. run range of 160051 – 162824 defining *phase2d3*. For a good comparison, only runs during which the atmospheric conditions are similar to those modelled in the simulation are selected. An estimation of the AOD per run is provided by the transparency coefficients (section 2.5.6), which are provided by Holch (2022) for the *phase2d3* run range, while the AOD of the simulation is defined in the atmospheric transmission table (section 4.1.3). An asymmetric AOD interval around the simulated AOD is established, allowing the number of photons detected by the telescope to vary by 5%. This AOD interval is identified using a correction scheme proposed by the MC validation group (Holch et al., 2022), linking atmospheric variations relative to a reference to a change in the number of detected photons.

Further, runs are selected by their zenith angles. To this end, a zenith binning is created with bin centres ranging from 0 deg to 70 deg in 10 deg steps and a bin width of 3.5 deg. The bin width is chosen such that each zenith bin contains at least 50 observation runs while not averaging over a too-large zenith range. Consequently, the useable observation runs are further reduced to  $\approx 500$ . For each zenith bin, the mono trigger rates of contained observation runs are read from the raw trigger file in the H.E.S.S. database. The mean is shown as the trigger rate of a given bin, with the standard deviation as the error.

The resulting zenith dependant trigger rates for the original and new *sim.telarray* configurations, including all presented adjustments and the observation results, are shown in Figure 97. The remaining results for CT2-4 are shown in Figure 119 (Appendix A).

A systematic error of  $\pm 10\%$  is expected for the *sim.telarray* simulation results (Bernlöhr, 2022a) and shown as an error band in Figure 97. This systematic error is later discussed in Figure 4.3.1. The simulated trigger rates produced by the original *phase2d3* configuration show large deviations up to 42% for CT1-4 and 30% for CT5 to the observation runs. A zenith-dependant percentile deviation could not be resolved due to the present trigger rate error for the selected observation runs. On the one hand, a stricter cut on the observational data regarding the AOD similarity to the simulation or zenith angle acceptance within a specific bin would be required, resulting in insufficient statistics per zenith bin. On the other hand, more diverse simulations with different atmospheric transmission profiles could be carried out to allow a looser cut on the observational data. Due to time limitations, such time-intensive simulations are not carried out.

The new simulation configuration, including all modifications introduced in previous sections, reduces the overall deviation to below 5% for all telescopes. In addition, the zenith angle-dependant trigger rates are calculated at different validation stages, with each stage containing all previously changed parameters. Each stage is assigned an identifier, as shown in Table 16.

The mean relative deviation between the simulated and observation trigger rates is



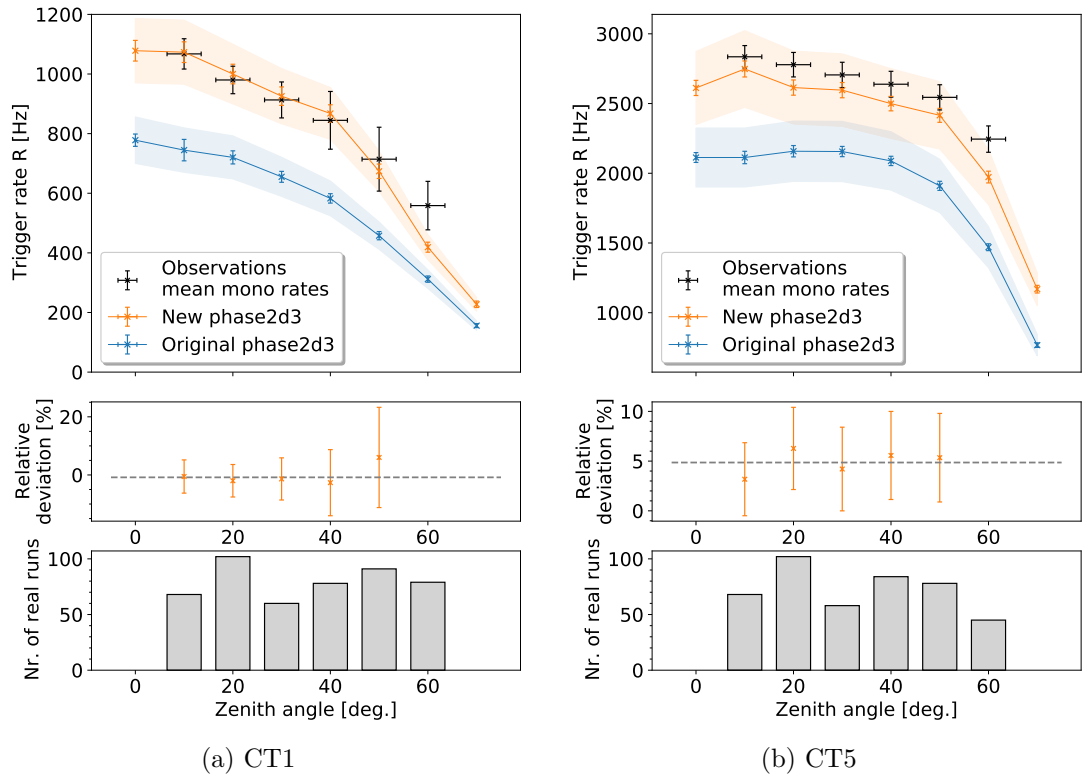


Figure 97: Zenith-dependant trigger rates of CT1 and CT5 for observation and simulated runs, with the relative deviation of the simulation to the observation data and the number of observation runs in each zenith bin. Results for the original *phase2d3* and the new simulation configuration are shown in blue and orange, respectively. The mean relative deviation between 10 deg to 50 deg to the observation runs is highlighted as the grey dashed line. An expected systematic error band of  $\pm 10\%$  is assigned to *sim\_telarray* results (Bernlöhr, 2022a).

Stage identifier	Description
A	Original <i>phase2d3</i> configuration
B	+ adjusted optical PSF
C	+ aerosol level and CT5 trigger threshold
D	+ reflectivity CT5
E	+ realistic NSB rates
F	+ CT1-4 reflectivities and thresholds (new <i>phase2d3</i> )

Table 16: Simulation stage identifier names in Figure 98 with corresponding changes added to the original *phase2d3* simulation configuration. Each stage contains all previously introduced configuration changes.

calculated for each stage. The results for CT1 and CT5 are shown in Figure 98

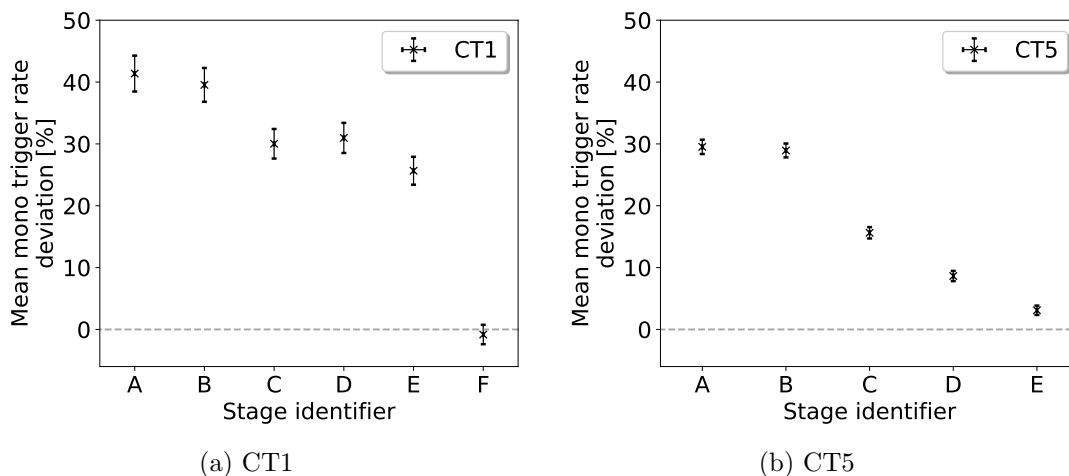


Figure 98: Mean relative deviation between the simulated and observation trigger rates between 10 deg to 50 deg zenith at different validation stages of the original *phase2d3* simulation configuration for CT1 (a) and CT5 (b). The stage identifiers are defined in Table 16. For CT5, only stages up to E are shown, as stage F did not contain changes to the CT5 configuration.

Generally, the adjustment of the optical PSF did not result in a significant change in the trigger rates, likely because the optical PSF was already contained within a single pixel. Thus, further reduction of the optical PSF size does not affect the trigger behaviour of the telescope.

The most significant improvements in the match between simulated and observation data are attributed to the change in the aerosol level and adjustments to the trigger thresholds and the mirror reflectivities. As expected, a reduced trigger threshold significantly increases the number of triggered events due to the spectral shape of the CR proton spectrum. The reduction of the aerosol level and the increase in mirror reflectivities result in a net increase in the number of photons entering the camera for any given Cherenkov shower. Thus, showers that previously were slightly below the trigger threshold of the telescope receive an increase in the flux of photons and, therefore, can trigger the telescope. Hence, an increase in mirror reflectivity or a decrease in aerosol level reduces the effective trigger threshold of the telescope, explaining the observed behaviour.

### 4.3 High-Level Array Validation

#### 4.3.1 Stereo Trigger Rates

During regular operation, the H.E.S.S. Telescopes are operated in hybrid mode, allowing a CT5 mono trigger and a stereo trigger between two H.E.S.S. telescopes, including CT5. This hybrid trigger is replicated in *sim\_telarray* by default and is used for high-level validation.

To validate this hybrid trigger mode, simulations with the new *phase2d3* configuration are created for zenith angles between 0 deg to 70 deg in 10 deg steps with ten runs each, resulting in  $\approx 5 \cdot 10^3$  triggered events per simulated zenith angle.

Following the example in section 4.2.3, the trigger rate of each H.E.S.S. telescope is calculated. Here, a trigger is counted towards a given telescope when it was part of the set of telescopes that triggered on a given Cherenkov shower. The resulting trigger rate is the stereo participation rate of the telescope.

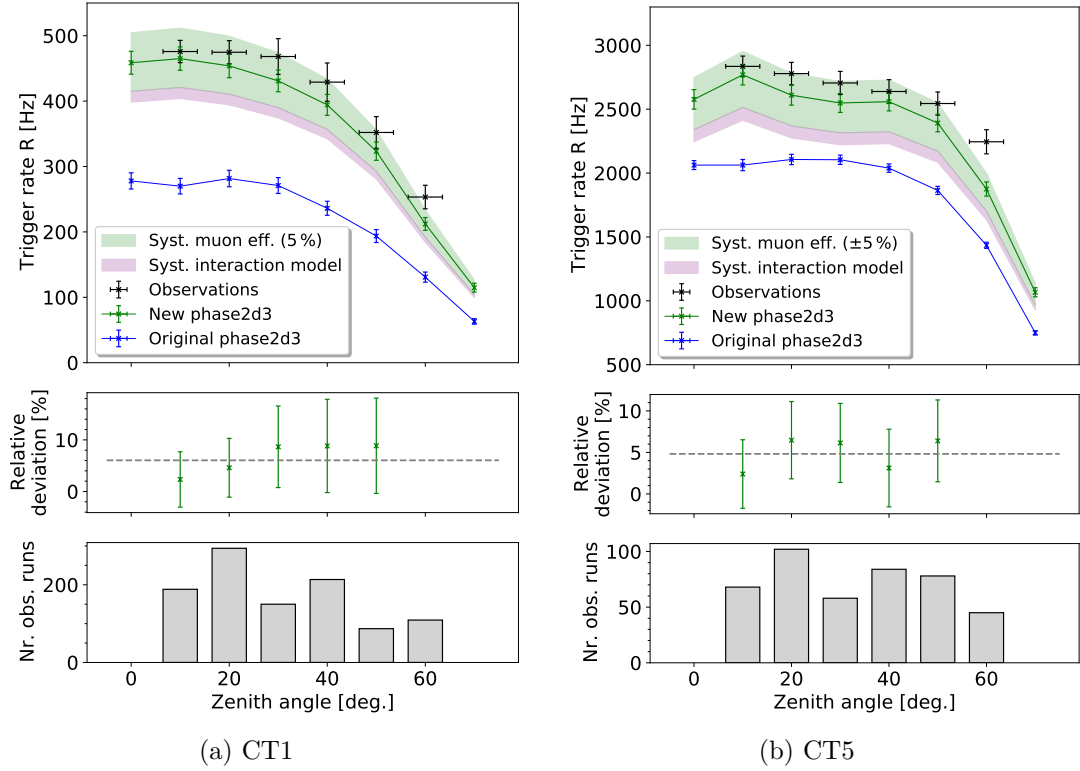


Figure 99: Zenith-dependant stereo participation trigger rates of CT1 and CT5 for observation and simulated runs, with the relative deviation of the simulation to the observation data and the number of observation runs in each zenith bin. Simulations performed with the new *phase2d3 sim.telarray* configuration simulation. The mean relative deviation between 10 deg to 50 deg to the observation runs is highlighted as the grey dashed line. The systematic errors due to the choice of the high-energy interaction model in CORSIKA and a realistic variation in muon efficiency of 5% are shown as error bands in pink and green, respectively.

The observation data selection follows the one introduced for the mono trigger rates in section 4.2.3. The stereo participation rates can be read directly from the H.E.S.S. database without requiring the raw trigger file, resulting in a total number of useable observation runs of  $\approx 1.3$  k. The resulting zenith angle dependant stereo participation rates are shown in Figure 99. The results for CT2-4 are shown in Figure 121 (Appendix A).

The simulated stereo participation rates show good agreement with the observation data within  $\approx 6\%$  and  $\approx 5\%$  for CT1-4 and CT5, respectively. The previously used  $\pm 10\%$  systematic error of *sim.telarray* assumed in Figure 97 is replaced with realistic systematic errors introduced by changes in the muon efficiency, and the choice of the

high-energy interaction model used in the CORSIKA Cherenkov shower simulation.

The muon efficiencies have been calculated in section 4.1.5 based on the mean muon efficiency in the *phase2d3* era. However, the muon efficiencies are subject to short-term variations on the scale of days. This variation is illustrated in Figure 100, showing the percentile deviation between the 48 h mean and long-term muon efficiency in the *phase2d3* era.

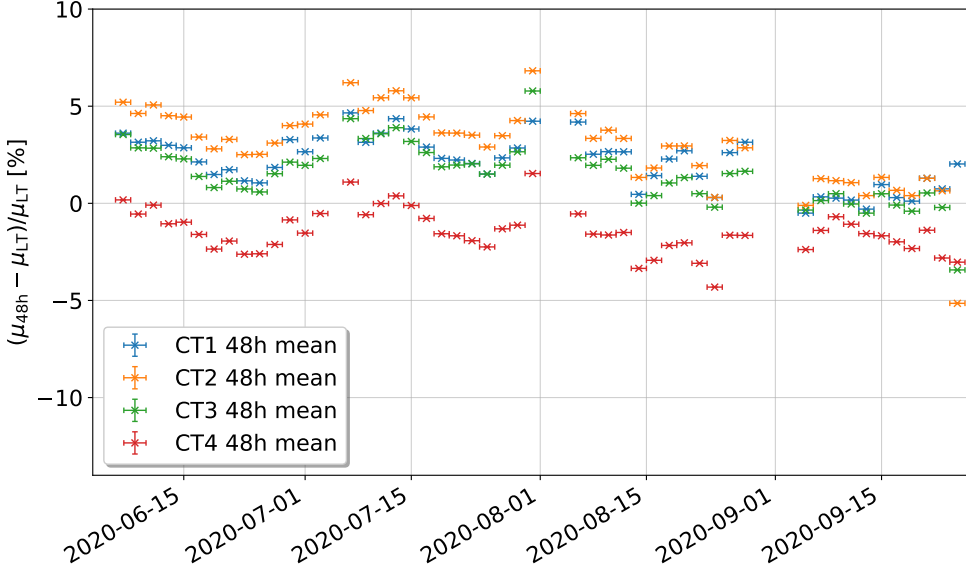


Figure 100: Percentile muon efficiency change of the 48 h mean muon efficiency  $\mu_{48h}$  from the long-term muon efficiency values  $\mu_{LT}$  during the timeframe of *phase2d3*. Values provided by Holch (2022).

From this temporal deviation, it can be concluded that a  $\pm 5\%$  systematic for the chosen muon efficiency and subsequent mirror reflectivity in the *sim\_telarray* simulation configuration represents a realistic systematic. The effect of this systematic on the stereo trigger rates is determined by creating new simulations with a  $\pm 5\%$  change of the mirror reflectivities. From these simulations, the zenith-dependent stereo participation rates are calculated, and the mean deviation to the previous simulations without the reflectivity change is determined as  $\text{sys. eff. }^{+10.1\%}_{-9.5\%}$  for CT1-4 and  $\text{sys. eff. }^{+6.6\%}_{-9.2\%}$  for CT5 shown in Figure 99.

Another systematic is introduced by choice of the high-energy interaction model in CORSIKA. Per default, the QGSJET-II-4 model is used in H.E.S.S. simulations, with EPOS and SYBILL as alternative models (section 2.7.1). New proton simulations are created for the latter two interaction models, and their influence on the stereo participation rates is determined. Here, the QGSJET-II model shows the highest trigger rates, followed by SYBILL and EPOS, with the lowest resulting trigger rates. This observation is in agreement with results presented in Parsons and Schoorlemmer (2019), showing that the photon density for proton-induced Cherenkov showers at an observation height of 1800 m after atmospheric absorption shows the same hierarchy at 100 GeV. Around this energy, the contribution towards the total trigger rate is the

largest (Figure 115). The observed difference between the QGSJET-II-4 model and EPOS is used for the estimation of the systematic error on the stereo participation rates, which is consistent with a telescope-independent shift of  $-4\%$  in the stereo participation rate, shown as a systematic band in Figure 99.

The results for the original *phase2d3* configuration before the validation show a mismatch of up to  $66\%$  for CT1-4 and  $\approx 29\%$  for CT5. The stereo participation rates for the validated simulation configuration show agreement with the observation data, with a remaining mean deviation of  $< 6\%$  for all telescopes. This match is further improved when the systematic fluctuations based on the selected high-energy interaction model and the variations in the muon efficiency are considered.

### 4.3.2 Image Cleaning

The established match between the simulation and observation data must persist after image cleaning. This validation is conducted in Steinmassl (2023) as part of the MC validation effort. The observation runs and proton simulations are subjected to tail cut cleaning, the implementation of which is shown in section 3.5.8. The physical differences between the small H.E.S.S. telescopes CT1-4 and CT5 require different tail cut parameters. A picture threshold of 5 p.e. and boundary threshold of 10 p.e. is used for CT1-4 while CT5 adapts a picture threshold of 9 p.e., a boundary threshold of 16 p.e. as tail cut parameters with a requirement of two next neighbour signal pixels (section 3.5.8) for each signal pixel. Using Hillas parametrization, the Hillas parameter of the cleaned shower images are extracted and filtered using preselection cuts, requiring at least 5 pixels signal pixels and an amplitude of 80 p.e. per image (Steinmassl, 2023). The resulting Hillas length over the image intensity distributions for CT1 and CT5 are shown in Figure 101.

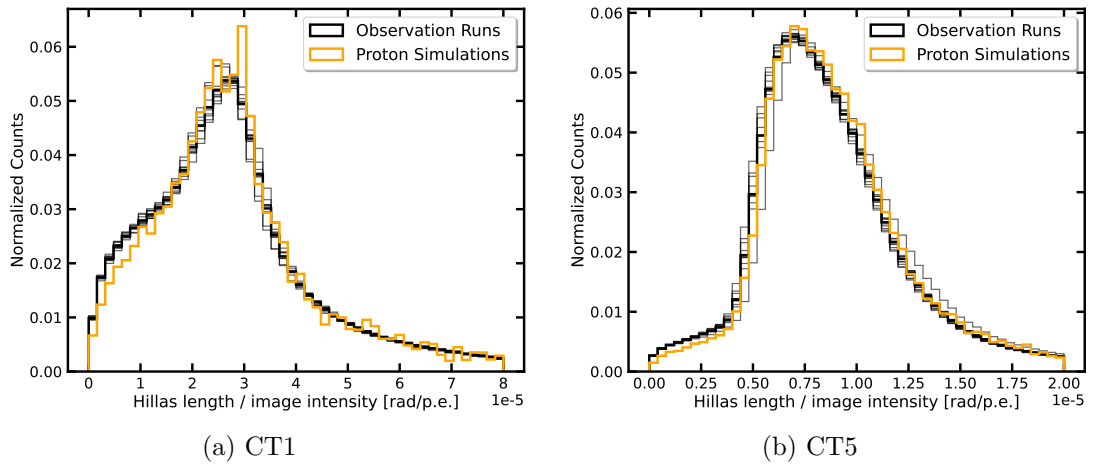


Figure 101: Comparison of the normalized Hillas length over image intensity distribution for CT1 (a) and CT5 (b) between observation runs (black) and proton simulations (orange), after applied image cleaning. The plots are taken from Steinmassl (2023).

The distributions of the proton simulations and the observation runs show a good agreement, concluding that the previously established match between simulation and observation persists after image cleaning and cuts.

## 4.4 Summary and Outlook

The MC validation effort presented in this section investigated sources of discrepancies between the simulated and observed telescope response for all H.E.S.S. telescopes. For this effort, the validation was performed starting from basic MC up to high-level consistency checks.

For the initial basic MC parameter checks, the optical PSF and mirror reflectivity in the *sim.telarray* telescope response simulations were validated. For the optical PSF, an up to 20% mismatch between simulation and observation was identified and subsequently reduced to  $\leq 5\%$  for all H.E.S.S. telescopes. The introduced changes to the optical PSF ( $< 0.13$  mrad) are small compared to the angular pixel size of CT1-4 ( $\approx 3.2$  mrad) and CT5 ( $\approx 1.4$  mrad), resulting in no significant impact on the simulated telescope trigger rates.

An impact on the trigger behaviour of the telescope would only be expected when the optical PSF size changes on the scale of multiple pixel diameters. For camera images with signals close to the telescope's trigger threshold, enlarging the optical PSF in this fashion can significantly increase the light spillover from a given pixel to its next neighbours while also altering the photon density in each pixel of the camera. In this scenario, the exact effect on the telescope's trigger behaviour is a function of the telescope's trigger criteria and the individual camera image.

The atmospheric transmission table, providing height and wavelength dependant attenuation of the atmosphere in the simulation configuration, is compared against measurements from AERONET, taken during the time of *phase2d3*. The comparison between the transmission table values and the observations yields a  $\approx 3\%$  reduction in the number of detected Cherenkov photons for the simulations. The atmospheric transmission table is modified by reducing the aerosol content by 50%. The resulting AOD, predicted by the modified transmission table, matches the mean AERONET AOD measurements during the *phase2d3* area. As expected, the trigger rates of all H.E.S.S. telescopes increased by up to 10% due to the reduced light attenuation in the atmosphere, resulting in an average of 2% increase in the number of arriving photons for any given Cherenkov shower.

The maximum impact distance of 1500 m is validated using proton simulations, and the simulated viewcone for diffuse proton simulations increased from the default of 5 deg to 8 deg, containing at least 99% of all showers that would result in a telescope trigger. This change also results in an up to 8% increase in the simulated telescope trigger rate due to the newly included triggered Cherenkov showers.

To calculate these telescope trigger rates, the GSF proton spectrum is used in conjunction with a heavy nuclei correction factor and the telescope's effective aperture. In addition to the BESS98 spectrum, the GSF proton spectrum is compared to a modelled proton spectrum to estimate the systematic differences in the resulting telescope mono trigger rates.

The resulting trigger rates for the GSF and modelled spectrum are consistent within  $1\sigma$ , while the BESS98 spectrum results in a  $(15.7 \pm 0.8)\%$  and  $(8.6 \pm 1.4)\%$  increase in the mono trigger rates of CT1-4 and CT5, respectively. The choice of the GSF

cosmic proton spectrum for the presented analysis is valid, since a different approach to model multi-instrument measurements of the cosmic ray proton flux resulted in matching trigger rates for all telescopes.

Besides the selected cosmic proton spectrum, a multiplicative heavy nuclei correction factor of  $(1.4 \pm 0.04)$  for CT1-4 and  $(1.33 \pm 0.03)$  is determined based on heavy nuclei simulations. These factors are consistent within  $1.5\sigma$  with the standard value of 1.34 currently used in H.E.S.S. simulations. Therefore, the established factor of 1.34 is further used.

New NSB rates of 134.22 MHz and 316.01 MHz are set for CT1-4 and CT5, respectively, establishing a match between the simulated pedestal-width and the one stored in the H.E.S.S. database within 2.4 % for CT1-4 and  $< 1\%$  for CT5. These new NSB rates represent an increase of 60 % for CT1-4 and 44 % for CT5 compared to the original values, resulting in a telescope-specific increase in the mono trigger rates up to 6 %.

The telescope mono trigger rate is determined for CT1-5 at different zenith angles from 0 deg to 70 deg, and the deviation to the observed mono trigger rates is calculated. For the original *phase2d3* configuration, deviations of up to 42 % and 30 % are identified for CT1-4 and CT5, respectively. The new *phase2d3* configuration, adapting all introduced changes to the simulation configuration, results in a match within 5 % between the observed and simulated mono trigger rates. The remaining deviation can be attributed to the systematic errors introduced by slight variations in the telescope’s muon efficiency.

During the time of *phase2d3*, the muon efficiency varied by up to  $\pm 5\%$  compared to the mean muon efficiency determined during this period. The resulting systematic effect on the stereo participation trigger rates was determined to be of the order of 10 %, with the effect on the mono trigger rates being on the same order of magnitude. The stereo participation rates, in turn, match the observation data within 6 %, improving upon the previous deviation by up to 65 % for CT1-4 and 25 % for CT5. The established match persists even on the Hillas parameter level after the traditional H.E.S.S. image cleaning.

Using this new validated simulation configuration, Steinmassl (2023) presents a new Crab spectrum shown in Figure 102. The significance of the presented MC validation is seen in the flux normalization (at 1 TeV). Using CT5 mono with the newly validated simulation configuration the normalization is  $(3.85 \pm 0.05) \cdot 10^{-11} \text{TeV}^{-1} \text{cm}^{-2} \text{s}^{-1}$  compared to the initial result of  $(5.04 \pm 0.08) \cdot 10^{-11} \text{TeV}^{-1} \text{cm}^{-2} \text{s}^{-1}$ . Compared to the older H.E.S.S. results presented in Aharonian et al. (2006), this is a large improvement<sup>22</sup> of  $1.7\sigma$  ( $\approx 34\%$ ). The remaining 12 % deviation is entirely within the 20 % systematic for the H.E.S.S. Crab flux normalization at 1 TeV, where before the deviation could not be explained with the systematic error.

Further, the reconstructed Crab flux of CT5 mono is now consistent with the one using CT1-4 stereo for the first time since FlashCam was installed. The presented simulation configuration with all introduced modifications has been adapted by the

---

<sup>22</sup>With respect to the 20 % H.E.S.S. systematic for the Crab normalization at 1 TeV.

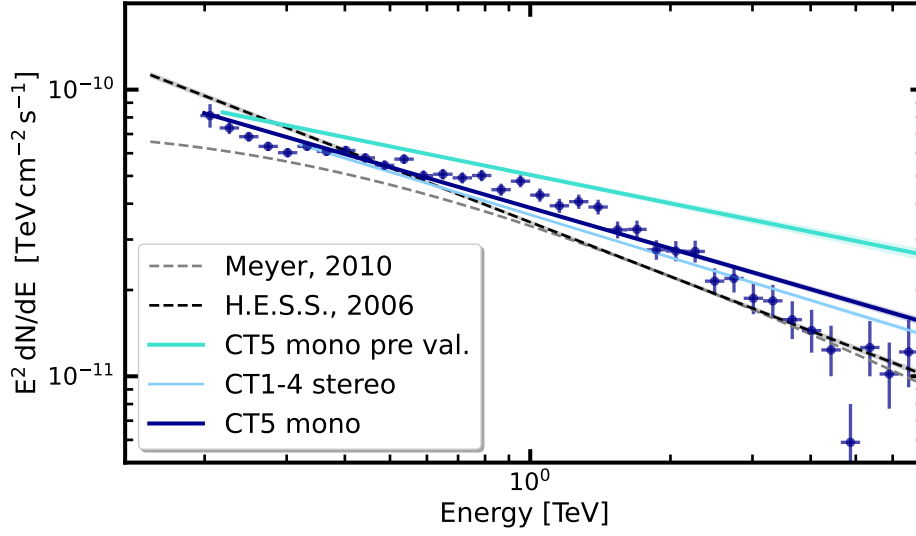


Figure 102: Reconstructed Crab flux for CT5 mono and CT1-4 stereo using the final validated simulation configuration presented in this work together with the CT5 mono results before the validation (pre val.), previous H.E.S.S. results (Aharonian et al., 2006) and the spectrum presented by Meyer et al. (2010). The figure is taken from Steinmassl (2023).

H.E.S.S. collaboration and is used for the next production of H.E.S.S. simulations. Further, the correction scheme presented in Holch et al. (2022), which was developed as a derivative of the MC validation effort, is currently under review as a candidate to be for implementation in the main software analysis chain (HAP) and can easily be applied to different types of IACTs.



## 5 3D Analysis of the Crab Using the ABRIR Method

### 5.1 The Crab Nebula

The Crab nebula is a SNR formed after a supernova explosion in 1054 at a distance of  $\approx 2$  kpc (Hester, 2008). As a product of this supernova, a central pulsar was formed that powers a Pulsar Wind Nebula (PWN) contained within the expanding SNR. In VHE astronomy, this PWN is commonly called the Crab nebula instead of the surrounding SNR. The structure of the Crab nebula can be resolved in X-rays and is shown in Figure 103.

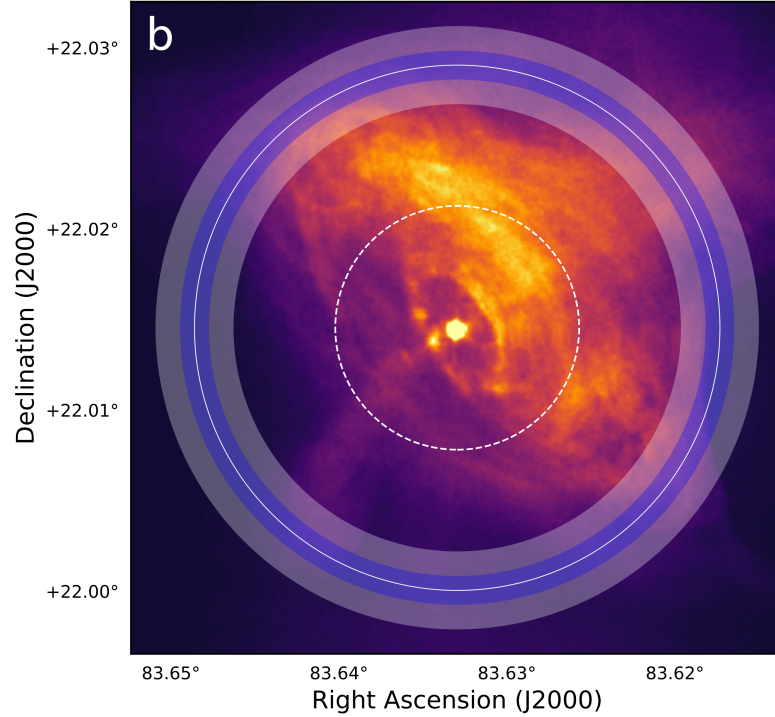


Figure 103: Chandra X-ray image of the Crab nebula with the H.E.S.S. extension shown with a solid white line. The colour bands highlight the statistical and systematic uncertainties. The dashed white line highlights the Chandra extension in X-Rays. The image is taken from H.E.S.S Collaboration et al. (2019).

The Crab pulsar (located in the centre of Figure 103) is a rotating neutron star with a rotational period of 33 ms. The strong magnetic field of  $\sim 10^{12}$  G (Jones, 1975) results in electric fields that pull ions from the surface of the pulsar. These ions travel along the magnetic field lines and emit synchrotron radiation, which initiates electromagnetic cascades, increasing the number of leptons (primarily electrons and positrons) by a factor of  $\sim 10^5$  to  $\sim 10^7$  (Amato and Olmi, 2021). This process forms the central X-ray emission seen in Figure 103. The outflow of leptons encounters the termination shock at a distance of  $\approx 0.1$  pc (Kennel and Coroniti, 1984), seen in Figure 103 as a ring-like structure close to the central pulsar. The leptons are accelerated in the termination shock and initially confined in the pulsar's dipole-like magnetic field, forming a torus structure. Within this pulsar wind, the electrons are subjected to a local magnetic

field ( $\sim 120 \mu\text{G}$  (Meyer et al., 2010)) and emit synchrotron radiation in the MeV range with ambient photons being upscattered towards TeV energies by the inverse-Compton process. The leptons are able to escape into the surrounding medium along open magnetic field lines. This process is also involved in forming the two jets.

The pulsar wind and its emission extend multiple parsecs and produce an extended source of VHE gamma rays. This emission was first detected by the Whipple telescope (Weekes et al., 1989) and has been established as the brightest known source of VHE gamma rays. Subsequently, the Crab nebula is one of the most observed and well-studied objects in the VHE gamma-ray sky. The spectral flux has been studied by space and ground-based experiments such as Fermi-LAT, MAGIC, and H.E.S.S.. An example spectrum based on Fermi-LAT and MAGIC data in the GeV to TeV energy range is shown in Figure 104.

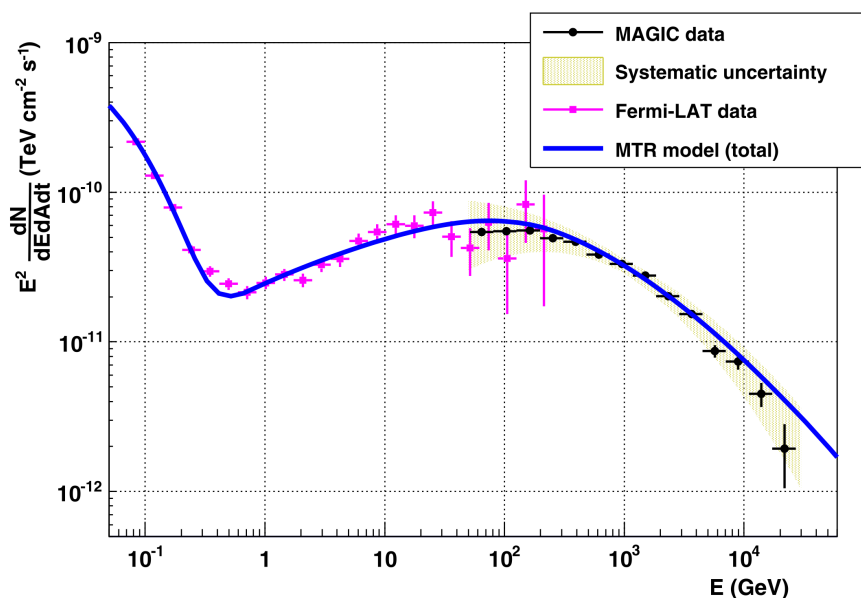


Figure 104: VHE gamma-ray spectrum of the Crab nebula with Fermi-LAT and MAGIC flux points (with systematic uncertainty band). The best fit based on the MRT model presented in Meyer et al. (2010) is shown in blue. The figure is taken from Aleksic et al. (2015).

H.E.S.S. has measured the extension of the Crab in the VHE range to be  $52.2'' \pm 2.9''_{\text{stat}} \pm 6.6''_{\text{sys}}$  (H.E.S.S. Collaboration et al., 2019). This extension is shown in Figure 103 overlaid on a Chandra X-Ray image.

## 5.2 The ABRIR Method

The significant hadronic background present in data acquired from Cherenkov telescopes must be reduced to enable the analysis of observations of gamma-ray sources. The rate of this hadronic background is  $\sim 10^4$  larger than the expected gamma rates (Olivera-Nieto et al., 2022). In the case of H.E.S.S., this gamma-hadron separation is performed using a Boosted Decision Tree (BDT) machine learning approach (Ohm et al., 2009). Initially, the Cherenkov camera images are tail cut cleaned (Figure 4.3.2), and the

higher moments of the camera images are extracted using the Hillas technique (Hillas, 1985) After applying preselection cuts on the image size and squared angular distance  $\theta^2$ , derivatives of the extracted Hillas parameters are used as the BDT input to classify events as gamma or hadron-like. The BDT training is done on simulated telescope data and considers information from all available telescopes. The output of the BDT is the hadron-likeness  $\zeta$  of a given event, describing how close the event resembles a hadronic event. A significant amount of hadronic background can be excluded from the data by introducing a cut ( $\sim 80\%$ ) on the percentage of retained gamma events (gamma-efficiency).

Despite the applied gamma-hadron separation, the data is not entirely free of hadronic background events, and misclassifications occur. The remaining hadronic events can be reduced further by different approaches. Along the electromagnetic component, hadron-induced Cherenkov showers produce charged pions that decay into muons. These, in turn, result in a characteristic full or partial ring-like structure in the camera images of Cherenkov telescopes (section 2.2). As shown in Olivera-Nieto et al. (2021), using muons alone to identify hadronic showers can enable total background rejection powers up to  $10^5$  for large-mirror-diameter telescopes<sup>23</sup>, and energies above 10 TeV. This background rejection power can only be reached if the muon signal can be perfectly identified in Cherenkov camera images. This identification, however, proves to be difficult for partially contained muon rings that approach the shape of a gamma-like shower (section 2.5.5).

The Algorithm for Background Rejection using Image Residuals (ABRIR), presented in Olivera-Nieto et al. (2022), builds on the existing H.E.S.S. preselection and BDT gamma-hadron separation cuts. It introduces a simplified approach to identifying pixel clusters beside the primary shower in the Cherenkov camera images of the central large-mirror-diameter H.E.S.S. telescope. The ABRIR method is summarised here.

The framework of the ABRIR method uses the output of the Image Pixel-wise fit for Atmospheric Cherenkov Telescopes (ImPACT) algorithm presented in Parsons and Hinton (2014) to identify hadronic shower components in the central large H.E.S.S. telescope. ImPACT is a template-based approach to shower parameter reconstruction based on Cherenkov camera images. Image templates characterise the average camera image for a set of shower parameters (shower direction, impact point,  $X_{\max}$ , and energy) and are created using CORSIKA and *sim\_telarray* simulations for the H.E.S.S. telescopes. These templates are fitted to all tail cut cleaned camera images to determine the most likely shower parameters.

---

<sup>23</sup>Ground-based telescopes with mirror diameters  $\gtrsim 15$  m.

This method has shown superior performance for the angular and energy resolution compared to the traditional Hillas reconstruction approach (Parsons and Hinton, 2014).

The workflow of ABRIR is illustrated in Figure 105. For each event, data of CT1-4 is used to determine the most likely shower parameters following the method described in Parsons and Hinton (2014). These parameters are then used as input to the CT5 ImPACT templates to determine the most likely CT5 camera image. As the templates are created for gamma-like events, they do not include additional pixel clusters attributed to side showers or muon events in hadronic showers. The template masks the primary shower in the observed CT5 camera image, and residual pixel clusters  $N$  are identified. The event is rejected and identified as hadronic background if the two conditions, C1 and C2, are fulfilled. Condition C1 is designed to identify pixel clusters far from the template-predicted primary shower position inside the camera. Condition C2 is designed to identify random fluctuations due to remaining NSB pixel noise.

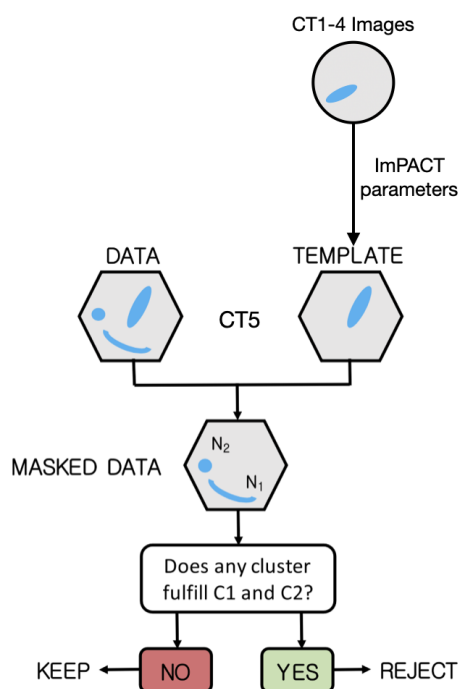


Figure 105: Workflow chart for the ABRIR method as implemented for the H.E.S.S. array.  $N_1$  and  $N_2$  are the identifiers for residual camera image clusters after subtraction of the template. C1 and C2 represent the two rejection criteria explained in the text. The illustration adapted from Olivera-Nieto et al. (2022).

The background rejection power and gamma-ray efficiency of the ABRIR method are investigated in Olivera-Nieto et al. (2022) using a traditional 1D spectral analysis, and results are shown in Figure 106. As seen in Figure 106a, the ABRIR method yields a background reduction of up to  $\approx 50\%$ . Whilst the simplified approach of the ABRIR reduces the hadronic background, it also removes a significant portion of the gamma-like events. As seen in Figure 106b, the gamma-ray efficiency is reduced by  $\approx 10\%$ . This can be caused by unusually high NSB rates, resulting in bright pixel clusters or high-energy

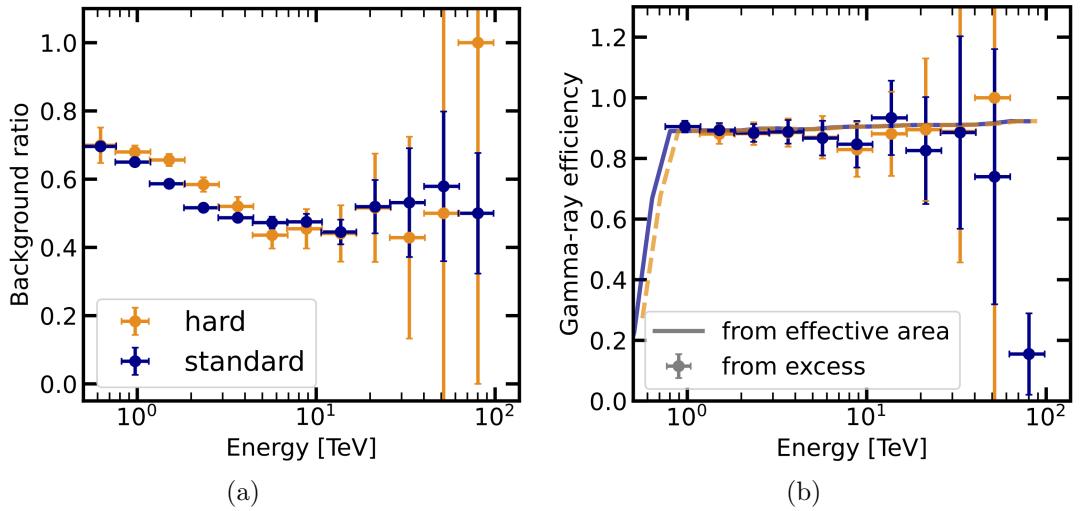


Figure 106: Background ratio between ABRIR and nonABRIR (a) and gamma-ray efficiency of ABRIR compared to the nonABRIR case (b). Both are shown for standard (blue) and hard (orange) preselection cuts. The gamma-ray efficiency is derived from the effective area and from the excess. The figures are taken from Olivera-Nieto et al. (2022).

gamma events containing muon light (Olivera-Nieto et al., 2022).

### 5.3 3D Crab Analysis With *gammapy*

As mentioned, the ABRIR method has proven capable of extending the current background rejection power of the BDT approach used for H.E.S.S. data. This chapter tests this new method on H.E.S.S. data of the Crab nebula and compares the resulting background rejection performance to the existing BDT-only approach in the context of a 3D-spectral-morphological analysis. An improved background rejection power could yield an increased detection significance for the highest energies in the observed Crab spectrum.

The presented analysis is performed with the *gammapy* (v0.19) python package, first presented in Deil et al. (2017). It is built on the widely used and tested *NumPy* (Harris et al., 2020), *Astropy* (Astropy Collaboration et al., 2022), and *SciPy* (Virtanen et al., 2020) python packages and enables high-level analysis of IACT data. It allows for the spectral and spatial modelling of observed gamma-ray sources with a wide array of provided models.

Traditionally, the spectral and morphological analysis of gamma-ray sources is done separately. Whilst this approach yields good results for point-like sources, it can result in incorrect spectral models for extended and overlapping sources. As the morphology of the sources is not considered in this case, the resulting model spectra are not easily recoverable. As shown in H.E.S.S. Collaboration et al. (2019), the Crab nebula is an extended source ( $\approx 52$  arcsec) at TeV energies and can be resolved by the H.E.S.S. array. In addition to this 1D spectral analysis, *gammapy* allows for a joint 3D Likelihood spectral-morphological analysis with a one-dimensional spectral and 2-dimensional

spatial model. This way, the spatial structure of the gamma-ray sources is considered when fitting the spectral model. This *gammapy* 3D spectral-morphological analysis approach has been validated for H.E.S.S. data in Mohrmann et al. (2019) and is used in this analysis.

### 5.3.1 Run Selection

In its current state, ABRIR is designed for the large central H.E.S.S. telescope CT5 using FlashCam. Therefore, available observation runs are initially restricted to after the time FlashCam was installed in 2019. An initial observation runlist in this H.E.S.S. era is created for array pointings within a 2 deg region around the Crab position (RA 83.633 deg, DEC 22.014 deg (H.E.S.S. Collaboration et al., 2019)) resulting in 170 runs ( $\approx 65$  h) of data.

Observation runs are further down selected by established standard criteria that impose quality cuts on the number of participating telescopes and environmental parameters. These quality cuts were outlined in Aharonian et al. (2006) but have undergone adjustments due to the new telescope hardware. The different quality cuts are outlined below.

#### Telescope Participation

As implemented, the ABRIR method relies on data from all of CT1-5 to function. Therefore, all telescopes are required to participate in a given run. The required telescope participation is therefore set to five.

#### Telescope Trigger Rate

As shown in section 4.1.3 and section 4.2.3, atmospheric conditions significantly impact the telescope trigger rates. The observation runs are selected for a maximal trigger rate deviation of 5% relative to the mean telescope trigger rate and a maximal timestamp-to-timestamp trigger rate variation of 30 Hz.

#### Broken Pixels

To protect the cameras PMTs, their high voltage is turned off in the event of a bright star or a satellite trail crossing the pixel (Aharonian et al., 2006). Further, pixels are identified as broken when no signal is received. The maximum number of turned-off pixels is set to 50, and the number of broken pixels must be less than 96 for each telescope.

#### Telescope Tracking

The RMS of the telescope tracking must be within 5 arcsec for altitude and azimuth and within 0.01 deg for RA and DEC.

#### Transparency Coefficient

To remove runs taken during bad atmospheric conditions, the derived transparency coefficient (section 2.5.5) must lie between 0.8 and 1.2, corresponding to acceptable weather conditions.

After these quality cuts, the available dataset is reduced to 89 observation runs with  $\approx 41$  h of data<sup>24</sup>. The list of used observation runs is shown in Table 21 (Appendix B).

### 5.3.2 3D Analysis

The event reconstruction is performed using ImPACT with event selection cuts shown in Table 17. In addition to the reconstructed events, the 3D analysis requires a 3D

Amplitude [p.e.]	$\theta^2$ [deg <sup>2</sup> ]	$\zeta_{BDT}$	Local distance [m]
200	0.36	0.80	0.525

Table 17: Event selection cuts for the presented analysis using ImPACT event reconstruction. Values taken from Olivera-Nieto, 2022.

background model. To compare the ABRIR method to the existing BDT-only approach, two background models were derived by Olivera-Nieto (2022). One background model using the standard BDT-only approach, and a second model using the ABRIR method for increased background rejection. This difference in the analysis is referred to as the background case using either nonABRIR or ABRIR as the identifier.

The spatial sky-target region around the Crab is combined with the reconstructed and true energy axis to form the target geometry. This target geometry contains the following parameters:

- Target region (centered around the Crab):  $5 \text{ deg} \times 5 \text{ deg}$ .
- Spatial bin size:  $0.02 \text{ deg}$ .
- Reconstructed energy axis:  $1 \text{ TeV}$  to  $100 \text{ TeV}$  ( $10 \text{ bins/decade}$ ).
- True energy axis:  $0.5 \text{ TeV}$  to  $120 \text{ TeV}$  ( $49 \text{ bins/decade}$ ).

Following the example of Mohrmann et al. (2019), the background model is fitted to each observation run individually using the Likelihood method to reduce the effect of incorrect background map normalization. The resulting data is combined into a stacked dataset. For the spectral-morphological fit, a spatial and spectral model must be defined. As the Crab is an extended source, a 2D Gaussian model is used (*GaussianSpatialModel*). For the spectral component, both a Power Law with Exponential Cutoff (ECPL) (see Equation 76) and Logarithmic Parabola (LogPar) (see Equation 77) are considered.

$$\phi(E)_{\text{ECPL}} = \phi_0 \cdot \left(\frac{E}{E_0}\right)^{-\alpha} \exp(-(\lambda E)^\alpha) \quad (76)$$

$$\phi(E)_{\text{LogPar}} = \phi_0 \cdot \left(\frac{E}{E_0}\right)^{-\alpha - \beta \log\left(\frac{E}{E_0}\right)} \quad (77)$$

With  $\lambda = 1/E_{\text{cut}}$  the inverse of the cutoff energy, and  $\beta$  the curvature for Equation 77. For both spectral models  $\alpha$  is the spectral index,  $\phi_0$  the spectral norm, and  $E_0 = 1 \text{ TeV}$  the fixed reference energy.

<sup>24</sup>The Crab analysis presented in Aharonian et al. (2006) used 22 h of data but with tighter quality selection criteria

Each spectral-morphological model is fit to the reconstructed data by the 3D Likelihood maximization method. The preferred spectral model is determined based on the total Test Statistic (TS) difference of a chosen spectral model referred to as  $\Delta$ TS-value. In this case, the  $\Delta$ TS is an interpretable value that compares the hypothesis that the spectral model describes the data to the alternative hypothesis without a model. By definition, models resulting in a larger total  $\Delta$ TS-value are preferred. The total TS-values for both spectral models and two background cases are shown in Table 18.

Spectral model	ABRIR		nonABRIR	
	LogPar	ECPL	LogPar	ECPL
Total $\Delta$ TS-value	35640.18	35636.87	32920.05	32917.35
Total significance ( $\sqrt{TS}$ ) [ $\sigma$ ]	188.79	188.78	181.44	181.43

Table 18: Total TS-value and significance for the LogPar and ECPL spectral model in the ABRIR and nonABRIR case as produced by the 3D Likelihood fit.

In both background cases, the LogPar spectral model is slightly preferred and will be used in the analysis. The fit parameters for the spectral and spatial model are provided in Table 19.

Parameter	Value	
	nonABRIR	ABRIR
$\phi_0$	$(3.93 \pm 0.20) \text{ cm}^{-2} \text{ s}^{-1} \text{ TeV}^{-1}$	$(3.76 \pm 0.21) \text{ cm}^{-2} \text{ s}^{-1} \text{ TeV}^{-1}$
$E_0$	1 TeV	1 TeV
$\alpha$	$2.41 \pm 0.08$	$2.40 \pm 0.09$
$\beta$	$0.145 \pm 0.027$	$0.16 \pm 0.03$
Longitude	$(83.633 \pm 0.001) \text{ deg}$	$(83.633 \pm 0.001) \text{ deg}$
Latitude	$(22.024 \pm 0.001) \text{ deg}$	$(22.024 \pm 0.001) \text{ deg}$
Gaussian $\sigma$	$(0.011 \pm 0.001) \text{ deg}$	$(0.011 \pm 0.001) \text{ deg}$

Table 19: Fit results for the spectral and spatial model in the ABRIR and nonABRIR background cases.

The spectral and spatial fit results of the ABRIR and nonABRIR background cases agree within their respective  $1 \sigma$  statistical error interval and are consistent. In both background cases, the determined position of the Crab is consistent with previous results within the chosen spatial bin size (H.E.S.S Collaboration et al., 2019).

The significance for every 3D bin is calculated considering the fitted background and spectro-morphological Crab model following Li and Ma (1983). For a good background fit, the significance distribution of this excess is expected to resemble a Gaussian distribution of the form

$$A \cdot e^{-(x-\mu)^2/2\sigma^2}, \quad (78)$$

with amplitude  $A$ , position  $\mu = 0$  and standard deviation  $\sigma = 1$  (Mohrmann et al., 2019). The significance distribution of the excess for both background models is shown in Figure 107 together with the best fit of Equation 78 and the ideal distribution.



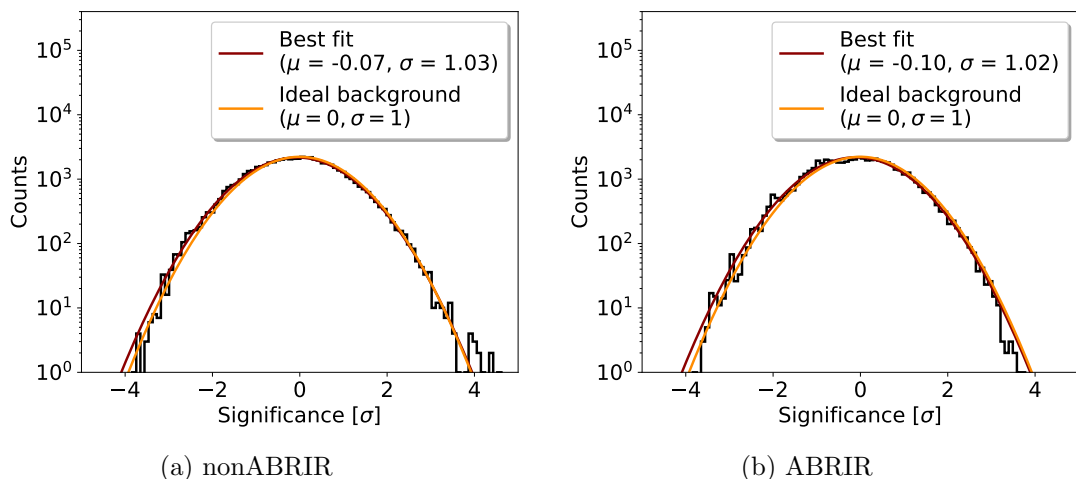


Figure 107: The target region’s significance distribution of the excess around the Crab for the nonABRIR (a) and ABRIR (b) background model. The fitted spectral and spatial source model has been taken into account. The best Gaussian fit and the ideal distribution are shown.

The background fit and model are accurate as both the ABRIR and nonABRIR excess significance distribution resemble the expected ideal distribution. The background count ratio between the two background scenarios is calculated to validate that the ABRIR method works as expected. This is done by determining the number of counts per energy bin outside a 0.5 deg circular region around the Crab position. Considering the  $\sim 0.01$  deg extension of the Crab, only background counts are expected outside this region. The result can be seen in Figure 108. The gamma-ray efficiency is calculated from the exposure and excess ratios between the two background scenarios separately and shown in Figure 108b.

The energy range in the background ratio reference data taken from Olivera-Nieto et al. (2022) is extended towards lower energies compared to the presented analysis. Nonetheless, the calculated background ratio (see Figure 108a) replicates the behaviour shown in Olivera-Nieto et al. (2022) within the statistical errors. The calculated gamma-ray efficiency (see Figure 108b) is consistent with the expected 90 % gamma-ray efficiency. It is concluded that the ABRIR method works as intended.

Spectral flux points are calculated for the specified reconstructed energy axis with upper limits calculated for the 95 % ( $2\sigma$ ) confidence level. As a reference, flux points from the Fermi-LAT satellite experiment are shown at lower energies. The result and the best fit LogPar spectral model are shown in Figure 109. Both spectral models connect with the Fermi-LAT flux points at lower energies with residuals below  $1\sigma$  for the presented energy range. Comparing both background cases, two significant flux points<sup>25</sup> are lost in the ABRIR background case. This is quantified in Table 20, listing the starting energy of each flux point energy bin with the corresponding TS-value and number of counts inside the bin.

<sup>25</sup>Flux points are significant when they show a confidence level of at least 95 % ( $2\sigma$ ), corresponding to a TS-value of four.

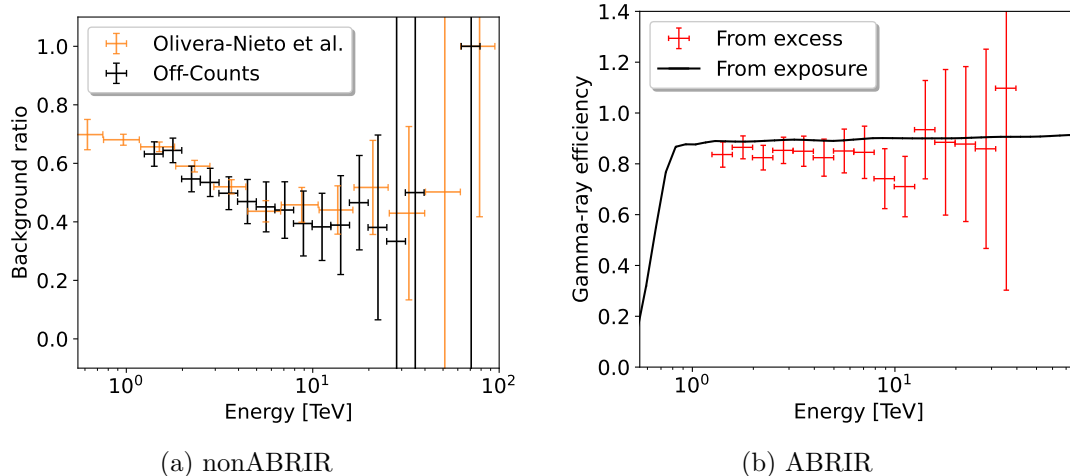


Figure 108: Background ratio between ABRIR and nonABRIR (a) and gamma-ray efficiency of ABRIR compared to the nonABRIR case (b). Results from Olivera-Nieto et al. (2022) are shown for the background ratio. The gamma-ray efficiency is derived from the exposure and the excess separately.

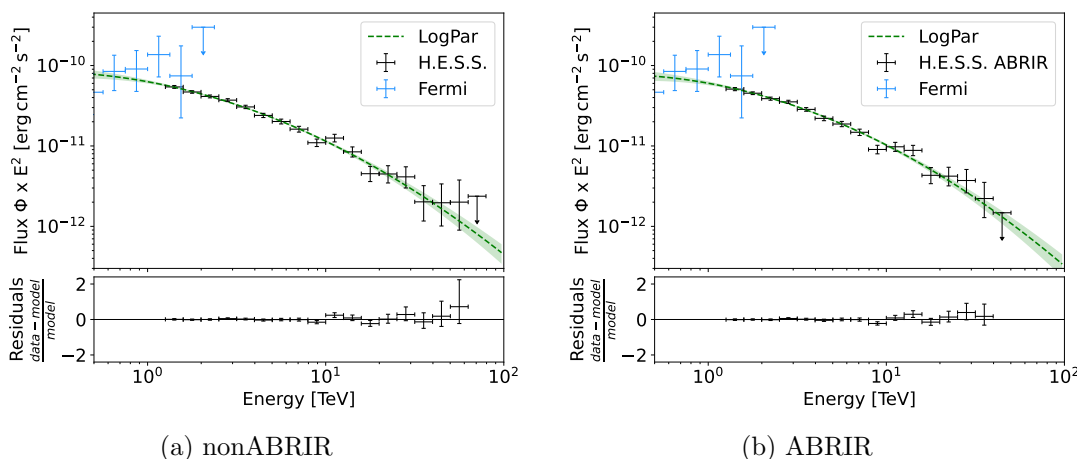


Figure 109: Best fit LogPar spectral model of the Crab with calculated flux points. Flux points of the Fermi-LAT experiment are provided by Unbehaun et al. (2023) and shown as a reference.

$E_{\min}$ [TeV]	nonABRIR		ABRIR	
	TS-value	Counts	TS-value	Counts
1.26	5216.64	1960	4679.63	1354
1.58	7057.81	2255	6551.23	1615
1.99	5543.69	1773	5093.41	1139
2.51	5236.80	1575	4907.95	1022
3.16	4127.27	1156	3832.02	722
3.98	2543.88	685	2308.62	422
5.01	1999.48	514	1864.78	314
6.31	1421.99	370	1286.88	219
7.94	768.40	239	634.66	126
10.00	745.32	218	571.60	110
12.59	430.08	122	481.33	75
15.85	195.15	81	205.81	46
19.95	156.28	38	159.47	22
25.12	122.33	17	138.33	11
31.62	38.41	10	113.98	7
39.81	23.64	5	0.00	0
50.12	26.14	4	0.00	0
63.10	0.27	1	0.00	0
79.43	0.08	0	0.00	0

Table 20: Starting energy of the calculated flux point bins with corresponding TS-value and number of counts in the bin for the nonABRIR and ABRIR background case.

Contrary to the initial expectation, the significance of the flux points below 10 TeV is reduced compared to the nonABRIR analysis. Whilst the significance is increased for energies above 10 TeV, two significant spectral flux bins are lost. The last significant energy bin in the nonABRIR case is 50.12 TeV and 31.62 TeV for the ABRIR case. As mentioned in section 5.2, ABRIR also rejects a significant fraction of gamma-like signal events. As seen in Table 20, the energy bins above 32 TeV contain less than six events. These events are an admixture of gamma (signal) and background events. Due to insufficient statistics, the exact background ratio between both background cases at these energies shows a large spread (see Figure 108a). Together with the expected gamma-efficiency of 90 %, all remaining events may be rejected by the ABRIR method. This, in turn, indicates that the current version of ABRIR may not be suited for analyses relying on flux bins with low statistics.

## 5.4 Summary and Outlook

This section presents a 3D spectral-morphological analysis in *gammapy* of the Crab nebula with and without the ABRIR method for enhanced background rejection. The analysis is performed on 89 observation runs that pass quality selection cuts based on the telescope participation, trigger rate, broken pixels, telescope tracking and atmospheric conditions. The background models with and without ABRIR are provided by Olivera-Nieto (2022). The analysis for the ABRIR and nonABRIR scenario is performed identically. The spatial component of the Crab is fitted with a 2D Gaussian, and the spectral component with a ECPL and LogPar. The latter spectral model is preferred based on the total  $\Delta TS$ -value and used in further analysis. In both cases, the excess distributions after the background fit are compatible with a normal distribution, indicating a good fit. The background ratio between the ABRIR and nonABRIR case is calculated based on the number of events outside a 0.5 deg radial region around the Crab position and shows agreement with previously published results for ABRIR. The gamma-ray efficiency is calculated with two methods: from the excess and the exposure. Both approaches replicate the expected  $\approx 90\%$  gamma-ray efficiency of the ABRIR method.

The derived spectra with and without the ABRIR agree within their respective statistical errors and connect with spectral flux points of the Fermi-LAT experiment. Further, spectral flux points are calculated with upper limits for the  $2\sigma$  confidence interval. Here, the flux points of the ABRIR scenario show two fewer significant flux points than the nonABRIR scenario with reduced significance for energy bins below 10 TeV. Above 10 TeV, the flux point significances increase consistently with the rising background rejection power. For flux bins with only a few counts, the enhanced background rejection power and reduced gamma efficiency can result in the rejection of most remaining events. ABRIR, as currently implemented, rejects all events that show significant residual image clusters after the primary shower is masked. This can be caused not only by a hadronic muon signal but also by large NSB rates and the muon signal of high-energy gamma-ray events. In the case of the Crab, the usage of the ABRIR method shows no improvement in the number of derived significant spectral flux points and the spectral model in the case of the presented 3D spectral-morphological analysis. It reduces the number of significant energy bins with the last significant bin for the ABRIR case at 31.62 TeV compared to 50.12 TeV for the nonABRIR case.

Improvements to the classification of the muonic component in the masked camera image could mitigate this issue as fewer gamma-ray events are rejected. As implemented, the ABRIR framework is expandable with additional criteria to further improve the background rejection power and reduce the fraction of misclassified shower images. As NSB pixel clusters constitute a significant contribution to the fraction of misclassified gamma-ray events, such extensions might include cuts on camera images of more than a single large-mirror-diameter telescope. As such NSB pixel clusters arise at random in a telescope camera, additional telescopes could be used as a veto before a potential gamma-ray event is rejected. This could be a suitable solution for CTA, which is planned to feature multiple large-mirror-diameter telescopes.

Furthermore, the ImPACT templates used for CT1-5 were created based on H.E.S.S. simulations performed before the presented MC validation effort (section 4). This effort resulted in a better match between the simulated and observed telescope responses for all telescopes. Spectra produced for the Crab matched between CT1-4 and CT5 for the first time since FlashCam was installed. This improved simulation will result in more accurate ImPACT templates and improve the predictions of the CT5 response based on the CT1-4 ImPACT parameters.



## Acronyms

- ABRIR** Algorithm for Background Rejection using Image Residuals. , 137, 138, 139, 140, 141, 142, 143, 144, 145, 146
- ADC** Analogue to Digital Converter. 19, 30, 83, 98
- AERONET** Aerosol Robotic Network. 108, 109, 110, 111, 132
- AGN** Active Galactic Nuclei. 5
- AMS-02** Alpha Magnetic Spectrometer. 8
- AOD** Atmospheric Optical Depth. 108
- ARS** Analogue Ring Samplers. 19
- ASIC** Application Specific Integrated Circuit. 29
- BDT** Boosted Decision Tree. , 136, 137, 141
- CHEC-S** Compact High Energy Camera with Silicon PMTs. 29, 37, 62, 65, 96, 97
- CMB** Cosmic Microwave Background. 2, 7
- CoG** Centre of Gravity. 25, 48, 54, 58, 96
- CORSIKA** Cosmic Ray Simulations for Kascade. , 31, 32, 33, 39, 65, 66, 67, 68, 69, 70, 75, 96, 97, 102, 115, 118, 129, 130, 137, 162
- CT5TEA** CTA-TARGET-5TEA version. 29, 30
- CTA** Cherenkov Telescope Array. 27, 28, 33
- CTC** CTA-TARGET-C version. 29
- DC** Davies-Cotton. 18, 28
- DesertACT** Desert Air Cherenkov Telescope. 35
- DSA** Diffusive Shock Acceleration. 2, 3, 4
- ECPL** Power Law with Exponential Cutoff. 141, 142, 146
- EGS4** Electron Gamma Shower system 4. 32
- Fermi-LAT** Fermi Large Area Telescope. 8, 136, 143, 144
- FoV** Field of View. 18, 19, 24, 28, 59, 67, 112
- GRBs** Gamma Ray Bursts. 5
- GSF** Global Spline Fit. 121

**GZK** Greisen–Zatsepin–Kuzmin. 2

**H.E.S.S.** High Energy Stereoscopic System. , 17, 136, 137, 138

**HAWC** High-Altitude Water Cherenkov Observatory. 35

**HEGRA** High Energy Gamma Ray Astronomy. 16, 33

**IACT** Imaging Air Cherenkov Telescope. , 21, 22, 32, 35, 139

**IACTs** Imaging Air Cherenkov Telescopes. 15, 16, 17, 27, 31

**IC** Inverse Compton. 7

**ImPACT** Image Pixel-wise fit for Atmospheric Cherenkov Telescopes. 137, 138, 141, 147

**IRF** Instrument Response Function. 100

**ISM** Interstellar Medium. 2, 4, 5, 7

**KASCADE** Karlsruhe Shower Core and Array Detector. 32

**KN** Klein-Nishina. 7

**LogPar** Logarithmic Parabola. 141, 142, 143, 144, 146

**LSTs** Large-Sized Telescopes. 27, 28

**MC** Monte Carlo. 31, 101, 132

**MODTRAN** Moderate resolution atmospheric Transmission software. 108

**MSTs** Medium-Sized Telescopes. 27, 28

**NSB** Night Sky Background. , 24, 34, 37, 38, 67, 80, 83, 112

**p.e.** Photo Electron. 62, 67, 118

**PDE** Photo Detection Efficiency. 43, 44, 63, 77, 109

**PMT** Photo Multiplier Tube. 18, 19, 20, 21, 24, 46, 114, 140

**PMTs** Photo Multiplier Tubes. 18, 20, 21, 29, 149

**PSF** Point Spread Function. , 25, 48, 52, 54, 58, 96, 100, 102

**PWN** Pulsar Wind Nebula. 135

**PWNe** Pulsar Wind Nebulae. 4

**RMS** Root Mean Square. 85



**SBGs** Starburst Galaxies. 4

**SC** Schwarzschild-Couder. 28, 29

**SiPM** Silicon Photomultiplier. 29, 37, 40, 43, 44, 62, 63, 80, 81

**SNRs** Supernova Remnants. 4

**SSTs** Small-Sized Telescopes. , 28, 29

**TARGET** TeV Array Readout electronics with GSa/s sampling and Event Trigger. , 29, 80, 96

**TF** Transfer Function. 30, 31, 83, 84, 87, 98

**TM** TARGET-Module. 29, 31, 36, 37, 39, 46, 47, 62, 83, 84, 87, 98

**TS** Test Statistic. 142, 143, 145, 146

**UrQMD** Ultra relativistic Quantum Molecular Dynamics. 32, 102

**VHE** Very High Energy. 27



# A Appendix A

## A.1 Ray Tracing Overview

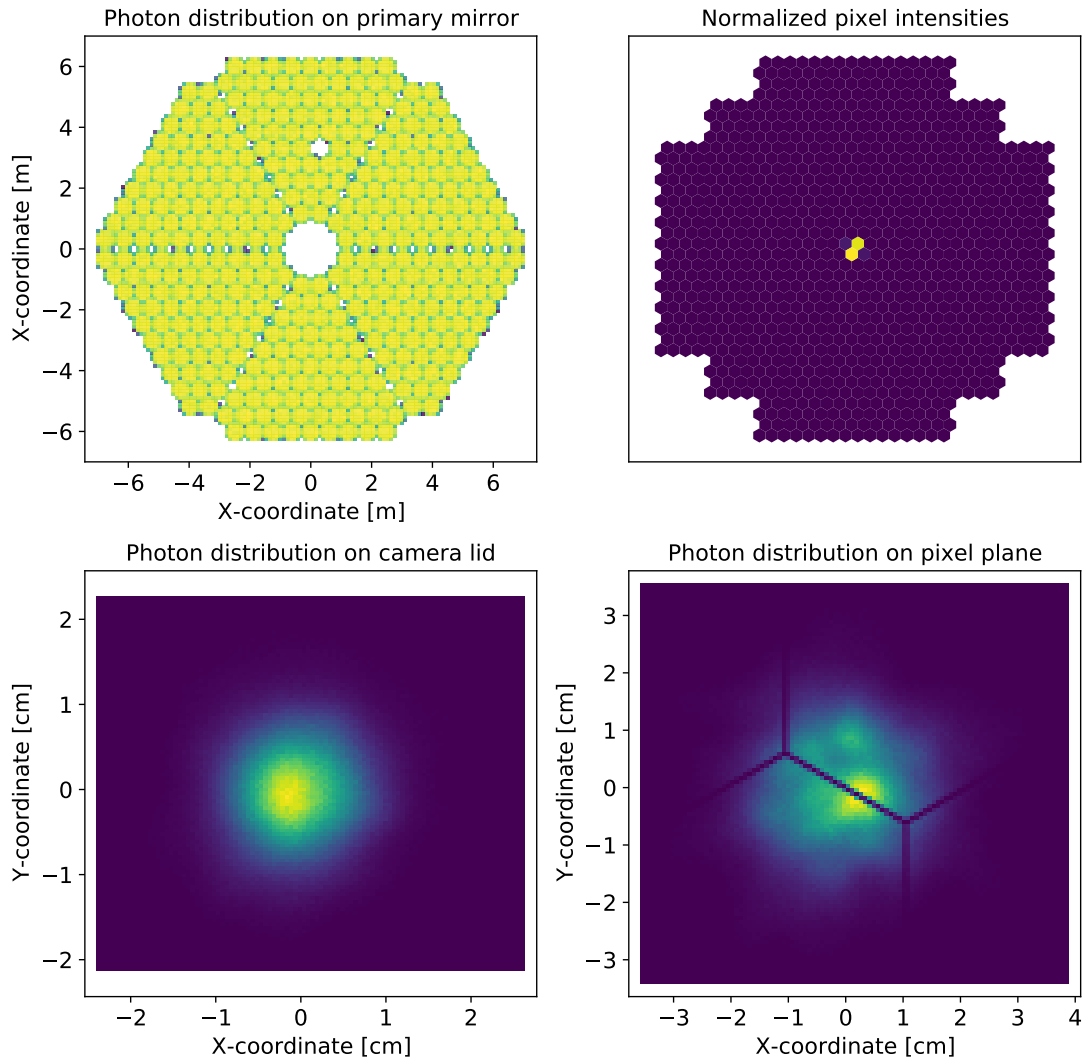


Figure 110: Ray tracing overview plot for the H.E.S.S. CT2 telescope pointing towards the zenith for incoming parallel light with an incidence angle of 0 deg to the telescopes optical axis. The overview contains the normalized photon distributions on the primary mirror (top left), camera lid (bottom left), pixel plane (bottom right), and the normalized pixel amplitudes (top right).

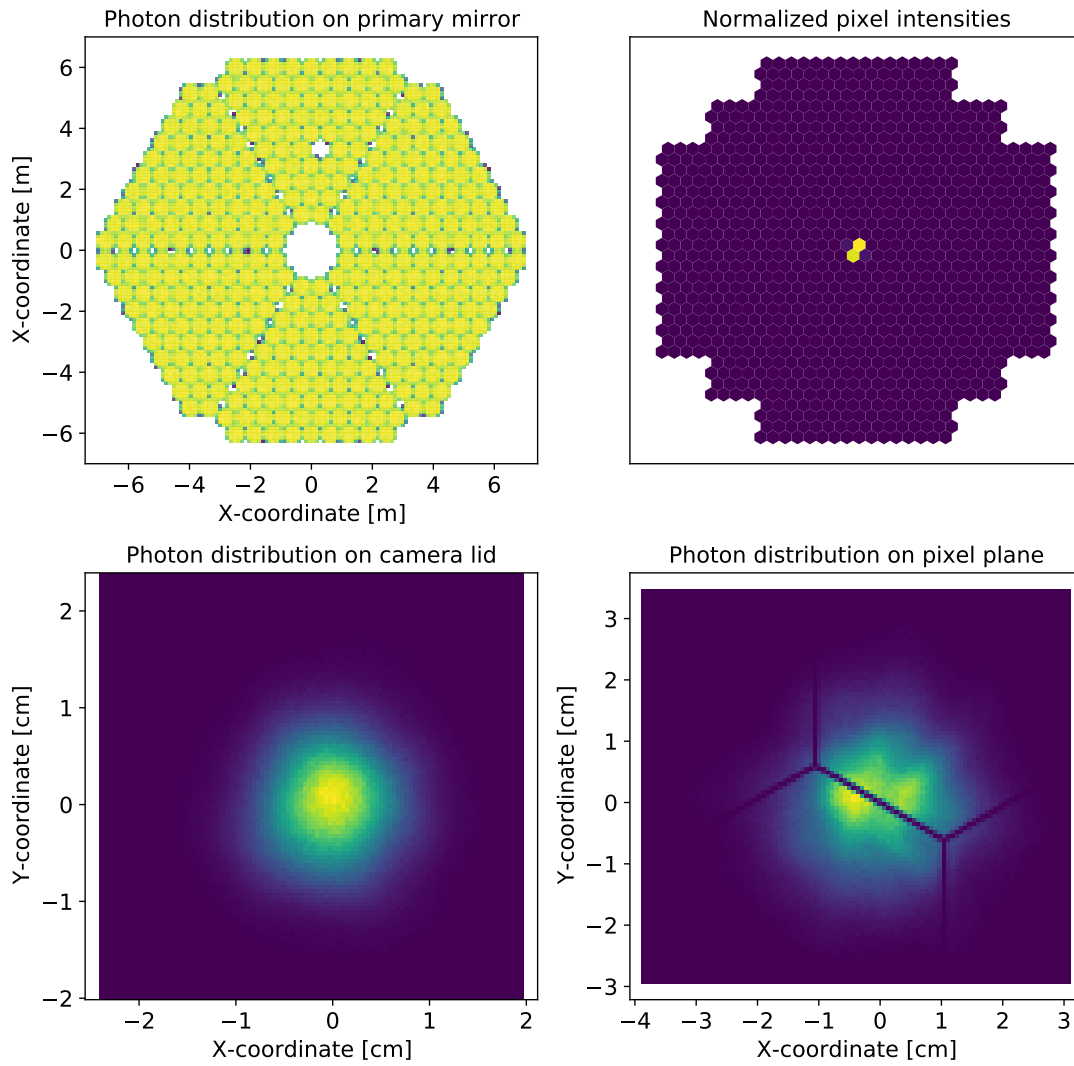


Figure 111: Ray tracing overview plot for the H.E.S.S. CT3 telescope pointing towards the zenith for incoming parallel light with an incidence angle of 0 deg to the telescopes optical axis. The overview contains the normalized photon distributions on the primary mirror (top left), camera lid (bottom left), pixel plane (bottom right), and the normalized pixel amplitudes (top right).

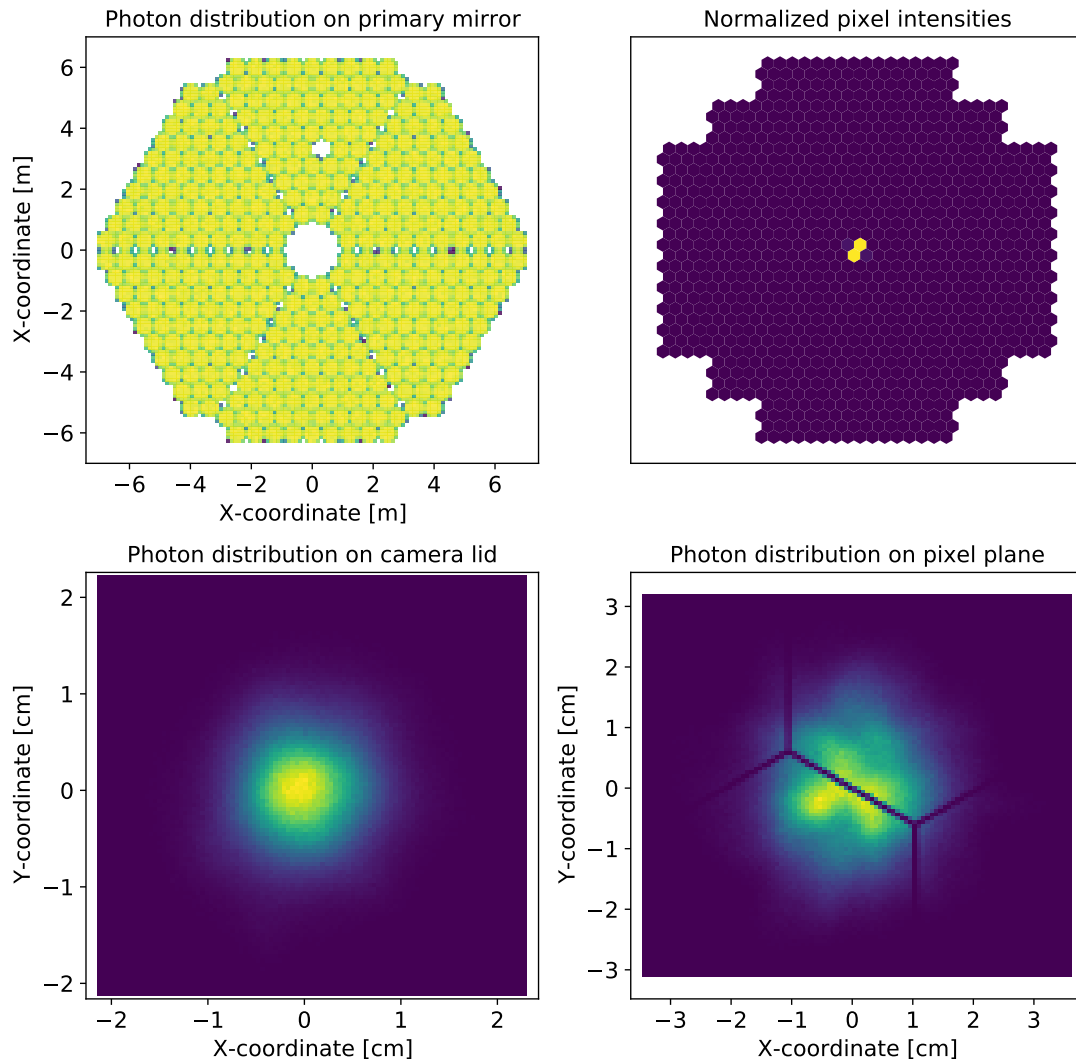


Figure 112: Ray tracing overview plot for the H.E.S.S. CT4 telescope pointing towards the zenith for incoming parallel light with an incidence angle of 0 deg to the telescopes optical axis. The overview contains the normalized photon distributions on the primary mirror (top left), camera lid (bottom left), pixel plane (bottom right), and the normalized pixel amplitudes (top right).

## A.2 Optical PSF

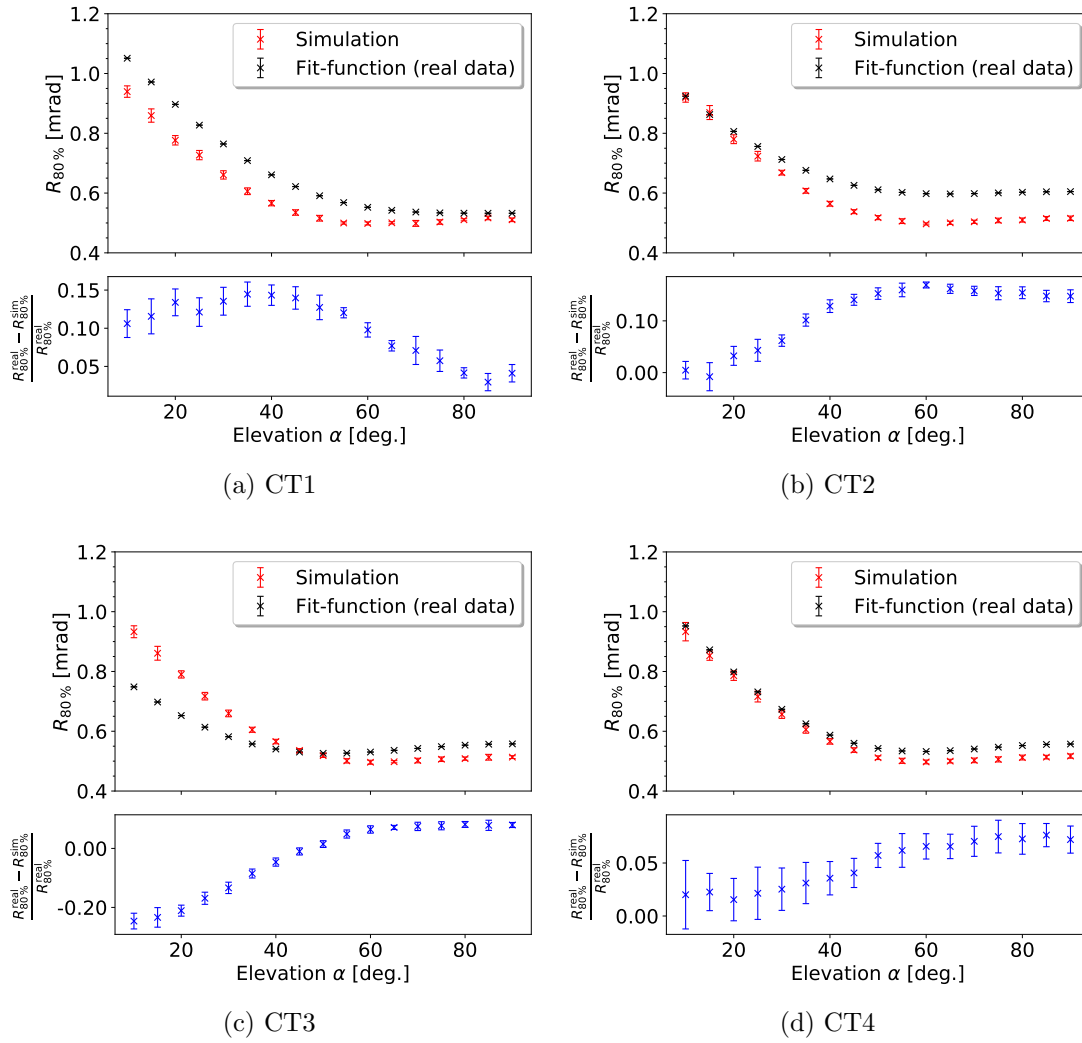


Figure 113: The elevation dependant 80% containment radius  $R_{80\%}$  of CT1-4 for the simulation and the fit function made to the real values, with the relative deviation between them.

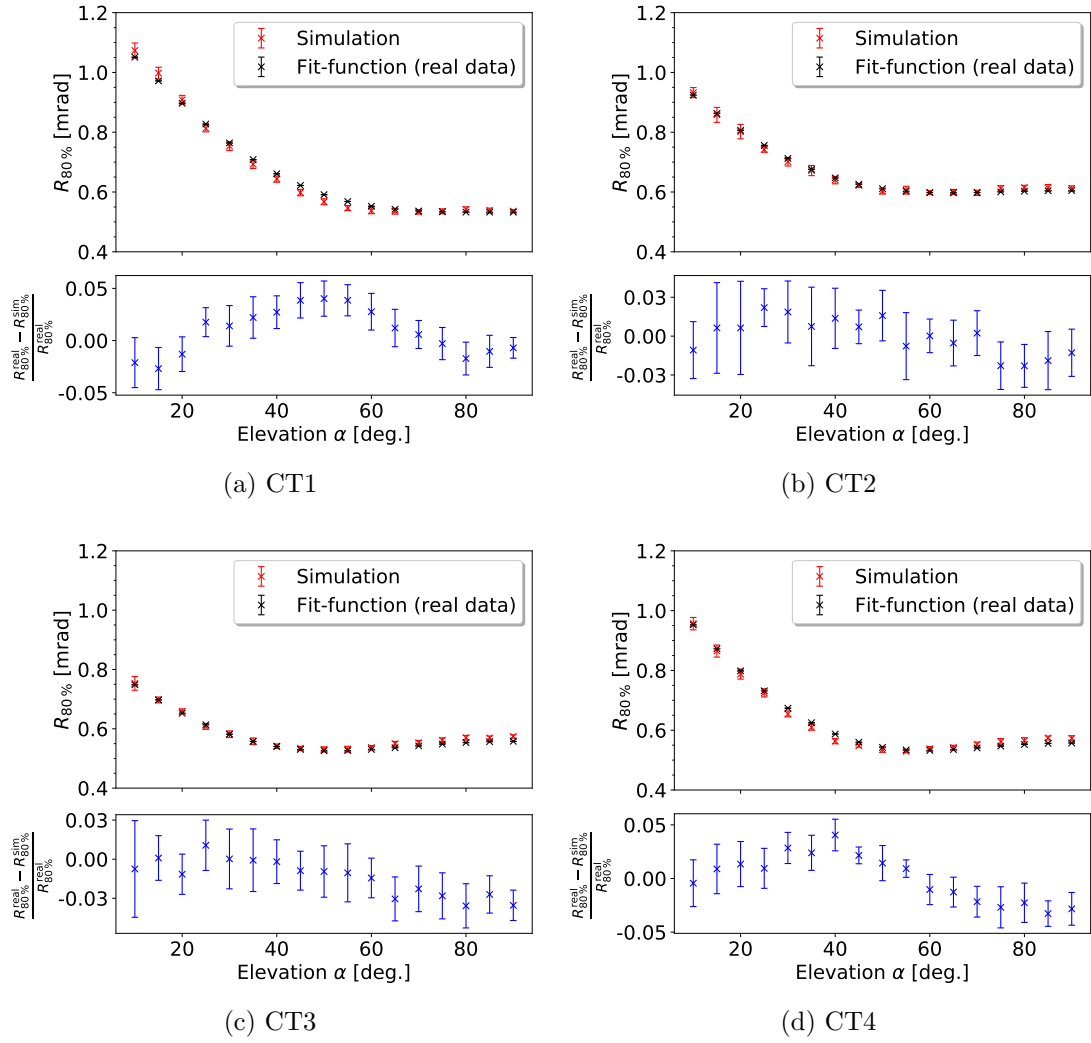


Figure 114: The elevation dependant 80 % containment radius  $R_{80\%}$  of CT1-4 for the telescope-dependant adjusted simulation and the fit function made to the real values, with the relative deviation between them.

### A.3 Heavy nuclei correction factor

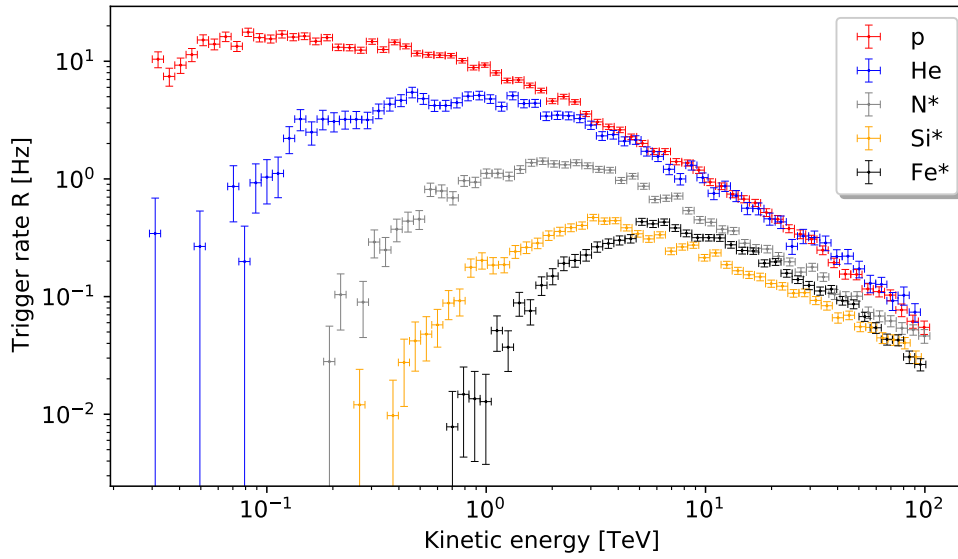


Figure 115: Simulated energy-dependant trigger rate of CT1 for different primary CR nuclei mass groups from 30 GeV to 100 TeV.

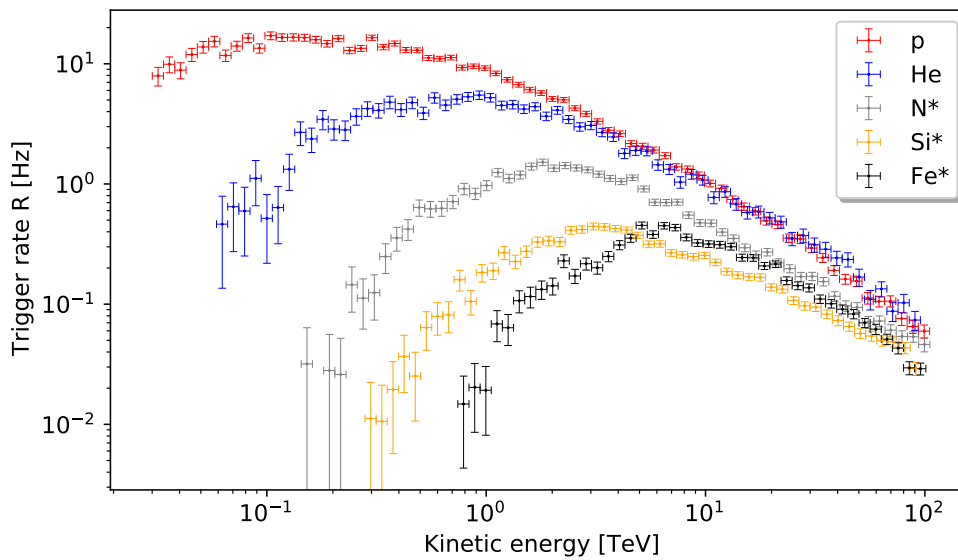


Figure 116: Simulated energy-dependant trigger rate of CT2 for different primary CR nuclei mass groups from 30 GeV to 100 TeV.



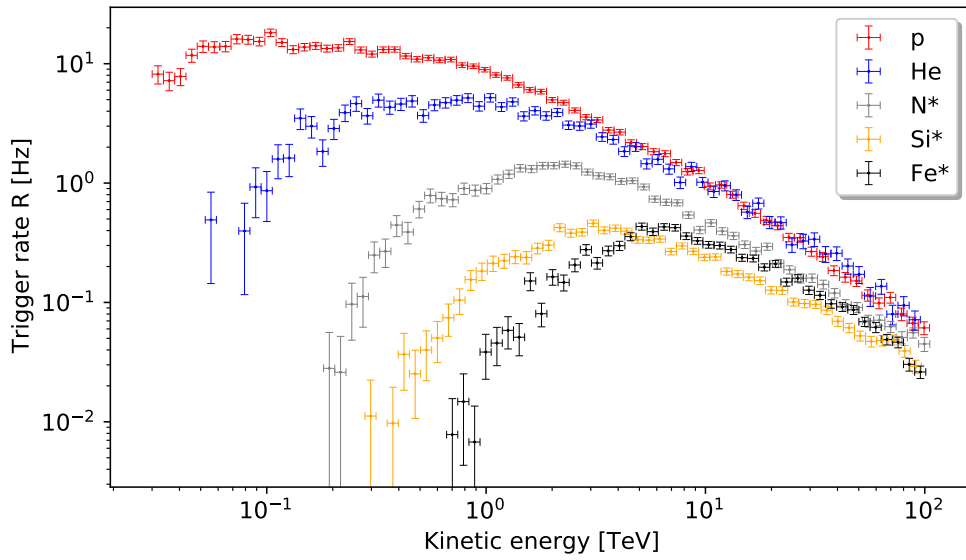


Figure 117: Simulated energy-dependant trigger rate of CT3 for different primary CR nuclei mass groups from 30 GeV to 100 TeV.

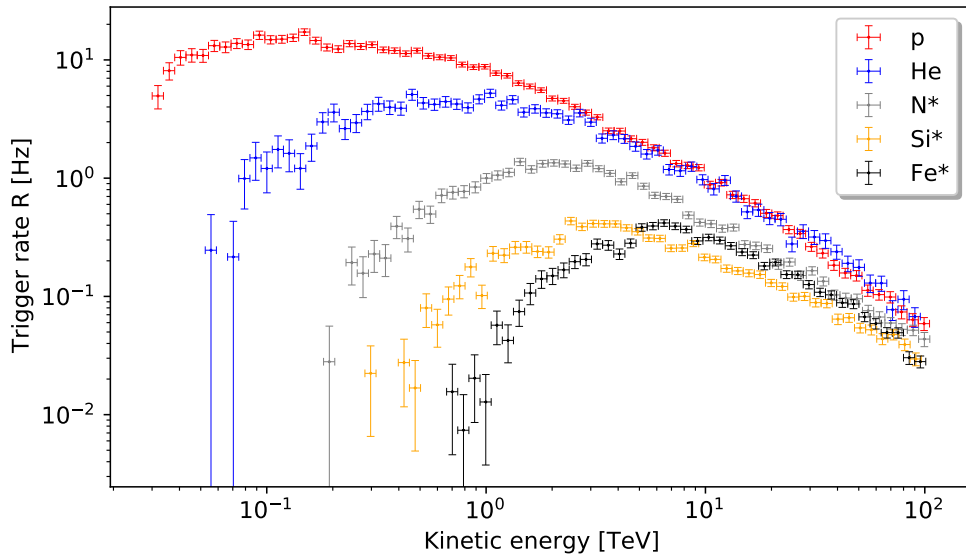


Figure 118: Simulated energy-dependant trigger rate of CT4 for different primary CR nuclei mass groups from 30 GeV to 100 TeV.

## A.4 Mono Trigger Rates

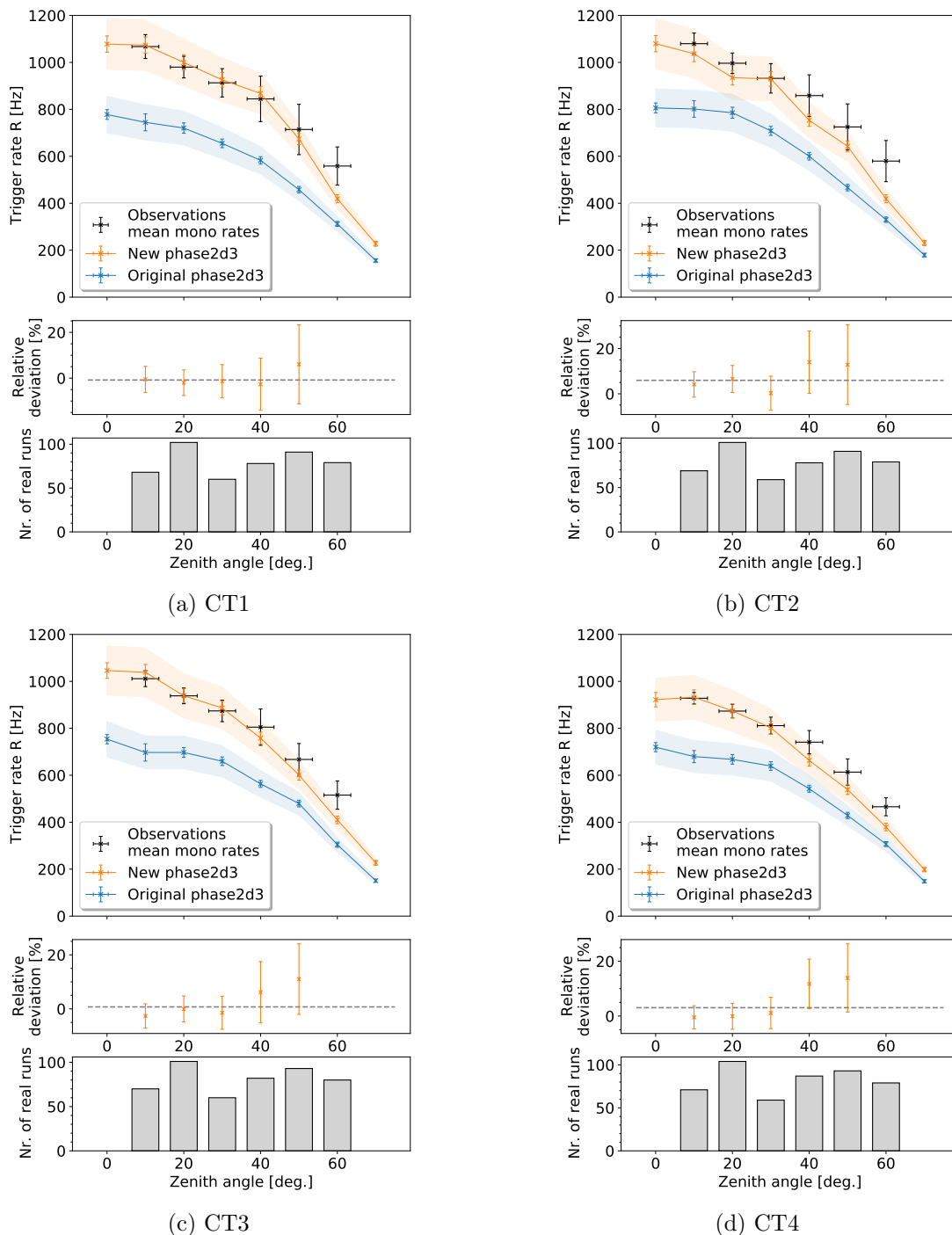


Figure 119: Zenith-dependant trigger rates of CT1-4 for observation and simulated runs, with the relative deviation of the simulation to the observation data and the number of observation runs in each zenith bin. Results for the original *phase2d3* and the new simulation configuration are shown in blue and orange, respectively. The mean relative deviation between 10 deg to 50 deg to the observation runs is highlighted as the grey dashed line. An expected systematic error band of  $\pm 10\%$  is assigned to *sim.telarray* results (Bernlöhner, 2022a).

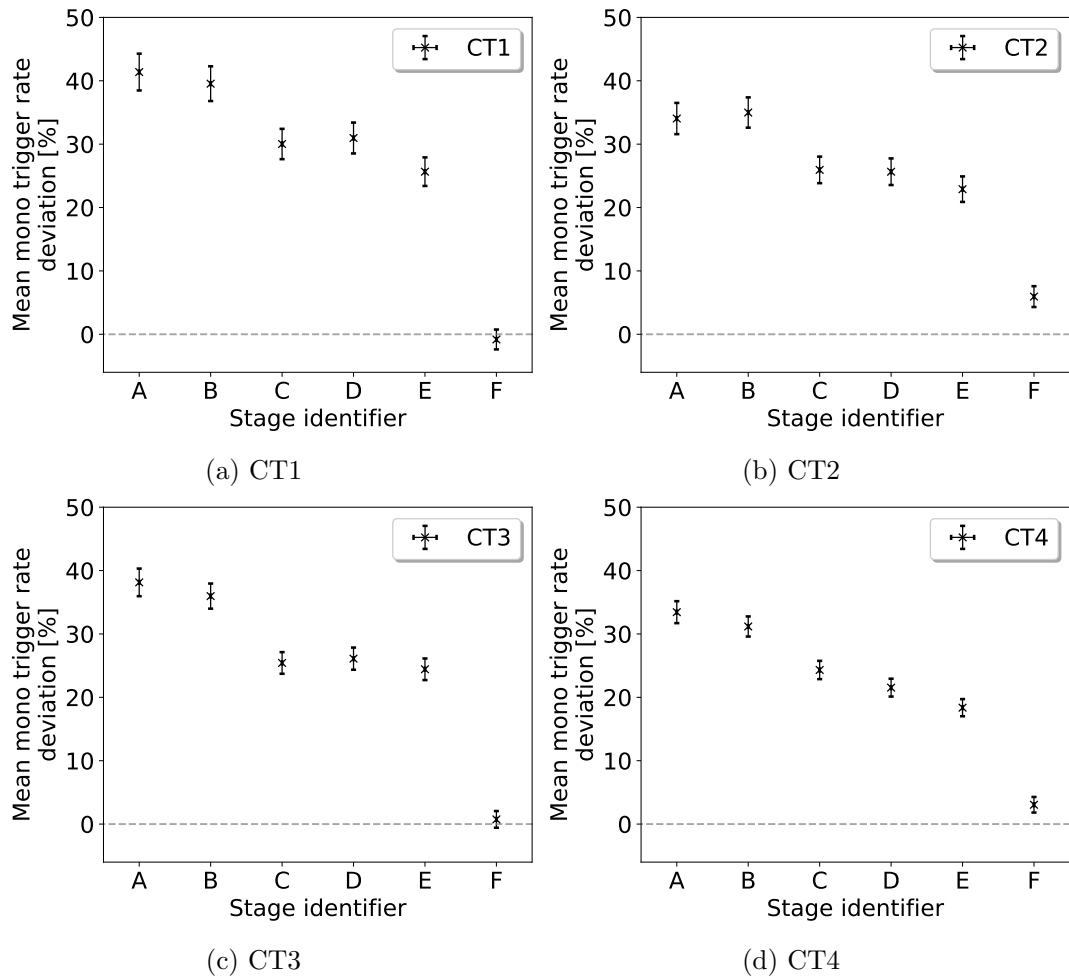


Figure 120: Mean relative deviation between the simulated and observation trigger rates between 10 deg to 50 deg zenith at different validation stages of the original *phase2d3* simulation configuration for CT1-4. The stage identifiers are defined in Table 16. For CT5 only stages up to E are shown as stage F did not contain changes to the CT5 configuration.

## A.5 Stereo Trigger Rates

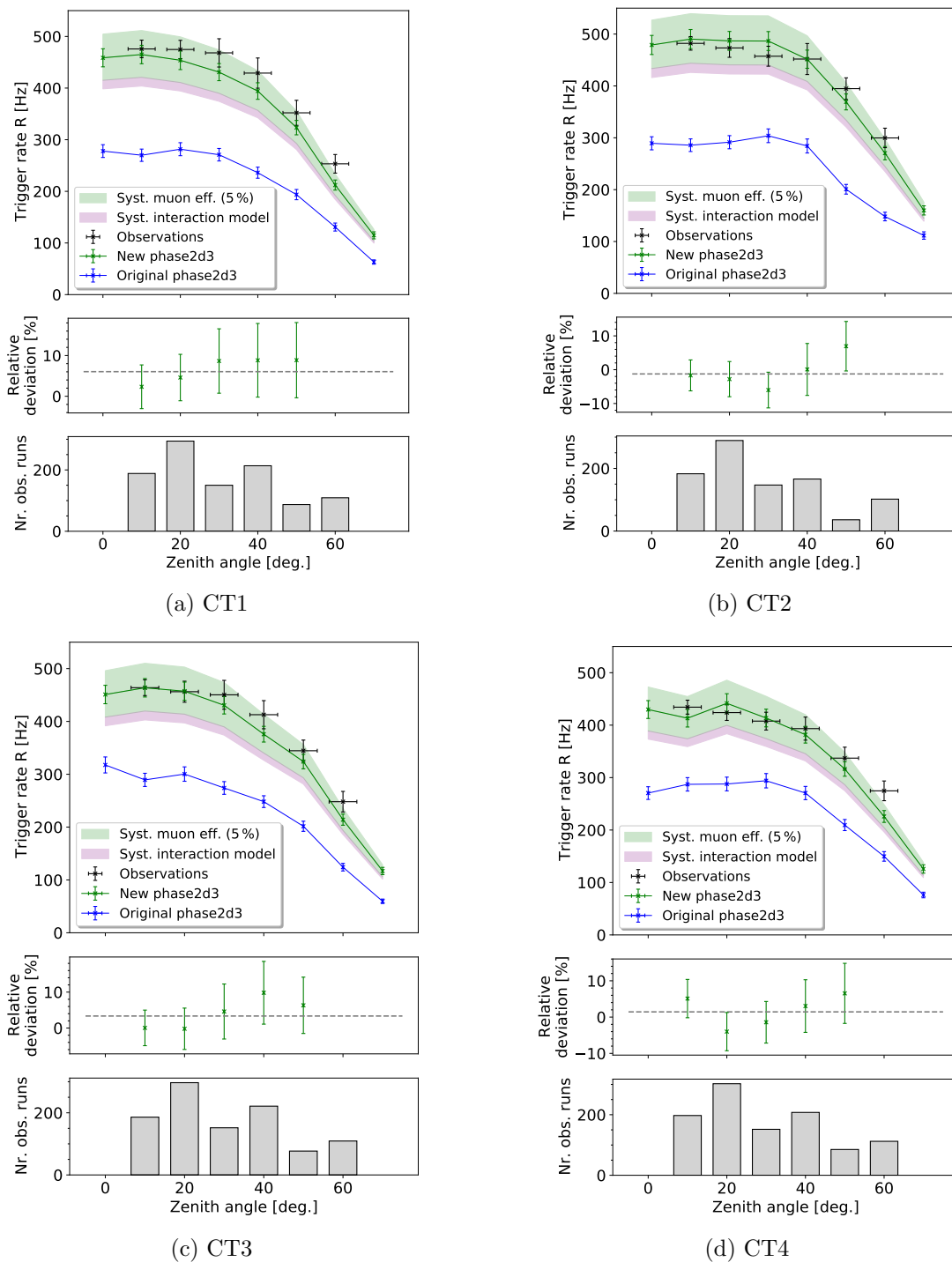


Figure 121: Zenith-dependant stereo participation trigger rates of CT1-4 for observation and simulated runs, with the relative deviation of the simulation to the observation data and the number of observation runs in each zenith bin. Simulations performed with the new *phase2d3 sim.telarray* configuration simulation. The mean relative deviation between 10 deg to 50 deg to the observation runs is highlighted as the grey dashed line. The systematic errors due to the choice of the high-energy interaction model in CORSIKA and a realistic variation in muon efficiency of 5% are shown as error bands in pink and green, respectively.

## B Appendix B

154848	154850	154851	154852	154853
154948	155964	155965	155967	156027
156028	156029	156030	156073	156074
156144	156145	156146	156147	156196
156202	156274	156425	156492	156493
156705	156847	157199	157200	157201
157288	157291	157321	157341	157342
157343	157374	157375	157376	157377
157396	157397	157398	157399	157441
157518	157519	157568	162473	162474
162501	162502	162528	162529	163044
163109	163110	163111	163138	163139
163140	163184	164094	164095	164096
164118	164119	164120	164121	164122
164164	164166	164167	164187	164211
164212	164213	164214	164215	164280
164281	164769	164770	164771	164995
165163	169895	169904	170205	

Table 21: H.E.S.S. observation run numbers used in the presented Crab analysis. Shown observation runs pass quality cut selection cuts provided in the text.



## Bibliography

- Aartsen, M.G., M. Ackermann, J. Adams, J.A. Aguilar, et al. (2017). „The IceCube Neutrino Observatory: instrumentation and online systems“. In: *Journal of Instrumentation* 12.03, P03012–P03012. ISSN: 1748-0221. DOI: 10.1088/1748-0221/12/03/p03012. URL: <http://dx.doi.org/10.1088/1748-0221/12/03/P03012>.
- Aartsen, M.G., M. Ackermann, J. Adams, J.A. Aguilar, et al. (2020a). „Design and performance of the first IceAct demonstrator at the South Pole“. In: *Journal of Instrumentation* 15.02, T02002–T02002. ISSN: 1748-0221. DOI: 10.1088/1748-0221/15/02/t02002. URL: <http://dx.doi.org/10.1088/1748-0221/15/02/T02002>.
- Aartsen, M.G. et al. (2020b). „Design and Performance of the first IceAct Demonstrator at the South Pole“. In: *JINST* 15.02, T02002. DOI: 10.1088/1748-0221/15/02/T02002. arXiv: 1910.06945 [astro-ph.IM].
- Abbasi, Rasha et al. (2021). „Observation of Cosmic Ray Anisotropy with Nine Years of IceCube Data“. In: *PoS ICRC2021*, p. 320. DOI: 10.22323/1.395.0320. arXiv: 2107.11454 [astro-ph.HE].
- Abdalla, H., H. Abe, S. Abe, A. Abusleme, et al. (Mar. 18, 2022). „The Cherenkov Telescope Array: Layout, Design and Performance“. In: *Proceedings of Science*. Vol. 395.
- Acharya, B. S., M. Actis, T. Aghajani, G. Agnetta, et al. (Mar. 1, 2013). „Introducing the CTA Concept“. In: *Astroparticle Physics. Seeing the High-Energy Universe with the Cherenkov Telescope Array - The Science Explored with the CTA 43*, pp. 3–18. ISSN: 0927-6505. DOI: 10.1016/j.astropartphys.2013.01.007.
- Adriani, O., G. C. Barbarino, G. A. Bazilevskaya, R. Bellotti, et al. (2011). „PAMELA Measurements of Cosmic-Ray Proton and Helium Spectra“. In: *Science* 332.6025, pp. 69–72. DOI: 10.1126/science.1199172. URL: <https://doi.org/10.1126/science.1199172>.
- Aerosol Robotic Network (AERONET) website* (2022). <https://aeronet.gsfc.nasa.gov/>. [Online; accessed 5-January-2023].
- Aharonian, F., A. Akhperjanian, A. Bazer-Bachi, M. Beilicke, et al. (Oct. 2006). „Observations of the Crab nebula with HESS“. In: *Astronomy & Astrophysics* 457. DOI: 10.1051/0004-6361:20065351. URL: <https://doi.org/10.1051/0004-6361:20065351>.
- Aharonian, F., A. G. Akhperjanian, K.-M. Aye, A. R. Bazer-Bachi, et al. (Oct. 2004). „Calibration of Cameras of the H.E.S.S. Detector“. In: *Astronomy & Astrophysics* 425.1, pp. L13–L17. ISSN: 0004-6361, 1432-0746. DOI: 10.1051/0004-6361:200400055. arXiv: astro-ph/0406658.
- Aharonian, F., A. G. Akhperjanian, A. R. Bazer-Bachi, M. Beilicke, et al. (Oct. 2006). „Observations of the Crab nebula with HESS“. In: *Astronomy and Astrophysics* 457.
- Aharonian, F., L. Bergström, C. Dermer, R. Walter, and M. Türler (2013). *Astrophysics at Very High Energies: Saas-Fee Advanced Course 40. Swiss Society for*

- Astrophysics and Astronomy*. Saas-Fee Advanced Course. Springer Berlin Heidelberg. ISBN: 9783642361340. URL: <https://books.google.de/books?id=LdpEAAAAQBAJ>.
- Aharonian, F., J. Buckley, T. Kifune, and G. Sinnis (Sept. 1, 2008). „High Energy Astrophysics with Ground-Based Gamma Ray Detectors“. In: *REPORTS ON PROGRESS IN PHYSICS Rep. Prog. Phys* 71, pp. 96901–56. DOI: 10.1088/0034-4885/71/9/096901.
- Ahn, Eun-Joo, Ralph Engel, Thomas K. Gaisser, Paolo Lipari, and Todor Stanev (2009). „Cosmic ray interaction event generator SIBYLL 2.1“. In: *Phys. Rev. D* 80 (9), p. 094003. DOI: 10.1103/PhysRevD.80.094003. URL: <https://link.aps.org/doi/10.1103/PhysRevD.80.094003>.
- Aleksić, J., S. Ansoldi, L. A. Antonelli, P. Antoranz, et al. (Jan. 2016). „The major upgrade of the MAGIC telescopes, Part II: A performance study using observations of the Crab Nebula“. In: *Astroparticle Physics* 72, pp. 76–94. DOI: 10.1016/j.astropartphys.2015.02.005. arXiv: 1409.5594 [astro-ph.IM].
- Aleksic, J., S. Ansoldi, L.A. Antonelli, P. Antoranz, et al. (2015). „Measurement of the Crab Nebula spectrum over three decades in energy with the MAGIC telescopes“. In: *Journal of High Energy Astrophysics* 5-6, pp. 30–38. ISSN: 2214-4048. DOI: <https://doi.org/10.1016/j.jheap.2015.01.002>. URL: <https://www.sciencedirect.com/science/article/pii/S2214404815000038>.
- Amato, Elena and Barbara Olmi (Nov. 2021). „The Crab Pulsar and Nebula as Seen in Gamma-Rays“. In: *Universe* 7.11, p. 448. ISSN: 2218-1997. DOI: 10.3390/universe7110448.
- Ashton, T., M. Backes, A. Balzer, D. Berge, et al. (Mar. 1, 2020). „A NECTAr-based Upgrade for the Cherenkov Cameras of the H.E.S.S. 12-Meter Telescopes“. In: *Astroparticle Physics* 118, p. 102425. ISSN: 0927-6505. DOI: 10.1016/j.astropartphys.2019.102425.
- Astropy Collaboration, Adrian M. Price-Whelan, Pey Lian Lim, Nicholas Earl, et al. (Aug. 2022). „The Astropy Project: Sustaining and Growing a Community-oriented Open-source Project and the Latest Major Release (v5.0) of the Core Package“. In: *The Astrophysical Journal* 935.2, 167, p. 167. DOI: 10.3847/1538-4357/ac7c74. arXiv: 2206.14220 [astro-ph.IM].
- Atwood, W. B., A. A. Abdo, M. Ackermann, W. Althouse, et al. (May 2009). „The Large Area Telescope on the Fermi Gamma-Ray Space Telescope Mission“. In: *The Astrophysical Journal* 697.2, p. 1071. ISSN: 0004-637X. DOI: 10.1088/0004-637X/697/2/1071. URL: <https://dx.doi.org/10.1088/0004-637X/697/2/1071> (visited on 03/23/2023).
- Baden, Till (2023). „Rekonstruktion von Luftschauerbildern mit Graph Convolutional Neural Networks fuer IceAct“. Bachelor’s Thesis. Fakultät für Mathematik, Informatik und Naturwissenschaften.
- Barrantes, Marco, Jose Valdes, O Musalem, A Hurtado, et al. (Oct. 2018). „Atmospheric corrections of the cosmic ray fluxes detected by the Solar Neutron Telescope at the



- Summit of the Sierra Negra Volcano in Mexico“. In: *Geofísica Internacional* 57, pp. 253–275. DOI: 10.22201/igeof.00167169p.2018.57.4.2105.
- Bass, Michael and Optical Society of America Optica, eds. (1995). *Handbook of Optics*. 2nd ed. New York: McGraw-Hill. ISBN: 978-0-07-047740-7 978-0-07-047974-6 978-0-07-135408-0 978-0-07-136456-0.
- Benbow, W. (Apr. 2005a). „The H.E.S.S. standard analysis technique“. In: *7th Workshop on Towards a Network of Atmospheric Cherenkov Detectors 2005*, pp. 163–171.
- Benbow, W. (Jan. 2005b). „The Status and Performance of H.E.S.S.“. In: DOI: 10.1063/1.1878471.
- Benn, C.R and S.L Ellison (1998). „Brightness of the night sky over La Palma“. In: *New Astronomy Reviews* 42.6-8, pp. 503–507. DOI: 10.1016/s1387-6473(98)00062-1. URL: [https://doi.org/10.1016/s1387-6473\(98\)00062-1](https://doi.org/10.1016/s1387-6473(98)00062-1).
- Bernlöhr, K., O. Carrol, R. Cornils, S. Elfahem, et al. (Nov. 2003). „The Optical System of the H.E.S.S. Imaging Atmospheric Cherenkov Telescopes, Part I: Layout and Components of the System“. In: *Astroparticle Physics* 20.2, pp. 111–128. ISSN: 09276505. DOI: 10.1016/S0927-6505(03)00171-3. arXiv: astro-ph/0308246.
- Bernlöhr, Konrad (Jan. 1, 2000). „Impact of Atmospheric Parameters on the Atmospheric Cherenkov Technique“. In: *Astroparticle Physics* 12.4, pp. 255–268. ISSN: 0927-6505. DOI: 10.1016/S0927-6505(99)00093-6.
- (2005). „eventio – ein maschinen-unabhängiges, hierarchisches Datenformat und seine Software-Schnittstelle“. In: URL: [https://www.mpi-hd.mpg.de/hfm/~bernlöhr/sim\\_telarray/Documentation/eventio\\_de.pdf](https://www.mpi-hd.mpg.de/hfm/~bernlöhr/sim_telarray/Documentation/eventio_de.pdf).
- (2008). „Simulation of imaging atmospheric Cherenkov telescopes with CORSIKA and sim telarray“. In: *Astroparticle Physics* 30.3, 149–158. ISSN: 0927-6505. DOI: 10.1016/j.astropartphys.2008.07.009. URL: <http://dx.doi.org/10.1016/j.astropartphys.2008.07.009>.
- (2022a). personal correspondence.
- (2022b). „CORSIKA and sim-telarray - sim\_telarray.pdf“. In: [Online; accessed 22-December-2022]. URL: [https://www.mpi-hd.mpg.de/hfm/~bernlöhr/sim\\_telarray/Documentation/sim\\_telarray.pdf](https://www.mpi-hd.mpg.de/hfm/~bernlöhr/sim_telarray/Documentation/sim_telarray.pdf).
- Bethe, H., W. Heitler, and Paul Adrien Maurice Dirac (1934). „On the stopping of fast particles and on the creation of positive electrons“. In: *Proceedings of the Royal Society of London. Series A, Containing Papers of a Mathematical and Physical Character* 146.856, pp. 83–112. DOI: 10.1098/rspa.1934.0140. eprint: <https://royalsocietypublishing.org/doi/pdf/10.1098/rspa.1934.0140>. URL: <https://royalsocietypublishing.org/doi/abs/10.1098/rspa.1934.0140>.
- Bi, Baiyang, Miquel Barcelo, Christian Bauer, Faical Ait Benkhali, et al. (July 4, 2021). „Performance of the New FlashCam-based Camera in the 28m Telescope of H.E.S.S.“. In: *Proceedings of 37th International Cosmic Ray Conference — PoS(ICRC2021)*, p. 743. DOI: 10.22323/1.395.0743. arXiv: 2108.03046 [astro-ph].

- Blumenthal, George R. and Robert J. Gould (1970). „Bremsstrahlung, Synchrotron Radiation, and Compton Scattering of High-Energy Electrons Traversing Dilute Gases“. In: *Rev. Mod. Phys.* 42 (2), pp. 237–270. DOI: 10.1103/RevModPhys.42.237. URL: <https://link.aps.org/doi/10.1103/RevModPhys.42.237>.
- Bolz, O. (2004). „Absolute Energiekalibration Der Abbildenden Cherenkov-Teleskope Des H.E.S.S. Experiments Und Ergebnisse Bisheriger Beobachtungen Des Supernova-U ueberrests RX J1713.7-3946“. PhD thesis. Ruprecht-Karl-Universitaet Heidelberg.
- Bose, D., V. R. Chitnis, P. Majumdar, and B. S. Acharya (Jan. 1, 2022). „Ground-Based Gamma-Ray Astronomy: History and Development of Techniques“. In: *The European Physical Journal Special Topics* 231.1, pp. 3–26. ISSN: 1951-6401. DOI: 10.1140/epjs/s11734-021-00396-3. URL: <https://doi.org/10.1140/epjs/s11734-021-00396-3> (visited on 03/23/2023).
- Breuhaus, M., J. A. Hinton, V. Joshi, B. Reville, and H. Schoorlemmer (2022). „Galactic gamma-ray and neutrino emission from interacting cosmic-ray nuclei“. In: *Astron. Astrophys.* 661, A72. DOI: 10.1051/0004-6361/202141318. arXiv: 2201.03984 [astro-ph.HE].
- Breuhaus, Mischa (2022). personal correspondence.
- Burden, Daniel L. and Gary M. Hieftje (Aug. 1, 1998). „Cerenkov Radiation as a UV and Visible Light Source for Time-Resolved Fluorescence“. In: *Analytical Chemistry* 70.16, pp. 3426–3433. ISSN: 0003-2700, 1520-6882. DOI: 10.1021/ac980016w.
- Celic, Jelena (2021). „Further studies with DesertACT and performance analysis of a new type of a tiny sized telescope“. MA thesis. Erlangen Centre for Astroparticle Physics (ECAP).
- Chalme-Calvet, R., M. De Naurois, and J.-P. Tavernet (Mar. 18, 2014). *Muon Efficiency of the H.E.S.S. Telescope*. arXiv: arXiv:1403.4550.
- Cherenkov, P. A. (1937). „Visible Radiation Produced by Electrons Moving in a Medium with Velocities Exceeding that of Light“. In: *Phys. Rev.* 52 (4), pp. 378–379. DOI: 10.1103/PhysRev.52.378. URL: <https://link.aps.org/doi/10.1103/PhysRev.52.378>.
- Condorelli, Antonio, Denise Boncioli, Enrico Peretti, and Sergio Petrerá (2023). „Testing hadronic and photohadronic interactions as responsible for ultrahigh energy cosmic rays and neutrino fluxes from starburst galaxies“. In: *Phys. Rev. D* 107 (8), p. 083009. DOI: 10.1103/PhysRevD.107.083009. URL: <https://link.aps.org/doi/10.1103/PhysRevD.107.083009>.
- Cornils, R., S. Gillessen, I. Jung, W. Hofmann, et al. (2003). „The optical system of the H.E.S.S. imaging atmospheric Cherenkov telescopes. Part II: mirror alignment and point spread function“. In: *Astroparticle Physics* 20.2, pp. 129–143. ISSN: 0927-6505. DOI: [https://doi.org/10.1016/S0927-6505\(03\)00172-5](https://doi.org/10.1016/S0927-6505(03)00172-5). URL: <https://www.sciencedirect.com/science/article/pii/S0927650503001725>.
- Corp., Pacific Telescope (2022). *Instruction manual EQ8 Mount*. [https://inter-static.skywatcher.com/downloads/eq8\\_221018v2.pdf](https://inter-static.skywatcher.com/downloads/eq8_221018v2.pdf). [Online; accessed 20-February-2023].

- CTA observatory website* (2023). [www.cta-observatory.org](http://www.cta-observatory.org). [Online; accessed 6-April-2023].
- Daum, A., G. Hermann, M. Heß, W. Hofmann, et al. (Dec. 1, 1997). „First Results on the Performance of the HEGRA IACT Array“. In: *Astroparticle Physics* 8.1, pp. 1–11. ISSN: 0927-6505. DOI: 10.1016/S0927-6505(97)00031-5.
- Davies, John M. and Eugene S. Cotton (Apr. 1, 1957). „Design of the Quartermaster Solar Furnace“. In: *Solar Energy* 1.2, pp. 16–22. ISSN: 0038-092X. DOI: 10.1016/0038-092X(57)90116-0.
- De Angelis, Alessandro and Manuela Mallamaci (2018). „Gamma-ray astrophysics“. In: *The European Physical Journal Plus* 133, pp. 1–18.
- Deil, C., R. Zanin, J. Lefaucheur, C. Boisson, et al. (Jan. 2017). „Gammapy - A prototype for the CTA science tools“. In: *35th International Cosmic Ray Conference (ICRC2017)*. Vol. 301. International Cosmic Ray Conference, 766, p. 766. DOI: 10.5281/zenodo.5721467. arXiv: 1709.01751 [astro-ph.IM].
- Dembinski, Hans, Ralph Engel, Anatoli Fedynitch, Thomas Gaisser, et al. (2017). „Data-driven model of the cosmic-ray flux and mass composition from 10 GeV to  $10^{11}$  GeV“. In: *Proceedings of 35th International Cosmic Ray Conference — PoS (ICRC2017)*. Vol. 301. International Cosmic Ray Conference. PoS, p. 533. DOI: 10.22323/1.301.0533. URL: <https://doi.org/10.22323/1.301.0533>.
- Dembinsky, Hans (2022). *Cosmic Ray Explorer*. <https://www.mpi-hd.mpg.de/personalhomes/hdembins>. [Online; accessed 28-January-2023].
- Dietz, Stefan (2018). „Set-up, South Pole field test and energy threshold determination of the Erlangen design of an IceAct telescope“. MA thesis. Erlangen Centre for Astroparticle Physics (ECAP).
- (2021). personal correspondence.
- Evans, Lyndon and Philip Bryant (2008). „LHC machine“. In: *Journal of instrumentation* 3.08, S08001.
- Fermi, E. (1954). „Galactic Magnetic Fields and the Origin of Cosmic Radiation.“ In: *Astrophys. J.* 119, pp. 1–6. DOI: 10.1086/145789.
- Fink, David, Alexander Hahn, Daniel Mazin, Juergen Hose, et al. (June 2016). „SiPM Based Focal Plane Instrumentation Prototype for the MAGIC Atmospheric Cherenkov Telescope“. In: p. 006. DOI: 10.22323/1.252.0006.
- Frank, I. and Ig. Tamm (1991). „Coherent Visible Radiation of Fast Electrons Passing Through Matter“. In: *Selected Papers*. Ed. by Boris M. Bolotovskii, Victor Ya. Frenkel, and Rudolf Peierls. Berlin, Heidelberg: Springer Berlin Heidelberg, pp. 29–35. ISBN: 978-3-642-74626-0. DOI: 10.1007/978-3-642-74626-0\_2. URL: [https://doi.org/10.1007/978-3-642-74626-0\\_2](https://doi.org/10.1007/978-3-642-74626-0_2).
- Fruck, Christian (2015). „The Galactic Center resolved with MAGIC and a new technique for Atmospheric Calibration“. PhD thesis. Technische Universitaet Muenchen.

- Funk, S., G. Hermann, J. Hinton, D. Berge, et al. (Nov. 2004). „The Trigger System of the H.E.S.S. Telescope Array“. In: *Astroparticle Physics* 22.3-4, pp. 285–296. ISSN: 09276505. DOI: 10.1016/j.astropartphys.2004.08.001. arXiv: astro-ph/0408375.
- Funk, S., D. Jankowsky, H. Katagiri, M. Kraus, et al. (2017). „TARGET: A digitizing and trigger ASIC for the Cherenkov telescope array“. In: *AIP Conference Proceedings* 1792.1, p. 080012. DOI: 10.1063/1.4969033. eprint: <https://aip.scitation.org/doi/pdf/10.1063/1.4969033>. URL: <https://aip.scitation.org/doi/abs/10.1063/1.4969033>.
- Funk, Stefan (2021). personal correspondence.
- Gaug, M., S. Fegan, A. M. W. Mitchell, M. C. MacCarone, et al. (2019). „Using Muon Rings for the Calibration of the Cherenkov Telescope Array: A Systematic Review of the Method and Its Potential Accuracy“. In: *The Astrophysical Journal Supplement Series* 243.1, p. 11. DOI: 10.3847/1538-4365/ab2123. URL: <https://doi.org/10.3847/1538-4365/ab2123>.
- Giavitto, Gianluca, Simon Bonnefoy, Terry Ashton, Michael Backes, et al. (Mar. 28, 2018). „Performance of the Upgraded H.E.S.S. Cameras“. In: *Proceedings of 35th International Cosmic Ray Conference — PoS(ICRC2017)*. Bexco, Busan, Korea: Sissa Medialab, p. 805. DOI: 10.22323/1.301.0805.
- Gottschall, Daniel (2018). „The Mirror Alignment and Control System of H.E.S.S. Phase II, and Observational Studies of TeV Shell Candidates and of the Nova Sgr 2015 No. 2 with H.E.S.S.“ PhD thesis. Eberhard Karls University of Tübingen.
- Hahn, J., R. de los Reyes, K. Bernlöhr, P. Krüger, et al. (2014). „Impact of aerosols and adverse atmospheric conditions on the data quality for spectral analysis of the H.E.S.S. telescopes“. In: *Astroparticle Physics* 54, pp. 25–32. ISSN: 0927-6505. DOI: <https://doi.org/10.1016/j.astropartphys.2013.10.003>. URL: <https://www.sciencedirect.com/science/article/pii/S0927650513001540>.
- Harris, Charles R., K. Jarrod Millman, Stéfan J. van der Walt, Ralf Gommers, et al. (Sept. 2020). „Array programming with NumPy“. In: *Nature* 585.7825, pp. 357–362. DOI: 10.1038/s41586-020-2649-2. URL: <https://doi.org/10.1038/s41586-020-2649-2>.
- Heck, D., J. Knapp, J. N. Capdevielle, G. Schatz, and T. Thouw (1998). *CORSIKA: A Monte Carlo code to simulate extensive air showers*. Tech. rep. 51.02.03; LK 01; Wissenschaftliche Berichte, FZKA-6019 (Februar 98). DOI: 10.5445/IR/270043064.
- Heck, D. and T. Pierog (2021). *Extensive Air Shower Simulation with CORSIKA: A User’s Guide (Version 7.7410 from May 1, 2021)*. <https://web.iap.kit.edu/corsika/usersguide/usersguide.pdf>. [Online; accessed 5-April-2023].
- Heitler, W. (1944). *The Quantum Theory Of Radiation Ed. 2*. URL: <http://archive.org/details/in.ernet.dli.2015.37198> (visited on 03/22/2023).
- Herrmann, Benedikt (2019). „Development and Characterization of a Test Stand for Compact High Energy Camera (CHEC-S) Mass Test“. MA thesis. Erlangen Centre for Astroparticle Physics (ECAP).

- H.E.S.S Collaboration, H. E. S. S., H. Abdalla, F. Aharonian, F. Ait Benkhali, et al. (2019). *Resolving the Crab pulsar wind nebula at teraelectronvolt energies*. DOI: 10.48550/ARXIV.1909.09494. URL: <https://arxiv.org/abs/1909.09494>.
- H.E.S.S. Collaboration, H. E. S. S., H. Abdalla, F. Aharonian, F. Ait Benkhali, et al. (Sept. 23, 2019). *Resolving the Crab Pulsar Wind Nebula at Teraelectronvolt Energies*. DOI: 10.48550/arXiv.1909.09494. arXiv: arXiv:1909.09494. URL: <http://arxiv.org/abs/1909.09494> (visited on 03/10/2023). preprint.
- H.E.S.S. website* (2022). [https://www.mpi-hd.mpg.de/hfm/HESS/pages/press/2012/HESS\\_II\\_first\\_light/](https://www.mpi-hd.mpg.de/hfm/HESS/pages/press/2012/HESS_II_first_light/). [Online; accessed 4-March-2023].
- Hester, J. Jeff (2008). „The Crab Nebula: An Astrophysical Chimera“. In: *Annual Review of Astronomy and Astrophysics* 46.1, pp. 127–155. DOI: 10.1146/annurev.astro.45.051806.110608. eprint: <https://doi.org/10.1146/annurev.astro.45.051806.110608>. URL: <https://doi.org/10.1146/annurev.astro.45.051806.110608>.
- Hillas, A. M. (Jan. 1984). „The Origin of Ultra-High-Energy Cosmic Rays“. In: *Annu. Rev. Astron. Astrophys.* 22, pp. 425–444. DOI: 10.1146/annurev.aa.22.090184.002233.
- (Aug. 1985). „Cerenkov Light Images of EAS Produced by Primary Gamma Rays and by Nuclei“. In: *19th International Cosmic Ray Conference (ICRC19), Volume 3*. Vol. 3. International Cosmic Ray Conference, p. 445.
- Hofmann, Werner (2012). *The H.E.S.S. Telescopes*. <https://www.mpi-hd.mpg.de/hfm/HESS/pages/about/telescopes>. [Online; accessed 10-December-2022].
- Holben, B.N., T.F. Eck, I. Slutsker, D. Tanré, et al. (1998). „AERONET—A Federated Instrument Network and Data Archive for Aerosol Characterization“. In: *Remote Sensing of Environment* 66.1, pp. 1–16. ISSN: 0034-4257. DOI: [https://doi.org/10.1016/S0034-4257\(98\)00031-5](https://doi.org/10.1016/S0034-4257(98)00031-5). URL: <https://www.sciencedirect.com/science/article/pii/S0034425798000315>.
- Holch, T L, F Leuschner, J Schäfer, and S Steinmassl (2022). „Assessing aerosol induced errors in Monte Carlo based air-shower reconstruction for atmospheric Cherenkov detectors“. In: *Journal of Physics: Conference Series* 2398.1, p. 012017. DOI: 10.1088/1742-6596/2398/1/012017. URL: <https://dx.doi.org/10.1088/1742-6596/2398/1/012017>.
- Holch, Tim Lukas (2022). personal correspondence.
- Holder, J. et al. (2009). „Status of the VERITAS Observatory“. In: *AIP Conf. Proc.* 1085.1. Ed. by Felix A. Aharonian, Werner Hofmann, and Frank Rieger, pp. 657–660. DOI: 10.1063/1.3076760. arXiv: 0810.0474 [astro-ph].
- IceCube Collaboration (2013). „Evidence for High-Energy Extraterrestrial Neutrinos at the IceCube Detector“. In: *Science* 342.6161, p. 1242856. DOI: 10.1126/science.1242856. eprint: <https://www.science.org/doi/pdf/10.1126/science.1242856>. URL: <https://www.science.org/doi/abs/10.1126/science.1242856>.

- Jankowsky, David (2020). „Measurement of the Cosmic Ray Proton Spectrum with H.E.S.S. and Characterization of the TARGET ASICs for the CTA“. doctoralthesis. Friedrich-Alexander-Universität Erlangen-Nürnberg (FAU).
- Jones, P. B. (Mar. 1, 1975). „The Alignment of the Crab Pulsar Magnetic Axis“. In: *Astrophysics and Space Science* 33.1, pp. 215–230. ISSN: 1572-946X. DOI: 10.1007/BF00646019.
- Kennel, C. F. and F. V. Coroniti (Aug. 1984). „Magnetohydrodynamic Model of Crab Nebula Radiation“. In: *The Astrophysical Journal* 283, p. 710. ISSN: 0004-637X, 1538-4357. DOI: 10.1086/162357.
- Klages, H. O., W. D. Apel, K. Bekk, E. Bollmann, et al. (Feb. 1, 1997). „The Kascade Experiment“. In: *Nuclear Physics B - Proceedings Supplements* 52.3, pp. 92–102. ISSN: 0920-5632. DOI: 10.1016/S0920-5632(96)00852-3.
- Kolanoski, Hermann and Norbert Wermes (2016). „Teilchendetektoren: Grundlagen und Anwendungen“. In: *Teilchendetektoren: Grundlagen und Anwendungen*. Ed. by Hermann Kolanoski and Norbert Wermes. Berlin, Heidelberg: Springer, pp. 719–805. DOI: 10.1007/978-3-662-45350-6\_17.
- Koschinsky, Jan Paul (2017). „Development of a 61-Pixel Camera for the IceAct Imaging Air Cherenkov Telescope“. MA thesis. Fakultät fuer Mathematik, Informatik und Naturwissenschaften Aachen.
- Kounine, Andrei (Aug. 2012). „THE ALPHA MAGNETIC SPECTROMETER ON THE INTERNATIONAL SPACE STATION“. In: *International Journal of Modern Physics E* 21.08, p. 1230005. ISSN: 0218-3013, 1793-6608. DOI: 10.1142/S0218301312300056. URL: <https://www.worldscientific.com/doi/abs/10.1142/S0218301312300056> (visited on 03/23/2023).
- Laufer, G. (1996). *Introduction to Optics and Lasers in Engineering*. Cambridge University Press. ISBN: 9780521452335.
- Leuschner, Fabian (2023). personal correspondence.
- Leuschner, Fabian (2023). „Title To Be Announced“. [Unpublished doctoral dissertation]. PhD thesis. Institute for astronomy and astrophysics, Eberhard Karls University in Tuebingen, Germany.
- Leuschner, Fabian, Johannes Schaefer, Simon Steinmassl, Tim Lukas Holch, et al. (2023). „Validating Monte Carlo simulations for an analysis chain in H.E.S.S.“. In: DOI: 10.48550/ARXIV.2303.00412. URL: <https://arxiv.org/abs/2303.00412>.
- Lewis, D. A. (July 1, 1990). „Optical Characteristics of the Whipple Observatory TeV Gamma-Ray Imaging Telescope“. In: *Experimental Astronomy* 1.4, pp. 213–226. ISSN: 1572-9508. DOI: 10.1007/BF00428516.
- Li, Ti-pei and Yu-qian Ma (1983). „Analysis methods for results in gamma-ray astronomy“. In: *ApJ*. . . 272.1.
- Lipatov, E. I., V. F. Tarasenko, M. V. Erofeev, V. S. Ripenko, and M. A. Shulepov (Mar. 1, 2020). „Vavilov–Cherenkov Radiation in the Region 200–300 Nm in the Earth’s Atmosphere“. In: *Atmospheric and Oceanic Optics* 33.2, pp. 195–197. ISSN:

- 2070-0393. DOI: 10.1134/S1024856020020049. URL: <https://doi.org/10.1134/S1024856020020049> (visited on 03/25/2023).
- Longair, Malcolm S. (2011). *High Energy Astrophysics*. 3rd ed. Cambridge ; New York: Cambridge University Press. 861 pp. ISBN: 978-0-521-75618-1.
- Matthews, J. (Jan. 2005). „A Heitler Model of Extensive Air Showers“. In: *Astroparticle Physics* 22.5-6, pp. 387–397. ISSN: 09276505. DOI: 10.1016/j.astropartphys.2004.09.003. URL: <https://linkinghub.elsevier.com/retrieve/pii/S0927650504001598> (visited on 03/23/2023).
- Meyer, M., D. Horns, and H. S. Zechlin (Nov. 2010). „The Crab Nebula as a standard candle in very high-energy astrophysics“. In: *Astronomy and Astrophysics* 523, A2, A2. DOI: 10.1051/0004-6361/201014108. arXiv: 1008.4524 [astro-ph.HE].
- Mohrmann, L., A. Specovius, D. Tiziani, S. Funk, et al. (Dec. 1, 2019). „Validation of Open-Source Science Tools and Background Model Construction in  $\gamma$ -Ray Astronomy“. In: *Astronomy & Astrophysics* 632, A72. ISSN: 0004-6361, 1432-0746. DOI: 10.1051/0004-6361/201936452. URL: <https://www.aanda.org/articles/aa/abs/2019/12/aa36452-19/aa36452-19.html> (visited on 03/15/2023).
- Naumann, Christopher, Julien Bolmont, Pascal Corona, Eric Delagnes, et al. (May 21, 2013). „NECTAR: New Electronics for the Cherenkov Telescope Array“. In: DOI: 10.22323/1.158.0030.
- Nelson, W. R. and Yoshihito Namito (Feb. 9, 1990). *The EGS4 Code System: Solution of Gamma-Ray and Electron Transport Problems*. SLAC-PUB-5193; CONF-900343-3. Stanford Linear Accelerator Center, Menlo Park, CA (USA).
- Niggemann, Tim (2016). „THE SILICON PHOTOMULTIPLIER TELESCOPE FAMOUS FOR THE DETECTION OF FLUORESCENCE LIGHT“. PhD thesis. RWTH Aachen University.
- Noethe, Maximilian, Karl Kosack, Lukas Nickel, and Michele Peresano (2021). „Prototype Open Event Reconstruction Pipeline for the Cherenkov Telescope Array“. In: *Proceedings, 37th International Cosmic Ray Conference*. Vol. 395. 744. Berlin, Germany. DOI: 10.5281/zenodo.7625554.
- Ohm, Stefan, Christopher Eldik, and Kathrin Egberts (June 2009). „Gamma-Hadron Separation in Very-High-Energy Gamma-Ray Astronomy Using a Multivariate Analysis Method“. In: *Astroparticle Physics* 31.5, pp. 383–391. ISSN: 09276505. DOI: 10.1016/j.astropartphys.2009.04.001. arXiv: 0904.1136 [astro-ph]. URL: <http://arxiv.org/abs/0904.1136> (visited on 03/11/2023).
- Olivera-Nieto, L., H. X. Ren, A. M. W. Mitchell, V. Marandon, and J. A. Hinton (Dec. 10, 2022). „Background Rejection Using Image Residuals from Large Telescopes in Imaging Atmospheric Cherenkov Telescope Arrays“. In: *The European Physical Journal C* 82.12, p. 1118. ISSN: 1434-6052. DOI: 10.1140/epjc/s10052-022-11067-5. URL: <https://doi.org/10.1140/epjc/s10052-022-11067-5> (visited on 03/09/2023).
- Olivera-Nieto, Laura (2022). personal correspondence.

- Olivera-Nieto, Laura, Alison M. W. Mitchell, Konrad Bernlöhr, and James A. Hinton (Dec. 2021). „Muons as a Tool for Background Rejection in Imaging Atmospheric Cherenkov Telescope Arrays“. In: *The European Physical Journal C* 81.12, p. 1101. ISSN: 1434-6044, 1434-6052. DOI: 10.1140/epjc/s10052-021-09869-0. arXiv: 2111.12041 [astro-ph]. URL: <http://arxiv.org/abs/2111.12041> (visited on 03/09/2023).
- Ostapchenko, S. (2014). „LHC data on inelastic diffraction and uncertainties in the predictions for longitudinal extensive air shower development“. In: *Phys. Rev. D* 89 (7), p. 074009. DOI: 10.1103/PhysRevD.89.074009. URL: <https://link.aps.org/doi/10.1103/PhysRevD.89.074009>.
- Parsons, R. D. and J. A. Hinton (Apr. 1, 2014). „A Monte Carlo Template Based Analysis for Air-Cherenkov Arrays“. In: *Astroparticle Physics* 56, pp. 26–34. ISSN: 0927-6505. DOI: 10.1016/j.astropartphys.2014.03.002. URL: <https://www.sciencedirect.com/science/article/pii/S0927650514000231> (visited on 03/11/2023).
- Parsons, R. D. and H. Schoorlemmer (2019). „Systematic differences due to high energy hadronic interaction models in air shower simulations in the 100 GeV-100 TeV range“. In: *Physical Review D* 100.2. DOI: 10.1103/physrevd.100.023010. URL: <https://doi.org/10.1103/physrevd.100.023010>.
- Paul, Larissa, Matthias Plum, Merlin Schaufel, Thomas Bretz, et al. (2021). *Hybrid cosmic ray measurements using the IceAct telescopes in coincidence with the IceCube and IceTop detectors*. DOI: 10.48550/ARXIV.2108.05572. arXiv: 2108.05572 [astro-ph.HE]. URL: <https://arxiv.org/abs/2108.05572>.
- Peters, B. (Nov. 1, 1961). „Primary Cosmic Radiation and Extensive Air Showers“. In: *Il Nuovo Cimento (1955-1965)* 22.4, pp. 800–819. ISSN: 1827-6121. DOI: 10.1007/BF02783106. URL: <https://doi.org/10.1007/BF02783106> (visited on 04/24/2023).
- Pierog, T. and K. Werner (2009). „EPOS Model and Ultra High Energy Cosmic Rays“. In: *Nuclear Physics B - Proceedings Supplements* 196. Proceedings of the XV International Symposium on Very High Energy Cosmic Ray Interactions (ISVHECRI 2008), pp. 102–105. ISSN: 0920-5632. DOI: <https://doi.org/10.1016/j.nuclphysbps.2009.09.017>. URL: <https://www.sciencedirect.com/science/article/pii/S0920563209006537>.
- Preuß, S., G. Hermann, W. Hofmann, and A. Kohnle (2002). „Study of the photon flux from the night sky at La Palma and Namibia, in the wavelength region relevant for imaging atmospheric Cherenkov telescopes“. In: *Nuclear Instruments and Methods in Physics Research Section A: Accelerators, Spectrometers, Detectors and Associated Equipment* 481.1, pp. 229–240. ISSN: 0168-9002. DOI: [https://doi.org/10.1016/S0168-9002\(01\)01264-5](https://doi.org/10.1016/S0168-9002(01)01264-5). URL: <https://www.sciencedirect.com/science/article/pii/S0168900201012645>.
- Puehlhofer, G., O. Bolz, N. Goetting, and the HEGRA Collaboration (Dec. 2003). „The Technical Performance of the HEGRA System of Imaging Air Cherenkov



- Telescopes“. In: *Astroparticle Physics* 20.3, pp. 267–291. ISSN: 09276505. DOI: 10.1016/j.astropartphys.2003.06.001. arXiv: astro-ph/0306123.
- Purvinskis, Robert, Dirk Giggenbach, Hennes Henniger, Nicolas Perlot, and Florian David (July 2003). „Multiple Wavelength Free-Space Laser Communications“. In: vol. 4975, pp. 12–19. ISBN: 0-8194-4775-7. DOI: 10.1117/12.478932. URL: <https://doi.org/10.1117/12.478932>.
- Riedl, M.J. (2001). *Optical Design Fundamentals for Infrared Systems*. SPIE tutorial texts. Society of Photo Optical. ISBN: 9780819440518.
- Roehm, GmbH (2002a). *PLEXIGLAS SUNACTIVE GS, UV-durchlaessig Farblos 2458*. [https://per-plex.de/wp-content/uploads/2019/03/SUNACTIVE\\_GS\\_1.pdf](https://per-plex.de/wp-content/uploads/2019/03/SUNACTIVE_GS_1.pdf). [Online; accessed 16-December-2022].
- (2002b). *PLEXIGLAS XT, UV-durchlaessig Farblos 0A770*. <https://www.plexiglas.de/files/plexiglas-content/pdf/technische-informationen/232-6-PLEXIGLAS-XT-UV-durchlaessig-farblos-0A770.pdf>. [Online; accessed 10-December-2022].
- Rohatgi, Ankit (2022). *Webplotdigitizer: Version 4.6*. URL: <https://automeris.io/WebPlotDigitizer>.
- Salzmann, Heiko (2020). „Investigation of the Optical and Gamma-Ray Point Spread Functions of H.E.S.S. CT5 after the Installation of NamCam“. MA thesis. Institut für Astronomie und Astrophysik.
- (2023). personal correspondence.
- Sanuki, T., M. Motoki, H. Matsumoto, E. S. Seo, et al. (Dec. 2000). „Precise Measurement of Cosmic-Ray Proton and Helium Spectra with the BESS Spectrometer“. In: *Astrophys. J.* 545.2, pp. 1135–1142. ISSN: 0004-637X. DOI: 10.1086/317873. URL: <https://iopscience.iop.org/article/10.1086/317873>.
- Schaefer, Johannes (2019). „Temperature dependent aspects of the Compact High Energy Camera (CHEC-S) Front-End Electronic (FEE) calibration“. MA thesis. Erlangen Centre for Astroparticle Physics (ECAP).
- Schwartz, M. (2002). *Encyclopedia of Materials, Parts and Finishes, Second Edition*. CRC Press. ISBN: 9781420017168.
- SCI, Semiconductor Components Industries (2021). *Silicon Photomultipliers (SiPM), High PDE and Timing Resolution Sensors in a TSV Package J-Series SiPM Sensors*. [https://www.mouser.de/datasheet/2/308/1/MICROJ\\_SERIES\\_D-1811589.pdf](https://www.mouser.de/datasheet/2/308/1/MICROJ_SERIES_D-1811589.pdf). [Online; accessed 22-December-2022].
- Sommers, Paul (July 2005). „First estimate of the primary cosmic ray energy spectrum above 3-EeV from the Pierre Auger Observatory“. In: *29th International Cosmic Ray Conference*. arXiv: astro-ph/0507150.
- Steinmassl, Simon (2023). „Probing particle acceleration in stellar binary systems using gamma-ray observations“. [Unpublished doctoral dissertation]. PhD thesis. Max Plank institute for nuclear physics in Heidelberg, Germany.

- Tavernier, Thomas, Jean-François Glicenstein, and François Brun (Sept. 4, 2019). *Status and Performance Results from NectarCAM – a Camera for CTA Medium Sized Telescopes*. DOI: 10.48550/arXiv.1909.01969. arXiv: arXiv:1909.01969.
- Tjus, Julia Becker and Lukas Merten (2020). *Closing in on the origin of Galactic cosmic rays using multimessenger information*. arXiv: 2002.00964 [astro-ph.HE].
- Ulrich, Ralf, Ralph Engel, and Michael Unger (Mar. 22, 2011). „Hadronic Multiparticle Production at Ultrahigh Energies and Extensive Air Showers“. In: *Physical Review D* 83.5, p. 054026. ISSN: 1550-7998, 1550-2368. DOI: 10.1103/PhysRevD.83.054026. URL: <https://link.aps.org/doi/10.1103/PhysRevD.83.054026> (visited on 03/22/2023).
- Unbehaun et al. (2023). „Constraints on the high-energy gamma-ray emission from the Crab nebula from a Fermi-LAT and H.E.S.S. multi-instrument analysis“. In preparation.
- Vacanti, G., P. Fleury, Y. Jiang, E. Paré, et al. (1994). „Muon Ring Images with an Atmospheric Cherenkov Telescope“. In: *Astroparticle Physics* 2.1, pp. 1–11. ISSN: 0927-6505. DOI: 10.1016/0927-6505(94)90012-4.
- Vassiliev, V. V., S. J. Fegan, and P. F. Brousseau (Sept. 2007). „Wide Field Aplanatic Two-Mirror Telescopes for Ground-Based Gamma-Ray Astronomy“. In: *Astroparticle Physics* 28.1, pp. 10–27. ISSN: 09276505. DOI: 10.1016/j.astropartphys.2007.04.002. arXiv: astro-ph/0612718.
- Vincent, P. (2005). „H.E.S.S. Phase II“. In: *29th International Cosmic Ray Conference*. ICRC 2005. Mumbai: Tata Institute of Fundamental Research. URL: <https://cds.cern.ch/record/963464/files/15163-fra-vincent-P-abs1-og27-oral.pdf> (visited on 03/29/2023).
- Virtanen, Pauli, Ralf Gommers, Travis E. Oliphant, Matt Haberland, et al. (2020). „SciPy 1.0: Fundamental Algorithms for Scientific Computing in Python“. In: *Nature Methods* 17, pp. 261–272. DOI: 10.1038/s41592-019-0686-2.
- W. Hanlon (2021). *Cosmic Ray spectra of various experiments*. <https://web.physics.utah.edu/~whanlon/spectrum.html>. [Online; accessed 11-April-2023].
- Watson, Jason John and Justus Zorn (2020). „Commissioning and Performance of CHEC-S – a compact high-energy camera for the Cherenkov Telescope Array“. In: *PoS ICRC2019*, p. 821. DOI: 10.22323/1.358.0821. arXiv: 1907.09252 [astro-ph.IM].
- Weekes, T. C., M. F. Cawley, D. J. Fegan, K. G. Gibbs, et al. (July 1, 1989). „Observation of TeV Gamma Rays from the Crab Nebula Using the Atmospheric Cherenkov Imaging Technique“. In: *The Astrophysical Journal* 342, p. 379. ISSN: 0004-637X. DOI: 10.1086/167599.
- White, R. (July 31, 2021). „The Small-Sized Telescopes for the Southern Site of the Cherenkov Telescope Array“. In: *Proceedings of 37th International Cosmic Ray Conference — PoS(ICRC2021)*, p. 728. DOI: 10.22323/1.395.0728. arXiv: 2110.14527 [astro-ph].

- Wilson, R.T. (2013). „Py6S: A Python interface to the 6S radiative transfer model“. In: *Computers & Geosciences* 51, pp. 166 –171. DOI: <http://dx.doi.org/10.1016/j.cageo.2012.08.002>. URL: <http://www.sciencedirect.com/science/article/pii/S0098300412002798>.
- World Health Organization (2022). *Radiation: Ultraviolet (UV) radiation*. [https://www.who.int/news-room/questions-and-answers/item/radiation-ultraviolet-\(uv\)](https://www.who.int/news-room/questions-and-answers/item/radiation-ultraviolet-(uv)). [Online; accessed 10-December-2022].
- Zink, Adrian (2021). personal correspondence.
- Zombeck, Martin V. (2006). *Handbook of Space Astronomy and Astrophysics*. 3rd ed. Cambridge University Press. DOI: 10.1017/CB09780511536359.
- Zorn, J., R. White, J.J. Watson, T.P. Armstrong, et al. (2018). „Characterisation and testing of CHEC-M—A camera prototype for the small-sized telescopes of the Cherenkov telescope array“. In: *Nuclear Instruments and Methods in Physics Research Section A: Accelerators, Spectrometers, Detectors and Associated Equipment* 904, 44–63. ISSN: 0168-9002. DOI: 10.1016/j.nima.2018.06.078. URL: <http://dx.doi.org/10.1016/j.nima.2018.06.078>.
- Zorn, Justus (Jan. 2020). „Cherenkov camera and analysis development for highest-energy gamma-ray astronomy“. PhD thesis. Ruprecht-Karls University of Heidelberg, Germany.



## Danksagung

An erster Stelle möchte ich mich erst einmal bei Herrn Prof. Dr. Stefan Funk bedanken, dass mir stets der Freiraum gegeben und Vertrauen geschenkt wurde, um Projekte auf meine ganz besondere Art anzugehen. Besonders bedanken möchte ich mich auch, dass mir der Platz im MC Validierungsteam angeboten wurde. Gerade durch die Arbeit an diesem Thema und mit den beteiligten Personen bin ich sehr gewachsen.

Ein weiterer spezieller Dank gilt meinen Eltern und meinem Bruder, die mich durch all die Studienjahre getragen und immer unterstützt haben. Ohne Sie wäre diese Arbeit nicht in dieser Form zustande gekommen.

Ich möchte im Nachhinein noch folgenden Personen und Gruppen danken:

- Jelena Celic für zahllose lustige Tage im Büro. An der Betreuung deiner Masterarbeit bin ich als Person sehr gewachsen. Gerade die langen Abende im Büro, wenn wir uns wieder an einem Thema festgesetzt haben, sind mir sehr in Erinnerung geblieben.
- Benjamin Schwab für die stetige Gesellschaft im alten Büro, die stete Gesprächsbereitschaft und das Korrekturlesen meiner Arbeit.
- Dr. Adrian Zink für seine stetige Begleitung seit meiner Bachelorarbeit und steten Hilfe rund um IceACT, TARGET und sonstiger Hardware.
- Dr. Alison Mitchell für das Korrekturlesen mehrerer Kapitel, die stetige Hilfsbereitschaft bei Fragen und zahlreiche interessante Diskussionen.
- Dr. Rodrigo Lang für das Korrekturlesen des MC Validierungskapitels und zahlreiche lustige Unterhaltungen.
- Das MC Validierungsteam für eine der besten Teamerfahrungen, die ich je hatte. Gemeinsam hat die Arbeit stets Spaß gemacht, vor allem durch die ganzen Scherze. Zusammen haben wir sogar den H.E.S.S. Preis gewonnen und ich freue mich auch auf zukünftige Zusammenarbeit.
- Dr. Konrad Bernlöhr für die stetige Unterstützung in Bezug auf *sim\_telarray* und sehr ausführliche E-Mails bei Fragen.
- Dr. Laura Olivera-Nieto für das Beantworten vieler Fragen zur ABRIR-Methode und für das Erstellen der Hintergrund-Templates.
- Meine Freunde für die emotionale Unterstützung auch in schweren Zeiten. Ganz besonderen Dank möchte ich hier Raphael Schwarz, Dominik Gunzelmann, Janik Koschinski, Maximilian Westermann, Peter Hellmann und Leon Kubecki aussprechen.
- Gabriele Eckner, dafür, dass sie stets ein Eckpfeiler für die gesamte Arbeitsgruppe ist und mit ihrem Wirken uns die Arbeit vereinfacht.
- Den besten Bürokollegen, die man sich wünschen kann: Tina Wach, Jelena Celic und Benedetta Bruno.

- Dem Shadow Office für das spontane Korrekturlesen der Einleitung und für die stetige Gastfreundschaft bei Spontanbesuchen.
- Dr. Andreas Specovious, Dr. Samuel Spencer, Dr. Vikas Joshi, Andreas Zmija und Katrin Streil für das Korrekturlesen von Teilen meiner Arbeit.
- Dem gesamten ECAP für die beste Arbeitsatmosphäre, die ich je erleben durfte, stets offene Ohren für Probleme und der Fachkompetenz, die jeder stets zur Verfügung stellt.